Study of the physics of shock ignition

Diego Viala

THÈSE PRÉSENTÉE
POUR OBTENIR LE GRADE DE

DOCTEUR
DE L'UNIVERSITÉ DE BORDEAUX

ÉCOLE DOCTORALE N°209 SCIENCES PHYSIQUES ET DE L'INGÉNIEUR

LASERS, MATIÈRE, NANOSCIENCES

Par **Diego VIALA**

Étude de la physique de l'allumage par choc

Directeur de thèse :
Dimitri BATANI

Soutenue le 05 Juillet 2024

Membres du jury :

M. Dimitri BATANI	Professeur	Université de Bordeaux	Directeur
M. Sébastien LE PAPE	Directeur d'étude	École Polytechnique	Rapporteur
M. Valeri GONCHAROV	Directeur de recherche	Rochester University	Rapporteur
M. Benoît CANAUD	Ingénieur-Chercheur	CEA/DIF	Examinateur
M. Javier HONRUBIA	Professeur	Uni. Poli. de Madrid	Examinateur
M. João SANTOS	Professeur	Université de Bordeaux	Président du Jury

Membres invités :

M. Arnaud COLAÏTIS	Chercheur	Rochester University	Co-encadrant
M. Didier RAFFESTIN	Ingénieur-Chercheur	CEA/CESTA	Invité

Étude de la physique de l'allumage par choc

Résumé : Une décennie d'expériences au "National Ignition Facility" a démontré que la fusion par confinement inertiel constitue une approche crédible pour la production d'énergie, avec des résultats allant au-delà du régime d'allumage. Cependant, l'approche par attaque indirecte se révèle inadéquate pour les implosions à gain élevé et une production d'énergie fiable. L'option d'allumage par attaque directe est privilégiée en raison de ses conceptions de cible plus simples et de son meilleur couplage énergétique. Actuellement, aucune installation laser à l'échelle d'allumage n'est configurée selon l'approche directe standard, posant ainsi un défi à relever. Les expériences intégrées d'allumage par attaque directe se sont principalement concentrées sur la compréhension de la physique à des échelles réduites, dans le but ultime de démontrer la nécessité et la faisabilité de construire une installation laser internationale dédiée à l'attaque directe.

Ce manuscrit de thèse présente une étude approfondie sur la validation de codes d'hydrodynamique radiative 3D à l'état de l'art, ainsi que sur la compréhension des bas modes d'éclairement laser et du couplage laser-cible, jouant un rôle crucial dans la fusion par confinement inertiel. L'examen attentif des modèles de CBET revêt une importance capitale dans ce contexte, assurant la précision des simulations et contribuant à la conception des futures installations à attaque directe. De plus, l'investigation de l'homogénéité du laser sur la cible est impérative pour appréhender son impact global sur le système.

Mots-clés : Fusion par confinement inertiel, Physique des hautes densités d'énergie, Interaction laser-plasma, CBET, Qualité d'éclairement, Simulations numériques, Asymétries de bas modes, Transfert d'énergie par faisceaux croisés, Hydrodynamiques

---

Study of the physics of shock ignition

Abstract: A decade of experiments at the National Ignition Facility has proven that inertial confinement fusion is a credible approach to energy production, with experiments having exceeded the ignition regime. However, the indirect-drive approach is not suited for high gain implosions and reliable energy production. The direct-drive ignition approach is favoured for energy production as it features simpler target designs and couples more energy to them. There are currently no ignition-scale laser facilities configured for the standard direct-drive approach. Integrated direct-drive experiments have mostly been focused on understanding the physics at reduced scales, with the ultimate goal of demonstration of necessity and feasibility of construction for an international direct-drive laser facility.

This thesis manuscript presents a study on the validation of state-of-the-art 3D radiative hydrodynamics codes and the understanding of low modes and laser coupling which play crucial roles in the study of inertial fusion energy. Careful examination of CBET models is of paramount importance in this context, ensuring the accuracy of simulations and contributing to the design of future direct-drive facilities. In addition, the investigation of laser homogeneity on target is imperative to understand its overall impact on the system.

Keywords: Inertial confinement fusion, High-energy density physics, Laser-plasma interaction, CBET, Irradiation quality, Numerical simulations, Low-modes asymmetries, Cross-beam energy transfer, Hydrodynamics

---

Centre Lasers Intenses et Applications
UMR 5107 Université de Bordeaux-CNRS-CEA, 33405 Talence, France.

Remerciements

Avant d'entrer dans le vif du sujet, je tiens à exprimer ma profonde gratitude à toutes les personnes qui ont contribué à la réalisation de ce manuscrit. Tout d'abord, je remercie mes encadrants de thèse : Dimitri Batani, Arnaud Colaïtis et Didier Raffestin. Merci de m'avoir offert l'opportunité de travailler au CELIA sur un sujet passionnant qui m'a occupé durant plus de trois ans.

Un merci tout particulier à toi, Arnaud, pour ta disponibilité constante et tes conseils toujours avisés. Ton implication tout au long de cette thèse a été précieuse. J'ai beaucoup appris à tes côtés, et sache que ta bienveillance, rare, m'a profondément marqué. Merci également de nous avoir encouragés, Romain et moi, à présenter nos travaux aux États-Unis. Pour notre premier talk, faire face aux chercheurs américains, dont nous connaissions les noms grâce à leurs nombreuses publications, fut un défi impressionnant (et une grande source de stress), mais aussi une formidable immersion dans le milieu. Si j'en suis arrivé là aujourd'hui, c'est en grande partie grâce à toi. Ce fut un réel plaisir de travailler avec toi, et j'espère que l'on aura l'occasion de collaborer à l'avenir (avec une relation à distance LLE-LULI par exemple ;)).

Je tiens à remercier les membres du jury : les rapporteurs Sébastien Le Pape et Valeri Goncharov, ainsi que les examinateurs Benoît Canaud, Javier Honrubia et João Santos, à qui j'ai eu l'honneur de présenter mon travail. Je remercie tout particulièrement les rapporteurs Le Pape et Goncharov pour le temps qu'ils ont consacré à la lecture et à la correction du manuscrit, ainsi que pour leurs commentaires pertinents. Un grand merci également à João Santos d'avoir présidé la soutenance. Sébastien, j'ai hâte de collaborer avec toi au LULI.

Je remercie chaleureusement les membres du staff informatique du CELIA, Gaëtan et Richard, qui ont toujours été présents pour me dépanner en cas de problème technique. Sans vous, la recherche scientifique avancerait bien plus lentement au CELIA. Un grand merci également à Sophie, Céline et Sonia pour leur gentillesse et leur disponibilité sans faille.

Merci Jean-Luc Feugeas et Matthieu Bardon d'avoir animé avec l'aide de Vladimir Tikhonchuk ces réunions FCI pendant ma rédaction de thèse ! Cela m'a permis de mettre certaines choses au clair. Aussi, merci Didier, Philippe et Patrick de m'avoir fait découvrir la pala, sport très défoulant, surtout pendant une thèse !

Je tiens également à exprimer ma profonde reconnaissance envers tous ceux qui ont enrichi mon quotidien durant cette période bordelaise. Un grand merci aux doctorants et postdocs du CELIA. Pour beaucoup d'entre vous, vous étiez d'abord des inconnus, puis des collègues, et très rapidement, vous êtes devenus des amis précieux. Mes premières

pensées vont à Edoardo, avec qui j'ai partagé deux ans et demi dans le même bureau, discutant de sciences, de jeux vidéo, et de culture geek en général. Merci pour ton accueil chaleureux au CELIA et pour tout ce qui a suivi.

Je tiens également à remercier celui que je considère comme mon premier ami au CELIA, Christos. Tu as été un soutien inestimable durant mes premiers mois à Bordeaux, et j'espère sincèrement pouvoir te rendre visite bientôt en Grèce. Au fil du temps, j'ai eu la chance de rencontrer d'autres personnes extraordinaires qui sont désormais des anciens du labo : Thibault, Donaldi, mais aussi Paul(s), Victorien, Adrien, Lena, Cori, Alessandro, et Guillaume. Merci à vous tous pour ces moments festifs et mémorables que nous avons partagés ensemble.

Il y a aussi ceux qui m'ont accompagné jusqu'à la fin de ma thèse. Des personnes avec qui j'ai partagé beaucoup de rires, de boissons (plus ou moins alcoolisées), de repas mais aussi des moments d'amitié sincère. Je ne vous oublie pas. Merci Romain (bon courage pour la soutenance !!), Morad (l'homme au grand coeur sauf quand Mored prend le dessus), Alexandre (top 1 plus aigri du labo), Alana (ce n'est que partie remise pour te rendre visite au Canada !), Diluka (#jamaisla mais tqt au moins y a des stories), Marine (un petit squash ?), Arthur (LE collègue pour parler sport), Phil (our most philosophical friend), Feufeu (empanadas?) , Thomas (empanadas?), Margaux (merci de m'avoir fait découvrir Hollow Knight), Florent (ou alors c'est toi le top 1 plus aigri du labo ?), Howel (toujours chaud pour sortir) et Clément (on se retrouvera à l'EPFL un jour tqt pas). Pour beaucoup d'entre vous, vous êtes en fin ou au milieu de thèse ; je vous envoie toutes mes forces et vous dis à bientôt.

Plus récemment, j'ai eu la chance de rencontrer de nouveaux arrivants que je tiens également à remercier : Letizia (GREAT encounter), Sotirios, Paul, Aurélia. Je vous souhaite une bonne continuation !

Special thanks to Duncan Barlow. We spent two years together in the same office, working on very similar subjects. While I am very grateful for the opportunity to work and learn so much with you, I am even more grateful to be your friend. I'm looking forward to working and seeing you around Paris for more adventures.

À mes amis de toujours, je vous dois quelques mots. Joseph, Tom, je ne sais pas si le destin a joué un rôle pour que nous nous retrouvions tous les trois à Bordeaux, mais quelle brillante idée ! C'était une chance inouïe de partager à nouveau des moments ensemble dans une ville qui, au départ, n'était pas la nôtre. À nos innombrables virées nocturnes, nos week-ends, et toutes ces aventures qui resteront gravées dans ma mémoire. Je suis également reconnaissant d'avoir pu compter sur les autres lascars qui sont venus loger à la maison et me rendre visite à plusieurs reprises : Thibault, Bastien, Valentin, François, Gauthier. Ces fins de semaine n'étaient peut-être pas les plus reposantes, mais elles m'ont fait un bien fou, me rappelant à quel point je peux compter sur des amis comme vous. Merci, sincèrement. Merci aussi à Terry avec qui on s'est retrouvés sur Bordeaux, franchement ce fut un vrai kiff !

Il est temps de remercier ceux qui m'ont toujours offert un soutien inconditionnel : ma famille. Ma réussite vous revient en grande partie. Papa, quand j'étais enfant, je rêvais de faire mieux que toi, l'ingénieur que j'admirais tant. En grandissant, j'ai compris qu'il n'y a pas de véritable mesure du succès. Je ne devais pas chercher à faire "mieux" que toi. Bien que je n'aie pas suivi exactement ton parcours, j'ai trouvé le mien. C'est grâce à toi et à ta passion pour les sciences que j'ai développé un amour pour les mathématiques et, plus largement, pour les sciences, éveillant ainsi la curiosité du petit garçon que j'étais. Ce

fondement m'a permis d'avancer et de grandir, et je t'en suis profondément reconnaissant.

Mais cette passion pour la recherche, c'est aussi, d'une certaine manière, à toi, Maman, que je la dois. Après plusieurs mois difficiles en prépa, tu as su déceler mon mal-être et m'encourager à reprendre mes études à l'université. À partir de ce moment, tout s'est éclairé. Mon goût pour les sciences s'est ravivé, et j'ai poursuivi mon chemin pour aller aussi loin que possible. Aujourd'hui, me voici en train d'écrire les remerciements de mon manuscrit de thèse. Así que te lo digo en español: este éxito es en gran parte gracias a ti y a una de tus mayores fuerzas: el amor y apoyo inquebrantables que tienes para los tuyos. Muchísimas gracias, mamá, este diploma es también tuyo.

Enfin, je tiens à exprimer toute ma gratitude à mes grands-parents. À toi, Papi Gilbert, merci pour ta sagesse, ton calme et tes encouragements constants tout au long de ce parcours. À ma Mamie, y a mis Abuelos qui nous ont quittés, où que vous soyez, votre amour et vos valeurs continuent de me guider. Merci du fond du coeur.

Aussi, merci à tous les autres membres de ma famille et belle-famille. Ce fut un grand plaisir de se retrouver tout au long de la thèse. Votre soutien et votre présence ont rendu cette aventure encore plus spéciale.

Clémence, il m'est impossible de conclure ces remerciements sans te rendre hommage. Par où commencer ? Ton soutien a été bien plus qu'une simple présence, tu as été le socle sur lequel j'ai pu m'appuyer dans les moments les plus difficiles. Ta patience (oui, tu as bien lu), ta bienveillance, et ta capacité à me redonner espoir ont fait toute la différence. Nous avons traversé ensemble cette aventure exigeante, et je suis profondément reconnaissant que tu aies été à mes côtés, je te dois beaucoup. Ce que nous avons construit ces dernières années est le début de bien d'autres belles histoires à venir, et je suis ravi de les écrire avec toi. Avec tout mon amour, merci d'être celle que tu es.

Contents

Abstract

Remerciements

Introduction en français **1**

1 Introduction **9**
1.1 Elements of controlled thermonuclear fusion . . . 10
1.1.1 Fusion reaction . . . 10
1.1.2 Cross sections . . . 11
1.1.3 The Lawson criterion . . . 12
1.2 Magnetic Confinement Fusion . . . 13
1.3 Inertial Confinement Fusion . . . 14
1.3.1 Conditions for ignition in ICF . . . 15
1.3.2 Indirect drive . . . 17
1.3.3 Direct drive . . . 18
1.3.4 Alternative schemes . . . 19
1.3.4.1 Fast ignition . . . 19
1.3.4.2 Shock ignition . . . 20
1.4 Limitations . . . 20
1.4.1 Parametric instabilities . . . 20
1.4.2 Long-wavelength perturbations . . . 22
1.5 Improving the laser irradiation and absorption . . . 22
1.6 Objective of this work . . . 23
1.7 Organization of the manuscript . . . 24

2 Hydrodynamics of the implosion **27**
2.1 The kinetic Boltzmann equation . . . 27
2.2 Fluid conservation equations . . . 29
2.2.1 0^{th} moment of the Boltzmann equation: mass conservation . . . 29
2.2.2 1^{st} moment of the Boltzmann equation: momentum conservation . . . 29
2.2.3 2^{nd} moment of the Boltzmann equation: energy flux conservation . . . 30
2.3 Acoustic waves . . . 30
2.3.1 Application to ideal gases . . . 31
2.4 Shock waves . . . 32
2.4.1 Shock formation . . . 32
2.4.1.1 Discontinuities . . . 32
2.4.1.2 Rankine-Hugoniot relations . . . 33
2.4.2 Hugoniot curves . . . 34

2.4.3 Weak and strong shocks: a matter of entropy deposition 35
2.4.4 Adiabat 37
2.5 Spherical implosion description 37
2.5.1 Target and laser driver choice 38
2.5.2 shell implosion diagramm 40
2.5.2.1 Adiabat shaping and compression phase 41
2.5.2.2 Acceleration phase 44
2.5.2.3 Deceleration and stagnation 50
2.5.2.4 Hot spot ignition and thermonuclear combustion 53
2.6 Target stability limiting effects 55
2.6.1 Hydrodynamic instabilities 55
2.6.1.1 Perturbations effects on system stability 55
2.6.1.2 The Rayleigh-Taylor instability 56
2.7 Radiative hydrodynamic codes used: *CHIC* and *ASTER* 60
2.7.1 *CHIC* 60
2.7.2 *ASTER* 61
2.8 Conclusion 61

3 Laser plasma interaction in the inertial confinement fusion framework 65
3.1 Electromagnetic wave propagation in a plasma 65
3.1.1 Light waves in plasma 65
3.1.1.1 Wave propagation equations for electromagnetic waves . . 65
3.1.2 Dielectric response of a non-collisional plasma 67
3.1.3 Dispersion relation of electromagnetic waves in the cold plasma approximation 68
3.2 Collisional absorption with a density dependent collision frequency and two different density profiles 71
3.2.1 Dielectric response of a collisional plasma 71
3.2.2 The WKB approximation for inhomogeneous plasmas 74
3.2.3 Laser absorption in a density gradient: linear and exponential profiles 75
3.3 Longitudinal waves in plasmas 77
3.3.1 Electron plasma waves 77
3.3.2 Ion acoustic waves 79
3.4 Nonlinear laser plasma instabilities and other laser absorption processes . . 80
3.4.1 Main suprathermal electron generation mechanisms 81
3.4.1.1 Stimulated Raman Scattering 81
3.4.1.2 Two-plasmon decay 82
3.4.1.3 Resonant absorption 83
3.4.2 Main absorption losses 85
3.4.2.1 Stimulated Brillouin scattering 85
3.4.2.2 Cross-Beam Energy Transfer 85
3.5 Modeling laser propagation in a plasma: the inverse ray-tracing code *IFRIIT* 93

4 Role of CBET in solid sphere ignition scale polar direct drive experiments at the National Ignition Facility 99
4.1 Motivations 99
4.2 Polar direct drive 100
4.2.1 Experimental setup description 101
4.3 Characterisation of 10 mm defocused NIF laser quads in vacuum 103

4.4 3D CBET radhydro simulation analysis of the SSS shots . . . 104
4.4.1 Hydrodynamics comparison . . . 104
4.4.1.1 High intensity shot: N190204-003 . . . 104
4.4.1.2 Low intensity shot: N210519-001 . . . 107
4.4.2 Offline calculations of N210519-001 . . . 111
4.4.3 Backscattered light comparison . . . 112
4.5 Conclusions . . . 114

5 Study of innovative beam ports arrangement geometries to assist in the design of future direct-drive laser facilities 117
5.1 Motivations . . . 117
5.2 Designs overview . . . 119
5.2.1 Charged particle method design . . . 119
5.2.2 Spherical t-sphere design . . . 120
5.2.3 Icosahedron design . . . 122
5.3 Initial optimisation study . . . 122
5.3.1 Spherical harmonics decomposition of the laser intensity on target . 122
5.3.2 Relevant laser parameters to scan: super-gaussian order and laser radius at $1/e$ . . . 123
5.3.3 Results of the scan . . . 124
5.4 Systematic errors: source of low modes . . . 127
5.4.1 Gaussian statistical sampling method for beam mispointing, target offset and power imbalance . . . 128
5.4.2 Results of the sampling . . . 129
5.4.3 Comparison to typical best laser performers at Ω60 . . . 131
5.4.4 Optimising spatial laser parameters including system errors . . . 133
5.4.5 Conclusion . . . 136
5.5 1D radhydro simulations for standard ignition and shock augmented ignition using *CHIC* . . . 137
5.5.1 Ignition window with α particle deposition . . . 138
5.5.2 Ignition criteria detection without α particle deposition . . . 140
5.6 3D radhydro simulations aiming to compare standard and shock ignition robustness to target offset using the coupled code *ASTER/IFRIIT* . . . 142
5.6.1 3D idealised simulations . . . 142
5.6.2 Target offset effects . . . 144
5.7 Conclusions . . . 149

6 Conclusion 153
6.1 Assessing the accuracy of the CBET linear kinetic model and laser coupling in the 3D radiative hydrodynamics coupled code *ASTER/IFRIIT* at the ignition scale . . . 154
6.2 Optimisation of novel beam chamber geometries for the future direct-drive facilities at the ignition scale . . . 155
6.3 Characterisation of two ignition schemes robustness to experimental errors at the ignition scale . . . 156
6.4 Perspectives . . . 157

Conclusion en français 159

Résumé détaillé **167**

Bibliography **175**

Introduction en français

Contexte scientifique

Dans l'ère de la transition énergétique, le développement de nouvelles sources d'énergie renouvelable revêt une importance cruciale. Malheureusement, les énergies éolienne, solaire et hydroélectrique ne suffisent pas à répondre aux besoins d'une population mondiale qui a presque quadruplé au cours des 100 dernières années. Les projections indiquent une population mondiale de 10 milliards de personnes d'ici la fin du XXIe siècle, accompagnée d'une demande croissante en électricité. Afin d'éviter les scénarios catastrophe prévus par le GIEC, l'humanité doit impérativement réduire ses émissions de CO_2, même si cela n'offre qu'une infime chance d'éviter ces issues redoutées. Cependant, même en réduisant considérablement la consommation énergétique, il sera crucial de maintenir une production d'énergie décarbonnée, dense et fiable. La fusion nucléaire se profile comme une solution prometteuse pour remplir ce rôle essentiel.

Par exemple, pour une combustion complète, environ 8 kWh d'électricité peuvent être générés à partir d'1 kg de charbon, tandis qu'environ 12 kWh peuvent être obtenus à partir d'1 kg de pétrole minéral. En revanche, 1 kg d'uranium enrichi (U-235) produit 24 000 000 kWh d'électricité. En termes de rendement énergétique par kilogramme, l'uranium-235 contient deux à trois millions de fois l'énergie équivalente au pétrole ou au charbon. En d'autres termes, l'utilisation d'1 kg d'uranium enrichi pour des réactions de fission au lieu de la combusion du pétrole ou du charbon permet d'éviter entre 6 et 11 kilotonnes de rejet de CO_2. La fission nucléaire offre la possibilité de réduire considérablement les émissions nocives. Cependant, la gestion des polluants radioactifs demeure un défi, notamment en ce qui concerne le stockage de ces déchets dont la durée de vie dépasse mille ans. De plus, des préoccupations subsistent en matière de sécurité, comme ont pu en témoigner certains désastres récents. Aussi, les réserves actuelles de combustible nucléaire fissile sont très inégalement réparties (3 pays détiennent 50% des resssources mondiales), pouvant créer une forte dépendance pour de nombreux pays et engendrer des conséquences potentielles en termes de coûts d'approvisionnement. Enfin, les réserves actuelles sont insuffisantes pour garantir une production d'énergie à long terme pour les centrales actuelles.

En août 2021, des chercheurs du National Ignition Facility (NIF) [1] ont dirigé 192 faisceaux laser vers la paroi intérieure d'une enceinte cylindrique en or et en uranium appauvri, appelée hohlraum. Les rayons X provenant de la paroi chauffée par le laser ont rempli la cavité cylindrique et ont ablaté la surface d'une capsule sphérique contenant du deutérium-tritium (DT), des isotopes de l'hydrogène, placée à l'intérieur du hohlraum. Cette expérience, appelée tir N210808 [2], visait à atteindre l'allumage et la combustion du combustible thermonucléaire en laboratoire pour la première fois, constituant ainsi une étape majeure dans la recherche sur la fusion nucléaire contrôlée. Cet exploit représente la culmination de nombreuses années de recherche et s'inscrit dans une initiative scientifique entamée il y a cinquante ans. En 1972, John Nuckolls [3] a posé les bases de la fusion par

confinement inertiel (FCI) et a présenté son idée fondatrice, consistant à comprimer une sphère irradiée par des faisceaux laser pour provoquer des réactions de fusion nucléaire.

Cette expérience a suivi une décennie d'expériences d'implosion avec des résultats progressivement améliorés, réalisées par une grande équipe de scientifiques et d'ingénieurs au NIF depuis 2009. Contrairement à ses prédécesseurs, le tir N210808 a atteint l'allumage, avec un rendement de fusion de 1.37 MJ, soit huit fois supérieur au rendement précédent. Bien que d'importants défis scientifiques et techniques persistent, la démonstration de l'allumage est considérée par de nombreux experts comme un événement pivot susceptible de stimuler le développement de la fusion laser en tant que source d'énergie viable. Depuis lors, plusieurs autres expériences ont franchi le seuil du "plasma brûlant", et l'allumage semble de plus en plus reproductible.

Le principe de la fusion par confinement inertiel

Dans le cadre de FCI, une petite cible, renfermant un milligramme de combustible deutérium-tritium, est exposée à un rayonnement laser intense pendant quelques nanosecondes, générant une énergie de l'ordre du mégajoule. Soumise à une compression rapide, la cible subit une montée en densité au centre, suivie d'un accroissement de température lorsque l'énergie cinétique se transforme en énergie interne. Une fois les conditions propices à l'allumage des réactions de fusion atteintes au cœur de la cible, des particules d'hélium-4 (alphas) et des neutrons de 14 MeV sont expulsés. En cas de densité surfacique adéquate de la cible (ρR), les particules alphas sont freinées, libérant leur énergie dans le combustible. La température du combustible persiste à s'élever, maintenant ainsi les réactions de manière auto-entretenue tant que la cible reste assemblée. Les neutrons, plus énergétiques, sont stoppés plus loin dans l'installation. Le gain de l'implosion se mesure par le rapport entre l'énergie libérée par les réactions de fusion et l'énergie laser injectée.

Cependant, l'expansion hydrodynamique de la cible constitue une limite à l'onde de combustion thermonucléaire. Pour réaliser un gain de cible suffisamment élevé, il est essentiel de maintenir l'onde de combustion pendant une durée considérable. Cela nécessite une inertie élevée de la cible en implosion pour confiner la matière. Selon la technologie laser utilisée, la FCI peut être envisagée pour un réacteur nucléaire lorsque le gain dépasse ~ 100.

Des installations laser imposantes, à l'image du Laser Mégajoule (LMJ) en France ou du National Ignition Facility (NIF) aux États-Unis, sont édifiées dans le but de démontrer la faisabilité de l'allumage des réactions de fusion en laboratoire. Toutefois, ces installations sont configurées pour fonctionner en attaque indirecte: le rayonnement UV du laser est converti en rayonnement X. Ainsi, par exemple au NIF, on estime que des 2 MJ en sortie de la chaîne laser, on obtient seulement 0.25 MJ d'énergie de rayonnement X couplée sur cible. Ce sont donc les rayons X qui chauffent la cible, ablatent la partie extérieure de la cible et permettent l'implosion des parties intérieures. Le principal atout de cette méthode est qu'elle permet une qualité d'éclairement élevée puisque la cible se retrouve éclairée par un bain homogène de rayons X. Cependant, le mécanisme de production des X induit une grande perte investie dans l'énergie laser. Dans le cadre de cette thèse nous nous intéressons à une approche dite d'attaque directe.

En attaque directe, les faisceaux lasers irradient l'ensemble de la surface de la cible. Le nombre fini de faisceaux laser introduit des imperfections dans la symétrie de l'illumination, entraînant des défauts dans le motif d'intensité sur la cible sphérique. De plus, il est essentiel que les faisceaux laser soient parfaitement synchronisés et possèdent une puissance

identique pour maintenir la symétrie sphérique de l'illumination. Tout écart de synchronisation ou de puissance peut entraîner des non-uniformités pendant l'implosion, provoquant le refroidissement du point chaud. Cela peut compromettre de manière significative la compression du cœur DT et l'atteinte des conditions d'allumage.

L'avantage principal de l'approche d'attaque directe réside dans le couplage direct de l'énergie laser dans la cible. Comparativement à l'attaque indirecte, des exigences moindres en énergie laser sont nécessaires pour des performances de cible similaires, ce qui pourrait entraîner des gains de cible plus élevés. Cette approche est couramment utilisée au sein de l'installation laser OMEGA60 située au LLE à Rochester, aux États-Unis, mais à des petites échelles comparées au NIF (laser de ~ 30 kJ, quelques nanosecondes et cibles de quelques centaines de microns de rayon).

Limitations

L'interaction entre un laser de haute intensité et la partie externe de la cible conduit à la création d'une région de plasma connue sous le nom de plasma coronal. Cette région de plasma présente une densité croissante en s'approchant de la cible, là où le laser se propage jusqu'à atteindre la densité critique n_c. La densité critique est définie comme la densité à laquelle les électrons du plasma oscillent à la fréquence du laser se comportent alors comme un mirroir et empêchent la propagation des ondes laser au-delà de cette densité. L'énergie du laser est principalement absorbée par rayonnement de freinage inverse par les électrons, qui se thermalisent rapidement lors de collisions avec les ions. Cette chaleur est ensuite transférée du plasma coronal à la partie plus dense de la cible par conduction thermique, dirigeant les phases de compression et d'allumage de la cible. Cependant, au cours de l'interaction, des processus non linéaires induisent des instabilités préjudiciables susceptibles de générer des électrons très énergétiques et de redistribuer le dépôt d'énergie du laser. Ces électrons, appelés *électrons chauds*, se propagent profondément dans les couches internes du combustible. Ils déposent de l'entropie le long de leur trajectoire et préchauffent la cible, compromettant le processus de compression. En particulier, le paramètre d'éclairement $I_L\lambda_L^2$ peut atteindre $\sim 10^{15}$ Wμm^2/cm^2. À ce stade, de nombreux couplages entre la lumière laser et les ondes plasma se produisent. Ces processus adoptent des comportements non-linéaires et sont néfastes à l'implosion. C'est notamment le cas du transfert d'énergie entre faisceaux croisés (CBET). Le CBET est un processus qui se produit lorsque deux ou plusieurs faisceaux laser se croisent dans un plasma et se couplent de façon résonnantes à travers les ondes acoustiques ioniques. Le CBET peut entraîner un transfert net d'énergie du faisceau et affecter à la fois la symétrie de l'implosion et le couplage laser-cible.

L'éclairement laser génère des perturbations sur le motif d'intensité de la cible, qui peuvent être mathématiquement évaluées par une décomposition en harmoniques sphériques de l'intensité laser sur la cible. Les modes bas de cette perturbation sont principalement influencés par la focalisation et l'intensité du rayonnement laser. La symétrie de l'illumination est intrinsèquement liée à la compression de la cible.

En considérant le rapport de convergence C_d comme le rapport du rayon initial de la cible R_0 au rayon final R_h du point chaud, une relation peut être établie entre la perturbation δR de ce rayon et la perturbation δv de la vitesse d'implosion : $\delta R/R_h = C_d\delta v/v_{\text{imp}}$. La perturbation tolérable au niveau du point chaud dépend de l'énergie cinétique résiduelle du combustible froid au moment de sa formation, c'est-à-dire de la marge d'allumage

de la cible. Dans tous les cas, il est impératif que les perturbations dans la forme du point chaud restent suffisamment petites pour obtenir des gains élevés. En fixant arbitrairement cette perturbation à un quart du rayon du point chaud, il en découle que la vitesse d'implosion doit demeurer uniforme à moins de 1/4C. La vitesse d'implosion, qui dépend de l'intensité du laser selon $I_L^{1/3}$ (voir l'équation (2.5.1)), impose une contrainte d'uniformité $\delta I_L/I_L \leq 3/4C_d$. Avec des valeurs typiques de C_d oscillant entre 30 et 50, cela implique qu'une uniformité d'éclairement inférieure à 1 ou 2% doit être atteinte.

Ces performances requièrent inévitablement l'utilisation d'un nombre considérable de faisceaux, ainsi qu'une maîtrise précise du rayon et de la configuration des points focaux à déployer. Comme souligné précédemment, l'approche indirecte présente l'avantage d'assurer une uniformité élevée grâce à la conversion du rayonnement laser en une source thermique dans le hohlraum. Dans ce scénario, tous les faisceaux lasers convergent vers les fenêtres d'entrée du hohlraum, délivrant ensuite leur énergie sur la surface interne de la paroi. Le contrôle de la symétrie de l'illumination s'effectue par des ajustements minutieux des positions et des configurations des points focaux. Afin de faciliter le passage à travers les fenêtres d'entrée, les faisceaux du LMJ et du NIF adoptent un profil spatial elliptique.

Le schéma d'attaque directe impose des contraintes bien plus strictes en matière de symétrie d'illumination. Plus précisément, il s'avère difficile d'atteindre un éclairement suffisamment homogène en focalisant simplement les faisceaux laser disponibles au NIF et au LMJ sur le centre de la cible. Cette approche présente un inconvénient majeur, car la partie équatoriale de la cible serait moins exposée aux faisceaux que les pôles. Cependant, des schémas d'attaque directe sont actuellement à l'étude dans ces installations, exploitant une géométrie spécifique connue sous le nom de Polar Direct Drive (PDD). Imaginé par des chercheurs de l'Université de Rochester aux États-Unis, ce schéma préconise la défocalisation et le déplacement stratégique de certains faisceaux laser pour une meilleure illumination de la partie équatoriale de la cible.

La FCI numérique

La simulation numérique en FCI revêt une importance cruciale pour appréhender et modéliser les processus physiques complexes liés à la réalisation de réactions de fusion contrôlées. Ces simulations font appel à des modèles sophistiqués afin de décrire l'interaction subtile entre le rayonnement, l'hydrodynamique et la physique des plasmas à l'intérieur de la cible, particulièrement lors des étapes de compression et d'allumage. Les outils numériques modernes ont considérablement amélioré notre capacité à explorer en profondeur ces processus théoriques, facilitant ainsi l'analyse de l'évolution de divers phénomènes. En plus de servir à la vérification des données expérimentales, les simulations permettent de prédire des tendances et des résultats.

Dans le cadre de la FCI, les simulations pertinentes abordent divers aspects de la cible, prenant en compte différentes échelles spatiales et temporelles. Les codes hydrodynamiques tels que *CHIC, DRACO, ASTER*, etc., se révèlent essentiels pour les simulations réalisées à des échelles spatiales de l'ordre de la cible de combustible (de l'ordre de quelques millimètres) et des échelles temporelles de l'ordre de la nanoseconde, correspondant à la durée de l'impulsion dans les expériences de FCI. Ces codes intègrent généralement des modèles hydrodynamiques spécifiquement conçus pour explorer des phénomènes au niveau de l'ensemble de la cible de FCI, jouant ainsi un rôle clé dans l'étude d'événements macro-

scopiques tels que les instabilités hydrodynamiques au sein du combustible, la propagation des chocs, et la simulation de divers phénomènes tels que l'absorption collisionnelle de la lumière laser ainsi que des modèles réduits des effets du CBET.

Le CBET représente l'un des nombreux phénomènes d'interaction laser-plasma présentant des défis numériques dans la conception des cibles. Ces obstacles découlent de la disparité des échelles spatiales et temporelles entre la modélisation hydrodynamique à grande échelle et l'évolution rapide et complexe des processus de couplage d'ondes inhérents au CBET.

Pendant des années, les simulations numériques ont persisté à surestimer l'absorption du laser dans les expériences menées à l'installation OMEGA60 de 10%. Plus récemment, le code d'hydrodynamique *ASTER* ([4]), [5], a été amélioré pour intégrer une implémentation en ligne du modèle laser 3D *IFRIIT* (développé par Colaïtis et al.), spécialement conçu pour cette application. Des études récentes ont démontré que lorsqu'il est utilisé dans les simulations d'implosions cryogéniques à OMEGA, le modèle *IFRIIT* offre une précision remarquable dans la reproduction des caractéristiques essentielles des implosions ([6]). Cette précision est obtenue sans nécessité d'ajustements de paramètres arbitraires, soulignant ainsi la robustesse du modèle. De manière significative, le modèle de CBET polarisé utilisé dans les simulations parvient à capturer avec succès la direction d'écoulement cohérente observée lors de nombreux tirs effectués récemment ([7]).

Bien que le CBET soit dorénavant bien compris au centre laser OMEGA grâce à des études approfondies à une échelle plus petite, son exploration à l'échelle de l'allumage demeure relativement limitée. La transition vers l'allumage présente de nouveaux défis et phénomènes nécessitant une compréhension approfondie des interactions complexes entre les lasers haute énergie, les matériaux de la cible et les réactions de fusion résultantes. Ainsi, l'étude du CBET à l'échelle de l'allumage est cruciale pour approfondir nos connaissances et améliorer l'efficacité de la FCI.

Enfin, bien que l'approche en attaque directe vise à améliorer le couplage énergétique par rapport à la méthode de l'attaque indirecte, l'utilisation du laser en attaque directe complexifie la réalisation d'une irradiation homogène. Jusqu'à présent, les recherches approfondies sur les schémas d'illumination en attaque directe se sont principalement concentrées sur les aspects géométriques [8]–[10]. Toutefois, garantir une illumination uniforme d'une bille de combustible demeure un défi majeur en FCI, influençant de manière significative les conceptions de la cible et du réacteur [11]. L'utilisation et l'exploration de conceptions innovantes visant à assurer une homogénéité d'éclairement élevée revêtent ainsi une importance toute particulière. C'est dans ce contexte que je mène mes recherches doctorales.

Objectifs et organisation du manuscrit

Le titre de ce travail est *Étude théorique de couplage laser et d'uniformité d'éclairement pour la fusion inertielle en attaque directe*. Les objectifs de la thèse sont énumérés comme suit :

- Le premier objectif consiste à valider les modules de CBET et de couplage laser-cible dans le code d'hydrodynamique radiative 3D *ASTER/IFRIIT*, à l'échelle de l'allumage. Cette validation s'effectuera dans des conditions caractéristiques im-

pliquant des géométries laser spécifiques et des intensités laser proches du régime d'allumage par choc, où le CBET joue un rôle prédominant.

- Le deuxième objectif vise à identifier et décrire de nouvelles géométries de disposition de faisceaux destinées aux futures installations d'attaque directe à l'échelle de l'allumage, en utilisant un code de tracé de rayons sur des sphères solides. Une comparaison des géométries innovantes sera réalisée pour évaluer leur robustesse face à des erreurs expérimentales persistantes. Il s'agit d'identifier les géométries qui permettent d'obtenir un éclairement laser et une intersection laser-cible les plus uniformes.

- Le troisième objectif consiste à caractériser la robustesse des schémas d'allumage à l'échelle de l'allumage en utilisant des géométries optimisées de chambre expérimentale, via des simulations d'hydrodynamique radiative en 3D. L'étude porte sur les performances de cible et du point chaud tout en augmentant linéairement les erreurs expérimentales, permettant ainsi une évaluation approfondie de la résilience des schémas d'allumage.

La validation du code couplé 3D *ASTER/IFRIIT*, ainsi que l'étude sur les géométries de chambre à faisceaux pour les futures installations d'attaque directe, sont réparties en quatre principaux chapitres. La présentation du manuscrit est la suivante :

- Le **Chapitre 2** présente les phénomènes physiques impliqués dans l'implosion d'une capsule de combustible allumée par un laser. Il établit les équations hydrodynamiques gouvernant le fluide en mouvement et la propagation des ondes de choc. Les modèles pour générer le point chaud central et amorcer son allumage sont élaborés. Enfin, les principaux effets limitants hydrodynamiques pouvant entraver à la fois l'implosion et l'allumage du combustible sont identifiés. Des exemples via des simulations 1D *CHIC* sont donnés tout au long du chapitre. Nous présentons également un aperçu des caractéristiques clés des codes de simulation hydrodynamique *CHIC* et *ASTER*, des outils largement utilisés dans cette étude.

- Le **Chapitre 3** explore la théorie linéaire de la propagation des ondes électromagnétiques dans les plasmas. Diverses descriptions de plasmas sont illustrées, et nous présentons l'évolution des ondes dans les plasmas, explorant leurs relations de dispersion. Les définitions des ondes de plasmas électroniques et des ondes acoustiques ioniques sont établies. Les sections suivantes fournissent des descriptions détaillées des instablilités paramétriques SRS, TPD, SBS et plus spécifiquement du CBET. Nous présentons un aperçu des caractéristiques clés du code de tracé de rayons inverse *IFRIIT*, qui a été utilisé pour modéliser la propagation et l'interaction du laser dans le plasma. Des équations détaillées sont présentées pour chaque instabilité.

- Le **Chapitre 4** rend compte des expériences menées sur des sphères solides en plastique au National Ignition Facility dans le cadre de l'attaque directe pour la fusion par confinement inertiel. Les principaux objectifs de ces expériences étaient de caractériser l'efficacité du couplage de l'énergie laser et de surveiller les positions des chocs à l'intérieur d'une cible solide sphérique en plastique. Les investigations ont été menées en utilisant le schéma d'éclairement en attaque directe polarisée

(PDD), qui est particulièrement sensible au CBET. La campagne présentée sert de validation pour le code couplé *ASTER/IFRIIT* en 3D à l'échelle complète. Le chapitre commence par une caractérisation des faisceaux laser hors foyer utilisés au NIF, d'un suivi des chocs et de l'analyse de la lumière rétrodiffusée avec des simulations d'hydrodynamique radiative en 3D, offrant ainsi une validation robuste des modèles physiques du code à l'échelle de l'allumage.

- Le **Chapitre 5** entreprend une analyse de la qualité d'éclairement dans des géométries de chambre à faisceaux innovantes proposées pour les futures installations d'attaque directe. Cette étude intègre des erreurs systématiques, fournissant une évaluation quantitative de la robustesse pour chaque conception. De plus, une comparaison avec la plus grande installation d'attaque directe actuelle, Ω60, est présentée. Le chapitre se conclut par la présentation des résultats de simulations d'implosions 3D, offrant des perspectives sur la conception d'allumage présentant une plus grande résilience aux asymétries persistantes de bas modes.

Les conclusions de ce travail sont présentées au **Chapitre 6**.

Chapter 1

Introduction

In the era of energy transition, the development of new renewable energy sources is crucial. Wind, solar, and hydroelectric energy, unfortunately, is not sufficient to meet the needs of the nearly quadrupled global population in the last 100 years. The projections indicate a global population of 10 billion people by the end of the 21st century, accompanied by an increasing demand for electricity. In order to avoid the catastrophic scenarios predicted by the IPCC, humanity must urgently reduce its CO_2 emissions, even if it offers only a tiny chance of avoiding these dreaded outcomes. However, even with a significant reduction in energy consumption, it will be crucial to maintain a decarbonized, dense, and reliable energy production. Nuclear fusion emerges as a promising solution to fulfill this essential role. As an example, for a complete combustion, approximately 8 kWh of electricity can be generated from 1 kg of coal, and approximately 12 kWh from 1 kg of mineral oil. On the other hand, 1 kg of enriched uranium (U-235) produces 24 000 000 kWh of electricity. Related to one kilogram, uranium-235 contains two to three million times the energy equivalent of oil or coal. This basically means that there is in between 6 to 11 kilo-tons of CO_2 that are not rejected when using 1 kg of enriched uranium for fission reactions, instead of oil or coal. Nuclear fission has the possibility to significantly reduce harmful atmospheric emissions. Furthermore, concerns persist regarding safety, as evidenced by certain recent disasters. Additionally, current reserves of fissile nuclear fuel are highly unevenly distributed (3 countries hold 50% of global resources), which could lead to strong dependence for many countries and entail potential consequences in terms of supply costs. Finally, current reserves are insufficient to ensure long-term energy production for existing power plants.

In August 2021, scientists at the National Ignition Facility (NIF) [1] fired 192 laser beams at the inner wall of a cylindrical enclosure made of gold and depleted uranium, called a hohlraum. X rays from the laser-heated hohlraum wall filled the cylindrical cavity and ablated the surface of a spherical capsule containing frozen deuterium–tritium (DT), hydrogen isotopes, placed inside the hohlraum. This experiment, known as shot N210808 [2], was an attempt at achieving ignition and burn of thermonuclear fuel in the laboratory for the first time, a milestone of controlled nuclear fusion research. This achievement is the culmination of many years of research and is part of a scientific initiative initiated fifty years ago. In 1972, John Nuckolls [3] introduced the foundations of ICF and presented his foundational idea, which involves compressing a sphere irradiated by laser beams to achieve nuclear fusion reactions.

This experiment followed a decade of implosion experiments with progressively better

results carried out by a large team of scientists and engineers at the NIF since 2009. But unlike its predecessors, N210808 achieved ignition, with a fusion yield of 1.37 MJ, 8 times larger than the previous record yield. Although major scientific and engineering challenges remain, the demonstration of ignition is seen by many experts as a pivotal event that can spearhead the development of laser fusion as a viable energy source. Since then, several other experiments have entered the burning plasma regime and ignition seems more and more repeatable.

The main use of fusion in the civil domain will be the development of nuclear fusion power plants, aiming to replace current fission-based power plants due to the advantages it offers:

- Virtually limitless fuel abundance: deuterium a natural isotope of hydrogen, which can be found in limitless quantities in seawater. Tritium, the other reactant, can be made in the reactor from lithium (${}^{6}_{3}\mathrm{Li} + {}^{1}_{0}\mathrm{n} \rightarrow {}^{4}_{2}\mathrm{He} + {}^{3}_{1}\mathrm{T}$),
- For equal weights of fuel, the energy released by fusion is greater than fission,
- No runaway risks as the plasma is confined by its own inertia or magnetic fields. It naturally tends to cool down and expand if the confinement is no longer applied, ceasing then all fusion reactions. The fundamental distinctions in the physics and technology employed in fusion reactors eliminate the possibility of a fission-type nuclear meltdown or a runaway reaction. The fusion process is inherently safe,
- Fusion reactors, unlike fission reactors, produce no high activity/long life radioactive waste. The "burnt" fuel in a fusion reactor is helium, an inert gas. Fast neutrons can activate elements that will produce wastes. They are classified as very low, low, or medium activity wastes, with half-lives mostly lower than ten years,
- There are no CO_2 or other harmful atmospheric emissions from the fusion process, and the high energy density of the fusion fuel means that few plants need to be constructed, which suggests that fusion does not contribute significantly to greenhouse gas emissions or global warming.

1.1 Elements of controlled thermonuclear fusion

1.1.1 Fusion reaction

The interest in nuclear energy, particularly fusion energy, arises from a remarkable property of matter, namely mass-energy equivalence. It has been observed that the mass of an atomic nucleus is less than the sum of the individual masses of the free constituent protons and neutrons. Einstein was the first to postulate that any change in the energy of a system can be associated with a change in mass: $\Delta E = \Delta m c^2$. This missing mass is known as the mass defect, and represents the energy that was released when the nucleus was formed. Concretely, this equation means that if a body loses part of its mass during a nuclear reaction, an energy corresponding to the product of this mass defect by the square of the speed of light, $c = 3 \times 10^8$ m/s, will be released. This energy corresponds to the nuclear binding energy U_A, highlighted by Francis William Aston [12], where he presents the measurement of binding energies per nucleon for each element. The classical representation as a function of the mass number is the famous Aston's curve 1.1.

While the nuclear transformation of very heavy elements (to the right of the Aston

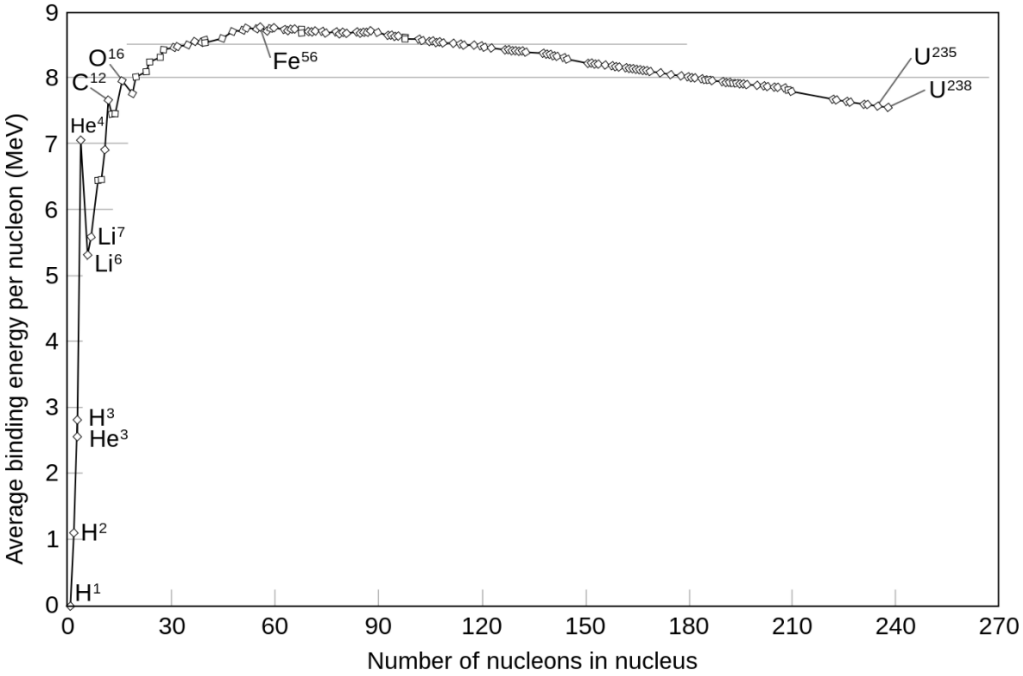

Figure 1.1 – Binding energy curve (average binding energy per nucleon in MeV against number of nucleons in nucleus) for a number of relatively common isotopes.

curve) involve converting heavy elements into lighter ones are fission reactions, a fusion reaction involves the pairing of two light nuclei, resulting in a heavier nucleus. However, the nuclei being positively charged, there is a Coulomb repulsion between them that repel them due do the electrostatic force. In order to overcome this Coulomb barrier, it is necessary to provide a significant amount of kinetic energy to the nuclei, typically on the order of a few hundred keVs or more. After overcoming the potential barrier, another fundamental interaction known as the strong force comes into play, exerting a net attractive force that pulls the two nuclei together. The Aston curve 1.1 highlights the importance of focusing on light elements such as hydrogen and its two isotopes, deuterium (D), and tritium (T), to optimise energy release. Indeed, as their binding energy is low, it is much easier to overcome their potential barrier than with uranium for example. The main reaction used for fusion related experiments is the following:

$$ {}^{2}_{1}\mathrm{D} + {}^{3}_{1}\mathrm{T} \rightarrow {}^{4}_{2}\mathrm{He}\,(3.5\,\mathrm{MeV}) + {}^{1}_{0}\mathrm{n}\,(14.1\ \mathrm{MeV}) + 17.6\,\mathrm{MeV}, \tag{1.1.1} $$

where the 17.6 MeV [1] of energy that this reaction produces are shared between a Helium nucleus, also called α-particle, and a fast neutron.

1.1.2 Cross sections

The cosmos is filled with objects of extreme masses that produce gravitational forces large enough for sustained fusion reactions to occur. Fusion reactions are prevalent processes in the universe as they provide the energy for stars, maintain high temperatures within cosmic objects, and generate, from protons and neutrons, all other elements in the periodic table up to iron (Fe^{14}, see Figure 1.1). However, replicating them on Earth in large amounts is very challenging and reproducing such gravitational attraction is unthink-

1. Note that 1 eV $\approx$ 11600 K

able. Another method needs to be found. The primary issue is that the cross-sections of these reactions are exceedingly small, thousands of times smaller than the cross-sections of elastic collisions. For this simple reason, harnessing energy by colliding accelerated projectiles with a cold, solid, or gaseous target is impossible. Despite producing some fusion reactions, a significant portion of the projectile energy will be transformed into the kinetic energy of target particles. Also, we need to confine the reactants a time long enough for fusion reactions to occur and compensate the losses of the system.

It is in 1972 that John Nuckolls [3] laid the foundations for Inertial Confinement Fusion (ICF) and presented his foundational idea, which involves compressing a sphere irradiated by laser beams to achieve nuclear fusion reactions. The matter becomes a hot and dense plasma allowing fusion reactions to occur. In this plasma, formed of electrons and nuclei, we can write the fusion reaction cross-sections of the particle that highly depend on the temperature of the particles at play. The cross-sections, $\sigma(v)$ give the probability of a fusion reaction between two particles to occur for a given temperature. For a plasma at thermal equilibrium described by Maxwellian velocity distributions, one can write the average thermal reactivity as:

$$\langle \sigma v \rangle = \int \sigma(v) v f(\mathbf{v}) \mathrm{d}\mathbf{v}, \tag{1.1.2}$$

with $v = |v_1 - v_2|$, the relative velocity between the 2 particles of mass M_1 and M_2 and f is the Maxwellian distribution function of $\mathbf{v}$:

$$f(\mathbf{v}) = \left(\frac{\mu}{2\pi k_b T}\right)^{3/2} \exp\left(-\frac{\mu \mathbf{v}^2}{2k_b T}\right), \tag{1.1.3}$$

with μ the reduced mass of the system given by: $\mu = M_1 M_2/(M_1 + M_2)$. The reactivity $\langle \sigma v \rangle$ is the reaction probability per unit of time and unit of density averaged over the distribution of reactants over the kinetic energy. The reactivity, denoted as $\langle \sigma v \rangle$, quantifies the reaction probability per unit of time and unit of density. It is averaged over the distribution of reactants with respect to kinetic energy. The Figure 1.2 illustrates the reactivities calculated using the Maxwellian particle distribution for the most significant fusion reactions at varying temperatures.

1.1.3 The Lawson criterion

For this reaction to be profitable and viable for industrial energy production, the energy obtained from the reaction must exceed the energy invested to initiate it. In other words, a positive gain is required. The minimal condition for a positive balance, known as the Lawson criterion [13], is achieved by considering the energy needed to create a plasma with thermonuclear temperatures, particle losses during confinement, the energy released from fusion, and the energy loss of a charged particle undergoing acceleration (Bremsstrahlung):

$$n\tau > 10^{15} \text{ cm}^{-3}\text{s}, \tag{1.1.4}$$

where n and τ are, respectively, the density (assuming globally neutral plasma $n_e \approx n_i = n$) and confinement time of the plasma. A plasma temperature of $T_i = 5$ keV is assumed, and the plasma is considered as an ideal gas. Two principal branches can then be explored. Either the plasma is heavily compressed and heated and confined for a small period of time. This corresponds to a plasma of density $n = 10^{25}$ cm^{-3} confined in a period of time τ of roughly 10 ps, this corresponds to Inertial Confinement Fusion (ICF). Either

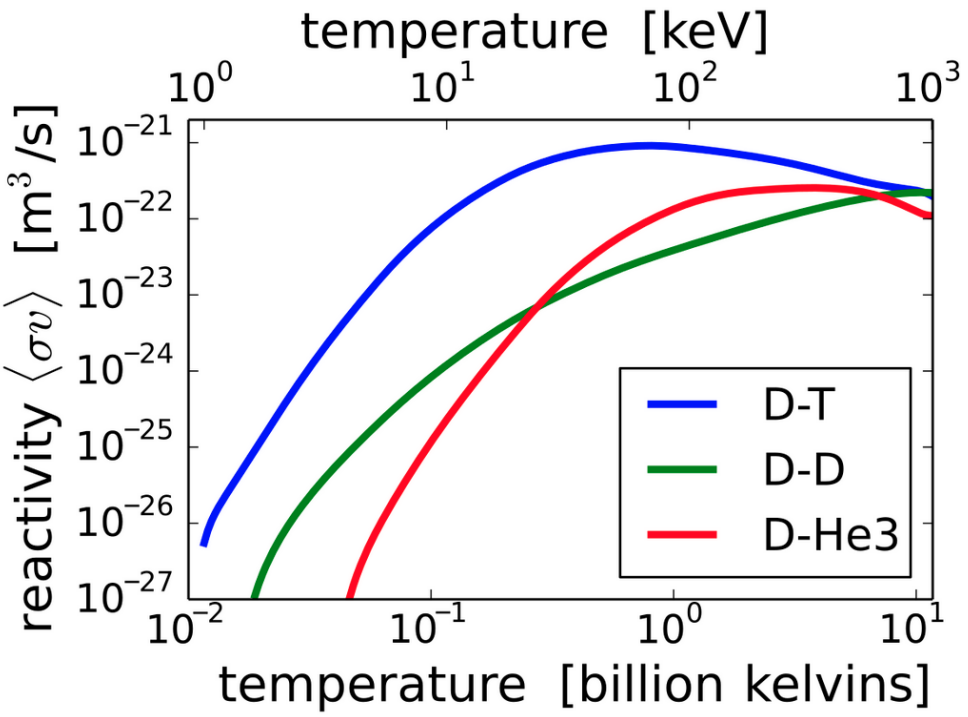

Figure 1.2 – Thermal reactivity for the fusion reactions (in m^3/s) as a function of the kinetic temperature in keV. The blue curve for DT mixture peaks at T $\approx$ 100 keV. The plot was made using data from the NRL Plasma Formulary, 2006 revision, and reproduced from Wikipedia.

the plasma is confined for a relatively long time at low densities: for a density of 10^{15} cm^{-3}, ignition is achieved if $\tau > 10$ s - this corresponds to Magnetic Confinement Fusion (MCF).

1.2 Magnetic Confinement Fusion

Magnetic confinement fusion is an approach to achieve controlled nuclear fusion. A mixture of deuterium-tritium gas is introduced into the Tokamak chamber. The gas is ionized by microwave emitters and confined into a plasma state within the magnetic field generated by superconducting coils. The magnetic field configuration promotes collisions between particles and heats the ionic populations (see Figure 1.3). Powerful magnetic fields are also employed to contain and control the extremely hot plasma, preventing it from coming into contact with the walls of the containment vessel.

The challenge lies in sustaining and controlling this process to achieve a net positive energy output, which is crucial for the practical implementation of magnetic confinement fusion as a sustainable and clean energy source. Research in this field is ongoing, with the hope of reaching ignition and moderate (see Equation (1.2.1)) $\mathcal{Q} \leq 10$ power gain (ITER project [14]). The primary advantage of MCF lies in its ability to achieve high confinement times, typically on the order of seconds. This extended confinement duration enhances the probability of fusion reactions occurring within the plasma. Even when using low-density gases in the chamber, the prolonged confinement allows for a greater chance of achieving the necessary conditions for fusion, such as high temperatures and pressures. This characteristic is crucial for sustaining the controlled fusion reactions needed for

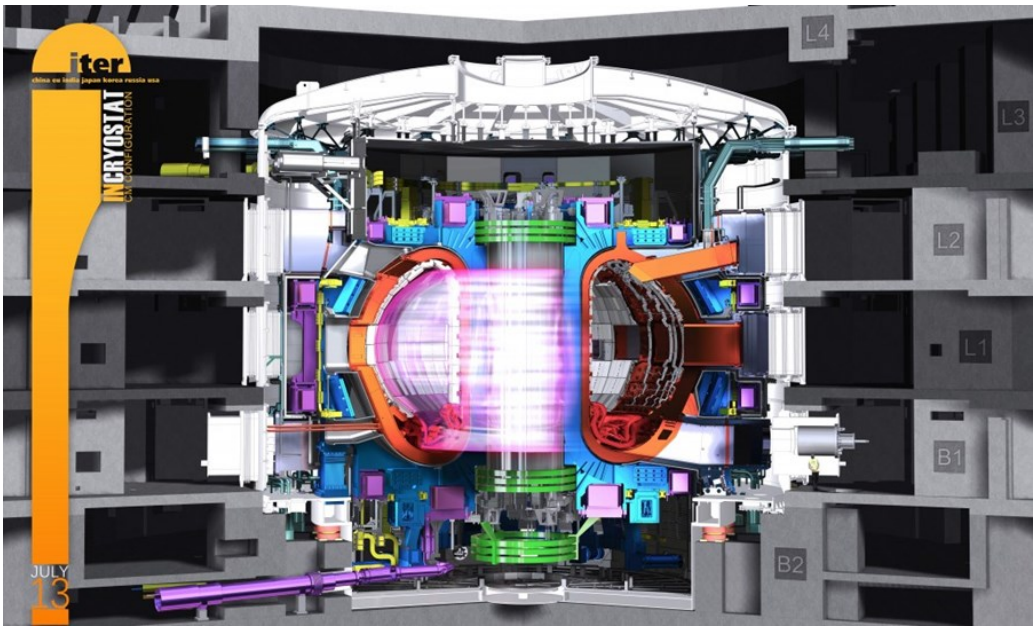

Figure 1.3 – Overlook of the inside of the ITER facility designed for MCF purposes. Located in France.

energy production in MCF devices like tokamaks and stellarators.

The efficiency of the fusion reactor can be written as:

$$\mathcal{Q} = \frac{P_{\text{fus}}}{P_{\text{aux}}}, \tag{1.2.1}$$

where P_{fus} corresponds to the theoretical power production of the reactor, and P_{aux} is the auxiliary power delivered to the reactor to maintain operating conditions and to compensate from the radiation and thermal losses.

Reactor designers aim to operate under conditions where the power losses of the fuel are offset by the power generated within the plasma through the fusion of alpha particles. This approach eliminates the need for auxiliary heating once the plasma has reached its operating temperature. For this case, $P_{\text{aux}} = 0$, so that $Q \to \infty$, and is the so called thermonuclear ignition conditions. The heat produced by nuclear reactions maintains the operating conditions and only fresh fuel needs to be added to compensate the loss of the burnt fuel.

For MCF, it is interesting to express the Lawson criterion in terms of plasma density, confinement time but also temperature. Ignition can be considered as achieved when:

$$n\tau T \approx 3.3 \times 10^{15}\ [\text{cm}^{-3}\ \text{keV s}], \tag{1.2.2}$$

for $8 \leq T \leq 25$ keV.

1.3 Inertial Confinement Fusion

Inertial Confinement Fusion (ICF) is a different approach based on the fact that compressed matter tends to maintain its high density due to its inertia during a short time interval before expanding again. To achieve such a reaction, high-energy lasers are used

to implode a shell of deuterium-tritium (DT), compressing the plasma to densities and temperatures high enough to initiate fusion reactions.

1.3.1 Conditions for ignition in ICF

Energy gain

In the context of energy production, as nuclear fusion reactions rapidly consume DT targets, ignition must occur repeatedly and at a given frequency. In this instance, a more meaningful comparison involves directly assessing the energy (E_{fus}) released by one target in relation to the energy (E_{d} delivered to it by the pulsed beams. The quantity of reference is the target energy gain:

$$\mathcal{G} = \frac{E_{\text{fus}}}{E_d}. \tag{1.3.1}$$

In ICF, achieving ignition is imperative for attaining high gain. This is in opposition with MCF where ignition is desired but not an absolute requirement, and in principle, corresponds to infinite power gain. A gain $\mathcal{G} \geq 100$ is usually required for inertial fusion energy production. As an example, recent best shots at the NIF reached $\mathcal{G} \approx 1.5 - 2$.

Lawson criterion

Additionally, since the confinement time is on the order of nanoseconds, it is necessary, to meet the Lawson criterion, to bring the fuel to very high densities (of the order of 10^{24} cm^{-3}). To achieve the ignition state (temperature and pressure), both heating and compression of the fuel are required, and these processes can occur simultaneously or separately.

The ignition process comprises several distinct stages. The initial stage involves the ablation of the external layer, initiating compression of the target through the outward ejection of ablated material (known as the "rocket effect"). Then, the target implodes and gains kinetic energy. The target eventually decelerates and communicates its kinetic energy into internal energy. The temperature rises and if the conditions are met, ignition is completed and DT combustion occur. The mass confinement time of the DT fuel needs then to be larger than the time in which the fusion reactions occur. We define the amount of fuel that is burnt within the confinement time by:

$$\frac{\tau_{\text{conf}}}{\tau_{\text{fus}}} = \langle \sigma v \rangle n_0 \tau_{\text{conf}}, \tag{1.3.2}$$

where n_0 is the ion number density of the plasma $\tau_{\text{conf}} = R_f/4c_s$ corresponds to the confinement time where we considered that the plasma sphere expands in the form of a rarefaction wave with speed $c_s^2 = 2T/m_i$ with T in eV. In ICF it is common to use the areal density ρR_f as it can be perceived as the opacity of the pellet. The higher it is the more confined are the α-particles and the more they deposit their energy in the plasma to maintain nuclear reactions. We can then write:

$$n_0 \tau_{\text{conf}} = \frac{1}{4 m_f c_s} \rho R_f, \tag{1.3.3}$$

where m_f is the the average mass of the fuel ions. The Lawson criterion can be expressed as follows:

$$n_0 \tau_{\text{conf}} = 2.3 \times 10^{15} \frac{\rho[\text{g}] R_f[\text{g/cm}^3]}{\sqrt{T_i[\text{keV}]}} \text{cm}^3 \text{ s}. \tag{1.3.4}$$

Expression (1.3.4) emerges as a fundamental parameter in inertial fusion, involving the product ρR of the hot spot. It directly links the mass confinement time enabling ignition with the quantities ρR and the temperature of the ions T within the hot spot. This already suggests a dependence of the ignition conditions of the hot spot on the areal density and temperature of the assembled plasma.

Burn efficiency

One can also define the burn efficiency in ICF. It is given by:

$$\Phi = \frac{N_{\text{fus}}}{N_0}, \tag{1.3.5}$$

which is the ratio between the total number of fusion reactions and the initial number of DT pairs N_0 within the target volume V_f. We have $N_0 = 1/2 n_i V_f$ with $V_f = 4/3\pi R_f^3$ supposing equimolar mixture of DT. If $\mathrm{d}N_{\text{fus}}$ is the number of fusions within the time interval dt we have : $\mathrm{d}N_{\text{fus}} = n_D n_T \langle\sigma v\rangle V(t)\mathrm{d}t$, with $V(t) = 4\pi/3(R_f - c_s t)^3$. By time-integrating the previous quantity it yields:

$$\begin{aligned} N_{\text{fus}} &= \frac{4\pi}{3} n_D n_T \langle\sigma v\rangle \frac{1}{4c_s} R_f^4 \\ &= \frac{1}{2} n_i \langle\sigma v\rangle N_0 \frac{R_f}{4c_s}. \end{aligned} \tag{1.3.6}$$

Using Equation (1.3.6), the burn efficiency can be written as follows:

$$\begin{aligned} \Phi &= \frac{n_i \langle\sigma v\rangle R_f}{8c_s} \\ &= \frac{\rho R_f}{\mathcal{H}_B}, \end{aligned} \tag{1.3.7}$$

where $\mathcal{H}_B = 8c_s m_f/\langle\sigma v\rangle$ is called the burn parameter. Therefore this quantity only depends on the areal density of the fuel and on the temperature. Nevertheless, Equation (1.3.7) does not consider the fact that the number of available nuclei for the reaction decreases with time. It is valid only if $\rho R_f \ll \mathcal{H}_B$, which is the low-burn limit, and in the case of full burn. When accounting for this effect in an homogeneous media, one can show that the burn efficiency can be written as such [15]:

$$\Phi = \frac{\rho R_f}{\mathcal{H}_B + \rho R_f}. \tag{1.3.8}$$

For a mixture of DT, the parameter $\mathcal{H}_B(T)$ has an almost constant average value ($\mathcal{H}_B \approx 7$ g/cm^2) over a wide temperature range 20 keV $\leq T \leq$ 100 keV [16]. Under optimal temperature conditions, the fraction of burnt DT depends solely on the areal density of the fuel at the stagnation moment. For a burn efficiency of 30%, it yields that $\rho R_f \approx 3$ g/cm^2.

Hot spot ignition

It is possible to estimate the energy required to bring a heated mass of fuel to 25 keV:

$$E_{\text{th}} = 3 n_e T_h V_h = 110 M_h[\text{g}] T[\text{keV}]\text{MJ}. \tag{1.3.9}$$

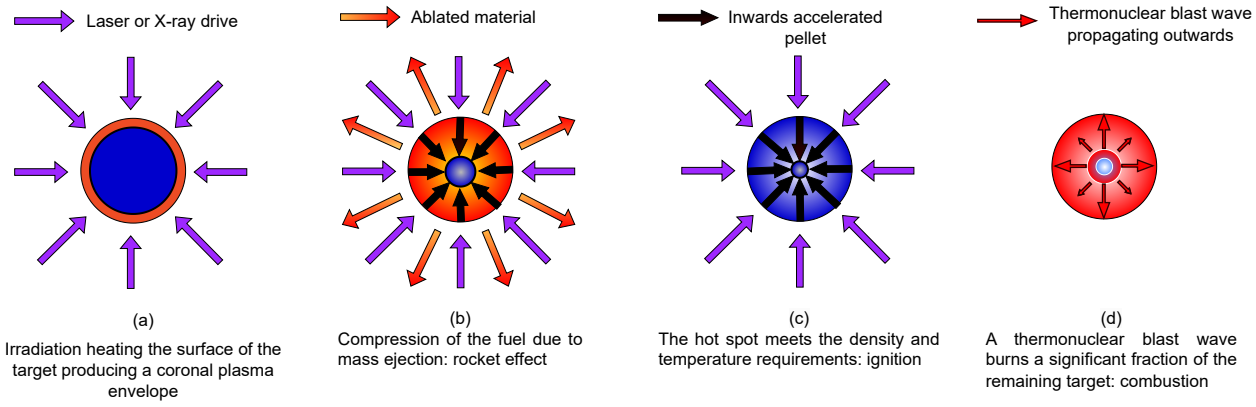

Figure 1.4 – Diagram illustrating the principle of inertial confinement fusion.

For a mass of DT of 1 mg, which produces 100 MJ of thermonuclear energy, it means that roughly 3 MJ of internal energy is needed to heat a whole solid DT ball volume to the required energies. No mention has been made of a source energy (laser or other) that would also involve a conversion efficiency. This simple calculation highlights the need for a significantly higher initial (or primary) energy. For comparison, at the NIF, in one of the best experiments aimed at maximizing thermonuclear energy, the energy invested in DT in the form of internal energy was estimated at about $\propto$ 10 kJ with a laser delivering almost 2 MJ (before α-particle energy deposition), resulting in a $E_{\mathrm{th}}/E_{\mathrm{d}}$ efficiency of about 0.5% [17]. With the same efficiency, raising 1 mg of DT to a temperature of 25 keV would require 600 MJ of primary energy.

Significant reduction in the energy required to ignite DT can be achieved by employing the concept of a hot spot and utilizing the energy deposited by alpha particles produced in fusion reactions. The idea is as follows: instead of raising the entire fuel to the desired thermonuclear temperature using an external energy source, only a small central part, constituting the hot spot, is brought to that temperature. The rest of the fuel is, as much as possible, kept at a relatively low temperature and high density until the ignition time. The energy from fusion reactions deposited in this hot spot by alpha particles is then used to heat the peripheral layers. A divergent thermonuclear burning wave can subsequently propagate throughout the entire target (see section 2.5.2.4 for more details about it). For the hot-spot to self-heat, to produce sufficient energy and for the α-particles to deposit their energy within the hot spot volume, one can generally say that it requires:

$$\rho_h R_h > 0.5 \text{ g/cm}^2, \qquad T_h > 5 \text{ keV}. \tag{1.3.10}$$

The general principle of hot spot ignition for ICF is shown in Figure 1.4.

1.3.2 Indirect drive

To deposit energy on the outer surface of the target, different types of radiation can be used:

— laser radiation; this is referred to as direct drive.

— X-ray radiation; this is known as indirect drive.

For the latter, instead of directly driving the fuel target with laser beams, one can choose to convert this UV radiation into secondary X-ray radiation. Beam ports are located at the poles of the experimental chamber. The fuel sphere is placed at the center of

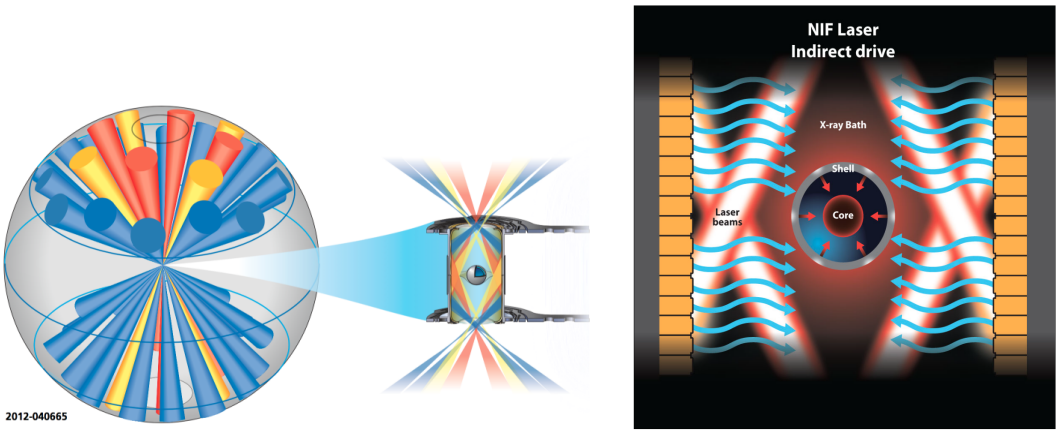

Figure 1.5 – Illustration of the experimental chamber geometry and of the indirect-drive scheme used at the NIF. Images taken from the NIF user guide and the LLE website.

a high-Z cavity (typically made of gold), commonly known as a hohlraum, perforated with two apertures on the sides. The principle is to irradiate the walls of the hohlraum with laser beams, passing through the apertures, to create a high-Z plasma that allows better absorption and conversion of laser energy. This plasma then emits X-ray radiation adapted to the cavity, ensuring the uniform compression of the fuel sphere. The idea is to create a chamber filled with radiation similar to that of a black body (with a temperature of around 300 eV). The hohlraum is filled with a low-Z gas (such as hydrogen or helium) at sufficient pressure to limit the expansion of the walls and, consequently, the movement of emissive surfaces, maintaining homogeneous irradiation and preventing the laser beam from interacting early into the gold bubble, which is a concern for some laser-plasma instabilities. This X-ray radiation then heats the fuel target, triggering the ablation of its outer layers and the implosion of the inner layers. To meet the conditions constrained by the Lawson criterion, the laser energy required is of the order of MJs, and the illuminations are such that the laser quasi-instantaneously ionizes the gas and the wall. This process, thanks to the thermal X-ray bath, achieves high irradiation symmetry. However, the main problem arises from the efficiency, as energy is lost during the conversion from laser energy to X-ray radiation by the cavity walls. This scheme is currently being used at the National Ignition Facility (NIF) in California, USA, and at the Laser Mega Joule (LMJ) [18] in Bordeaux, France. A schematic of the indirect-drive configuration is shown in Figure 1.5.

1.3.3 Direct drive

In the direct-drive approach, the entire surface of the target is irradiated with laser beams. Having a finite number of laser beams implies that the symmetry of illumination will not be perfect, and defects in the intensity pattern on the sphere will exist. In addition, the laser beams must be perfectly synchronised and have exactly the same power; otherwise, the spherical symmetry of the illumination would be broken. This can lead to non-uniformities that may develop during implosion, resulting in the cooling of the hot spot by the fuel. The compression of the DT core and reaching the ignition conditions would then be significantly compromised. The main advantage of direct drive lies in the direct coupling of the laser energy into the target. The requirements for laser energy are lower than for in indirect drive for the same target performances, meaning that target gains would be higher. Figure 1.6 shows a picture of the size of an ICF target and an

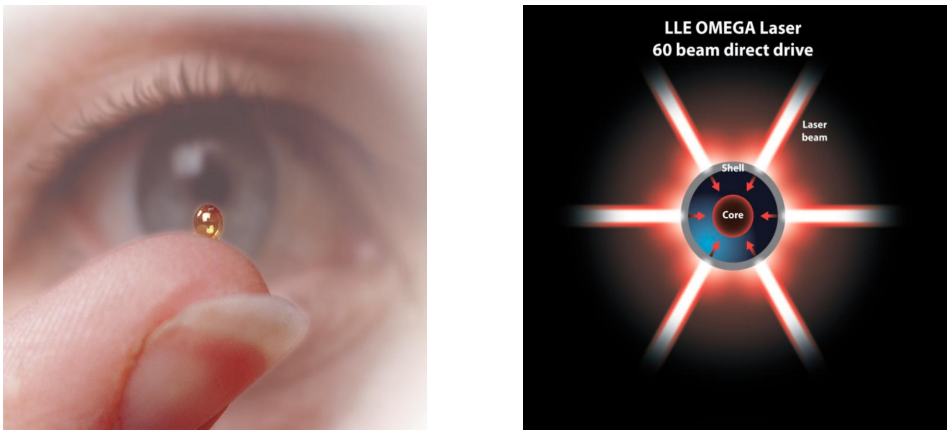

Figure 1.6 – Picture of a micrometer scale target used in ICF at the NIF (left) and illustration of the direct-drive approach (right).

illustration of the direct-drive scheme, typically used at the OMEGA60 (located at the LLE, Rochester, USA) laser facility.

1.3.4 Alternative schemes

The standard hot spot ignition is confronted with the limitations of the compression and heating of the fuel occurring simultaneously. One can show that that the work needed to compress cryogenic DT to the required densities is approximately 10 times less energy demanding than heating it to the ignition temperature. The direct consequence is the need to achieve a high implosion velocity, requiring the delivery of a significant amount of laser energy to the target. Alternative approaches to decouple these two processes have been proposed.

1.3.4.1 Fast ignition

In *fast ignition* [19], the fuel is first compressed via a moderate intensity (10^{14}-10^{15} W/cm^2) nanosecond laser pulse. The shell is set in motion with a moderate implosion velocity, enabling better stability during implosion. This assembles the fuel but does not create ignition. Finally, the hot spot is ignited by suprathermal electrons, produced in the high-intensity laser-plasma interaction with the gold cone, which then propagate from critical density to this high-density core. Another variant of this scheme employs protons, propelled by these fast electrons, to transmit the energy to the fuel. This scheme presents the potential for higher gains, reduced driver energy and cost for economically viable gains, flexibility in compression drivers like lasers, pulsed power, and heavy ion beam accelerators, innovative reactor chamber concepts, and lower susceptibility to the effects of hydrodynamic mix compared to the conventional inertial fusion scheme [20]. However, standard ICF target designs are already very complex. It is even more challenging to control the efficiency of converting laser energy into an electron beam, its divergence, and the survival of the cone during the implosion phase. These aspects remain to be considered to demonstrate its feasibility.

1.3.4.2 Shock ignition

In *shock ignition* [21], [22], a strong converging shock wave is launched by a high intensity laser pulse (10^{15}-10^{16}W/cm^2), called the laser *spike*. The spike usually lasts for a few 100s ps. The ignitor shock is amplified when colliding with the rebound of the compression shock at the inner surface of the shell. This enhanced amplified shock will provide the necessary energy to ignite the hot spot. The timing of the spike should be precisely selected to maximize the shock pressure after its interaction with previously launched shocks. Figure 1.7 show the differences between SI and conventional hot spot ignition.

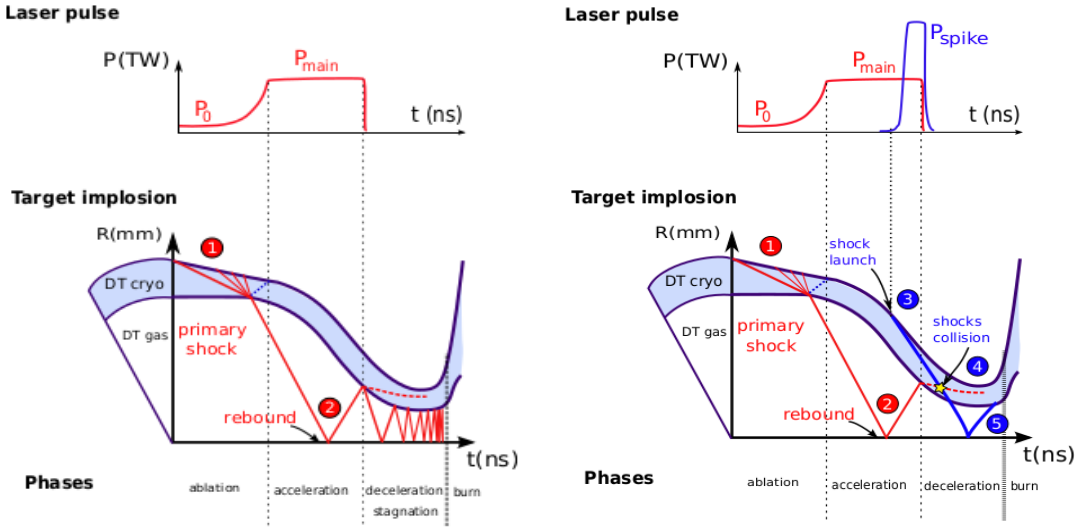

Figure 1.7 – Schematic representation of a standard hot spot ignition implosion (left) and shock ignition implosion (right). Images taken from Reference [23].

However, contrary to fast ignition, this scheme presents fewer technological challenges. The laser pulses involved in the SI process are in the nanosecond range, and the same laser can produce both the compression pulse and the ignition pulse. This approach enables achieving a greater gain with an implosion that is less prone to hydrodynamic instability problems. In this ignition method, the energy used for compressing the target is minimised, and a shock is initiated at the conclusion of the implosion to provide the additional energy required for ignition.

1.4 Limitations

1.4.1 Parametric instabilities

The interaction between a high-intensity laser and the outer shell of the target leads to the creation of a region of plasma known as coronal plasma. This plasma region exhibits an increased density closer to the ICF target, where the laser travels until it reaches a critical density n_c. Critical density is defined as the density at which the electrons, oscillating at the laser frequency, generate a field strong enough to prevent the propagation of laser waves beyond this density. The laser energy is primarily absorbed through inverse bremsstrahlung by the electrons, which rapidly thermalize through collisions with the ions. This heat is then transferred from the coronal plasma to the denser part of the

target through thermal conduction, driving the target compression and ignition phases. However, during the interaction, non-linear processes induce detrimental instabilities that can generate highly energetic electrons and redistribute the laser energy deposition. These *hot electrons* (HEs) propagate deeply into the inner layers of the fuel. They deposit entropy along their path and preheat the target compromising the compression process. In particular in SI, irradiance parameter $I_L\lambda_L^2$ can reach $\sim 10^{15}$ W μm^2/cm^2. In this regime, numerous couplings between laser light and plasma waves occur. Here is a concise overview of these so called parametric instabilities, with a focus of those capable of generating HEs and those susceptible to break laser irradiation symmetry in addition to increase the coupling losses:

- Preheat hazards
  - *Stimulated Raman Scattering* (SRS): an electromagnetic wave couples with an Electron Plasma Wave (EPW) and a scattered electromagnetic wave. If the EPW phase velocity is high enough, electrons can acquire suprathermal energies ($\sim$ 100 keV) that preheat the target and increase the entropy in the shell. The scattered light can also decrease the laser-target coupling. This effect is nefarious to the compression of the target and is driven in a region where $n_e \leq n_c/4$.
  - *Two-plasmon Decay* (TPD): an electromagnetic wave decays into two EPWs. As for SRS, TPD only involves EPWs. It occurs in the vicinity of the quarter critical density ($n_e \approx n_c/4$). As for SRS, the damping of these EPWs in the plasma transfers a significant amount of energy to electrons. These instabilities have the potential to propel electrons to energies in the range of several hundred keV. This phenomenon could result in an elevation of the adiabat of the shell, consequently leading to a reduction in the hydrodynamic efficiency of the implosion.
- Symmetry breaking hazards
  - *Stimulated Brillouin Scattering* (SBS): an electromagnetic wave couples with a scattered light wave and an IAW. This instability develops in the whole underdense plasma ($n_e < n_c$) and may be present almost everywhere in the coronal plasma. This effect can enhance reflectivity of the plasma and scatter a certain fraction of the light towards region of lower densities. This is detrimental to the laser irradiation homogeneity considering that irradiation uniformity must be kept below $\sim 1\%$ (see Section 1.4.2).
  - *Cross-Beam Energy Transfer* (CBET): in configurations where laser beams overlap, the crossing of laser beams induces periodic density perturbations through the ponderomotive force. These density modulations of the plasma can allow energy exchange from the ongoing to the outgoing laser beams. Understanding the transfer between intense laser beams is crucial for ICF, as it allows for the control of laser-plasma coupling in both direct drive and indirect drive schemes and for the control of the implosion symmetry.
- Coupling losses
  - *Cross-Beam Energy Transfer*: incident laser beams see a fraction of their energy being transferred to outgoing laser light in the underdense plasma, causing coupling losses.
  - Arguably, SBS and SRS also cause coupling losses.

1.4.2 Long-wavelength perturbations

The low modes are mainly controlled by the focusing and intensity of the laser radiation. The illumination symmetry depends on the compression of the target. If we consider the convergence ratio C_d as the ratio of the initial radius of the target R_0 to the final radius R_h of the hot spot, we can relate the perturbation δR of this radius to the perturbation δv of the implosion velocity by $\delta R/R_h = C_d \delta v/v_{\text{imp}}$. The tolerable perturbation at the hot spot depends on the residual kinetic energy of the cold fuel at the time of its formation, i.e., the ignition margin of the target. But in any case, the perturbations in the shape of the hot spot must be small enough to ensure ignition. If we arbitrarily set this perturbation to one-quarter of the hot spot radius, it follows that the implosion velocity must be uniform to within 1/4C. The implosion velocity, depending on the laser intensity as $I_L^{1/3}$ (2.5.1), implies that the uniformity constraint is given by $\delta I_L/I_L \leq 3/4C_d$. The typical values of C_d range from 30 to 50, implying that an irradiation uniformity lower than 1 or 2% must be achieved.

These performances naturally require the use of a large number of beams, as well as precise control over the radius and shape of the focal spots to be employed. Note that indirect drive allows for a high degree of uniformity through the transformation of laser radiation into thermal radiation in the hohlraum. In this case, all beams are focused on the entrance windows of the hohlraum and then deposit their energy on the inner surface of the wall. Control of the illumination symmetry is achieved by adjusting the positions and shapes of the focal spots. To facilitate the passage of the entrance windows, the beams from LMJ and NIF have an elliptical shape.

The direct-drive scheme is much more demanding in terms of illumination symmetry. In particular, it is not possible to achieve sufficiently uniform illumination with a simple focus on the center of the target using the laser beams available at NIF and LMJ because the equatorial part of the target will be less irradiated than the poles. Nevertheless, direct-drive schemes will be studied at these facilities using specific beam focusing, such as Polar Direct Drive. This scheme proposed by researchers at the University of Rochester in the USA advocates for defocusing and displacing the laser beams to better illuminate the equatorial part of the target. Some innovative designs directly optimised for direct-drive ICF will be discussed later in chapter 5.

1.5 Improving the laser irradiation and absorption

In contrast to indirect drive, laser direct drive couples most of its energy on the target, as the focal spot size is comparable to the initial capsule size. However, the presence of LPIs, such as SRS, SBS, and CBET introduces coupling losses that significantly diminish drive (ablation) pressures, limiting fuel mass and areal density. Addressing and mitigating these losses are paramount in advancing next-generation ICF technology.

The use of new broadband lasers shows promise in countering the adverse effects of LPI. By combining bandwidth with beam zooming, absorption efficiency is expected to exceed 90%. Laser focal spot zooming involves reducing the spot size of the laser during the implosion, preventing the loss of laser light that is not absorbed as the target decreases in size. Various concepts have been proposed for achieving focal spot zooming. In the case of excimer lasers [24], induced spatial incoherence has been demonstrated as an effective

method, as showcased on the Nike KrF facility [25]. For the solid-state laser technology considered in this context, zooming would be implemented through the use of multiple beam lines, specific phase plates and chirped beams.

If the application of bandwidth is proven to elevate convergent ablation pressure above 200 Mbar (and possibly beyond 300 Mbar with zooming) without inducing excessive fuel preheat from hot-electrons generated by LPI, laser direct drive becomes an appealing candidate for an ICF driver in an IFE facility.

1.6 Objective of this work

Numerical ICF plays a crucial role in understanding and simulating the complex physical processes involved in achieving controlled fusion reactions. These simulations employ sophisticated models to describe the intricate interplay of radiation, hydrodynamics, and plasma physics within the target during the compression and ignition stages. Modern numerical tools have improved our ability to thoroughly study theoretical processes. They facilitate the study of the evolution of various processes. Simulations also serve as a means for verifying experimental data and predicting tendencies and outcomes. In the context of ICF, pertinent simulations address various facets of the target, encompassing considerations for distinct spatial and temporal scales. Hydrodynamic codes (*CHIC, DRACO, ASTER, ...*) are key for simulations conducted at spatial scales approximately on the order of the fuel target (mm-scale) and nanosecond time scales, corresponding to the pulse duration in ICF experiments. These codes typically incorporate hydrodynamic models designed to explore phenomena at the level of the entire ICF target. They are instrumental in studying macroscopic events, including hydrodynamic instabilities within the fuel, the propagation of shocks, and simulating various phenomena such as the collisional absorption of laser light and reduced models of the effects of CBET. At the OMEGA laser facility, CBET is well understood, thanks to extensive studies at a smaller scale. However, at the ignition scale, CBET remains relatively understudied in direct-drive configurations. The transition to ignition introduces new challenges and phenomena that demand a deeper understanding of the complex interactions between high-energy lasers, target materials, and the resulting fusion reactions. Investigating CBET at the ignition scale is crucial for advancing our knowledge and improving the efficiency of inertial confinement fusion.

The subject of this work is entitled *Theoretical study of laser coupling and irradiation uniformity in direct-drive inertial fusion*. The objectives of the thesis are listed as follows:

- The first objective is the validation of the CBET module and laser-target coupling models implemented in the 3D radiative hydrodynamics coupled code *ASTER-/IFRIIT* at the ignition scale, even in the characteristic case of specific laser geometries and laser intensities close to the SI regime where CBET is prominent.

- The second objective is the identification and description of novel beam chamber geometries for the future direct-drive facilities at the ignition scale using ray-tracing on solid spheres. Innovative geometries are compared to study their robustness to persistent experimental errors. It aims to identify which geometries give the optimum laser irradiation for direct-drive ICF.

- The third objective is the robustness characterisation of ignition schemes at the ignition scale using optimised beam chamber geometries in 3D radiative hydrodynamics simulations. The investigation of target and hot spot performances while increasing experimental errors is performed.

1.7 Organization of the manuscript

The validation of the 3D *ASTER/IFRIIT* coupled code as well as the study on the beam chamber geometries for the next-drive facilities have been divided into four main Chapters. The manuscript presentation is as follows:

- **Chapter 2** introduces the physical phenomena involved in the implosion of a fuel capsule ignited by laser. It establishes the hydrodynamic equations governing the fluid in motion and the propagation of shock waves. The models for generating the central hot spot and initiating its ignition are elaborated. Last, the key limiting effects that could hinder both the implosion and ignition of the fuel are identified. Examples via 1D *CHIC* simulations are given throughout the Chapter. Here, we also provide an overview of the key characteristics of the hydrodynamic simulation codes *CHIC* and *ASTER*, tools extensively used in this study.

- **Chapter 3** delves into the linear theory of electromagnetic wave propagation in plasmas. Various plasma descriptions are illustrated, and we give the evolution of waves in plasmas, exploring their dispersion relations. The definitions for EPWs and IAWs are established. The subsequent sections provide detailed descriptions of SRS, TPD, SBS and specifically CBET. We provide an overview of the key characteristics of the Inverse Ray Tracing code *IFRIIT* which was used to model the laser propagation and interaction in the plasma. Detailed equations are presented for each instability.

- **Chapter 4** provides an account of plastic solid-sphere experiments conducted at the National Ignition Facility as part of the direct-drive approach to inertial confinement fusion. The primary objectives of these experiments were to characterize coupling efficiency and monitor shock positions within a solid-sphere plastic target. The investigations were carried out using the polar direct-drive (PDD) irradiation scheme, which is particularly sensitive to CBET. The presented campaign serves to assess the accuracy of the CBET linear kinetic model and laser modelling in the *ASTER/IFRIIT* coupled 3D code at ignition scale. The chapter starts with a characterization of defocused laser beams utilized at the NIF, followed by shock tracking and backscattered light analysis with 3D radiative hydrodynamics simulations, offering a robust validation physics models of the code at the ignition scale.

- **Chapter 5** undertakes an analysis of irradiation quality in innovative beam chamber geometries proposed for future direct-drive facilities. This study incorporates system errors, providing a quantitative assessment of robustness for each design. Additionally, a comparison with the current largest direct-drive facility, Ω60, is presented. The chapter concludes with the presentation of 3D simulation results, offering insights into which ignition design exhibits greater resilience to persistent low-mode asymmetries.

The conclusions of this work are presented in Chapter 6.

Chapter 2

Hydrodynamics of the implosion

This chapter is devoted to the hydrodynamics of an ICF target implosion. It provides the main physical phenomena involved and equations used in the laser implosion of an ICF-type capsule. The classic mechanisms of laser energy transport through the target, as well as the formation and ignition of the hot spot, will be briefly discussed. The limiting effects jeopardizing the efficiency and stability of the capsule implosion will be addressed at the end of the chapter.

2.1 The kinetic Boltzmann equation

At its most accurate level, the classical microscopic depiction of a plasma involves describing each particle based on its position ($\mathbf{r}$) and momentum ($\mathbf{p}$) as they evolve over time. The forces acting on the particles can be categorised into two parts: external forces exerted on the plasma and internal forces arising from interactions between individual particles. The internal force governs the collective behaviour of the entire system. While this force exhibits rapid fluctuations in both space and time, the global external forces applied to the plasma exhibit macroscopic variations.

In a kinetic description of a system of particles interacting electromagnetically, our objective is to understand the evolution of the distribution function f_α for each species alpha. This function is continuous and can be interpreted as the probability density of finding a particle within the spatial interval $[\mathbf{r},\ \mathbf{r} + \mathrm{d}\mathbf{r}]$, with momentum in the interval $[\mathbf{p},\ \mathbf{p} + \mathrm{d}\mathbf{p}]$, at time t.

Let us start by examining the single-species distribution function $f_\alpha(r, v, t)$. From there, we explore rapid phenomena that occur on timescales shorter than the collision time. On this shorter timescale, the plasma dynamics are primarily shaped by the effects of electromagnetic fields: $\mathbf{E}(r,t)$ and $\mathbf{B}(r,t)$. As each particle is subjected to the Lorentz force arising from its interaction with these fields, the objective is to describe this microscopic behaviour in terms of the evolution of the distribution function.

In the non-collisional regime, its evolution is governed by the Vlasov equation

$$\left(\frac{\partial}{\partial t} + \mathbf{v}\cdot\nabla_{\mathbf{r}} + \mathbf{F}_\alpha\cdot\nabla_{\mathbf{p}}\right) f_\alpha = 0, \tag{2.1.1}$$

where $\mathbf{F}_\alpha$ is the Lorentz Force arising from the self-consistent fields $\mathbf{E}$ and $\mathbf{B}$ governed by the Maxwell's Equations (3.1.1) in the plasma:

$$\mathbf{F}_\alpha = \frac{q_\alpha}{m_\alpha}\big(\mathbf{E} + \mathbf{v}\times\mathbf{B}\big), \tag{2.1.2}$$

where q_α and m_α are respectively the charge and mass of the α-species. It is worth noting that the Vlasov equation also expresses the fact that the value of the distribution function remains conserved along the trajectory of each particle, as it can still be written as:

$$\frac{\mathrm{d}}{\mathrm{d}t} f_\alpha(\mathbf{r}, \mathbf{p}, t) = 0. \tag{2.1.3}$$

In the absence of interactions between particles, the total derivative of $\mathrm{d}f/\mathrm{d}t$ becomes zero, meaning that the number of particles per unit volume remains constant as we track the particles in their motion through phase space. The Vlasov equation reveals that particle interactions are the sole source of density variations in this Lagrangian perspective.

In the collisional regime, the Vlasov Equation (2.1.1) reads:

$$\left(\frac{\partial}{\partial t} + \mathbf{v} \cdot \nabla_{\mathbf{r}} + \mathbf{F}_\alpha \cdot \nabla_{\mathbf{p}}\right) f_\alpha = \left(\frac{\delta f_\alpha}{\delta t}\right)_{\text{coll}}, \tag{2.1.4}$$

which is known as the kinetic Boltzmann equation. The interpretation in this form is also clear: the variation of the average number of particles in the fixed element of volume $\mathrm{d}\mathbf{r}\mathrm{d}\mathbf{v}$ between times t and $t+\mathrm{d}t$ now has two origins:

— particles entering or exiting through the surfaces that limit the volume.

— particles being created or transformed within the volume due to interactions/collisions.

Specifically, spatial inhomogeneities give rise to the term $\nabla_r(f_\alpha)$, velocity inhomogeneities lead to the term $\nabla_p(f_\alpha)$, while particle interactions cause particles to enter or exit the volume element, represented by the term $(\delta f_\alpha/\delta t)_{\text{coll}}$.

The kinetic Boltzmann equation is not homogeneous: collisions result in a source term in the 6-dimensional phase space. In the following chapter, we will demonstrate that this source term can be expressed through an integral involving a product of the two distribution functions of the particles involved in the collision. As a result, the Boltzmann equation takes on an integro-differential and nonlinear character.

For a specific population of charged particles, hydrodynamics quantities can be easily defined. The particle density and mass density can be calculated via the different moments of its distribution function:

$$\begin{aligned}
n_\alpha(\mathbf{r}, t) &\equiv \int_0^\infty f_\alpha(\mathbf{r}, \mathbf{v}, t) d\mathbf{v}, \\
\rho_\alpha(\mathbf{r}, t) &\equiv m_\alpha n_\alpha(\mathbf{r}, t), \\
\mathbf{v}_\alpha(\mathbf{r}, t) &\equiv \frac{\int_0^\infty \mathbf{v} f_\alpha(\mathbf{r}, \mathbf{v}, t) d\mathbf{v}}{n_\alpha(\mathbf{r}, t)}, \\
\overline{\overline{P_\alpha}}(\mathbf{r}, t) &\equiv m_\alpha \int_0^\infty \left[\mathbf{v}_\alpha(\mathbf{r}, t) - \mathbf{v}\right] \left[\mathbf{v}_\alpha(\mathbf{r}, t) - \mathbf{v}\right] f_\alpha(\mathbf{r}, t) \mathrm{d}\mathbf{v}.
\end{aligned} \tag{2.1.5}$$

The set of Equations (2.1.5) define different hydrodynamic observables. First, the particle density $n_\alpha(\mathbf{r}, t)$ and the volumetric mass density $\rho_{m,\alpha}(\mathbf{r}, t)$, second, the first-order moment allows defining the α-species fluid Eulerian velocity $\mathbf{v}_\alpha(\mathbf{r}, \mathrm{t})$, which is the average velocity of all particles located at $\mathbf{r}$ at time t. Finally, the pressure tensor $\overline{\overline{P_\alpha}}(\mathbf{r}, t)$ measures the quadratic deviation between this average velocity and the individual particle velocities.

2.2 Fluid conservation equations

2.2.1 0^{th} moment of the Boltzmann equation: mass conservation

The fluid quantities are obtained from integrals over velocity of the distribution function of a particle species, multiplied by an appropriate velocity-dependent function. Similarly, we can derive the hydrodynamic equations from the Boltzmann kinetic equation. By integrating each term of Equation (2.1.4) over velocity, we obtain the conservation equation for the number of particles of species α that lead to the emergence of dynamic couplings between moments:

$$\begin{aligned} \int_0^\infty \frac{\mathrm{d}}{\mathrm{d}t} f_\alpha(\mathbf{r},\mathbf{v},t)\mathrm{d}\mathbf{v} &= \int_0^\infty \left(\frac{\delta f_\alpha}{\delta t}\right)_{\text{coll}} \mathrm{d}\mathbf{v} \\ \Leftrightarrow \frac{\partial n_\alpha(\mathbf{r},t)}{\partial t} + \nabla\cdot\Big[n_\alpha(\mathbf{r},t)\mathbf{v}_\alpha(\mathbf{r},t)\Big] &= \int_0^\infty \left(\frac{\delta f_\alpha}{\delta t}\right)_{\text{coll}} \mathrm{d}\mathbf{v} = 0. \end{aligned} \tag{2.2.1}$$

which is the continuity equation for the number of particles. Here, to establish this result, we made the assumption that the collision term cannot be responsible for the appearance of new particles. This excludes ionizing collisions or those leading to recombination. By multiplying Equation (2.2.1) by the mass and summing over all the α-species, it yields that:

$$\frac{\partial \rho}{\partial t} + \nabla\cdot\mathbf{j} = 0. \tag{2.2.2}$$

where ρ is the space charge density and $\mathbf{j} = \rho\mathbf{v}$ is the current density.

2.2.2 1^{st} moment of the Boltzmann equation: momentum conservation

A second fluid equation can be derived thanks to the 1^{st} moment of the Boltzmann equation:

$$\frac{\partial \rho_\alpha \mathbf{v}_\alpha}{\partial t} + \nabla : (\rho \mathbf{v}_\alpha \mathbf{v}_\alpha + \overline{\overline{P_\alpha}}) = n_\alpha q_\alpha(\mathbf{E} + \mathbf{v}_\alpha \times \mathbf{B}) + \mathbf{R}_\alpha, \tag{2.2.3}$$

where

$$\mathbf{R}_\alpha = m_\alpha \int_0^\infty \left(\frac{\delta f_\alpha}{\delta t}\right)_{\text{coll}} \mathbf{v}\mathrm{d}\mathbf{v}. \tag{2.2.4}$$

The overall conservation of momentum during collisions between different species of particles is expressed by the condition:

$$\sum_\alpha \mathbf{R}_\alpha = 0. \tag{2.2.5}$$

Equation (2.2.3) can be easily interpreted in terms of the fundamental dynamics for a fluid particle. When the magnetic field is such that the magnetic pressure is much greater than the kinetic pressure, the equation of state (EOS) couples not only pressure and density but all three variables: pressure, density, and magnetic field. In such situations, when collisions are not efficient enough to ensure rapid isotropization of velocities, the pressure tensor becomes anisotropic, and the pressure along the magnetic field lines differs from the pressure perpendicular to the field.

2.2.3 2^{nd} moment of the Boltzmann equation: energy flux conservation

As we derive fluid equations from the kinetic equation, we encounter a chain of implications where the equation for the average velocity leads to the divergence of the pressure tensor. Similarly, the evolution equation for the pressure tensor leads to the divergence of a higher-order tensor, leading to an infinite hierarchy of fluid equations. This hierarchy can be made equivalent to the original kinetic equation. However, in practice, we face the challenge of dealing with an infinite set of equations, so we truncate the hierarchy by making a closure assumption on the highest-order term retained in the fluid equations. This closure assumption simplifies the system and allows us to study the fluid behavior effectively.

We shall augment the previously presented fluid equations concerning the conservation of particle number and momentum with the equation associated with energy conservation. It can be obtained by multipyling the Boltzmann Equation (2.1.4) by $1/2v_\alpha^2$, the kinetic energy density and integrating over velocity:

$$\frac{\partial}{\partial t}\left(\frac{1}{2}\rho_\alpha v_\alpha^2 + \rho_\alpha e_\alpha\right) + \vec{\nabla}\cdot\left[\rho_\alpha \mathbf{v}_\alpha\left(\frac{1}{2}\rho_\alpha v_\alpha^2 + e_\alpha\right) + \overline{\overline{P_\alpha}}\mathbf{v}_\alpha + \mathbf{q}_\alpha\right] = Q_\alpha \tag{2.2.6}$$

In the given equation, Q represents the external sources of energy, e denotes the specific internal energy related to hydrodynamic parameters through the equation of state $e \equiv e(\rho, T)$, $\mathbf{q}$ is the heat flux. The inclusion of an additional equation is imperative to establish a comprehensive relationship between thermodynamic quantities, enabling a complete solution to the system under consideration. This vital equation is none other than the equation of state specific to the material under study. For plasmas, a reasonable first-order approximation entails adopting the ideal gas equation, which holds true under the assumption of quasi-neutrality, expressed as $n_e = Zn_i$, where n_e and n_i denote the electron and ion densities, respectively, while Z represents the atomic number. This assumption remains valid when the Debye screening length is considerably smaller than the characteristic size of the plasma. Note that more accuracy over a larger range can be achieved with a semi-empirical, tabulated EOS. Hence, we emphasise the importance of the ideal gas law in this context:

$$P = nk_bT, \tag{2.2.7}$$

with k_b the Boltzmann constant and T the temperature. A commonly used equation system closure is the adiabatic equation of state. For an ideal gas with a polytropic exponent γ (the ratio of the specific heat capacities at constant pressure and constant volume), the equation of adiabatic evolution is given by:

$$P = P_0\left(\frac{\rho}{\rho_0}\right)^\gamma, \tag{2.2.8}$$

The three Equations (2.2.1), (2.2.3) and (2.2.6) are the tools used to describe acoustic and shock waves.

2.3 Acoustic waves

An acoustic wave corresponds to the propagation of a small pressure variation, causing the initial pressure P_0 to change to $P = P_0 + \Delta P$. This pressure change induces a

corresponding variation in density from its initial value ρ to $\rho = \rho_0 + \Delta\rho$.

To gain a better understanding of this phenomenon, let us consider a scenario where a perturbation is generated by a piston located at one end of the medium. The piston moves towards the other end with a constant velocity $\mathbf{u}$. As a result of this perturbation, the velocity of the medium becomes $\Delta\mathbf{u}$, considering that the initial velocity $\mathbf{u_0}$ is negligible compared to the perturbation-induced velocity change $\Delta\mathbf{u}$, so that $\mathbf{u} = \mathbf{u_0} + \Delta\mathbf{u} \simeq \Delta\mathbf{u}$. We can consider the case of a one-dimensional plane wave with small perturbations:

$$\frac{\partial(\rho_0 + \Delta\rho)}{\partial t} + \frac{\partial}{\partial x}\big((\rho_0 + \Delta\rho)\Delta u\big) = 0. \tag{2.3.1}$$

At the first order, it yields:

$$\frac{\partial \Delta\rho}{\partial t} = -\rho_0 \frac{\partial \Delta u}{\partial x}. \tag{2.3.2}$$

The momentum conservation Equation (2.2.3) gives:

$$\frac{\partial}{\partial t}\big[(\rho_0 + \Delta\rho)\Delta u\big] + \frac{\partial}{\partial x}\Big[(\rho_0 + \Delta\rho)(\Delta u)^2 + (P_0 + \Delta P)\Big] = 0. \tag{2.3.3}$$

By keeping only first order perturbation terms, one obtains:

$$\rho_0 \frac{\partial \Delta u}{\partial t} = -\frac{\partial \Delta P}{\partial x}. \tag{2.3.4}$$

However, the particle motion in a sound wave is a reversible phenomenon, and heat transfers do not have enough time to occur. This leads to an adiabatic transformation. Consequently, we can express $\Delta P = \left(\frac{\partial P}{\partial \rho}\right)_S \Delta\rho$. It is worth noting that the term $(\partial P/\partial\rho)_S$ appears as a square of velocity. We define the acoustic velocity as:

$$c_s \equiv \sqrt{\left(\frac{\partial P}{\partial \rho}\right)_S}. \tag{2.3.5}$$

The subscript "S" denotes that the derivative is calculated at constant entropy. By time-differentiating Equation (2.3.2), space-differentiating (2.3.4), and using the acoustic velocity definition in Equation (2.3.5), we can derive the acoustic wave propagation equation for the density:

$$\frac{\partial^2 \Delta\rho}{\partial t^2} = c_s^2 \frac{\partial^2 \Delta\rho}{\partial x^2}, \tag{2.3.6}$$

or in pressure:

$$\frac{\partial^2 \Delta P}{\partial t^2} = c_s^2 \frac{\partial^2 \Delta P}{\partial x^2}. \tag{2.3.7}$$

2.3.1 Application to ideal gases

In the framework of an ideal gas in an adiabatic process, with equation of state (2.2.7), the acoustic velocity can be written in the form:

$$c_s = \sqrt{\gamma \frac{P}{\rho}}, \tag{2.3.8}$$

so that we can exhibit the acoustic velocity ratio between two media:

$$\frac{c_s}{c_{s0}} = \left(\frac{\rho}{\rho_0}\right)^{\frac{\gamma-1}{2}}. \tag{2.3.9}$$

2.4 Shock waves

Shock waves are characterized by discontinuities in pressure, density, and velocity within a material medium. In the context of inertial confinement fusion, these shock waves play a crucial role in achieving the necessary temperature and pressure conditions for ignition. To fully understand the generation and propagation of shock waves, we first established the general equations of fluid mechanics. Then, we explore specific wave types, such as acoustic waves. Finally, we focus on shock waves and their dynamic propagation. Understanding these phenomena is essential for advancing our knowledge of inertial confinement fusion and its potential applications.

2.4.1 Shock formation

2.4.1.1 Discontinuities

In ICF, shock waves have a key role in setting the entropy within the fuel during the progression of the target implosion. To realise a state of nearly isentropic compression, meticulous management of shock intensity becomes imperative, often achieved through the careful modulation of the driving pulse (as will be exposed in the future sections). This segment offers a concise derivation of shock relations for reference, while those seeking a more comprehensive exposition can turn to sources such as the work authored by [26].

In the precedent section, we have considered the propagation of small perturbations, which are modeled using linear equations due to their minor induced variations. In Equations (2.3.2) and (2.3.4), nonlinear effects are disregarded. However, it is precisely the nonlinear effects inherent in the conservation equations that give rise to shock wave formation.

A shock is a disturbance that propagates through a medium at a speed greater than the material sound speed, causing a sudden change in its density, pressure, and temperature. Let us consider an external force acting on an ideal gas, compressing it from an initial pressure P_0 to a final pressure P_1 so rapidly that the material cannot reach an equilibrium state. We can envision this pressure wave as a superposition of small perturbations dP propagating in a medium with pressure P_0. Consequently, a point A with higher density compared to a point B (as illustrated in Figure 2.1 a)) will move faster, initiating wave deformation (Figure 2.1 b)). Indeed, according to the definition of sound velocity for an ideal gas, as density increases, velocity also increases, particularly for a polytropic ideal gas (refer to Equations (2.3.8) and (2.2.8)). The speed of the perturbed wave, $c_s(P+dP)$, will be greater than the speed in the unperturbed wave, $c_s(P)$, leading to the former eventually catching up with the latter which is a physically implausible scenario as it would entail multiple densities for the same point (2.1). The wavefront then becomes vertical, creating a discontinuity that propagates into the undisturbed material. The velocity of this discontinuity becomes greater than the local sound speed, thus termed a shock wave. Discontinuity can be perceived as the limiting case of a temperature, pressure, density, etc., gradient across an interface, with the thickness approaching zero. However, in experimental scenarios, when considering dissipative phenomena and the discontinuous nature of matter, a finite and thin transition shock front thickness emerges, rather than an actual discontinuity.

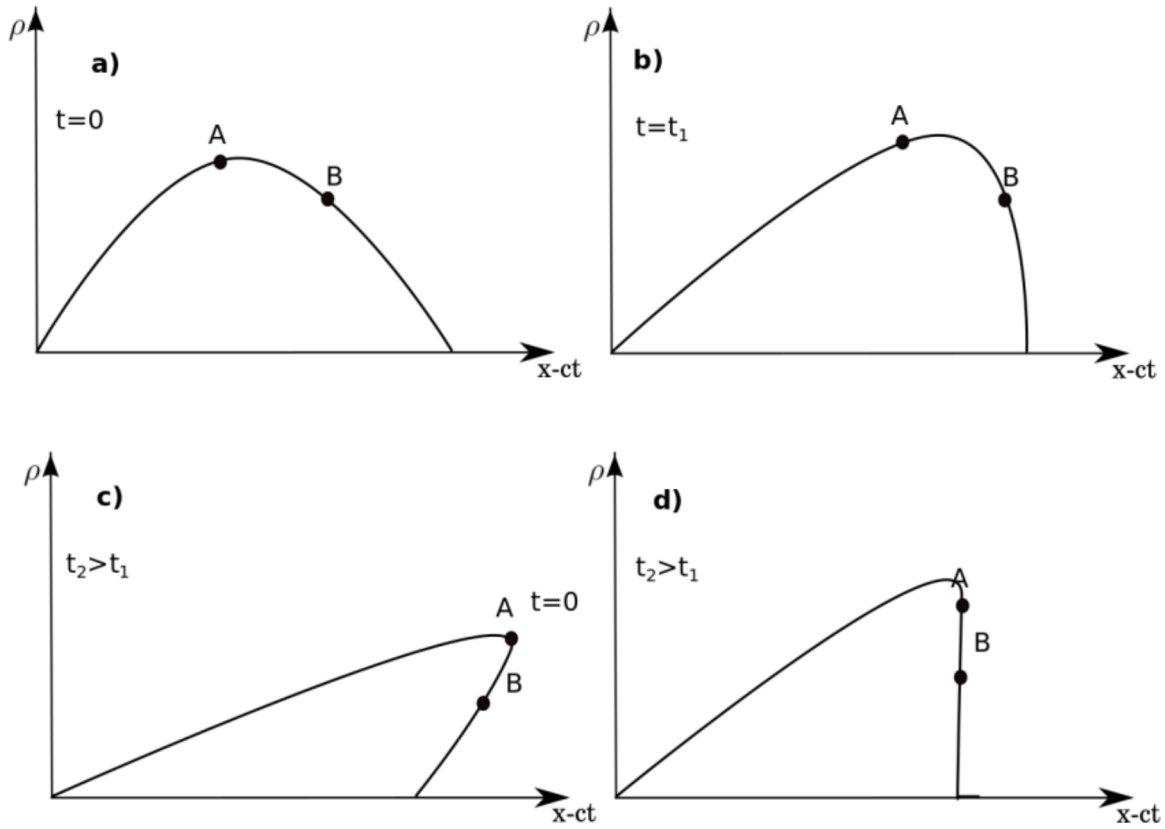

Figure 2.1 – Illustration of a shock wave formation: Initially, at $t = 0$, point A possesses a higher density compared to point B (a). Consequently, it accelerates, initiating wave deformation (b). Subsequently, at $t_2 > t_1$, point A overtakes point B (c). As this outcome lacks physical validity, the wavefront becomes rigid, assuming a vertical profile, thereby generating a shock wave (d).

2.4.1.2 Rankine-Hugoniot relations

As discussed previously, shocks induce discontinuities in numerous physical quantities (including their spatial derivatives). Jump conditions at the interface between an upstream and downstream ("shocked" and "unshocked") region are derived using the set of conservation laws (2.2.1), (2.2.3) and (2.2.6). As described in figure 2.2, if we consider a thin interface moving with velocity $\mathbf{u}_s$ in the x-direction and the local cartesian frame co-moving with the interface, downstream and upstream velocities in this coordinate system are given by:

$$\mathbf{v}_{d/u} = \mathbf{u}_{d/u} - \mathbf{u}_s. \tag{2.4.1}$$

One can restrict to the ideal gas dynamics considering that the heat flux $\mathbf{q}$ is equal to zero. Hydrodynamic equations must be matched either side of the shock (black line in Figure 2.2) to avoid discontinuous change in a continuous fluid. By doing so, jump conditions describing the media upstream and downstream of the discontinuity for a planar shock in a fluid are given by the Rankine-Hugoniot conditions:

$$\begin{aligned} \rho_d v_d &= \rho_u v_u, \\ \rho_d v_d^2 + P_d &= \rho_u v_u^2 + P_u, \\ e_d + \frac{P_d}{\rho_d} + \frac{v_d^2}{2} &= e_u + \frac{P_u}{\rho_u} + \frac{v_u^2}{2}. \end{aligned} \tag{2.4.2}$$

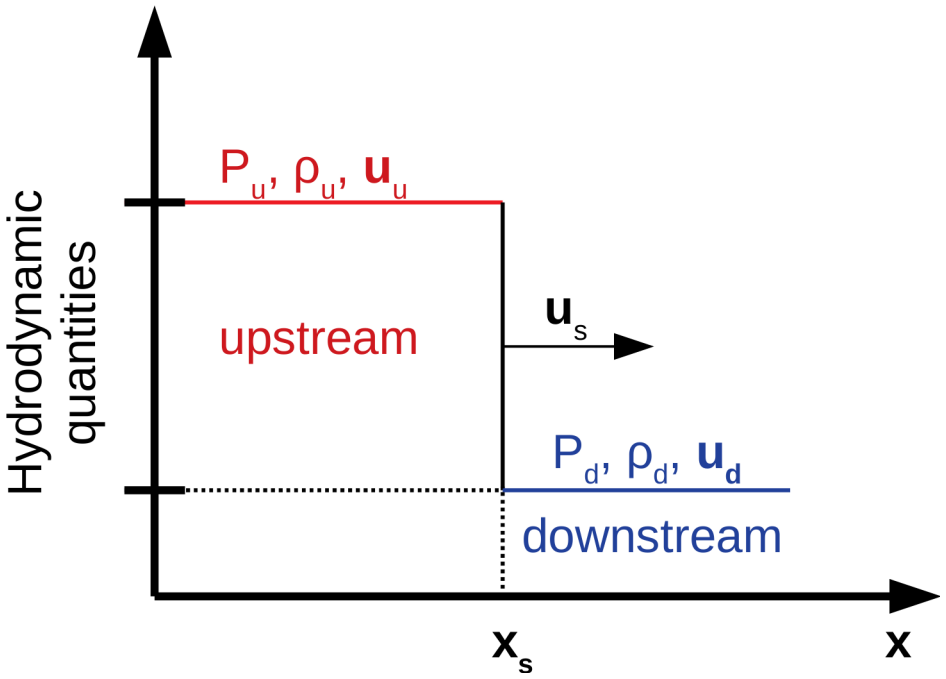

Figure 2.2 – Image in the laboratory frame of a shock propagating in the x-direction. As the fluid traverses the shock, its density and pressure increase, while its velocity decreases from (u_d) to (u_u), ensuring mass conservation at the shock front. In the laboratory reference frame, the shock would propagate from left to right at a velocity $(\mathbf{u}_s)$, impinging on stationary fluid denoted by subscript d, ultimately accelerating it to a velocity of $(|\mathbf{u}_d - \mathbf{u}_u|)$.

2.4.2 Hugoniot curves

If we characterise the mass flow as $j = \rho_d v_d = \rho_u u_u$ being constant along the propagation of the shock, we obtain:

$$\begin{aligned} j &= \sqrt{\frac{P_u - p_d}{V_d - V_u}}, \\ e_u - e_d &= \frac{1}{2}\left(P_d + P_u\right)\left(V_d - V_u\right), \end{aligned} \tag{2.4.3}$$

where V_u and V_d are the specific volumes. Last of Equation (2.4.3) is known as the Hugoniot condition. For an ideal gas, the internal energy e is given by:

$$e = \frac{P}{(\gamma - 1)\,\rho}, \tag{2.4.4}$$

and the Hugoniot condition (2.4.3) can be rewritten in the form:

$$\frac{\rho_u}{\rho_d} = \frac{(\gamma+1)P_u + (\gamma-1)P_d}{(\gamma+1)P_d + (\gamma-1)P_u} = \frac{(\gamma+1)M_s^2}{(\gamma-1)M_s^2 + 2}, \tag{2.4.5}$$

which can be written with the pressure ratio:

$$\frac{P_u}{P_d} = \frac{(\gamma+1)V_d - (\gamma-1)V_u}{(\gamma+1)V_u - (\gamma-1)V_d} = 1 + \frac{2\gamma}{\gamma+1}\left(M_s^2 - 1\right), \tag{2.4.6}$$

and in terms of the internal energy:

$$\frac{e_u}{e_d} = \frac{P_u\left[(\gamma-1)\,P_u + (\gamma+1)\,P_d\right]}{P_d\left[(\gamma+1)\,P_u + (\gamma-1)\,P_d\right]}. \tag{2.4.7}$$

We have introduced into these expressions the Mach number $M_s = u_u/c_s$, which is defined as the ratio of the local velocity of a fluid to its sound speed. Here, c_s represents the speed of sound in that same fluid.

For $M_s < 1$, the flow is termed subsonic, while $M_s > 1$ corresponds to supersonic flow. When $M_s = 1$, the flow is said to be sonic. This parameter categorises flows into these three types.

The upstream and shock velocities in the laboratory frame can be deduced from the previous equations. They read:

$$\begin{aligned} u_u &= u_d \pm \sqrt{\frac{2\left(P_u - P_d\right)^2}{\rho_d\left[(\gamma+1)\,P_u + (\gamma-1)\,P_d\right]}}, \\ u_s &= u_d \pm \sqrt{\frac{(\gamma+1)\,P_u + (\gamma-1)\,P_d}{2\rho_d}}. \end{aligned} \tag{2.4.8}$$

2.4.3 Weak and strong shocks: a matter of entropy deposition

The concept of entropy is crucial in understanding shock dynamics. For an ideal gas characterised by constant specific heat, the change of entropy due to the propagation of a shock is quantified by the equation:

$$\Delta S = c_v \ln\left(\frac{P_u V_u^\gamma}{P_d V_d^\gamma}\right), \tag{2.4.9}$$

where V denotes the specific volume of the gas and c_v represents the specific heat capacity at constant volume. This leads to the distinction in entropy between the two sides of the shock front:

$$\begin{aligned} S_u - S_d &= c_v \ln\left(\frac{e_u}{e_d}\left(\frac{V_u}{V_d}\right)^\gamma\right) \\ &= c_v \ln\left(\frac{P_u}{P_d}\left[\frac{(\gamma-1)\,P_u + (\gamma+1)\,P_d}{(\gamma+1)\,P_u + (\gamma-1)\,P_d}\right]^\gamma\right) > 0. \end{aligned} \tag{2.4.10}$$

Weak shocks

Figure 2.3 shows the Hugoniot and adiabatic curves for compression. The Hugoniot shows all the accessible states starting from an initial state (V_1, P_1) after the passage of a shock wave (V_2, P_2). As can be noticed from Equation (2.4.10), if we consider a weak shock strength ($P_2 \approx P_1$), the Hugoniot follows the isentrope before deviating from it. The internal energy variation is reduced to $\mathrm{d}e = -P\mathrm{d}V$ and as $T\mathrm{dS} = \mathrm{d}e + P\mathrm{d}V$ it produces very small amounts of entropy so that $\Delta S \to 0$, and the process can be treated as almost adiabatic. From figure 2.3, Hugoniot and isentropic compression curves (solid versus dashed lines) are almost in the region close to $(V_1,\, P_1)$ for the case of a perfect gas. The propagation of the front of a weak shock wave is analogous to that of sound waves, following the velocity described by Equation (2.3.8).

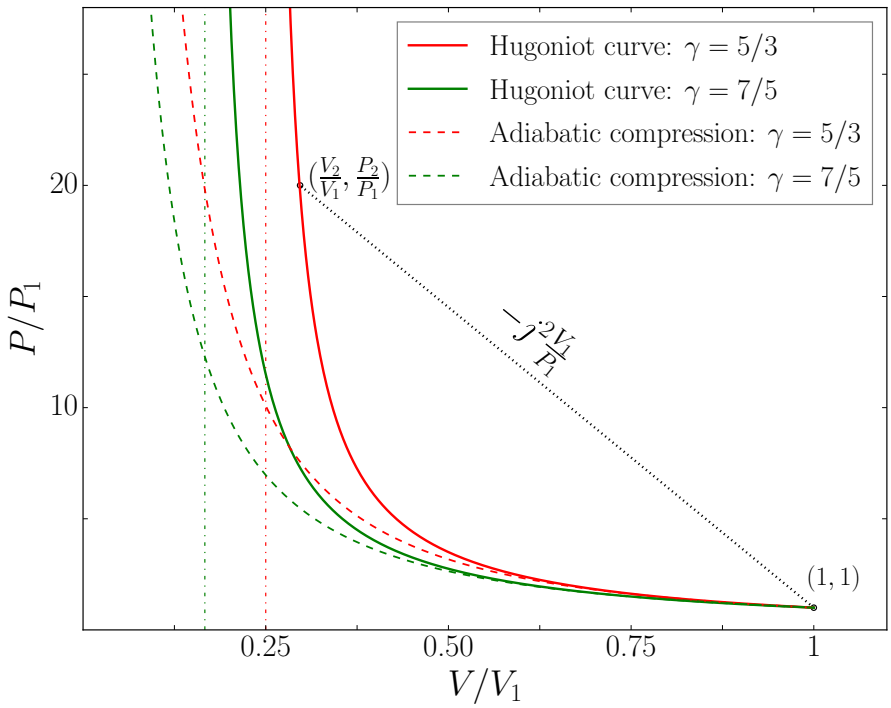

Figure 2.3 – Hugoniot curves (solid lines) and adiabatic compressions (dashed lines) for monoatomic and diatomic gas media (in red $\gamma = 5/3$, in green $\gamma = 7/5$). The dotted dashed line corresponds to the slope of the secant between the downstream and upstream regions of the shock and is proportional to the mass flow j^2. Adiabatic compression can theoretically compress a media as long as the pressure increases whereas the compression is limited in the case of a single shock (see the dashed-dotted vertical asymptotes).

Strong shocks

In the context of ICF, pressure is applied abruptly with $P_2 \gg P_1$. Hence, even though the curves representing the expressions originate from the same point, it is the expression (2.4.5) that describes the shell compression by the shock. Indeed, the adiabatic compression curve grows continuously. In contrast, if we consider two points (V_1, P_1) and (V_2, P_2) in the Hugoniot, the curve shows a maximum compression for $(\rho_2/\rho_1)_{P_2 \gg P_1} = (V_1/V_2)_{P_2 \gg P_1} = (\gamma+1)/(\gamma-1)$. For a monoatomic ideal gas with $\gamma = 5/3$, it can be compressed up to 4 times by a shock wave (red vertical dash-dotted line in figure 2.3). For a diatomic media ($\gamma = 7/5$), the maximum compression factor reaches 6 (green vertical dash-dotted in figure 2.3). Both Hugoniots deviate from the isentropic curve, which means that this single shock transformation generates states with significantly higher entropy.

With the augmentation of shock strength (P_u/P_d), a corresponding increase in ΔS is observed, exhibiting a monotonic increase that asymptotically approaches infinity as $(P_u/P_d \to \infty)$ (2.4.10). This progressive augmentation of entropy differential highlights the dissipative and irreversible nature inherent of shock waves. A single strong shock, resulting in significant entropy generation, is thus unsuitable for shell compression, as it would lead to high adiabats α and thus weak shell compressibility. However, the isentrope can be approximated by a sequence of weaker shocks, which lead to lower entropy generation, and results in quasi-isentropic compression.

Therefore, the approach adopted in the context of ICF involves a multi-shock preliminary compression stage to mitigate entropy deposition [3]. In the particular case of SI, it is then succeeded by the initiation of ignition via a potent shock, thereby depositing a substantial amount of entropy into the hot spot region to ignite it. This implies controlling entropy through shaping laser pulses. The design of the implosion of the capsule relies on devising a laser power profile in a series of approximately spaced shocks, closely aligned with the isentropic compression law, utilizing a spherical implosion strategy.

2.4.4 Adiabat

In the particular case of an ideal gas with polytropic coefficient γ, the adiabatic condition ((2.2.8)) can also be written:

$$P = \alpha(s)\rho^{\gamma} \ , \tag{2.4.11}$$

where $\alpha(s)$ is a function related to the specific entropy s, also called as adiabat.

The dimensionless adiabatic parameter α is defined as the ratio of the fluid pressure P to the Fermi pressure P_F of a degenerate electron gas. For a plasma composed of DT (deuterium-tritium), the expression for α is given by:

$$\alpha = \frac{P[\text{Mbar}]}{(2.17\rho[\text{g.m}^{-3}])^{5/3}}. \tag{2.4.12}$$

In the context of fusion and ICF, the primary objective is to achieve the maximum feasible compression for a given pressure. This in turn requires minimizing the adiabatic parameter, as it plays a crucial role in determining the compression achievable within the system. The adiabatic index averaged over mass within the cold fuel is the standard reference for implosion and will be adopted throughout this manuscript. Although it is possible to execute an ICF implosion with $\alpha < 1.5$, such conditions have been shown to trigger more hydrodynamic instabilities ([27]), and the adiabatic parameter in current experiments is kept higher ($\alpha \geq 3$).

2.5 Spherical implosion description

An ICF micro-pellet possesses an initial structure comprising several concentric spherical shells of various materials. Given the diminished hydrodynamic efficiency associated with high-Z materials—necessitating elevated energies for ionization and leading to the re-emission of X-rays, thereby preheating the target—the preferable interaction domain for ICF lies within low/medium-Z ablators. These commonly include materials such as plastic, carbon, or beryllium. The outermost shell (called ablator) is then composed of relatively light material, typically plastic CH, possibly doped (e.g., CH(DT)6, CHBr, ...). This outer material is intended to be ablated by laser radiation during implosion, exerting a piston effect on the inner shell, imparting inward motion. The inner shell consists of fuel, usually deuterium-tritium (DT) in cryogenic form. Finally, at the core of the capsule is a low-density gas (DT or D2) that is used for igniting a hot-spot. In conventional ICF, the aim is to transfer the kinetic energy from the shell to the target centre during the formation of the hot spot, so that ignition conditions are reached locally. Alpha particles generated in the hotspot then propagate into the dense surrounding shell to ignite.

2.5.1 Target and laser driver choice

A schematic of a typical ICF target is shown in figure 2.4. In the context previously

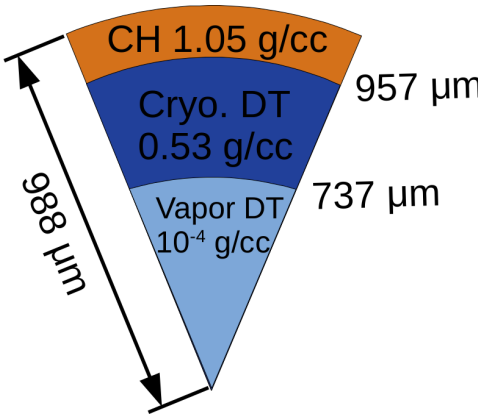

Figure 2.4 – Schematic of a typical ICF target based on a NIF polar direct drive SI experiment.

discussed in the Introduction, ICF relies on achieving a significant compression of the target, alongside the subsequent heating of a central hot-spot. This goal necessitates the delivery of energy in the megajoule range, all within a brief temporal window of approximately 10 nanoseconds. While it is worth noting the viability of alternative methods like Z-pinches or heavy-ion accelerators, our focus remains exclusively on the utilisation of a conventional laser driver, and we have opted not to delve into specific details in this manuscript. However, we encourage the interested reader to refer to the comprehensive review papers ([28], [29]) for a more in-depth exploration of both subjects.

The irradiation of the target can be achieved through two main avenues: indirect and direct laser drives. In the indirect drive configuration, the target is placed at the center of a cylindrical gold cavity known as a "Holhraum". Lasers drive their energy on the inner surfacer surface of the Holhraum. This absorption leads to the generation of X-rays, which, in turn, heat the ablator and facilitate the implosion of the target. One notable advantage of this configuration is the mitigation of laser beam non-uniformities, resulting in the reduction of hydrodynamic instabilities (refer to subsection 2.6.1 for further details). In contrast, in a direct-drive implosion, the laser directly irradiates the target. For the scope of this thesis, we confine our examination only to the direct irradiation of the target which involves the direct irradiation of the target material, capitalising on the higher coupling efficiency this strategy yields.

Under the influence of high-intensity laser light the target material undergoes a transition into plasma state. The incident laser light, characterised by a wavelength λ_L, propagates into the underdense plasma until reaching a critical density, denoted as n_c (3.1.24). This critical point arises where the frequency of the laser pulse aligns with the plasma frequency. Within this region of absorption, the laser energy is absorbed in the plasma and converted into thermal energy. This absorbed energy is subsequently propagated through the medium via thermal electronic conduction, including into higher density regions of the target. Preceding the shock wave (1), the matter remains motionless and may experience preheating due to radiation and supra-thermal electrons. The phenomenology of all these processes is described in Figure 2.5, which shows the different zones where incident energy is absorbed in the outer layers of the target and transported to the cold, dense inner material. The following paragraphs give a more detailed description of these zones.

The ablation zone

The ablation zone ((4) in Figure 2.5), also referred to as the corona, encompasses regions where the electronic density of the plasma is below critical density, and where mechanisms for laser energy absorption occur (see Chapter 3). The electronic temperature is nearly uniform, typically in the keV range. The absorbed energy is transferred to ions through collisions, causing the high-density plasma region to expand. Laser radiation absorption leads to the ejection of matter outward from the target by conservation of momentum — a phenomenon known as ablation. Sustained laser irradiation gradually consumes the target in this process.

Consider a solid target subjected to laser ablation in a planar geometry, where laser energy deposition predominantly occurs at the critical surface and the material undergoes partial or complete ionisation. A solid target under ablative conditions generates a shockwave guided by a stationary ablation pressure (P_{abl}), which emerges due to a rate of ablated mass ($\dot{m}_{\text{abl}}$) and a cutoff temperature. These scaling laws are described by the following relations [30]:

$$\begin{aligned} P_{\text{abl}}[\text{Mbar}] &= 57 \left(\frac{I_L[10^{15}\text{W.cm}^{-2}]}{\lambda_L[\mu\text{m}]} \right)^{2/3}, \\ \dot{m}_{\text{abl}} &= 3.2 \times 10^5 \left(\frac{I_L[10^{15}\text{W.cm}^{-2}]}{\lambda_L^4[\mu\text{m}]} \right)^{1/3} \text{g.cm}^{-2}\text{.s}, \\ T_c &= 13.7 \left(I_L[10^{15}\text{W.cm}^{-2}]\lambda_L^2 \right)^{2/3} \text{keV}. \end{aligned} \tag{2.5.1}$$

It is important to observe that the efficiency of laser light coupling to the target is increased for shorter wavelengths.

The conduction zone

The conduction zone is the region where the laser energy absorbed in the corona is transported to the cooler inner layers of the target by electronic conduction. The ablation of the outer part plays a role similar to the burnt gases of a rocket and generates the formation of a centripetal shock wave ahead of the ablation front. The pressure at this point is termed the ablation pressure, denoted as P_{abl}. During the initial phases of irradiation, the velocity of the ablation front, represented by v_{abl}, exceeds the local speed of sound, c_s. With a subsequent rise in laser intensity, the sound velocity accelerates at a faster rate compared to the ablation front velocity. Once v_{abl} equals c_s, a shock wave is initiated, marking the hydrodynamic separation point. Following this juncture, the target profile evolves into a quasi-stationary configuration, as depicted in Figure 2.5. The material is ablated at supersonic speeds while the thermal wave propagates towards the interior of the target at subsonic speed. The speed of the centripetal thermal ablation wave decreases with increasing electron temperature. The shock wave is detached upstream of the thermal wave, propagating towards the centre of the target: this is hydrodynamic separation. Inside the conduction zone, the transport of energy is mediated through the electron heat flux, which is influenced by the temperature gradient as described by [31]:

$$Q_e = -\chi_e \nabla T_e, \tag{2.5.2}$$

with $\chi_e = K_e T_h^{5/2} / \ln\Lambda$ the Spitzer–Härm thermal conductivity,
$K_e = 9.5 \times 10^{19}\text{erg.s}^{-1}\text{.cm}^{-1}\text{.keV}^{-7/2}$, and $\ln\Lambda$ the Coulomb logarithm. The maximum value of the electron flux $Q_{\text{lim}} = n_e T_e v_{\text{th}}$ can be estimated by assuming that all electrons

move in the opposite direction of the temperature gradient with their thermal velocity v_{th}.

Furthermore, insights from electron kinetic theory reveal that the applicability of the Spitzer-Härm formula is constrained to scenarios where the length of the temperature gradient is much larger than the mean free path of electrons. To address this constraint within hydrodynamic simulations, an approach introduced by [32] introduces an adjustable flux limiter f, which is used in the calculation of the flux:

$$Q = \min(Q_e, fQ_{\text{lim}}). \tag{2.5.3}$$

The specific value of f is determined by comparing simulation outcomes - especially parameters like the absorption coefficient and shell velocity - with empirical data. Typically, f falls within the range of 3% to 10%, while $f = 6\%$ is a commonly used value.

More sophisticated methodologies take into account non-local effects within the electron flux at the kinetic level. As electron energy increases, the mean free path of electrons also increases. This implies that non-local effects play a significant role for supra-thermal electrons responsible for energy transport across scales similar to the temperature gradient scale length. The Spitzer-Härm thermal conduction model assumes a mild anisotropy. The computation of heat flux relies on the electron distribution function, expressed as $f_e(\mathbf{v}) = f_e^0(\mathbf{v}) + \frac{\mathbf{v}}{|\mathbf{v}|} \cdot f_e^1(\mathbf{v})$. In the Spitzer model, $f_e^0(\mathbf{v})$ adopts a Maxwellian form $f_{eM}^0(\mathbf{v})$. Non-local theories account for deviations of f_e^0 from the Maxwellian distribution, especially concerning supra-thermal electrons. A refined heat flux is computed by considering that in the domain of high electron velocities ($v \gg v_{th}$), the distribution function can be approximated as $f_e^0(\mathbf{v}) = f_{eM}^0(\mathbf{v}) + \Delta f_0$. The correction factor Δf_0 is computed by segmenting the kinetic Fokker-Planck equation into distinct energy groups. For a comprehensive understanding of the non-local model integrated into the CHIC code, further details can be found in Reference [33].

The shocked zone
The shocked zone is demarcated by the shockwave propagating inwards within the target downstream, and the ablation front of the matter located at the upstream foot of the thermal wave. Density is higher here than in the solid, attributed to the passage of the shockwave through the solid material, with an electronic temperature in the range of a few eV.

The unshocked zone
The unshocked zone lies upstream of the shockwave front. Electronic temperature and density mirror those of the solid material.

2.5.2 shell implosion diagramm

The design of the capsule is a critical step in achieving implosion, encompassing the choice of materials, laser pulse shaping, and inherent technological constraints in capsule production. As an illustrative example, a simple capsule consisting of a central region of gaseous DT enclosed by a cryogenic DT shell and CH outer abalator is usually considered.

A basic capsule concept (inner gaseous DT and outer cryogenic DT shell serving as both fuel and ablator) was introduced by [34] during the preparatory phase of the HiPER project, initially intended for fast ignition scheme. This capsule design features a single internal interface, enhancing our understanding of shock trajectories.

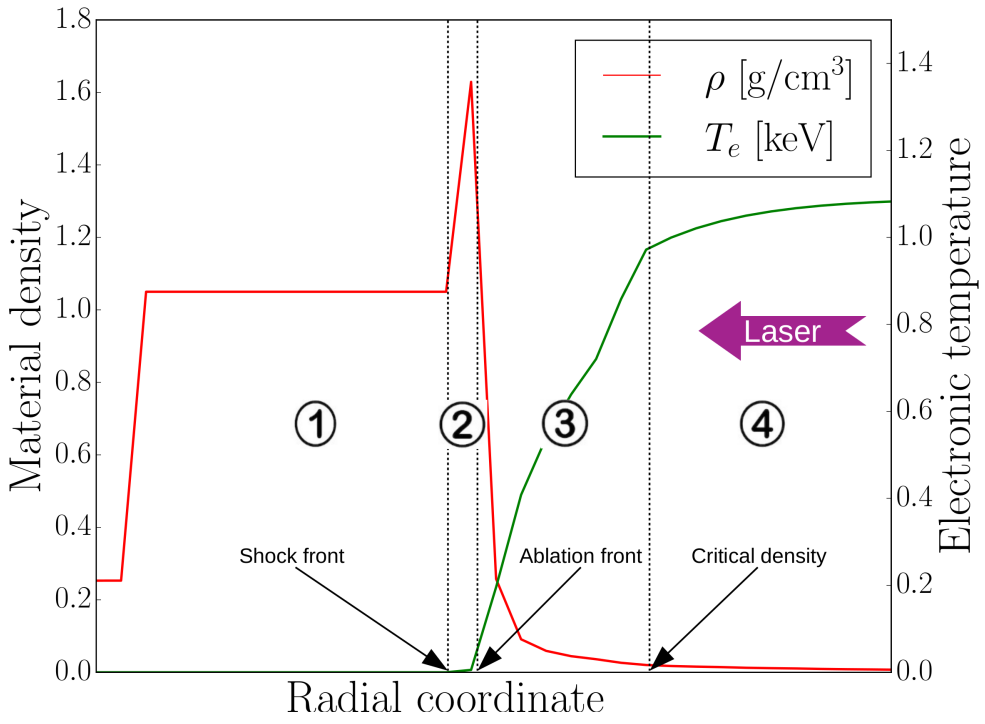

Figure 2.5 – In the direct drive scheme, the process of laser energy absorption takes place within a distinct zone. This energy absorption primarily occurs in the subcritical zone ($n_e \leq n_c$) (4). Subsequently, the energy is effectively conveyed through the medium by means of electrons within the conduction zone (3). Notably, as this energy transfer unfolds, a shockwave propagates upstream, playing a significant role in shaping the dynamics of the system. (2) and (1) correspond respectively to the shocked and unshocked zones. Curves are obtained from an hydrodynamics implosion profile simulation.

2.5.2.1 Adiabat shaping and compression phase

Figure 2.6 depicts the grid evolution in a typical implosion simulation using the *CHIC* code. Given that the code is written in Lagrangian formalism, the grid dynamically follows the flow. It shows the trajectory of constant mass cells of the capsule in the time-radius plane, also known as the flow diagram. This representation provides insight into the evolution of various shell layers and the trajectory of shocks within the core over time. A substantial quantity of cells (741 in total but only 185 are represented here for more visual clarity) is selected for the target shell. These trajectories are densely concentrated in this area to the extent that it appears as a shaded region in the illustration. Cell masses exhibit non-uniform distribution and are denser in regions requiring finer resolution. To prevent the occurrence of non-physical discontinuities, cell masses transition smoothly as they vary with radius.

At t = 0, lasers reach the target, and its energy deposition lead to ionization, vaporization, and expansion of the outer shells (1). The ablation of matter is evident through the ejection of external layers throughout the laser pulse. The sudden increase of pressure creates an inward-propagating shock, generated by the precursor phase of the pulse and ablated mass, ensues. This initial shock elevates the entropy in the fuel and is used to set the target adiabat to the desired value depending on shell stability. To achieve this, the laser pulse initiates with a preliminary pre-pulse of power P_0. This pre-pulse generates an ablation pressure $P_{\mathrm{abl},0}$ that sets in motion a shock wave propagating through the

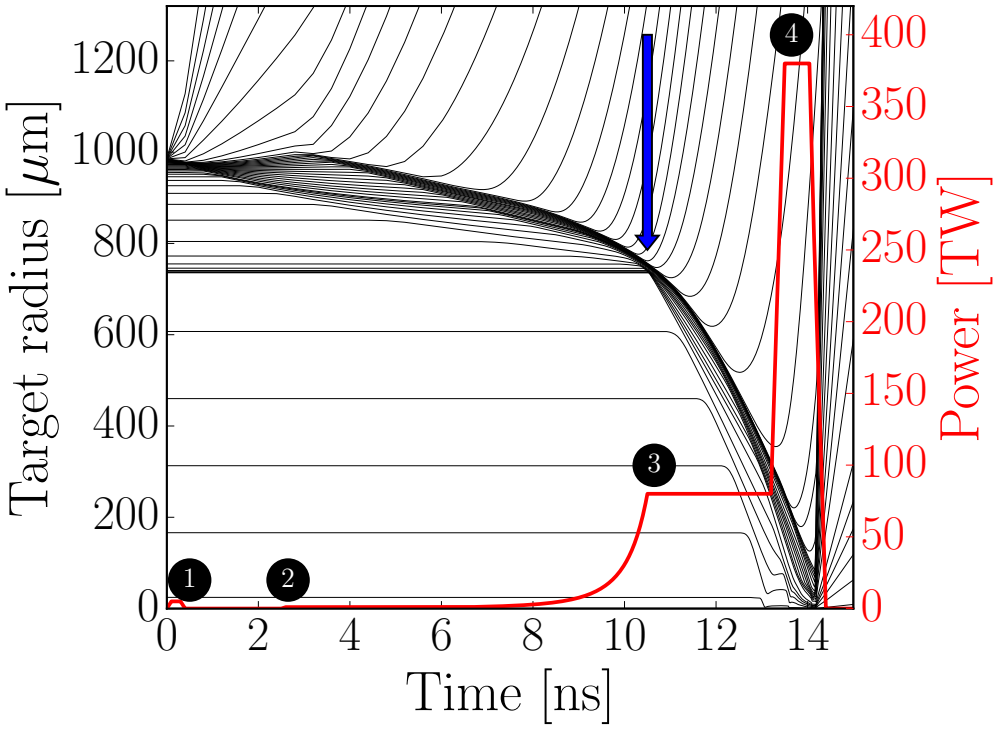

Figure 2.6 – Typical flow diagram illustration with its associated SI laser pulse. A quarter of the total lagrangian meshes are represented. The rise in power is timed so that the shocks coalesce on the inner surface of the target (indicated via the blue arrow). An ignitor shock is then launched (4) as the previous shocks bounce back at the center of the target. Inward and backward shock Numbers from 1 to 4 show the start of each new shock. The laser delivers 606 kJ of energy. These are 1D simulation results obtained via the hydrodynamics code *CHIC* [35].

shell. Subsequent to the shock propagation, the matter situated behind it undergoes a compression factor of approximately 4. Figure 2.7 illustrates the evolution of the adiabat within the shell during the implosion, clearly highlighting that it is kept almost constant in the shell, avoiding an entropy increase.

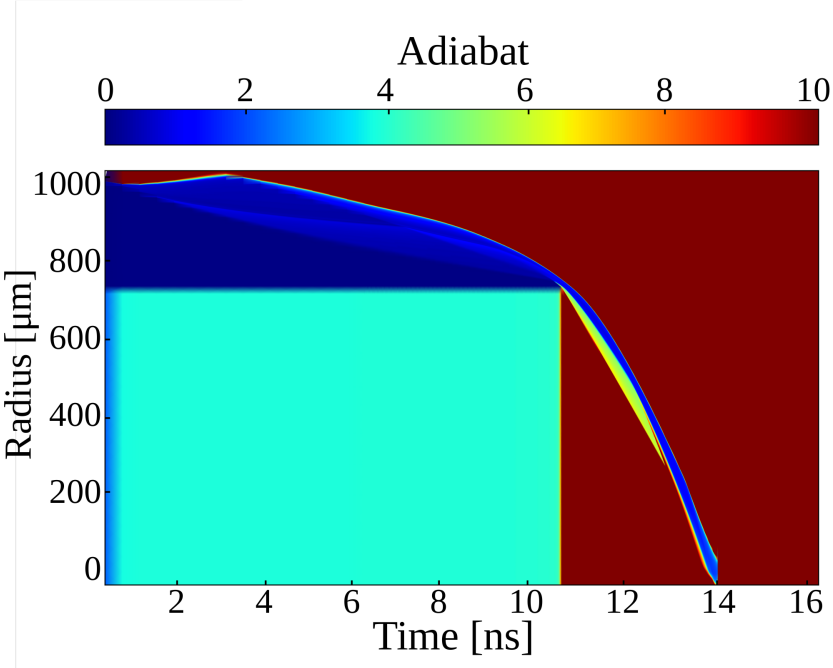

Figure 2.7 – Evolution of the adiabat in the time-space phase during the implosion of the target shown in 2.4.

The Kidder-type ramp up [36] (starting at $t \approx 2.5$ns in Figure 2.6) aims to achieve the most isentropic compression of the shell up to the onset of the shock at the gas-cryogenic DT interface. The temporal variation of the power $P(t)$ follows a proportional relationship to $(1-(t/t_0)^2)^{-5/2}$, where t_0 represents a characteristic time of the flow. This characteristic implies that energy sources used to achieve the implosion of an inertial confinement fusion (ICF) target all exhibit a temporal shape similar to the Kidder law. This compression sequence involves a series of weak shocks (2), carefully timed through laser pulse shaping to prevent excessive entropy production. In theory, this controlled increment generates compression waves, which are strategically designed not to amalgamate into shocks while traversing the shell. In practice, the pulse shaping is not that precise.

The gradual increase in laser power is constrained by the available laser energy and the emergence of parametric instabilities at high intensities. Therefore, the power increase continues until it reaches a maximum value, P_m, which remains constant during the primary pulse (refer to bullet 3 in Figure 2.6). At the instant the primary shock reaches the inner surface of the shell, a reflected rarefaction wave occurs within the shell, concurrently with the transmission of a shock wave into the gas. Let t_{sb} denote the time at which the shock emerges on the inner shell surface, commonly referred to as the shock breakout time. These shocks, moving inwards under the action of ablation pressure, break out simultaneously in the inner surface of the fuel layer at $t_{sb} \approx 10.5$ns (where the blue arrow is pointing at).

The compression waves, persistently propagating within the shell, interact with the

flow behind the rarefaction wave. The density and pressure gradients in this flow accelerate the transformation of compression waves into shock waves. This fast transformation guarantees that the compression waves reach the inner shell face shortly after the primary shock, preventing excessive entropy deposition in the shell. As the rarefaction wave encounters the ablation front, the rapid drop in density triggers a localised pressure increase. Consequently, a second shock wave rebounds into the shell. Following this event, the shell enters an acceleration phase, marked by the onset of its acceleration.

The shell aspect ratio, represented as $\mathcal{A} = R/\Delta R$ is a key factor in this scenario. Throughout the ablation phase, the shell experiences compression, resulting in a reduction of its thickness, ΔR, and a corresponding rise in the aspect ratio. This aspect ratio attains its maximum value at t_{sb} (noticeable in Figure 2.6 where the blue arrow is pointing at). In summary, the ablation phase initiates with the launch of a shock at the base of the laser pulse (1). This shock sets the shell adiabat parameter as shown in Equation (2.4.12).

During this phase, the shell compression evolves isentropically, with density proportional to P_{abl}. When the shock breakout time t_{sb} is reached, the shell density is:

$$\rho_{sb} = 4\rho_0 \left(\frac{P_{\text{abl,m}}}{P_{\text{abl,0}}} \right)^{3/5}$$

Notably, the shell aspect ratio experiences an increase during the ablation phase, reaching its peak value at t_{sb} called *In-Flight Aspect Ratio* (*IFAR*) estimated as:

$$IFAR = \frac{\rho_{sb}}{\rho_0} \mathcal{A}_0 \tag{2.5.4}$$

At this moment (3), the pulse reaches its maximum compression power: 80 TW, causing stronger ablation and increasing the ablation pressure - the shell accelerates. We enter the acceleration phase. At this time, the ablation pressure reaches 150 Gbar.

2.5.2.2 Acceleration phase

The rocket effect

We now turn our attention to the models describing the centripetal acceleration of the shell containing the DT fuel. The outer layers of the shell expand into the surrounding vacuum, while the inner layers are propelled in the opposite direction. A scheme of the geometry and physical quantities at play for the rocket effect are represented in figure 2.8.

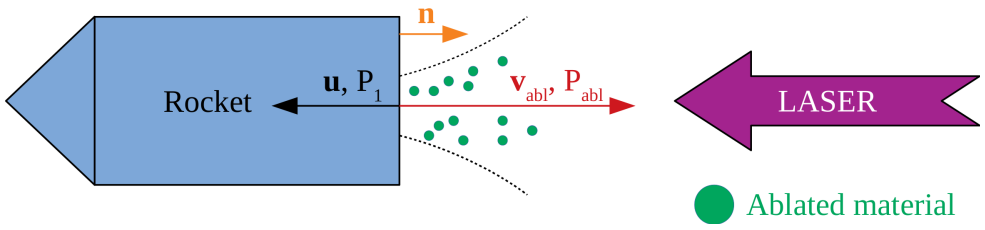

Figure 2.8 – Schematic representation of the rocket effect.

This phenomenon is referred to as the "rocket effect" drawing an analogy with the acceleration of a rocket due to the expulsion of combustion gases. To relate this to rocket behaviour, several simplifications are necessary:

— the internal pressure of the cavity enclosed by the shell is neglected.

— it is assumed that the inner layers are accelerated uniformly (meaning that it is assumed the shock passes through the entire shell in a very short time, and the acceleration of the inner layers is uniform).
— the analysis is conducted in a planar geometry.
— it is assumed that the ablated plasma is propelled into the vacuum at a velocity v_{abl} relative to the rest of the target.

We denote the initial mass of the rocket as m_0, its instantaneous mass as $m(t)$, and the flux mass loss rate as $\dot{m}_{\text{abl}}$, so that :

$$m(t) = m_0 - m_{\text{abl}}(t) = m_0 - 4\pi R^2(t)\dot{m}_{\text{abl}}t, \tag{2.5.5}$$

assuming $t = 0$ corresponds to the initiation of matter ejection. The speed of the shell is denoted $u = \mathrm{d}R/\mathrm{d}t$ with its radius R. v_{abl}, the velocity of ejection of hot gases to the exterior of the target, depends on the plasma temperature, which in turn is influenced by the laser illumination absorbed in that part of the target. The conservation of momentum in the target system is given by:

$$\frac{\mathrm{d}\left(m(t)u(t)\right)}{\mathrm{d}t} = 4\pi R^2(t)\dot{m}_{\text{abl}}\left(v_{\text{abl}} - u\right), \tag{2.5.6}$$

and as $\mathrm{d}m(t)/dt = -4\pi R(t)^2\dot{m}_{\text{abl}}$, it yields:

$$\mathrm{d}u = -v_{\text{abl}}\frac{\mathrm{d}m}{m}. \tag{2.5.7}$$

Integrating the previous equation gives the equation for implosion velocity:

$$u(t) = v_{\text{abl}}\ln\left(\frac{m_0}{m(t)}\right) = v_{\text{abl}}\ln\left(1 - \frac{m_{\text{abl}}(t)}{m_0}\right) = -v_{\text{abl}}\ln\left(\mu(t)\right), \tag{2.5.8}$$

where $\mu(t) = m(t)/m_0 \in [0;1]$ is the remaining fraction of fuel mass.

Hydrodynamic efficiency

The energy efficiency of the rocket effect can also be estimated, which measures how effectively energy from the ejected hot gases is transferred to the massive shell. The energy efficiency η is defined as the ratio between the kinetic energy of the shell and the exhaust energy being ablated:

$$\eta = \frac{\varepsilon_{\text{kin}}}{\varepsilon_{\text{ex}}}, \tag{2.5.9}$$

where ε_{kin} and ε_{ex} can be written as such:

$$\begin{aligned} \varepsilon_{\text{kin}} &= \frac{1}{2}m(t)u^2(t) = \frac{1}{2}m(t)v_{\text{abl}}^2\left[\ln(\mu(t))\right]^2, \\ \varepsilon_{\text{ex}} &= \frac{1}{2}\left(m_0 - m(t)\right)v_{\text{abl}}^2, \end{aligned} \tag{2.5.10}$$

so that the energy efficiency reads:

$$\eta = \frac{\frac{1}{2}m(t)v^2(t)}{\frac{1}{2}\left(m_0 - m(t)\right)v_0^2(t))} = \frac{\mu(t)}{1-\mu(t)}\left(\ln\mu(t)\right)^2, \tag{2.5.11}$$

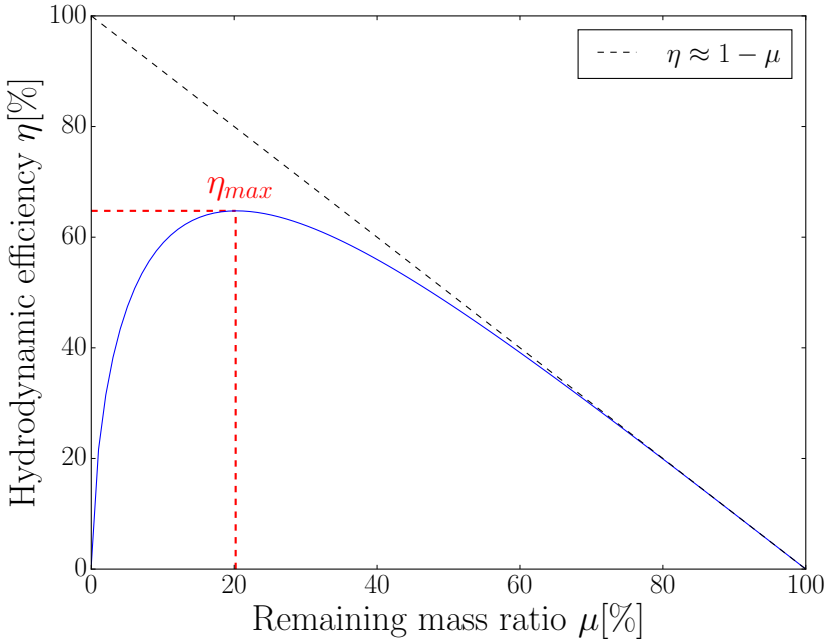

Figure 2.9 – Hydrodynamic efficiency η as a function of the remaining fuel mass $m(t)/m_0$.

The graph of the function (2.5.11) is illustrated in figure 2.9. It is clear that η is capped at a maximum of $\approx 65\%$. As depicted in the figure, the most significant acceleration of the shell occurs at the initial stages before the radius undergoes significant reduction. Therefore, it is reasonable to cease the acceleration when the radius has decreased to approximately half of its initial value. In typical ICF implosion scenarios, the ratio $m(t)/m_0$ doesn't usually surpass $50 - 60\%$, so that $\eta \geq 50 - 60\%$, thus allowing us to approximate η as: $\eta \approx 1 - \dfrac{m(t)}{m_0} = \dfrac{m_{\text{abl}}}{m_0}$.

In this simplified discussion, the flux of enthalpy and the energy flux required to maintain a consistent temperature in the corona region are disregarded. More comprehensive numerical simulations [37] that incorporate more detailed physics reveal that the overall hydrodynamic efficiency is approximately one third of the ideal expression (2.5.11), denoted as $\eta = \dfrac{\eta_{\text{ideal}}}{3}$.

This analysis highlights that the process of shell acceleration through ablation is characterised by relatively low efficiency. For direct drive scenarios, the maximum efficiency generally reaches about 20%. However, in real scenarios, it is essential to consider the energy required to ionise the corona, as well as losses due to radiation. This observation favours the use of a low atomic number ablative material. Ultimately, the target does not absorb the entirety of the incident laser energy. The absorption rate, which also depends on irradiation conditions, is, for example, 60% for DT and 75% for the plastic ablator CH, excluding scattering LPIs (see Chapter 3).This reduces the maximum hydrodynamic yield to less than 10%.

Relations between hydrodynamic quantities

Let us now establish the relationship between the shell aspect ratio, the ablated mass, and the implosion velocity. Assuming a thin shell thickness, we can express the change

in mass as:

$$\frac{\mathrm{d}m}{\mathrm{d}t} = \frac{\mathrm{d}m}{\mathrm{d}R}\frac{\mathrm{d}R}{\mathrm{d}t} = u\frac{\mathrm{d}m}{\mathrm{d}R}. \tag{2.5.12}$$

Then, by integrating the expression for the shell velocity (2.5.8) over the mass, we get:

$$\int_{m_0}^{m} u \ \mathrm{d}M = -4\pi \int_{R_0}^{R} \dot{m}_{\mathrm{abl}} r^2 \ dr. \tag{2.5.13}$$

Solving the integral on the left-hand side, substituting the expression for $u \ \mathrm{d}M$ and solving for M gives:

$$\int_{m_0}^{m} u \ \mathrm{d}M = u\int_{m_0}^{m} \ln\left(\frac{M}{m_0}\right) \mathrm{d}M = um_0\left[1 + \frac{m}{m_0}\left(\ln\left(\frac{m}{m_0}\right) - 1\right)\right]. \tag{2.5.14}$$

If we consider that $\Delta R_0 \ll R_0$, the initial mass of the shell is $m_0 = 4\pi\rho_0 R_0^2 \Delta R_0$, with ΔR_0 the initial thickness, Equation (2.5.13) can be rewritten as:

$$1 + \mu\left(\ln\left(\mu\right) - 1\right) = \frac{X}{3}\left[1 - \left(\frac{R}{R_0}\right)^3\right]. \tag{2.5.15}$$

Where X is the implosion parameter defined by [16]. This equation represents the dependence of the ablated mass M on the ratio shell radius R. The implosion parameter is defined as such:

$$X = \frac{\dot{m}_{\mathrm{abl}}}{v_{\mathrm{abl}}\rho_0}\mathcal{A}_0. \tag{2.5.16}$$

This expression illustrates the relationship between the ablated mass and the shell radius during the shell collapse. The ablated mass increases as the shell converges and approaches a maximal value when the shell radius reaches zero.

The dependence of the remaining mass on the shell radius is depicted in figure 2.10 (left), showing how the ablated mass grows during the shell convergence and peaks at $R = 0$ for different implosion parameters (ranging from 1 to 3). The blue curve in figure 2.10 (right) highlights the connection between the ablated mass at $R = 0$ and the shell implosion parameter X. This parameter has a practical range of values where $X < 3$, as beyond this limit the shell becomes entirely vaporised before the collapse. For X values below 3, the remaining mass ratio at $R \ll R_0$ can be approximated by:

$$\mu \simeq 1 - \left(\frac{X}{3}\right)^{1/3}, \tag{2.5.17}$$

and is shown as the dashed dark line in figure 2.10 (right). Now, we can establish a connection between the terminal velocity of the shell at the end of the ablation phase, denoted as $v_{\mathrm{imp}} = -u$, and the aspect ratio, represented as $IFAR = R/\Delta R$. The ablation rate is influenced by both the ablation pressure and the exhaust velocity, as expressed in equation (2.27) as $\dot{m}_{\mathrm{abl}} = P_{\mathrm{abl}}/u$. Consequently, by using Equation (2.5.4), we can infer that the implosion parameter exhibits a direct proportionality to the $IFAR$:

$$X = \frac{P_{\mathrm{abl}}}{u^2\rho_{\mathrm{sb}}} IFAR. \tag{2.5.18}$$

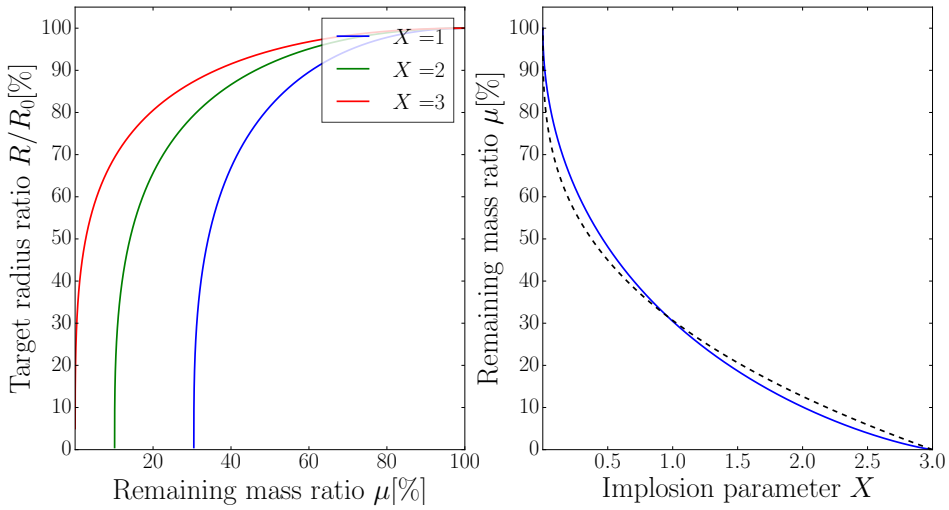

Figure 2.10 – The left panel illustrates the change in the remaining mass ratio $\mu = m/m_0$ throughout the shell convergence process, while the right panel shows how the remaining mass depends on the implosion parameter X. In the right panel, you can also observe a dark dashed line representing the approximate relation (2.5.17).

At the end of the acceleration phase, the shell radius is significantly smaller than the initial radius $(R/R_0)^3 \ll 1$, and the shell velocity $u = -v_{\text{imp}}$. Consequently, Equation (2.5.15) transforms into:

$$f\left(\frac{v_{\text{imp}}}{v_{\text{abl}}}\right) = \frac{X}{3}. \tag{2.5.19}$$

Here, the function f is given by: $f(x) = 1 - \exp(-x)(1+x)$. In the practical scenario where $x \leq 1$, we can approximate the function f as $f(x) \simeq 0.3x^2$. Both functions are plotted in figure 2.11. In cases where the implosion velocity is lower than the exhaust velocity, denoted as $v_{\text{imp}} \leq v_{\text{abl}}$ (typical in direct drive scenarios for specific laser intensities), we can express the *IFAR* as a function of the implosion velocity as:

$$IFAR = 0.9\left(\frac{v_{\text{imp}}^2}{P_{\text{abl}}/\rho_{sb}}\right). \tag{2.5.20}$$

The in-flight sound speed at the outer boundary of the compressed shell, assuming a polytropic index $\gamma = 5/3$, can be represented as $c_{s,\text{if}}^2 \approx 5P_{\text{abl,m}}/(3\rho_{sb})$. Consequently, the dependence of the *IFAR* on the shell maximal Mach number, denoted as $\mathcal{M}_0 = v_{\text{imp}}/c_{s,\text{if}}$, can be expressed as follows:

$$IFAR \approx 1.5\mathcal{M}_0. \tag{2.5.21}$$

This relation establishes a link between the *IFAR* and the implosion velocity v_{imp}. The in-flight adiabat is $\alpha_{\text{if}} = P_{\text{abl,m}}/\rho_{sb}^{5/3}$. Using the expression for ablation pressure (2.5.1), the implosion speed can be written to be proportional to:

$$v_{\text{imp}} \propto \alpha_{\text{if}}^{3/10}\left(\frac{I_L}{\lambda_L}\right)^{2/15} IFAR^{1/2}. \tag{2.5.22}$$

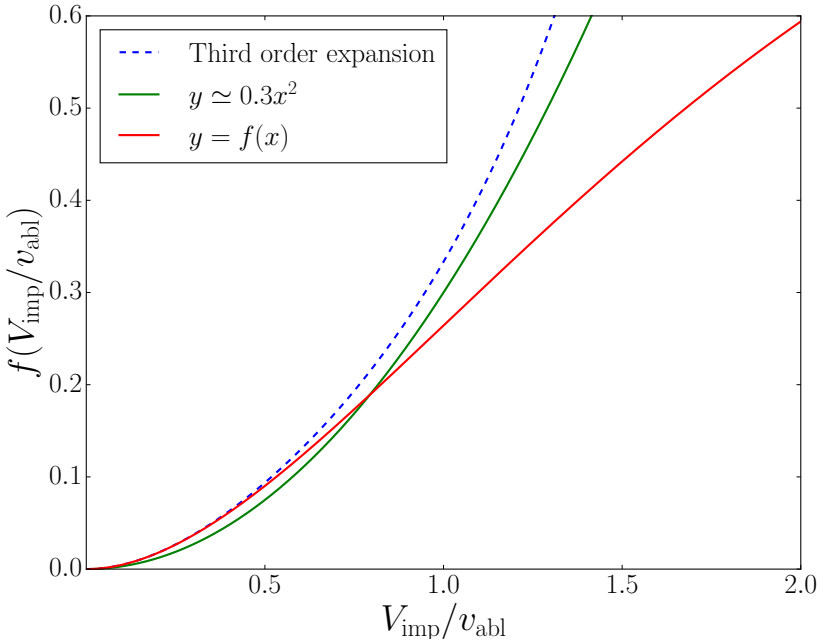

Figure 2.11 – The function $f(x) = 1 - \exp(-x)(1 + x)$ (red), its corresponding approximation $y = 0.3x^2$ (green) and its third order Taylor's expansion $y = x^2/2 - x^3/3 + x^4/6$ (dashed blue).

According to Equations (2.5.17), (2.5.18), and (2.5.21), the ablated mass scales as:

$$\frac{m_{\rm abl}}{m_0} \propto v_{\rm imp} \left(\frac{\dot{m}_{\rm abl}}{P_{\rm abl}} \right)^{2/3}. \tag{2.5.23}$$

Expressing the mass ablation rate and the ablation pressure in terms of the laser intensity, as per Equations (2.5.1), the hydrodynamic efficiency η scales as:

$$\eta \propto v_{\rm imp} \left(\frac{1}{I_L \lambda_L^2} \right)^{2/9} \left(\frac{m_{\rm abl}}{m_0} \right)^{2/9}. \tag{2.5.24}$$

For a given laser irradiation, an increase in hydrodynamic efficiency can be obtained through higher implosion velocity. Among the parameters, the laser wavelength plays a significant role, as higher laser wavelengths result in reduced hydrodynamic efficiency.

Increasing the implosion velocity can be achieved by elevating both the *IFAR* and the shell adiabat. Nevertheless, it is important to note that increasing the adiabat would lead to a reduction in the target compressibility. Conversely, increasing the *IFAR* might result in a decrease in implosion efficiency due to hydrodynamic instabilities (as disccused in the next section). The mass of the shell is related to the shell aspect ratio, as follows:

$$m = \frac{4\pi\rho R^3}{\mathcal{A}}. \tag{2.5.25}$$

Therefore, the shell aspect aspect ratio evolves in time as:

$$\frac{\mathcal{A}}{IFAR} = \left(\frac{\rho}{\rho_{\rm sb}} \right) \left(\frac{R}{R_0} \right)^3 \left(\frac{m_0}{m} \right). \tag{2.5.26}$$

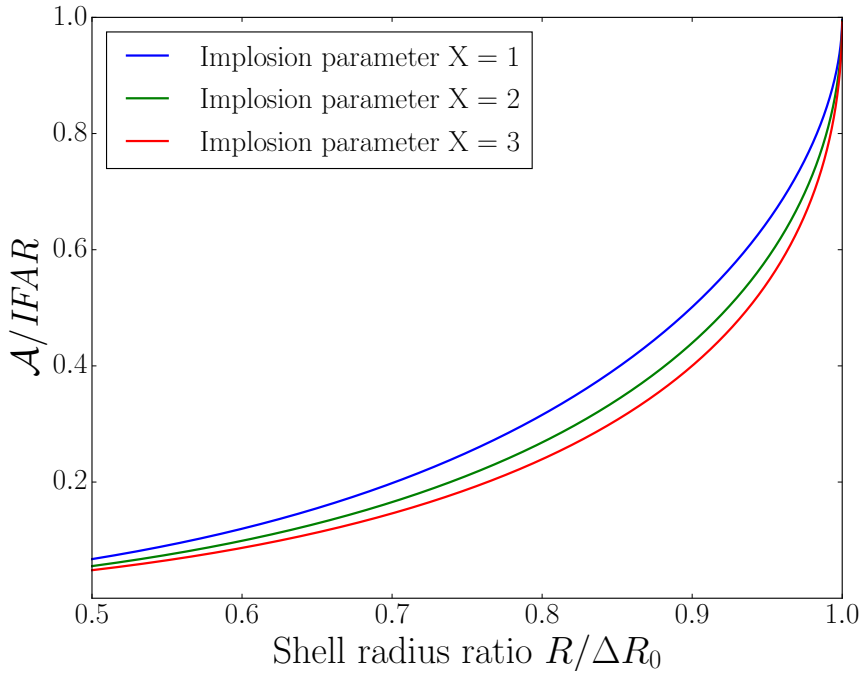

Figure 2.12 – The change in the shell aspect ratio $\frac{\mathcal{A}}{IFAR}$ in relation to the shell radius $\frac{R}{R_0}$ is depicted for various values of the implosion parameter X.

If the acceleration is nearly isentropic, and the shell density $\rho \propto \alpha_{if}$ remains relatively constant, with $\frac{\rho_{sb}}{\rho} \approx 1$, then by substituting Equation (2.5.26) into Equation (2.5.15), we derive a relationship between the shell aspect ratio and its radius:

$$y = -\frac{x^3 W\left(\frac{-ax^3 + a - 1}{e}\right)}{ax^3 - a + 1}, \tag{2.5.27}$$

where $y = \mathcal{A}/IFAR$, $x = R/R_0$, $a = X/3$ the implosion parameter divided by 3, and W is the Lambert function. Notably, the aspect ratio decreases during the target acceleration, as illustrated in Figure 2.12.

2.5.2.3 Deceleration and stagnation

We can identify the acceleration phase, which ends when the implosion velocity reaches its maximum, $v_{\max}$, the shorter deceleration phase, which corresponds to the time interval between $v_{\max}$ and 0, and the stagnation phase where the velocity is zero. It is at this last moment that the ignition of the target must occur. When the bouncing shock reaches the inner shell interface, the shell deceleration phase starts.

We will now give more insights on the physical quantities at play. Let us define R_d as the radius of the hot-spot at the end of the acceleration phase t_d, and $v_d = \frac{4\pi R_d^3}{3}$ as its volume. At that moment, the shell velocity $u = \frac{dR}{dt}$ reaches its maximum value, v_{imp}. When the shell comes to a halt, the final radius of the hot-spot is R_h. We introduce $C_d = R_d/R_h$ as the convergence ratio during the deceleration phase. Assuming an adiabatic compression of the gas inside the piston, the pressure is related to the density by $P \propto \rho^{5/3}$

for an ideal gas. Mass conservation in the hot-spot implies $\rho \propto R^{-3}$. Therefore, we have:

$$P = P_d \left(\frac{R_d}{R}\right)^5. \tag{2.5.28}$$

Subsequently, the pressure and density at the stagnation time can be expressed as $P_h = P_d C_d^5$ and $\rho_h = \rho_d C_d^3$.

During the deceleration phase, the shell trajectory can be integrated from Newton's second law:

$$m\frac{\mathrm{d}u}{\mathrm{d}t} = 4\pi P R^2 \tag{2.5.29}$$

Using relation (2.5.28), we can express the shell velocity as a function of its radius:

$$u^2 = v_{\text{imp}}^2 + \frac{4\pi P_d R_d^3}{m}\left[1 - \left(\frac{R_d}{R}\right)^2\right]. \tag{2.5.30}$$

At the stagnation time, when the shell velocity $u = 0$ and the shell radius $R = R_h$, the convergence ratio can be expressed as:

$$C_d = \sqrt{1 + \frac{\epsilon_{\text{kin}}}{\epsilon_{\text{int}}}} \tag{2.5.31}$$

Where $\epsilon_{\text{kin}} = \frac{1}{2} m v_{\text{imp}}^2$ represents the kinetic energy of the shell, and $\epsilon_{\text{int}} = \frac{3}{2} P_d V_d$ is the internal energy of the hot-spot at the end of the acceleration phase.

At the start of the deceleration phase, the internal energy of the hot-spot is negligible compared to the kinetic energy of the shell [38]. We can approximate C_d as $C_d \approx \epsilon_k/\epsilon_{\text{int}} \propto v_{\text{imp}}$. The maximum hot-spot pressure at the stagnation is given by:

$$P_h = P_d C_d^5 = \left(\frac{m v_{\text{imp}}^2}{P_d^{3/5} V_d}\right)^{5/2}. \tag{2.5.32}$$

To achieve a high pressure in the hot-spot, it is crucial for the volume of the hot-spot and its pressure at the start of the deceleration phase to be low. For an ideal monoatomic gas, the temperature is proportional to the square of the sound velocity: $T \propto c_s^2$ where $c_s^2 = 5P/3\rho$. Consequently, the hot-spot temperature scales as:

$$T_h \propto v_{\text{imp}}^2. \tag{2.5.33}$$

The final pressure and temperature (Equations (2.5.32) and (2.5.33)) within the hot-spot are highly dependent on the implosion velocity. In our approach, we made a preliminary estimation of the hot-spot pressure at stagnation time, presupposing the shell role as a rigid piston with a defined mass acting on the hot-spot. In reality, however, electron heat conduction induces ablation of the shell inner surface. As the mass within the hot-spot increases, the shell mass decreases, resulting in a denser yet cooler hot-spot at stagnation. While this phenomenon exerts a more substantial influence on temperature (T), its impact on pressure ($P \propto \rho T$) is comparatively less pronounced. Upon reaching a critical pressure, ignition ensues, and the hot-spot initiates a propagating burning wave within the shell.

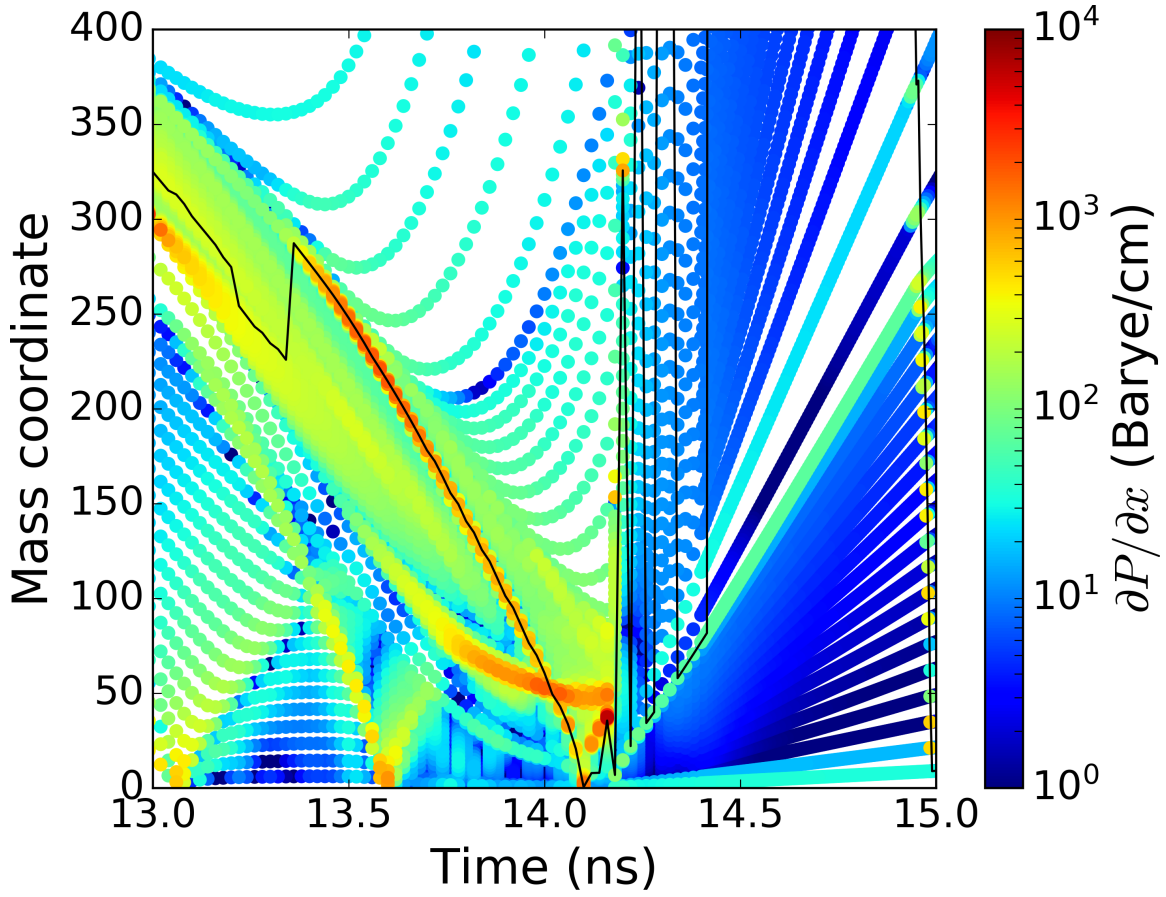

Figure 2.13 – Flow diagram of the target 2.4 with pulse 2.6. It is focused on the deceleration phase, stagnation, ignition and burn. Shocks bouncing back and forth at the center of the shell and at the inner surface of the dense DT layer are clearly visible. Stagnation occurs around 14.0 ns, a thermonuclear blast wave occurs a few picoseconds later, heating and burning the remaining target. In black solid line is depicted the more powerful shock.

Example through a SI simulation

We here present results from the same simulation previously discussed, performed with the *CHIC* code. The target and laser pulse were designed for SI ICF. The shell deceleration phase starts when the shock bouncing from the center of the target reaches the inner part of the shell (around $t_d \approx 13.3$ ns in Figure 2.13).

At this point, maintaining pressure through laser irradiation is no longer necessary, and ignition conditions are not reached yet. The spike is then launched (4) to collide with the shock that rebounded at the center near the inner surface of the shell at the beginning of the deceleration phase. The collision of these two shocks generates two new shocks propagating in opposite directions, each with pressures higher than the initial shocks. This collision leads to the conversion of the incident shock kinetic energy into internal energy, resulting in the amplification of the emerging shocks ([23]). Several analyses have been conducted to model this phenomenon for strong shocks [39], as well as in more general cases as shown in [23], and [40]. This part is crucial for shock ignition since, just before ignition, the strong shock created by the spike collides with the outgoing shock resulting from the compression phase at the outer surface of the cryogenic DT (4) in Figure 2.6. The resulting converging shock enters the DT gas, raising its temperature

above the ignition threshold after one or more rebounds around $t_s = 14$ ns.

As the pressure and the temperature rise, the shell motion gradually slows until it becomes motion less at the moment of stagnation. At this instant, the dense shell has dissipated its kinetic energy, which is converted into internal energy. The shell compression reaches its maximum, and the material forming the hot spot experiences pressure buildup due to confinement in an increasingly compacted volume, leading to pressure uniformity in the hot spot.

2.5.2.4 Hot spot ignition and thermonuclear combustion

The final pressure (2.5.32) and temperature (2.5.33) in the hot-spot are highly dependent on the implosion velocity. This estimation is based on the assumption that the shell behaves as a rigid piston with a fixed mass, neglecting the influence of electron heat conduction that leads to the ablation of the inner part of the shell. As a result, the hot-spot at stagnation becomes denser but cooler. However, the pressure $P \propto T\rho$ is less sensitive to this phenomenon. When the hot-spot pressure is sufficiently high, ignition occurs, and the hot-spot generates a burn wave that propagates within the shell.

Figure 2.13 displays a close-up view of the reference simulation grid flow during the deceleration phase, ignition, and burn. Starting from time 14.0 ns, the temperature and areal density in the hot-spot exceeds the ignition conditions. Ignition starts and a burn wave is generated just after, propagating within the shell in just a few picoseconds.

We will examine the energy balance of an initiating sphere. In its most basic form, the model addresses the energy balance of a sphere filled with uniform hot fuel, surrounded by a larger sphere of colder fuel. We are specifically referring to two cases: isobaric and isochoric initial conditions. In the standard ICF or SI scenarios, the conditions of the imploded fuel at the time of ignition are nearly isobaric. This means that the hot spot is surrounded by colder and denser fuel, resulting in nearly constant pressure over most of the fuel. On the other hand, isochoric conditions are more relevant to the alternative fast-ignition and shock ignition approaches. Generally, we can express the rate of change of the internal energy density e in the hot spot as:

$$\frac{\mathrm{d}e}{\mathrm{d}t} = W_{\mathrm{dep}} - W_m - W_r - W_e, \tag{2.5.34}$$

where:

- $W_{\mathrm{dep}} = A_\alpha \rho_h^2 \langle \sigma v \rangle_{\mathrm{DT}} f_\alpha$ represents the power density deposited by the fusion products. $A_\alpha = 8 \times 10^{40}$ erg/g^2, $\langle \sigma v \rangle_{\mathrm{DT}}$ is the DT reactivity and f_α is the individual fraction associated with α-particles.
- $W_m = A_m \rho_h R_h^{-1} T_h^{3/2}$ is the power density contribution from mechanical work due to the hot fuel sphere exchanging energy with the surrounding plasma in the isochoric regime (the pressure is much higher in the hot spot than in the surrounding fuel). It is derived from the ideal-gas equation of state. We have: $A_m = 5.5 \times 10^{22}$ cm^{3}s^{-3}keV$^{-3/2}$ for isochoric ignition, $A_m = 0$ for isobaric ignition.
- $W_r = A_b \rho_h^2 T_h^{1/2}$ corresponds to the power radiated for a DT plasma in the range of a few keV. The dominant mechanism is electron bremsstrahlung, so that $W_r \equiv W_b$. We have: $A_b = 3.05 \times 10^{23}$ erg cm^{3}g^{-2}s^{-1}keV$^{-1/2}$.
- $W_e \approx \dfrac{3 c_e A_e}{\ln \Lambda} \dfrac{T_h^{7/2}}{R_h^2}$ corresponds to the average power density loss due to electron thermal conduction. It is derived from the Spitzer theory [31] and dimensional arguments. We have: $A_e = 9.5 \times 10^{19}$ erg s^{-1}cm^{-1}keV$^{-7/2}$, and $c_e \approx 1$ is a numerical

coefficient.

Considering ion thermal conduction is crucial, particularly in the hotspot where ion temperatures may exceed electron temperatures during the burn. Indeed, as $W \propto T^{7/2}$, if $T_i > T_e$ the difference in mass ratio ($m_i/m_e \approx 1836$), can be compensated. It is not uncommom to have $W_i/W_e \approx 0.10$, which is small but not negligible. However, electrons quickly reach equilibrium with ion temperatures, and due to their lower mass, they facilitate faster energy transport. For this model, it is assumed that the hot spot is optically thin, leading to the neglect of neutron deposition and stopping of X-ray photons by the fuel. The hot spot temperature increases when:

$$\begin{aligned} \frac{\mathrm{d}E}{\mathrm{d}t} &> 0, \\ \Leftrightarrow W_{\mathrm{dep}} &> W_e + W_r + W_m. \end{aligned} \tag{2.5.35}$$

In this context, "ignition" refers to a state where the power deposition by fusion products is greater than the total power losses:

$$\left(A_a \langle \sigma v \rangle_{\mathrm{DT}} f_\alpha - A_b T_h^{1/2}\right) (\rho_h R_h)^2 - A_m T_h^{3/2} (\rho_h R_h) - \frac{3 c_e A_e T_h^{7/2}}{\ln \Lambda} > 0 \tag{2.5.36}$$

Equation (2.5.36) is known as the hot-spot self-heating condition, which is analogous to the Lawson criterion for magnetic fusion. In the isobaric limit (when $A_m = 0$), the self-heating condition can be expressed in a particularly simple and insightful manner:

$$\rho_h R_h > \left(\frac{3 c_e A_e \left(\ln \Lambda\right)^{-1} T_h^{7/2}}{A_\alpha \langle \sigma v \rangle_{\mathrm{DT}} f_\alpha - A_h T_h^{1/2}} \right)^{1/2}. \tag{2.5.37}$$

Example through a SI simulation

From Figure 2.14, the thermodynamic curve of the previously discussed 1D DT shell implosion simulation using *CHIC* is shown. The hot spot reaches a peak temperature. The achieved ablation pressure of approximately 100 Mbar exerted on the capsule surface induced the inward acceleration of the shell, reaching peak velocities of about 400 km/s. This pressure buildup at the center subsequently decelerated the imploding shell, which functioned as a piston, compressing and heating the central plasma. The hot-spot first gets denser along the implosion, and once the areal density lies within (or just at the boundary) of the isobaric limit, then the temperature of the hot spot increases to reach very high values $T_i > 10$ keV. The hotspot is surrounded by a dense, colder shell with densities reaching several hundreds of g/cm^3. $T_h \approx 50$keV, and confinement parameter $\rho_h R_h \approx 1.0$ g/cm^2. The hot-spot is then considered as self-heating and eventually ignites. It has reached density and temperature values high enough for fusion reactions to be triggered in large numbers, for the alphas to remain confined within it and for it to ignite, creating a blast wave burning the rest of the fuel. The fuel remains under confinement and undergoes efficient combustion for approximately $t_{burn} \approx 40$ ps. During this period, the burning fraction corresponds to approximately 25.75% of the total fuel mass, resulting in the release of 44 MJ of fusion energy. This energy release corresponds to a target gain of $\mathcal{G} = 73$.

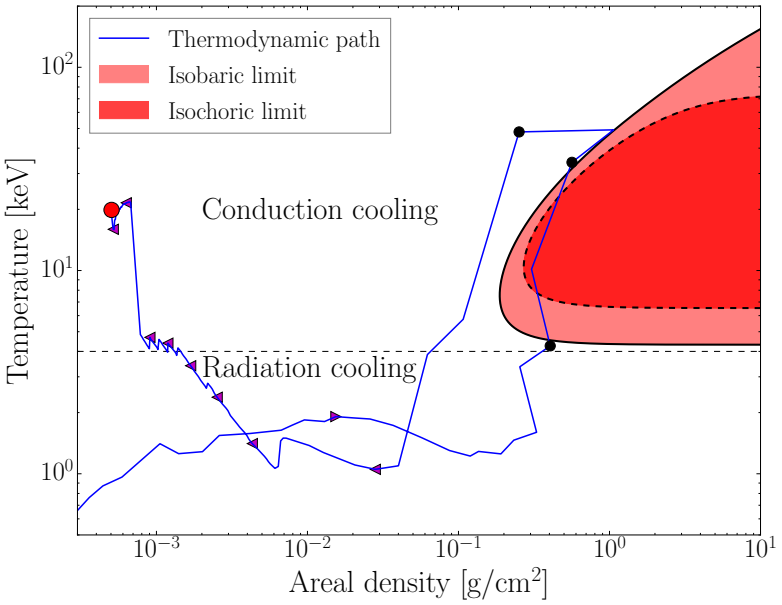

Figure 2.14 – Thermodynamic diagram of the hot spot during the implosion is shown in blue. Purple markers show the direction of the thermodynamic path. The dark circle markers represent points at $t = [14.10, 14.15, 14.18]$ ns. The red circle marker corresponds to the last time-step of the simulation. Self-heating conditions (2.5.37) and (2.5.36) are shown respectively in plain and dashed red lines. Hot spot with parameters within the red lines heat due to α-particle heating.

2.6 Target stability limiting effects

2.6.1 Hydrodynamic instabilities

2.6.1.1 Perturbations effects on system stability

Because of the inclusion of advection terms $\nabla \cdot \mathcal{F}$ with $\mathcal{F} = [\rho\mathbf{v}; \rho\mathbf{v}\mathbf{v}; \rho e\mathbf{v}]$, the Euler equations exhibit nonlinearity and are susceptible to the development of instabilities. Let us examine the impact of perturbative transverse modulations on the stability of these equations. The analytical study of hydrodynamic instabilities involves deriving the dispersion relation, which essentially establishes the connection between the rate of temporal growth β and the spatial modes k of the interface. To simplify the problem and eliminate the complications introduced by convergence effects, we employ planar targets in our fundamental study of instabilities. The perturbative approach for the fluid equations entails representing each scalar quantity X as a combination of a steady one-dimensional average X_0 and a small-amplitude two-dimensional time-dependent perturbative term $\tilde{X}$:

$$X(x, y, t) = X_0(x) + \tilde{X}(x, y, t) \quad \text{with } \tilde{X} \ll X_0(x). \tag{2.6.1}$$

The average quantity $X_0(x)$ satisfies the stationary 1D Euler equations. The perturbed quantity $\tilde{X}$ follows the linearized first-order time-dependent 2D Euler equations. It is decomposed in Fourier space as follows:

$$\tilde{X}(x, y, t) = \tilde{X}(x) \exp(\gamma t + iky), \tag{2.6.2}$$

where $\tilde{X}(x)$ is the amplitude, k the interface mode and γ the growth rate of the studied instability. This parameter is the characteristic rate at which rate a perturbation grows

in an unstable system.

In this way, the amplitude η of the interface can be decomposed in Fourier space as the sum of contributions from all the modes k:

$$\eta(x, y, t) = \sum_k \tilde{\eta}(x) \exp(\gamma t + iky). \tag{2.6.3}$$

Any linear and unstable phase can be described within this mathematical framework. The distinction in the treatment of instabilities lies in the selection of source terms to be considered in the Euler equations and in the boundary conditions.

2.6.1.2 The Rayleigh-Taylor instability

ICF capsule implosions inherently exhibit instabilities, notably the Rayleigh–Taylor instability (RTI), which initially deforms and damages the imploding shell and subsequently impedes the formation of the central hot spot. It is evident that achieving ignition in the central hot spot is profoundly contingent upon the effective minimisation of this instability. Controlling this instability poses a significant challenge for ICF.

Significant Rayleigh-Taylor (RT) growth typically occurs during the initial phase of implosion when the ablation pressure, resulting from the absorption of energy in the outer layers of the shell, sets it in motion. It can also happen during the final phase when the central hot spot exerts opposing pressure, slowing down the shell and transforming the implosion into an explosion. In both cases, there is a scenario where a light fluid exerts pressure on a heavy fluid. Such a situation is unstable, and the associated instability is known as the Rayleigh-Taylor Instability. Figure 2.15 shows the evolution the instability.

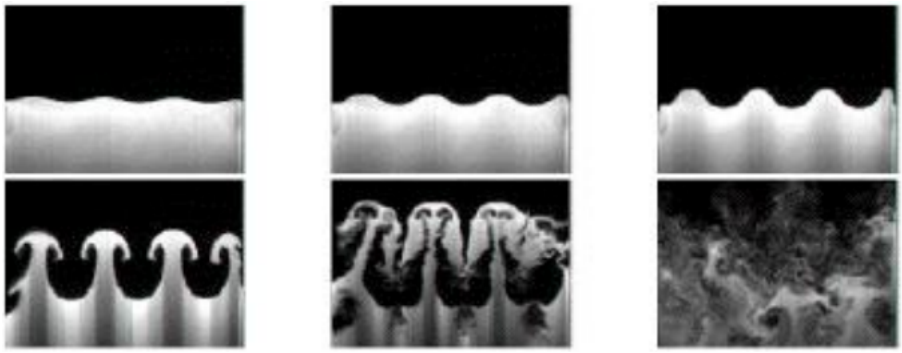

Figure 2.15 – Density slice at the ablation front of an imploding ICF target under the effect of the Rayleigh-Taylor instability at different stages.

The RTI [41], [42], named after the two first scientists who identified it and put it into an equation, occurs when a light fluid with density ρ_1 supports a heavy fluid with density ρ_2 in an acceleration field or when density and pressure gradients are opposed. Even if the interface between the two fluids is initially nearly flat, any deviation from flatness tends to amplify the amplitude of the initial interface disturbance.

Mechanical analogy

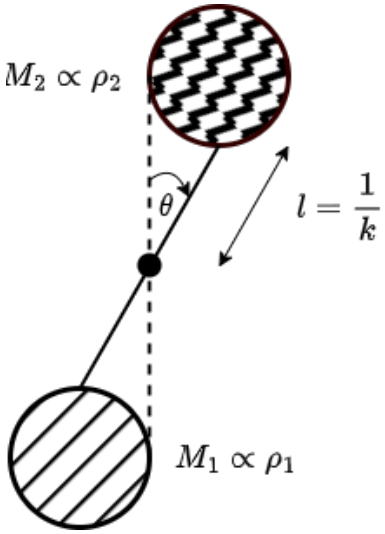

Figure 2.16 – Mechanical analogy scheme for the RTI.

Before we proceed with the calculation, let us introduce an unstable pendulum, corresponding to the configuration in Figure 2.16. The two weights have different masses, and are connected by a rod of half-length l. The weights and the rod form an angle θ. The whole system is subjected to a gravity field g and can be seen as a simple mechanical analogy to RTI. For this case, we can write:

$$(M_1 + M_2)l^2 \frac{\mathrm{d}^2\theta}{\mathrm{d}t^2} = (M_2 - M_1)gl\sin\theta. \tag{2.6.4}$$

As long as θ is small, we can approximate $\sin\theta \approx \theta$, and equation (2.6.4) becomes:

$$(M_1 + M_2)l^2 \frac{\mathrm{d}^2\theta}{\mathrm{d}t^2} = (M_2 - M_1)gl\theta, \tag{2.6.5}$$

for which a solution is:

$$\theta = \Re[\theta_0 \exp(-i\omega t)], \tag{2.6.6}$$

with:

$$\omega^2 = \frac{M_1 - M_2}{M_1 + M_2} kg. \tag{2.6.7}$$

If the masses M_1 and M_2 are respectively proportional to the densities ρ_1 and ρ_2, and if we consider that $l = 1/k$, we have:

$$\omega^2 = \frac{\rho_1 - \rho_2}{\rho_1 + \rho_2} kg. \tag{2.6.8}$$

In the precise case where $\rho_2 > \rho_1$, the solution is known as unstable:

$$\theta = \theta_0 \exp(\gamma t), \tag{2.6.9}$$

with:

$$\gamma = \sqrt{\frac{\rho_2 - \rho_1}{\rho_1 + \rho_2} kg} = \sqrt{A_T kg}, \tag{2.6.10}$$

and A_T is the dimensionless Atwood number given by:

$$A_T = \frac{\rho_2 - \rho_1}{\rho_1 + \rho_2}. \tag{2.6.11}$$

which defines the density contrast at the interface between the two media. In this configuration, $\rho_2 > \rho_1$, $A_T > 0$, $\gamma \in \mathbb{R}$, the amplitude of the perturbation θ follows an exponential increase until it diverges when $k \to \infty$.

ICF scenarios

In real configurations, the stabilizing effects of viscosity and surface tension need to be considered for small wavelengths. In its classic configuration, numerical studies on the impact of viscosity [43], compressibility, and Atwood number dependence [44] had already demonstrated the presence of stabilizing effects on the evolution of the Rayleigh-Taylor instability. In the context of ICF, laser ablation on the target front surface also induces stabilizing effects. In ICF, the hydrodynamic profiles are not homogeneous, and the interface, which is virtual, is located near the ablation front. Therefore, the RTI is modified by several effects:

— the fluids are not incompressible, and precisely the expansion of the outer layers plays a significant role in accelerating the inner part of the shell,

— thermal conduction and, especially, ablation itself tend to slow down the instability.

The model developed by Takabe presents a phenomenological growth rate based on numerical calculations [45]:

$$\gamma = \alpha\sqrt{A_T g k} - \beta k v_{\text{abl}}, \tag{2.6.12}$$

where v_{abl} is the ablation velocity, α and β are dimensionless coefficients between 0.8 and 3.0. The ablation growth rate demonstrates a stabilizing effect on all interface modes and total suppression for modulations where $\lambda < \lambda_c$:

$$\lambda_c = \frac{2\pi}{k_c} = \left(\frac{\beta}{\alpha}\right)^2 \frac{2\pi v_{\text{abl}}^2}{A_T g}. \tag{2.6.13}$$

The growth rate (2.6.12) is modified by introducing the front thickness [46]:

$$\gamma = \sqrt{\frac{A_T g k}{1 + kL}} - \beta k v_{\text{abl}}. \tag{2.6.14}$$

Here, L represents the length of the density gradient at the ablation front.

At the ablation front, the density contrast between the shocked material and the coronal plasma is very high, so that $A_T \sim 1$. The stabilizing term $\sqrt{1 + kL}$ accounts for the effects related to the thickness of the ablation front, which is assumed to be infinitesimally thin in the classic instability treatment in (2.6.12).

It is known that the wave modes that pose the greatest challenge in ICF experiments are those with lengths that closely match the thickness of the shell [47]. To address this issue, laser pickets, as depicted in Figure 2.6 bullet (1), offer a solution by increasing the ablation velocity (v_{abl}) without ramping up acceleration (g) (as proposed by [27]).

Reducing the implosion velocity has a positive effect as it lowers both acceleration and deceleration, thereby mitigating RTI. Figure 2.17 illustrates that, in NIF experiments, stable implosions can be achieved with implosion velocities (v_{imp}) below 300 km/s. However,

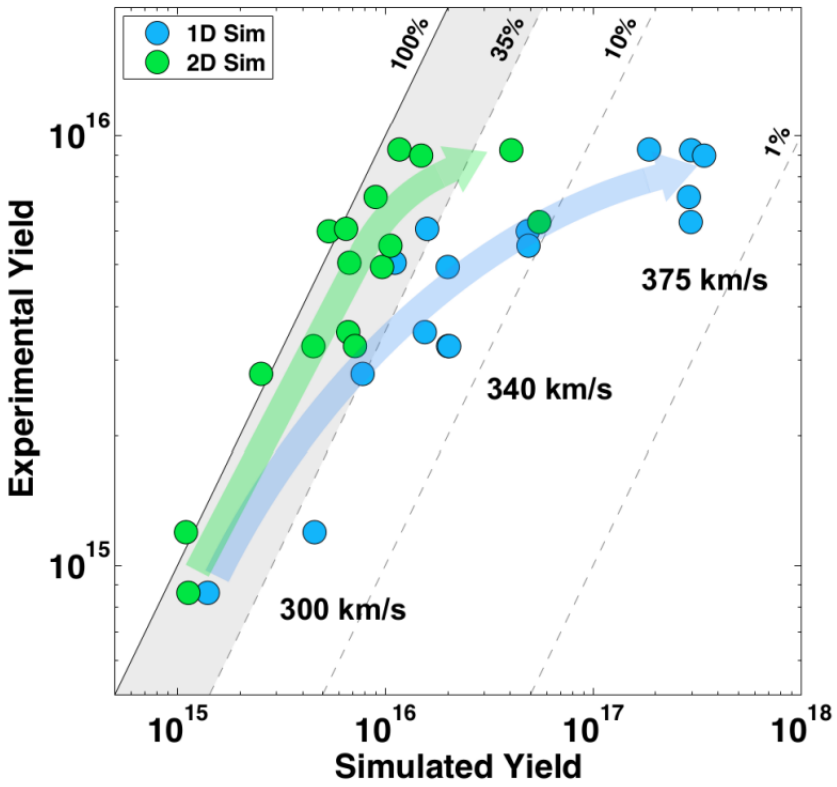

Figure 2.17 – Comparing the predictive capabilities of 1D simulations (shown in blue) and 2D simulations (shown in green) to actual experiments for various implosion velocities, we can observe that the dashed lines indicate the reduction in yield compared to experimental results. These lines also correspond roughly to increased implosion velocities. In cases where implosion velocities are high in 1D simulations, significant yields are predicted. However, due to the growth of hydrodynamic instabilities, both experimental results and 2D simulations indicate that there is no overall benefit from further increasing implosion velocity to the levels required for ignition. This figure is sourced from a presentation by Richard Town at NIF in 2017.

these implosions fall short in terms of the required kinetic energy and areal density for ignition. Conversely, higher velocities lead to accelerated instability growth, decreased yield, and ultimately provide no tangible benefits. The key takeaway is that stable implosions maintain a velocity limit of $v_{\text{imp}} < 300$ km/s, and a similar limit empirically applies to adiabat ($\alpha > 3$) as proposed in Reference [48]. It is worth noting that a higher adiabat reduces fuel compressibility but simultaneously raises ablation velocity and curbs RT growth.

This is the main objective of SI: to initiate ignition in an implosion characterised by low velocity and low convergence, using a substantial burst of laser energy precisely as the shell attains its maximum velocity. This approach effectively addresses many of the hydrodynamic challenges just discussed.

2.7 Radiative hydrodynamic codes used: *CHIC* and *ASTER*

2.7.1 *CHIC*

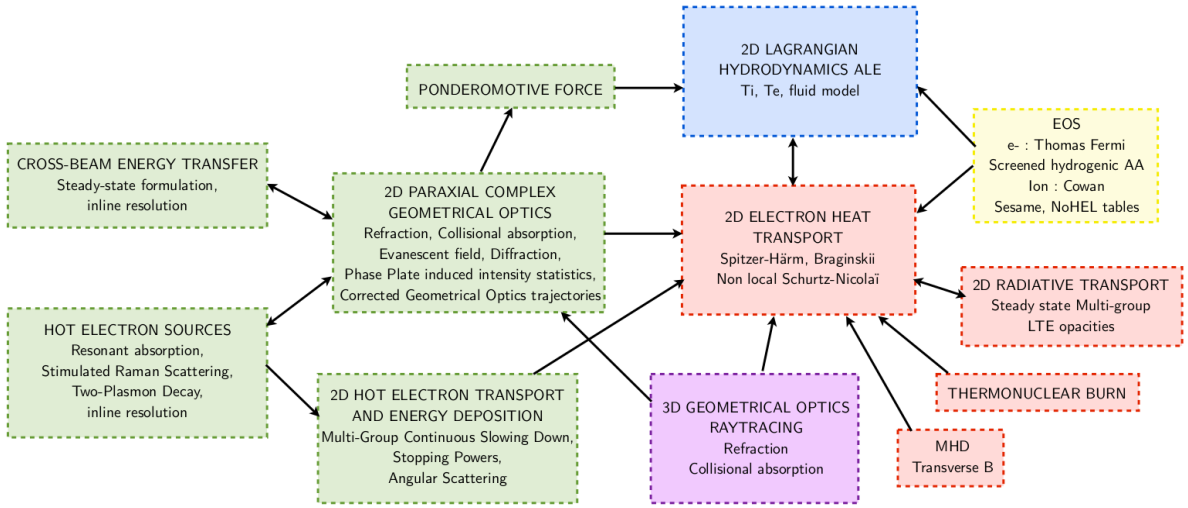

Figure 2.18 – Figure courtesy of A; Colaïtis [49]. The primary structure of the *CHIC* code is depicted. The Ray-Tracing package, shown in purple, represents the historical optical module integrated into the CHIC code. Additionally, the green packages, have been subsequently developed.

CHIC [35] is a 2D Arbitrary Lagrangian-Eulerian (ALE) integrated ICF code developed at CELIA. It is designed for simulating ICF target experiments. The plasma is modeled as a quasi-neutral mixture comprising electrons and N_i ion species. The behaviour of the plasma is governed by fluid equations, and it is characterised by two distinct temperatures. The code solves the hydrodynamics equations (2.2.1, 2.2.3, 2.2.6) in a two-dimensional Lagrangian formalism, i.e. in a co-moving frame with the fluid. Ion and thermal or non-local electron heat conduction [33], thermal coupling of electrons and ions, and multi-group radiation transport are also treated. The ALE method is employed to enhance the geometric quality of grid elements, optimising accuracy, robustness, and computational efficiency. The ionization and opacity data are tabulated, assuming either Local Thermal Equilibrium (LTE) or non-LTE based on plasma parameters. Radiative transport is

computed under the assumption that the radiation field weakly anisotropic with respect to angular dependency (multigroup diffusion). The equations of state implemented in the code are QEOS [50] and SESAME [51]. Laser propagation, refraction, collisional absorption, etc. are handled using a Geometrical Optics-based Ray Tracing algorithm [49]. Additionally, a resistive Magnetohydrodynamics (MHD) package considers azimuthal magnetic fields generated by thermal sources (crossed gradients of density and electron temperature), that can be used for other laser fusion studies. *CHIC* also includes non-linear laser-plasma interaction processes (such as the generation and propagation of hot electrons), and burn physics (α-particle energy deposition) in its simulations. The various physical models in *CHIC* are coupled to the hydrodynamics model, as illustrated in Figure 2.18.

2.7.2 *ASTER*

ASTER ([4], [52]) is a three-dimensional Eulerian hydrodynamic code designed specifically for direct-drive ICF applications. *ASTER* resolves the radiation hydrodynamics equations on a polar spherical mesh. It employs a fixed angular resolution and a radially moving grid, enabling the tracking of the shell as it undergoes implosion. It models the evolution of plasma flows using a two-temperature (for ions and electrons) fluid plasma model. The plasma can consist of various materials treated as separate media, yet constrained to share the same velocity (single-fluid approximation). The spatial distribution of hydrodynamic quantities is defined on a spherical orthogonal grid (R, θ, ϕ), with momentum components expressed using Cartesian coordinates ($M = M_x, M_y, M_z$). This two-coordinate approach eliminates the Coriolis and centrifugal force terms in the momentum equation. The code utilizes the hydrodynamic equations, including the mass-conservation equation for each material, the total (ion and electron) energy equation and the electron energy equation. *ASTER* incorporates the ideal gas and tabulated equation-of-state options (in this context SESAME [51] and Astrophysical Opacity Library [53] tables). These tables help determine the ionization state of the material, providing estimates for thermal conductivity coefficients. *ASTER* also accounts for plasma cooling and heating resulting from radiation transport. As of now, *ASTER* does not include nonlocal heat transport, the generation and propagation of hot electrons, and burn physics in its simulations.

2.8 Conclusion

This chapter delves into the initiation of fusion reactions through the implosion of a shell target containing DT fuel. Achieving the right conditions for ignition and securing high energy gain hinges is based on increasing enough the temperature and areal density of the fuel. However, these prerequisites need a robust compression of the target, constrained by challenges like pre-heating and hydrodynamic instabilities. We also presented the tools and hydrodynamics codes that were used through numerous 1D and 3D simulations during this thesis.

The shock ignition strategy emerges as a solution for attaining greater gain while mitigating hydrodynamic instability concerns during implosion. This approach trims down the energy required for compressing the target, and, at the implosion culmination, a shock is initiated to provide an additional boost. However, SI involves higher laser intensities which may enhance non-linear plasma coupling processes. In the next chapter,

we will delve into the intricate interplay between laser-plasma absorption mechanisms and non-linear plasma coupling processes within the context of ICF. We will explore how the higher laser intensities inherent in SI strategies can amplify non-linear plasma interactions, influencing both the efficiency of laser energy deposition and the onset of instabilities.

Chapter 3

Laser plasma interaction in the inertial confinement fusion framework

This chapter serves to provide the necessary context for the work presented in this thesis. It focuses on describing the main physical phenomena involved in the laser-plasma interaction of an Inertial Confinement Fusion (ICF)-type target. The standard mechanisms of laser energy absorption within the framework of a fluid description will be explained. Additionally, the section will discuss the nonlinear limiting effects that pose challenges to the efficiency and stability of the implosion process.

3.1 Electromagnetic wave propagation in a plasma

This section gives a description of the most relevant features of the electromagnetic wave propagation in a plasma. This is done by coupling the Maxwell's equations to the fluid equations of each species. When considering thermal and collisional effects, we show that the electromagnetic wave is absorbed and gives energy to the plasma through different mechanisms, such as collisional absorption and non-linear laser plasma interactions.

3.1.1 Light waves in plasma

3.1.1.1 Wave propagation equations for electromagnetic waves

The change in propagation of an electromagnetic wave in a plasma is primarily attributed to the presence of charged particles (ions and electrons). These charged particles respond to the electric and magnetic fields of the electromagnetic wave, altering its behaviour compared to its propagation in a vacuum or other mediums. Leading to several effects like dispersion, refraction, absorption and scattering, plasma wave oscillations, and other nonlinear effects. A description of the wave propagation can be obtained by (written here in CGS units):

$$\begin{cases} \nabla \cdot \mathbf{E}(\mathbf{r},t) = 4\pi\rho(\mathbf{r},t) & \textit{Gauss' law}, \\ \nabla \cdot \mathbf{B}(\mathbf{r},t) = 0 & \textit{Gauss' law for magnetism}, \\ \nabla \times \mathbf{E}(\mathbf{r},t) = -\dfrac{1}{c}\dfrac{\partial \mathbf{B}(\mathbf{r},t)}{\partial t} & \textit{Maxwell-Faraday}, \\ \nabla \times \mathbf{B}(\mathbf{r},t) = \dfrac{4\pi}{c}\mathbf{J}(\mathbf{r},t) + \dfrac{1}{c}\dfrac{\partial \mathbf{E}(\mathbf{r},t)}{\partial t} & \textit{Maxwell-Ampère}, \end{cases} \tag{3.1.1}$$

where ρ and $\mathbf{j}$ are respectively the charge and current densities, as follows:

$$\begin{cases} \rho = \sum_\alpha n_\alpha q_\alpha, \\ \mathbf{J} = \sum_\alpha n_\alpha q_\alpha v_\alpha, \end{cases} \tag{3.1.2}$$

where n, q and v are respectively the density, charge and speed of species $\alpha = e, i$ for electrons or ions. The set of equations (3.1.1) constitute the basis of the classical theory of electromagnetic (EM) fields. In this form, it describes the evolution of EM fields with respect to punctual charges and currents. To describe the EM wave propagation in plasmas, we use the set of Equation (3.1.1). By taking the curl of Maxwell-Faraday law, and using the Maxwell-Ampère's law, we get:

$$\nabla \times \nabla \times \mathbf{E} + \frac{1}{c}\frac{\partial}{\partial t}\left(\nabla \times \mathbf{B}(\mathbf{r}, t)\right) = 0. \tag{3.1.3}$$

We consider a stationary plasma and an electromagnetic wave oscillating at the frequency ω, with :

$$\mathbf{E}(\mathbf{r}, t) = \Re[\mathbf{E}(\mathbf{r}) \exp(-i\omega t)]. \tag{3.1.4}$$

For a small amplitude EM wave, the plasma response is linear and the electric current $\mathbf{J}$ follows the same temporal dependency as the electric field:

$$\mathbf{J}(\mathbf{r}, t) = \Re[\mathbf{J}(\mathbf{r}) \exp(-i\omega t)]. \tag{3.1.5}$$

The linear response theory links the current density $\mathbf{J}(\mathbf{r}, t)$ in the plasma to the electric field $\mathbf{E}(\mathbf{r}, t)$ via the dielectric susceptibility $\chi(\mathbf{r}, \omega)$:

$$\mathbf{J}(\mathbf{r}) = -i\frac{\omega}{4\pi}\chi(\mathbf{r}, \omega)\mathbf{E}(\mathbf{r}). \tag{3.1.6}$$

The same way, we define the dielectric function:

$$\epsilon(\mathbf{r}, \omega) = 1 + \chi(\mathbf{r}, \omega). \tag{3.1.7}$$

The fourth equation in (3.1.1) can therefore be written as follows:

$$\nabla \times \mathbf{B}(\mathbf{r}, t) = -i\frac{\omega}{c}\epsilon(\mathbf{r}, \omega)\mathbf{E}(\mathbf{r}, t). \tag{3.1.8}$$

Eliminating the magnetic field in equation(3.1.3) gives:

$$\Delta\mathbf{E}(\mathbf{r}, t) - \nabla\big(\nabla \cdot \mathbf{E}(\mathbf{r}, t)\big) + \frac{\omega^2}{c^2}\epsilon(\omega)\mathbf{E} = 0, \tag{3.1.9}$$

where we used the following vector identity: $\nabla \times \nabla \times \mathbf{A} = \nabla(\nabla \cdot \mathbf{A}) - \Delta\mathbf{A}$. This equation can be referred to as the wave equation for the electric field. A similar expression can be derived for the magnetic field by taking the curl of Equation (3.1.8), it yields:

$$\nabla\big(\nabla \cdot \mathbf{B}(\mathbf{r}, t)\big) - \Delta\mathbf{B}(\mathbf{r}, t) + i\frac{\omega}{c}\nabla \times \big[\epsilon(\mathbf{r}, \omega)\mathbf{E}(\mathbf{r}, t)\big] = 0. \tag{3.1.10}$$

Using the vector identity: $\nabla \times (f\mathbf{A}) = f\nabla \times \mathbf{A} + \nabla f \times \mathbf{A}$ and the Gauss' law for magnetism from (3.1.1), Equation (3.1.10) reads:

$$\Delta\mathbf{B}(\mathbf{r}, t) + \frac{1}{\epsilon(\mathbf{r}, \omega)}\nabla\epsilon(\mathbf{r}, \omega) \times \nabla \times \mathbf{B}(\mathbf{r}, t) + \frac{\omega^2}{c^2}\epsilon(\mathbf{r}, \omega)\mathbf{B}(\mathbf{r}, t) = 0. \tag{3.1.11}$$

3.1.2 Dielectric response of a non-collisional plasma

To describe the EM wave propagation in a plasma with the fluid approach, a first assumption is to neglect thermal effects and collisions. This assumption is called the *cold plasma approximation* and is valid only when the phase velocity of the EM wave is very large in comparison to the thermal velocity of electrons: $\omega/\nu_{ei} \ll 1$, and $(k\lambda_D)^{-1}\,\omega/\omega_{pe} = v_\phi/v_{the} \gg 1$. In this particular case, χ and ϵ are scalar quantities as all sources of anisotropy are removed in the case of a non-magnetised cold plasma.

The α-species equation of motion is as follows:

$$\frac{\partial \mathbf{v}_\alpha(\mathbf{r},\mathbf{t})}{\partial t} + \big[\mathbf{v}_\alpha(\mathbf{r},\mathbf{t})\cdot\nabla\big]\mathbf{v}_\alpha(\mathbf{r},t) = \frac{q_\alpha}{m_\alpha}\big[\mathbf{E}(\mathbf{r},t) + \frac{\mathbf{v}_\alpha(\mathbf{r},t)}{c}\times\mathbf{B}(\mathbf{r},t)\big]. \tag{3.1.12}$$

The aim is to quantify the contribution to the electric current of these particles, where $\mathbf{J}_\alpha = n_\alpha(\mathbf{r},t)q_\alpha\mathbf{v}_\alpha(\mathbf{r},t)$. We are interested in the unperturbed quantities represented with small amplitude perturbations in density, velocity, and EM fields, and considering an homogeneous plasma with no external electromagnetic field imposed:

$$\begin{cases} n_\alpha = n_{0\alpha} + \tilde{n}_\alpha, \\ \mathbf{v}_\alpha = \mathbf{v}_{0\alpha} + \tilde{\mathbf{v}}_\alpha = \tilde{\mathbf{v}}_\alpha, \\ \mathbf{E} = \mathbf{E}_0 + \tilde{\mathbf{E}} = \tilde{\mathbf{E}}, \\ \mathbf{B} = \mathbf{B}_0 + \tilde{\mathbf{B}} = \tilde{\mathbf{B}}. \end{cases} \tag{3.1.13}$$

In a power expansion of the electric field, the terms $(\mathbf{v}_\alpha\cdot\nabla)\mathbf{v}_\alpha$ and $\mathbf{v}_\alpha/c\times\mathbf{B}$ are of order two and can be neglected. In the framework of the linear response theory the equation of motion simplifies and it yields:

$$\frac{\partial\tilde{\mathbf{v}}_\alpha}{\partial t} = \frac{q_\alpha}{m_\alpha}\tilde{\mathbf{E}}. \tag{3.1.14}$$

For a plane wave electric field (3.1.4), the perturbed quantities solutions, as the velocity, are also plane-wave like, so that $\tilde{\mathbf{v}}_\alpha = \Re[\mathbf{v}_\alpha(\mathbf{r})\exp(-i\omega t)]$. By Fourier-transforming Equation (3.1.14), we get the following relation for the perturbed transverse quiver velocities and associated density currents:

$$\tilde{\mathbf{v}}_\alpha = \frac{iq_\alpha}{m_\alpha\omega}\tilde{\mathbf{E}}, \tag{3.1.15}$$

$$\Leftrightarrow \qquad \tilde{\mathbf{J}}_\alpha = \frac{in_\alpha q_\alpha^2}{m_\alpha\omega}\mathbf{E} = \frac{i\omega_{p\alpha}^2}{4\pi\omega}\tilde{\mathbf{E}}, \tag{3.1.16}$$

where $\omega_{p\alpha}$ is the α-species plasma frequency defined by:

$$\omega_{p\alpha}^2 = \frac{4\pi n_\alpha e^2}{m_\alpha}. \tag{3.1.17}$$

When using (3.1.6), it gives:

$$\chi_\alpha = -\frac{\omega_{p\alpha}^2}{\omega^2}. \tag{3.1.18}$$

Yet, $\chi = \sum_\alpha \chi_\alpha$, and $\epsilon(\omega) = 1 + \chi(\omega)$ so that, if we consider a fully ionized plasma with only electrons and ions, it yields:

$$\epsilon(\omega) = 1 + \chi_e + \chi_i \approx 1 + \chi_e = 1 - \frac{\omega_{pe}^2}{\omega^2} \tag{3.1.19}$$

Indeed, as $\omega_{pi} \ll \omega_{pe}$ ($m_i \gg m_e$), the total dielectric permittivity of the plasma is essentially due to the electrons. Equation (3.1.19) is known as the dielectric permittivity function for a cold plasma.

3.1.3 Dispersion relation of electromagnetic waves in the cold plasma approximation

Let us consider the case of an homogeneous plasma in which a light wave is propagating through. In this particular case, $\nabla \cdot \mathbf{E} = 0$ and $\nabla\epsilon = 0$. Equations (3.1.9) and (3.1.11) reduce to:

$$\begin{cases} \Delta\mathbf{E}(\mathbf{r},t) + \frac{\omega^2}{c^2}\epsilon(\omega)\mathbf{E} = 0, \\ \Delta\mathbf{B}(\mathbf{r},t) + \frac{\omega^2}{c^2}\epsilon(\omega)\mathbf{B} = 0. \end{cases} \tag{3.1.20}$$

These equations do not couple transverse and longitudinal directions and can be treated as scalar *Helmholtz equations*. We are looking for solutions of the form: $\mathbf{E}(\mathbf{r},t) = \Re\big[\mathbf{E}(t)\exp(-i\mathbf{k}\cdot\mathbf{r})\big]$.

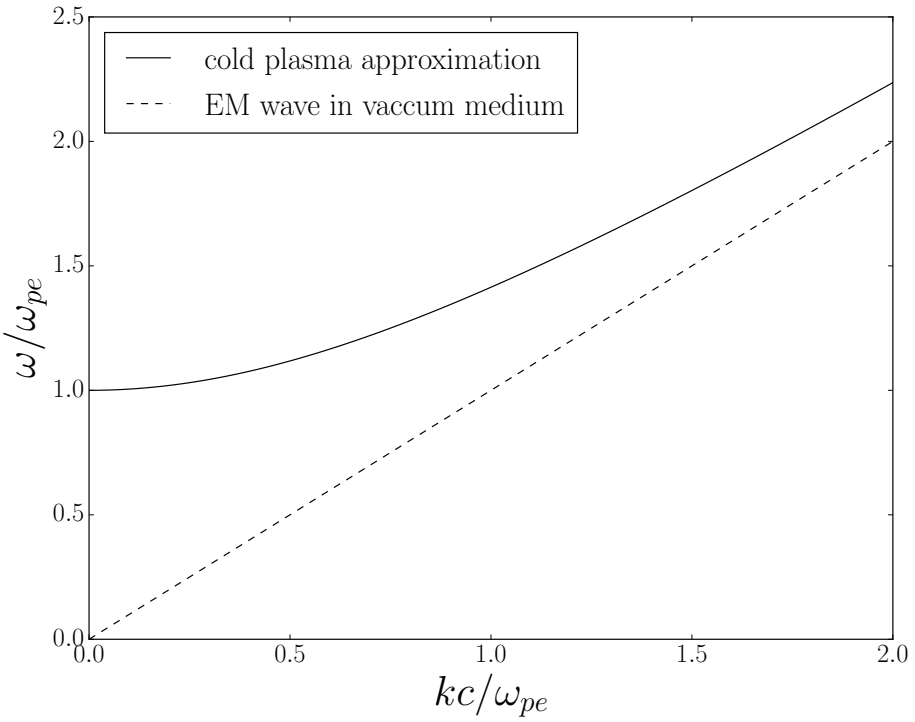

Figure 3.1 – Dispersion relation for EM waves in the cold plasma approximation. In dotted lines is also displayed the dispersion relation in vacuum, $\omega = kc$.

We can Fourier-transform (3.1.20) and use the dielectric permittivity function derived in (3.1.19), leading to:

$$\begin{cases} \big[-k^2 + \frac{\omega^2}{c^2}(1 - \frac{\omega_{pe}^2}{\omega^2})\big]\mathbf{E} = 0, \\ \big[-k^2 + \frac{\omega^2}{c^2}(1 - \frac{\omega_{pe}^2}{\omega^2})\big]\mathbf{B} = 0. \end{cases} \tag{3.1.21}$$

By rearranging the terms we get:

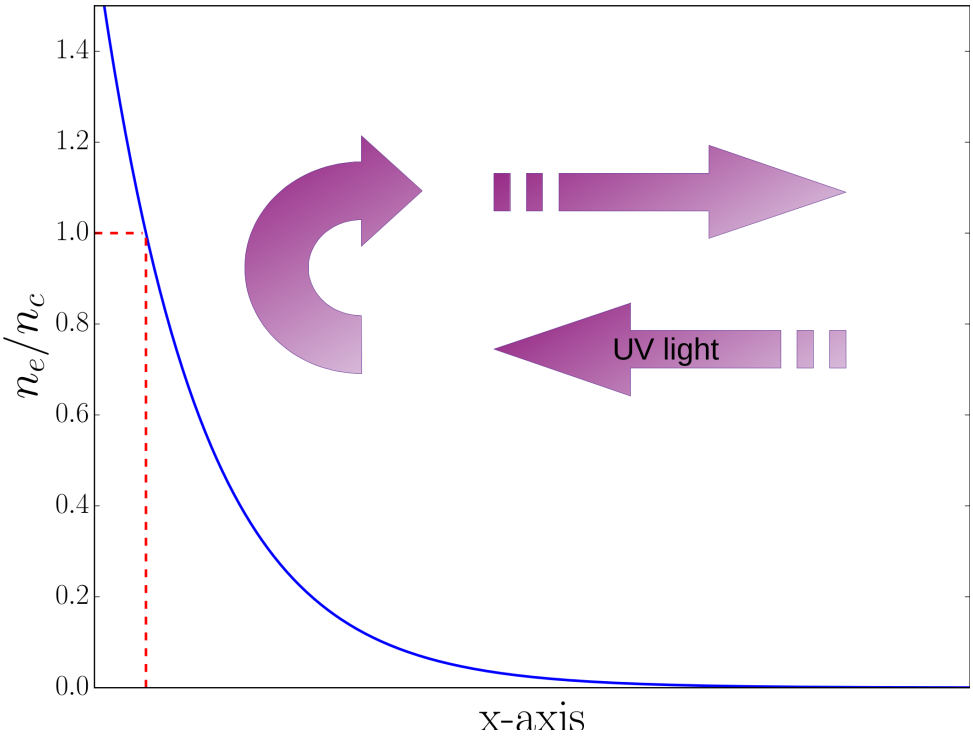

Figure 3.2 – Plasma density profile along the x-axis created by laser irradiation of a solid material. A laser at normal incidence is reflected backwards once it reaches $n_e = n_c$.

$$k = \frac{1}{c}\sqrt{\omega^2 - \omega_{pe}^2}, \tag{3.1.22}$$

or even:

$$\omega^2 = k^2c^2 + \omega_{pe}^2. \tag{3.1.23}$$

These equations constitute different forms of the dispersion relation for electromagnetic waves in a plasma. A plot of ω as a function of wave number k is shown in Figure 3.1.

From Equation (3.1.22), it is clear that the EM wave cannot propagate into the plasma if $\omega^2 < \omega_{pe}^2$. This condition can be defined as $n_e < n_c$, with n_c the critical density above which the plasma acts as a reflecting mirror for the EM wave. Figure 3.2 shows the typical behaviour of a laser propagating in a plasma along the x-axis with an exponential density profile. The critical density can be written as follows (in CGS):

$$n_c = \frac{m_e\omega^2}{4\pi e^2}. \tag{3.1.24}$$

It is useful to express this quantity as a function of wavelength alone:

$$n_c[\mathrm{cm}^{-3}] = \frac{1.1 \times 10^{21}}{\lambda^2[\mu\mathrm{m}]}. \tag{3.1.25}$$

In the ICF-context, Neodymium-doped glass (Nd:Glass) lasers are mainly used as these can produce high powers in the infrared spectrum. The 1ω light is frequency tripled to its third harmonic, 3ω, to produce UV beams, so that the wavelength on target is $\lambda = 0.351$ μm, which gives $n_c = 8.9 \times 10^{21}\mathrm{cm}^{-3}$.
From Equation (3.1.23), we can calculate the phase velocity of the EM wave:

$$v_\phi = \frac{\omega}{k} = c\left(1 - \frac{\omega_{pe}^2}{\omega^2}\right)^{-1/2} \geq c, \tag{3.1.26}$$

and its group velocity:

$$v_g = \frac{\partial \omega}{\partial k} = c\left(1 - \frac{\omega_{pe}^2}{\omega^2}\right)^{1/2} \leq c. \tag{3.1.27}$$

We check that the group velocity is lower than the light speed, whereas the phase velocity is higher than c, with $v_g v_\phi = c^2$. The group velocity being a function of ω, $v_g = v_g(\omega)$, it is clear that a plasma is a dispersive material: a light wave is refracted according to its frequency ω.

It is also interesting to derive the refractive index $n = \sqrt{\epsilon}$ which describes how an EM wave is refracted during its propagation in a medium:

$$n(\omega) = \sqrt{\epsilon(\omega)} = \sqrt{1 - \frac{\omega_{pe}^2}{\omega^2}} = \sqrt{1 - \frac{n_e}{n_c}}, \tag{3.1.28}$$

which is ≤ 1 in plasmas. This is opposite to wave propagation in solid or gaz materials (like air), where the refraction index is ≥ 1. In those media, the index of refraction increases with density, meaning that the light bends towards regions of high densities. On the contrary, for plasmas the higher the density the lower the index of refraction, meaning that the EM waves tend to curve towards lower densities.

As discussed previously, an EM wave cannot propagate in a plasma if the electronic density is greater than the critical density defined in (3.1.24). At the critical density, the wave vector k becomes a imaginary number, and the EM wave is then an evanescent wave: an exponentially decaying wave along its imaginary part direction,

$$k = \frac{i}{c}\left(\omega_{pe}^2 - \omega^2\right)^{1/2}, \tag{3.1.29}$$

so that, the electric field evolves as:

$$\mathbf{E}(\mathbf{r}, t) = \Re\left[\mathbf{E_0} \exp\left(-\frac{1}{c}\left(\omega_{pe}^2 - \omega^2\right)^{1/2}\right) \exp(-i\omega t)\right]. \tag{3.1.30}$$

To end this paragraph, we can notice that it is possible to get rid of the "cold plasma approximation" hypothesis in the general case of EM waves. First, we can write the pressure as proportional to density in the adiabatic approximation, $P \propto n^\gamma$, so that the pressure tensor divergence reads:

$$\nabla \cdot \overline{\overline{P_\alpha}} = \gamma_\alpha k_B T_\alpha \nabla n_\alpha, \tag{3.1.31}$$

and the linearized equation of motion considering pressure anisotropy is:

$$\frac{\partial \tilde{\mathbf{v}}_\alpha}{\partial t} = \frac{q_\alpha}{m_\alpha}\mathbf{E} - \gamma_\alpha \frac{k_B T_\alpha}{n_{0\alpha} m_\alpha} \nabla \tilde{n}_\alpha = \frac{q_\alpha}{m_\alpha}\mathbf{E} - \gamma_\alpha v_{th\alpha}^2 \nabla\left(\frac{\tilde{n}_\alpha}{n_{0\alpha}}\right). \tag{3.1.32}$$

where $\tilde{n_\alpha}$ is the density perturbation for α-species particles. This perturbed density is also linked to the fluid speed of α-species particles via the linearized continuity equation:

$$\frac{\partial \tilde{n}_\alpha}{\partial t} = -\nabla \cdot (n_\alpha \tilde{\mathbf{v}}_\alpha). \tag{3.1.33}$$

When an EM wave propagates through a homogeneous plasma, the condition $\nabla \cdot \mathbf{E}$ implies that $\nabla \cdot \tilde{\mathbf{v}}_\alpha = 0$, leading to $\tilde{n}_\alpha = 0$. This indicates that the wave propagates without perturbing the density profile of the various species, resulting in no charge density separation. The charged particles oscillate in planes parallel to each other, causing the pressure-related correction term in equation 3.1.32 to vanish. Consequently, the inclusion of density or velocity dispersion does not alter the results derived from the cold plasma approximation. The transverse dielectric susceptibility ($\mathbf{k} \perp \mathbf{E}$) then corresponds to the cold plasma approximation:

$$\chi_{\alpha\perp} = -\frac{\omega_{p\alpha}^2}{\omega^2}. \tag{3.1.34}$$

3.2 Collisional absorption with a density dependent collision frequency and two different density profiles

3.2.1 Dielectric response of a collisional plasma

So far, our focus has been on the behavior of collisionless plasmas. In this subsection, we will shift our attention to a dissipative plasma where collisions play a significant role in transferring energy from waves to particles. Specifically, we will investigate the collisional absorption of EM waves, also known as "inverse bremsstrahlung." This term refers to the quantum process in which an electron absorbs a photon when passing near an ion, which is the inverse of the free-free emission or bremsstrahlung.

Now, let us proceed with deriving the dielectric response of a collisional plasma. Our discussion will be limited to EM waves, allowing us to neglect the thermal and pressure effects in the equation of motion. Consequently, we will focus solely on the electron response while including the collisional term. The linearized equation of motion for electrons in a collisional plasma can be expressed as follows:

$$\frac{\partial \tilde{\mathbf{v}}_e}{\partial t} = -\frac{e}{m_e}\tilde{\mathbf{E}} - \nu_{ei}\tilde{\mathbf{v}}_e, \tag{3.2.1}$$

where ν_{ei} is the collision frequency which describes electron scattering by ions. It is given by the following formula (in CGS):

$$\nu_{ei} = \frac{4(2\pi)^{1/2}}{3}\frac{n_i Z^2 e^4}{(m_e T_e^3)^{1/2}} \ln \Lambda, \tag{3.2.2}$$

where $\ln \Lambda$ is the Coulomb logarithm. The latter is defined as the logarithmic ratio of the maximum and minimum cutoffs of the impact parameter, b, involved in binary elastic collisions between electrons and ions for ICF conditions. Typical values of $\ln \Lambda$ are given in Table 3.1.

The velocity response to a plane-wave like electric field is also a plane-wave like solution. By linearizing and Fourier-transforming the Lorentz equation of motion 3.2.1, it yields:

Table 3.1 Typical Coulomb logarithm values for different plasma parameters.

T_e[eV]	n_e [cm^{-3}]				
	10^{17}	10^{19}	10^{21}	10^{23}	10^{25}
10	7.1	4.8	2.5	-	-
10^2	9.4	7.1	4.8	2.5	-
10^3	11.7	9.4	7.1	4.8	2.5
10^4	14.0	11.7	9.4	7.1	4.8

$$\tilde{\mathbf{v}}_e = -\frac{i}{\omega + i\nu_{ei}} \frac{e\tilde{\mathbf{E}}}{m_e}, \tag{3.2.3}$$

immediately giving us the induced current:

$$\tilde{\mathbf{J}}_e = -en_e\tilde{\mathbf{v}}_e = \sigma_e\tilde{\mathbf{E}}, \tag{3.2.4}$$

where σ_e is the electrical conductivity of the plasma due to small perturbations, and is given by:

$$\sigma_e = \frac{i\omega_{pe}^2}{4\pi\omega(1 + i\nu^*)}, \tag{3.2.5}$$

with $\nu^* = \nu_{ei}/\omega$. The association of these two previous equations can be seen as Ohm's law for a plasma subjected to an oscillating electric field with a friction term due to coulomb collisions. We can now also use Equation (3.1.6), so that:

$$\begin{aligned} \chi &= -\frac{\omega_{pe}^2}{\omega^2} \frac{1}{1 + i\nu^*}, \\ \Leftrightarrow \epsilon &= 1 - \frac{\omega_{pe}^2}{\omega^2} \frac{1}{1 + i\nu^*}, \end{aligned}$$

and using the dielectric constant ϵ function into Equation (3.1.20), we get the following dispersion relation for an homogeneous plasma:

$$-k^2 + \frac{\omega^2}{c^2}\left(1 - \frac{\omega_{pe}^2}{\omega^2} \frac{1}{1 + i\nu^*}\right) = 0. \tag{3.2.6}$$

It can also be written as $k = (\omega/c)n(\omega)$ (as defined in (3.1.28)). In that case, it implies that the wavenumber is complex as soon as we consider coulomb collisions. Real and imaginary parts of k are linked via the following equations:

$$\begin{cases} \Re(k)^2 - \Im(k)^2 = \dfrac{\omega^2}{c^2}\Re(\epsilon), \\ 2\Re(k)\Im(k) = \dfrac{\omega^2}{c^2}\Im(\epsilon). \end{cases} \tag{3.2.7}$$

In laser-created coronal plasmas, it is reasonable to assume that the binary electron-ion collision frequency is significantly smaller than the electron plasma frequency. Thus, we can approximate $|\Im(k)| \ll |\Re(k)|$, as derived from Equations (3.2.7). However, it is important to note that this approximation is not valid when the electronic density approaches the critical density. Using this assumption, it yields:

$$\Re(k) \simeq \frac{\omega}{c}\sqrt{\Re(\epsilon)} \simeq \frac{\omega}{c}\left(1-\frac{n_e}{n_c}\right)^{1/2}, \tag{3.2.8}$$

$$\Im(k) \simeq \frac{1}{2}\frac{\nu_{ei}}{c}\frac{n_e}{n_c}\left(1-\frac{n_e}{n_c}\right)^{-1/2}. \tag{3.2.9}$$

If we consider the electron-ion collision frequency to be a linear function of the electronic density, such as: $\nu_{ei} = \nu_0 n_e/n_c$, then we get:

$$\Im(k) = \frac{1}{2}\frac{\nu_0}{c}\left(\frac{n_e}{n_c}\right)^2\left(1-\frac{n_e}{n_c}\right)^{-1/2}, \tag{3.2.10}$$

where ν_0 is the maximum electron-ion collision frequency reached when $n_e = n_c$. The imaginary part of the wave vector corresponds to the spatial attenuation of the electromagnetic fields. It can also be seen as the rate at which the energy decays in space. Figure 3.3 shows the dependence of the absorption coefficient $\Im(k)$ with n_e. The higher n_e, the more the electric field is damped and absorbed by the particles due to collisions. At $n_e = n_c$, the absorption coefficient diverges and the derived Equations (3.2.9) are no longer correct. For an EM wave propagating along the x-axis, it yields:

$$|\mathbf{E}| \propto \exp(-\Im(k)x), \tag{3.2.11}$$

and,

$$\left\langle \mathbf{E}^2 \right\rangle \propto \exp\big(-2\Im(k)x\big), \tag{3.2.12}$$

where the sign $\langle ... \rangle$ corresponds to an average over the electromagnetic wave period. The absorption length after which the wave intensity is reduced by a factor of 1/e is given by:

$$L_{abs} = \frac{2}{\Im(k)} = \frac{c}{\nu_0}\left(\frac{n_c}{n_e}\right)^2\left(1-\frac{n_e}{n_c}\right)^{1/2}. \tag{3.2.13}$$

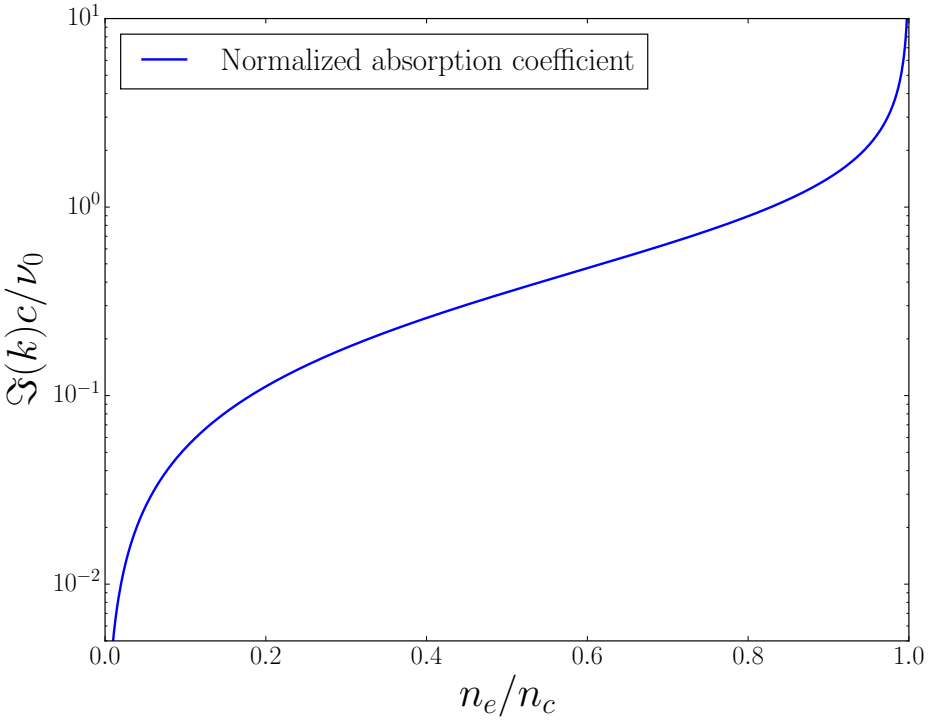

Figure 3.3 – Absorption coefficient $\Im(k)$ normalized to ν_0/c where ν_0 is the collision frequency calculated at the critical density. We supposed that ν_{ei} was linearly proportional to the electronic density n_e. The y-axis is logscaled.

3.2.2 The WKB approximation for inhomogeneous plasmas

The application of the Wentzel-Kramers-Brillouin (WKB) method, widely used in mathematical physics, allows us to solve the Helmholtz Equations (3.1.20) approximately. This method is particularly useful for tackling linear differential equations with spatially varying coefficients. In our specific case, we employ the WKB method under the assumption of slow-varying fields. We consider an EM wave propagating along the x-axis within an inhomogeneous plasma, where the density gradient is also oriented along the x-axis. One can define the local wavenumber as:

$$k(\omega, x) = \frac{\omega}{c} n(\omega, x), \tag{3.2.14}$$

where $n(x) = \sqrt{\epsilon(\omega, x}$ is local optical index. We can then rewrite the Helmholtz (3.1.20) equation as such:

$$\frac{\mathrm{d}\mathbf{E}}{\mathrm{d}x^2} + k^2(x)\mathbf{E} = 0. \tag{3.2.15}$$

We introduce a new quantity, the local wavelength, $\lambda\!\!\!^{-} = 1/k(\omega, x)$. We suppose that the local wavelength is much lower than the characteristic length associated to the variation of k:

$$\left|\lambda\!\!\!^{-} \frac{\mathrm{d}^2 \lambda\!\!\!^{-}}{\mathrm{d}x^2}\right| \ll \frac{\mathrm{d}\lambda\!\!\!^{-}}{\mathrm{d}x} \ll 1. \tag{3.2.16}$$

In an homogeneous media, the solution can be written:

$$\mathbf{E}(x) = \mathbf{E}_0 \exp \pm\left(i\frac{\omega}{c} n x\right). \tag{3.2.17}$$

The product nx represents the optical path length between 0 and x, and the resulting phase shift can be obtained by multiplying it with $kx = k_0 nx$, where k_0 is the wave number in vacuum. In an inhomogeneous medium, the optical paths related to each infinitesimal slice $\mathrm{d}x$ accumulate, leading to a solution of the following form:

$$\mathbf{E}(x) = \mathbf{E_0}(x) \exp\left[\pm i\frac{\omega}{c} \int_0^x n(x')\mathrm{d}x' \right], \tag{3.2.18}$$

where $\mathbf{E}_0(x)$ corresponds to the complex amplitude of the electric field at $x = 0$, and is a slowly varying function, such as $n(x)$. The $\pm$ sign accounts for the fact that the wave can propagate either inwards or outwards. In order to describe a stationary wave, it is necessary to consider the contributions of both counter-propagating waves. By substituting Equation (3.2.18) into Equation (3.2.15), we obtain:

$$\frac{\mathrm{d}^2\mathbf{E}_0}{\mathrm{d}x^2} \pm i\frac{\omega}{c}\left[2n(x)\frac{\mathrm{d}\mathbf{E}_0}{\mathrm{d}x} + \frac{\mathrm{d}n(x)}{\mathrm{d}x}\mathbf{E}_0\right] = 0. \tag{3.2.19}$$

The condition of slow variation in density and, consequently, in the optical index $n(x)$ indicates that both $\mathbf{E}_0$ and its corresponding derivative change gradually. In the first order, we can disregard the second derivative $\mathrm{d}^2/\mathrm{d}x^2$, which corresponds to the WKB approximation when the preceding condition (3.2.16) holds true. When solely considering the terms of the first order, the solution to the approximated equation is as follows:

$$\begin{aligned} 2n\frac{\mathrm{d}\mathbf{E}_0}{\mathrm{d}x} &= -\frac{\mathrm{d}n}{\mathrm{d}x}\mathbf{E}_0, \\ \Leftrightarrow \mathbf{E}_0(x) &= \frac{C}{\sqrt{n(x)}} = \frac{E_{FS}}{\sqrt{n(x)}}. \end{aligned} \tag{3.2.20}$$

where C is a constant equal to the free-space electric field E_{FS}. This result emphasizes that as the wave propagates towards the critical density, the amplitude of the electric field increases proportionally to $n^{-1/2}E_{FS}$. To get these results we assumed in Equation (3.2.19) that $\mathbf{E}_0'' \ll 2i(\omega/c)n(\omega, x)\mathbf{E}_0' + i(\omega/c)n'(\omega, x)\mathbf{E}_0$ (where the prime denotes spatial derivative with respect to x). A sufficient condition for this assumption to be valid can be expressed as follows:

$$\begin{aligned} \left|\frac{\mathrm{d}\mathbf{E}_0}{\mathrm{d}x}\right| &\ll \frac{\omega}{c} n(\omega, x)\mathbf{E}_0, \\ \Leftrightarrow \frac{1}{n}\left|\frac{\mathrm{d}n}{\mathrm{d}x}\right| &\ll \frac{2}{\lambda\!\!\!^{-}}. \end{aligned} \tag{3.2.21}$$

This assumption indicates that the validity of the WKB approximation decreases in the presence of steep density gradients and near the critical density, where the optical index n approaches zero ($n \to 0$) and the wavelength $\lambda\!\!\!^{-}$ becomes infinitely long ($\lambda\!\!\!^{-} \to \infty$). Consequently, the WKB approximation is only applicable in the regime of weak plasma inhomogeneity and when the system is sufficiently distant from the critical density.

3.2.3 Laser absorption in a density gradient: linear and exponential profiles

Using the previously established results, in the general case of a wave propagating towards increasing x, we can express the following:

$$|\mathbf{E}(x)|^2 \propto \frac{1}{n(x)} \exp\left[-2\int_0^x \Im\big(k(x')\big)\mathrm{d}x' \right]. \tag{3.2.22}$$

The exponential factor that appears on the right-hand side of Equation (3.2.22) represents the wave attenuation resulting from collisional absorption. The transmission rate between two points, denoted as x_a and x_b, can be expressed as:

$$T = \exp\left[-2\int_{x_a}^{x_b} \Im\big(k(x')\big)\mathrm{d}x'\right]. \tag{3.2.23}$$

and the absorption rate by: A = 1 - T. For the case of the superposition of an incident and reflected wave, the solution can be written as follows:

$$\begin{aligned}\mathbf{E}(x) = &\frac{\mathbf{E}_+}{n^{1/2}(x)} \exp\left[\int_0^x \Im\big(k(x')\big)\mathrm{d}x'\right] \\ &+ \frac{\mathbf{E}_-}{n^{1/2}(x)} \exp\left[-\int_0^x \Im\big(k(x')\big)\mathrm{d}x'\right].\end{aligned} \tag{3.2.24}$$

Considering Equations (3.2.24) and (3.2.23), the absorption coefficient can be written as:

$$\begin{aligned}A &= 1 - \exp\left[-4\int_{-\infty}^{x_{tp}} \Im\big(k(x)\big)\mathrm{d}x\right], \\ &\simeq 1 - \exp\left[-2\int_{-\infty}^{x_{tp}} \frac{\nu_{ei}(x)}{c}\frac{n_e(x)}{n_c}\left(1-\frac{n_e(x)}{n_c}\right)^{-1/2}\mathrm{d}x\right].\end{aligned} \tag{3.2.25}$$

while accounting for the round trip path of light in the density gradient. The parameter x_{tp} represents the tuning point, which is the location where the wave is reflected ($\epsilon(x_{tp}) = 0$) and its position depends on the density gradient.

We will now determine the total fraction of collisional absorption for different density plasma profiles.

Linear density profile

A linear density profile of the form is considered:

$$n_e(x) = n_c\frac{x}{L}. \tag{3.2.26}$$

If we approximate ν_{ei} as linearly varying with the density (see Equation (3.2.10)), we get the following results:

$$\begin{aligned}A &= 1 - \exp\left[-2\frac{\nu_0}{c}\int_0^L \left(\frac{x}{L}\right)^2\left(1-\frac{x}{L}\right)^{-1/2}\mathrm{d}x\right] \\ &= 1 - \exp\left[-\frac{32\nu_0 L}{15c}\right].\end{aligned} \tag{3.2.27}$$

For an oblique incidence of the light wave in a linear plasma density, it yields:

$$A = 1 - \exp\left[-\frac{32\nu_0 L}{15c}\cos^5(\theta)\right], \tag{3.2.28}$$

where θ is the angle of incidence. Note how the absorption is a sensitive function of the angle of incidence. Since an obliquely incident wave reflects at a lower density, less collisional plasma is traversed.

Exponential density profile
An exponential density profile of the form is considered:

$$n_e(x) = n_c \exp\left(\frac{x}{L}\right) \tag{3.2.29}$$

The isothermal expansion of a plasma in a vacuum results in such an exponential behaviour, rather than linear, characterized by $L = c_s t$, where t represents the specified expansion time. The turning point now reads $x_{\text{tp}} = L\ln(cos^2\theta)$, for an obliquely incident wave. The absorption rate is given by:

$$A = 1 - \exp\left[-\frac{8\nu_0 L}{3c}\cos^3(\theta)\right]. \tag{3.2.30}$$

Finally, we note that the collisional absorption will depend in detail on the density profile of the plasma.

3.3 Longitudinal waves in plasmas

Through the utilization of the two fluid model (wherein electrons constitute one fluid and ions form the other), an extensive spectrum of plasma phenomena can be examined. The capacity of plasma to facilitate waves or collective modes of interaction represents a distinctive attribute. In the most basic scenario, these waves align with fluctuations in charge density at a frequency inherent to the electrons and/or ions. In the absence of substantial externally imposed magnetic fields, two distinct kinds of plasma waves emerge: electron plasma waves (EPW) characterized by high frequencies and ion acoustic waves (IAW) characterized by low frequencies.

3.3.1 Electron plasma waves

We start our examination into the high frequency charge density fluctuations, which are linked to the movement of electrons. Due to the high frequency oscillatory nature, it is acceptable to consider the more massive ions as stationary, uniform entities constituting a neutralizing background, possessing a density denoted by n_{0i}. Considering the electrostatic nature of the wave and the predominant electron motion aligned with the wave vector (assumed to be in the x-direction), a simplified one-dimensional analysis proves to be adequate. The linearized continuity, motion and closure equations for electrons are as follows:

$$\begin{aligned}
\partial_t \tilde{n}_e &= -\partial_x(n_{0e}\tilde{v}_e),\\
\partial_t \tilde{v}_e &= -\frac{e}{m_e}\tilde{E} - \frac{\gamma_e v_{te}^2}{n_{0e}}\partial_x \tilde{n}_e,\\
\frac{\tilde{p}_e}{\tilde{n}_e^{\gamma_e}} &= \text{constant},
\end{aligned} \tag{3.3.1}$$

where the third equation of (3.3.1) uses the adiabatic equation of state under the assumption that the phase velocity of the wave is much larger than the electron thermal velocity. By differentiating the first equation with respect to time and substituting the second equation into it, we obtain:

$$\partial_{tt}\tilde{n}_e = \frac{en_{e0}}{m_e}\partial_x\tilde{E} + \gamma_e v_{te}^2 n_{e0}\partial_{xx}\tilde{n}_e. \tag{3.3.2}$$

According to Gauss' law in Maxwell's equations 3.1.1 and assuming that $\partial_x\tilde{E} \neq 0$, it yields that:

$$\left(\partial_{tt} - 3v_{te}^2\partial_{xx} + \omega_{pe}^2\right)\tilde{n}_e = 0. \tag{3.3.3}$$

where we used $\gamma_e = 3$ for the electrons as we assume that they follow an adiabatic law with a single degree of freedom. When searching for wave-like solutions as in equation 3.1.4, the dispersion relation for electron plasma oscillations:

$$\omega_{\text{EPW}}^2 = \omega_{pe}^2 + 3k^2v_{te}^2 = \omega_{pe}^2\left(1 + 3k^2\lambda_D^2\right). \tag{3.3.4}$$

where $\lambda_D = k_B T_e/(n_e e^2)$ is the Debye length. With each Debye length the charges are increasingly electrically screened and the electric potential decreases in magnitude by $1/e$. The frequency of these waves primarily corresponds to the electron plasma frequency (ω_{pe}), with a minor thermal correction that is dependent on the wavenumber. It is important to note that in the limit of wave vector k approaching zero (or $k\lambda_D \ll 1$), the behaviour predicted by the cold plasma approximation is replicated, resulting in Langmuir oscillations occurring at the electron plasma frequency ($\omega_{\text{EPW}} = \omega_{pe}$). The phase and group velocity of the EPWs are readily obtained:

$$v_\phi = \frac{\omega}{k} \simeq \frac{\omega_{pe}}{k} = \frac{v_{te}}{k\lambda_d} \quad (\text{if } k\lambda_D \ll 1), \tag{3.3.5}$$

and:

$$\begin{aligned} 2\omega\partial\omega &= 6v_{te}^2 k\partial k, \\ \Leftrightarrow v_g = \frac{\partial\omega}{\partial k} &= \frac{3v_{te}^2 k}{\omega} \simeq 3v_{te}(k\lambda_D). \end{aligned} \tag{3.3.6}$$

The observed waves correspond to the propagation of electron charge density fluctuations within a plasma, given that the phase velocity (v_g) is nonzero (see Equation (3.3.6)). The condition of existence of the EPWs can also be seen as $v_\phi \gg v_{te}$.

Electrostatic waves, being manifestations of charge density fluctuations and the electric fields associated with them, remain confined within the plasma. Their energy is gradually transferred to the plasma particles through linear or nonlinear damping mechanisms. For example, applying a kinetic approach to derive the dispersion relation would reveal the occurrence of a growth or damping wave phenomenon known as "Landau damping." This non-collisional damping effect is influenced by the electron distribution function and the difference between the phase velocity of the wave and the electron thermal speed. Specifically, particles with velocities slightly lower than the phase velocity (v_ϕ) of the wave will experience energy gain, while particles with velocities slightly higher than v_ϕ will undergo energy loss. The efficiency of energy exchange is determined by the slope of the velocity distribution at the wave's phase velocity and is primarily governed by the resonant particles, where their velocities (v_e) align precisely with v_ϕ. This mechanism can result in the emergence of a supra-thermal population of electrons, which are accelerated to velocities significantly higher than the electron thermal velocity (v_{te}).

3.3.2 Ion acoustic waves

In addition, a plasma can exhibit charge density oscillations at a significantly lower frequency determined by the inertia of the ions. To examine these oscillations, we must consider the movement of both the electron and ion fluids in a plasma. As the frequency of these oscillations is significantly lower than the characteristic frequency at which electrons respond (ω_{pe}), we can disregard the inertia of electrons by assuming their mass to be negligible. Generally, these waves exist within the range of phase velocities $v_{ti} \ll \omega/k \ll v_{te}$, where the thermal velocity of electrons (v_{te}) is much greater than the wave frequency over the wavenumber (ω/k), which is in turn much greater than the thermal velocity of ions (v_{ti}). In this regime, both ion and electron susceptibilities play a role in determining the dielectric permittivity:

$$\epsilon_{\parallel}(\omega, k) = 1 + \chi_{e\parallel} + \chi_{i\parallel} = 1 - \frac{\omega_{pe}^2}{\omega^2 - \gamma_e k^2 v_{te}^2} - \frac{\omega_{pi}^2}{\omega^2 - \gamma_i k^2 v_{ti}^2}, \tag{3.3.7}$$

which can be approximated by:

$$\epsilon_{\parallel}(\omega, k) \simeq 1 + \frac{1}{\gamma_e k^2 \lambda_D^2} - \frac{\omega_{pi}^2}{\omega^2 - \gamma_i k^2 v_{ti}^2} \quad (\text{as } \omega/k \ll v_{te}) \tag{3.3.8}$$

This equation corresponds to the ion acoustic modes. The condition in Equation (3.3.8) implies that the phase velocity of the wave is much smaller than the thermal velocity of electrons. Consequently, electrons have ample time to reach Boltzmann equilibrium with the electrostatic potential of the wave. This condition corresponds to the isothermal assumption with $\gamma_e = 1$. On the other hand, the phase velocity of the ion acoustic wave must remain significantly greater than the thermal velocity of ions, $v_\phi \gg v_{ti}$. Ions are then considered in the fluid regime, which justifies the value of $\gamma_i = 3$. Solving (3.3.8) with the previous assumptions gives:

$$\omega_{\text{IAW}}^2 = \frac{k^2 c_s^2}{1 + k^2 \lambda_D^2} + 3k^2 v_{ti}^2. \tag{3.3.9}$$

where c_s is the ion acoustic speed defined by: $c_s^2 = (Zk_B T_e/m_i) = (ZT_e/T_i)v_{ti}$. The ions hydrodynamic description needs $v_{ti} \ll v_\phi$. This is satisfied when $ZT_e/T_i \gg 1$, and $k^2\lambda_D^2 \ll ZT_e/T_i$. In the specific case where $k^2\lambda_D^2 \ll 1$, we get:

$$\omega_{\text{IAW}} \simeq k c_s. \tag{3.3.10}$$

The wave travels undisturbed and without dispersion as $v_\phi = v_g = c_s$. If we consider that $1 \ll k^2\lambda_D^2 \ll ZT_e/T_i$, the dispersion relation becomes:

$$\omega \simeq \omega_{pi}. \tag{3.3.11}$$

Equations (3.3.10) and (3.3.11) correspond to the behaviour of the IAW at the extremities of the definition domain. Figure 3.4 shows the dispersion relation for both the EPW and the IAW as a function of the product of the wavevector and the Debye length.

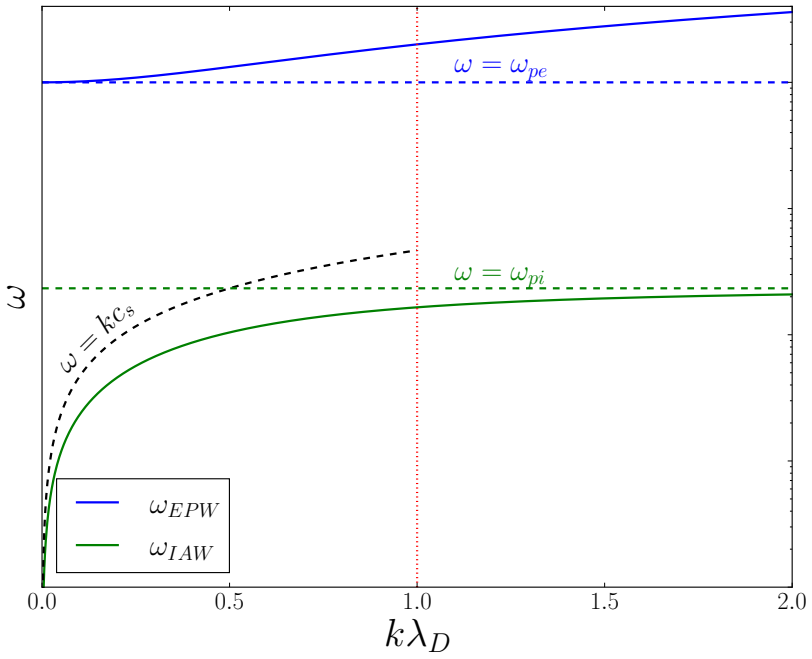

Figure 3.4 – Dispersion relation of the EPW and IAW. The horizontal coloured dashed lines represent respectively the minimum and maximum attainable frequencies for the EPW and IAW. The y-axis is displayed in log-scale.

3.4 Nonlinear laser plasma instabilities and other laser absorption processes

The laser-plasma interaction in ICF regimes involves electromagnetic waves that can be of high intensity. Similarly, waves excited in the plasma can also reach high amplitudes. Nonlinear effects, known as "parametric instabilities", arising from these high intensities start to play a crucial role once the interaction parameter $I\lambda_L^2$ overcomes a threshold value, for typical ICF conditions of $\simeq 10^{14}$ Wμm^2/cm^2. In the context of fusion laser plama interactions, these instabilities include processes of Stimulated Brillouin Scattering (SBS), Stimulated Raman Scattering (SRS), Two Plasmon Decay (TPD) and Cross-Beam Energy Transfer (CBET). Specifically, SRS and TPD have the potential to cause pre-heat issues, while SBS and CBET influence the symmetry of the laser drive. These additional processes typically exhibit nonlinear behaviours and can be detrimental to the experiments. These effects are susceptible to modify the location of the laser deposition and create a population of highly energetic particles (suprathermal electrons) that will speed up the shock and deposit their energy further in the target. These two effects combined result in affecting both the laser irradiation symmetry and degrading the implosion, therefore making it difficult to reach ignition conditions in the hot spot. Fig 3.5 displays a schematic representation of a three wave interaction occurring in the coronal plasma. This section outlines the fundamental principles of parametric instabilities. The goal is to provide insights into the primary regimes in which these instabilities operate in ICF.

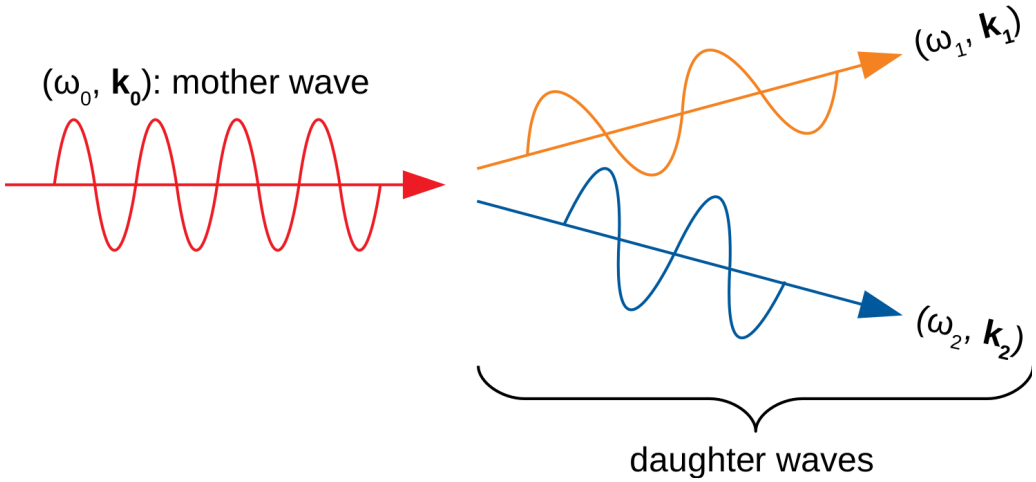

Figure 3.5 – Schematic representation of resonant three-wave coupling, which is the source of parametric instabilities.

3.4.1 Main suprathermal electron generation mechanisms

3.4.1.1 Stimulated Raman Scattering

The Stimulated Raman Scattering (SRS) is a parametric instability that arises from the resonant coupling of a high amplitude light wave with an electron plasma wave and a scattered light wave. The coupling relations are as follows:

$$\begin{cases} \omega_0 = \omega_s + \omega_{\text{EPW}} \\ \mathbf{k}_0 = \mathbf{k}_s + \mathbf{k}_{\text{EPW}} \end{cases} \tag{3.4.1}$$

where the subscript "0" is for the incident light wave, and "s" stands for "scattered".

As ω_0 and ω_s satisfy their respective dispersion relations of the electromagnetic and electrostatic waves, we have that $\omega_0,\ \omega_s \geq \omega_{pe}$, and hence $\omega_0 \geq 2\omega_{pe}$. The matching conditions can furthermore only occur when $n_e \leq 1/4 n_c$, in the sub-quarter critical zone. When such coupling occurs, a fraction of the incident energy is backscattered into a daughter EM wave, and another part is given to the EPW. This laser energy loss is able to heat the plasma and specifically electrons when the EPW undergoes any sort of damping. The higher the phase velocity of the EPW, the more electrons can be generated with very high energies. It is in this context that the Raman instability is of significant concern in ICF, as these electrons have the potential to damage the target and prevent optimal compression.

The equation of propagation for the electron plasma wave can be obtained by differentiating the linearized continuity Equation (2.2.1) with respect to time, using the equations of motion, where the usual adiabatic assumption is used to express the pressure gradient in terms of the density gradient, and eliminating the electric field using Poisson's equation. We also expressed the electric and magnetic fields in terms of the vector potential in the Coulomb gauge ($\mathbf{A}$) The resulting equation is:

$$\left(\partial_{tt} - c^2\nabla\right)\tilde{\mathbf{A}} = -\frac{4\pi e^2}{m_e}\mathbf{A}_0\tilde{n}_e, \tag{3.4.2}$$

where we considered small perturbations $\mathbf{A} = \mathbf{A}_0 + \tilde{\mathbf{A}}$ and $n_e = n_0 + \tilde{n}_e$.

The equation of propagation for the scattered electromagnetic wave is obtained by linearizing fluid equations and the electron equation of motion, so that it yields:

$$\left(\partial_{tt} + \omega_{pe}^2 - 3v_{te}^2\nabla^2\right)\tilde{n}_e = \frac{n_0 e^2}{m_e^2 c^2}\nabla^2\left(\mathbf{A}_0 \cdot \tilde{\mathbf{A}}\right). \tag{3.4.3}$$

Here, $\tilde{\mathbf{A}}$ represents the vector potential of the scattered EM wave, $\mathbf{A}_0$ represents the field of the pump wave, and $\tilde{n}_e$ represents the electron density fluctuation. The first Equation (3.4.2) describes an EM wave driven by the current generated by the oscillating electron density perturbations in the presence of the pump field. The second Equation (3.4.3) describes the propagation of an electron plasma wave driven by the coupling between the pump field $\mathbf{A}_0$ and the scattered field $\tilde{\mathbf{A}}$.

To derive the growth rate γ (mathematically described in 2.6.1.1) of SRS, we consider a plane wave-like solution and Fourier-analyse the previous equations. We also take $\omega = \omega_{\text{EPW}} + \delta\omega$ where $\Re(\delta\omega) \ll \omega_{pe}$ and $\delta\omega = i\gamma_0$. We consider this assumption as the "weakly coupled regime". The growth rate γ_0 is an increasing function of k, which depends on the respective geometries of the wave vectors k_s and k_{EPW}, subject to the matching conditions. The growth rate is maximum for backscattering, where k is the largest. Indeed, growth rates for forward scattering and backscattering of the EM wave are given by:

$$\gamma_{0,\text{SRS}}^{f} \simeq \frac{\omega_0}{2}\left(\frac{n_e}{n_c}\right)^{3/4}\left(\frac{v_{os}}{c}\right), \tag{3.4.4}$$

$$\gamma_{0,\text{SRS}}^{b} \simeq \omega_0\left(\frac{n_e}{n_c}\right)^{1/4}\left(\frac{v_{os}}{c}\right). \tag{3.4.5}$$

As mentioned previously, the laser intensity should cross a certain threshold value to start triggering such instabilities. For the absolute SRS, [54] gives a threshold intensity as:

$$I_{L,\text{SRS}}^{\text{threshold}} = \frac{2^{1/3}}{\sqrt{3}}\left(\frac{c}{\omega_0 L}\right)^{4/3}\frac{m_e^2\omega_0^2 c^3}{8\pi e^2} \quad \text{(in c.g.s. units)} \tag{3.4.6}$$

In SI regime, where $\lambda_L = 351$ nm, and density scale length L are a few hundreds of microns, we find that $I_{L,\text{SRS}}^{\text{threshold}} \simeq 2.0 \times 10^{14}$ W/cm^2 (when $L = 500\mu$m). These intensities are routinely obtained during ICF experiments. When intensities surpass this threshold, the high-phase-velocity EPWs can induce the acceleration of electrons to high energy levels. These energetic electrons have the ability to transfer their energy to the cold fuel, thereby diminishing the compressibility of the capsule.

3.4.1.2 Two-plasmon decay

In an inhomogeneous plasma, a transverse electromagnetic mother wave $(\omega_0, \mathbf{k}_0)$ can undergo decay into two waves of EPW type $(\omega_{\text{EPW},1-2}, \mathbf{k}_{\text{EPW},1-2})$. The parametric resonance conditions are the following:

$$\begin{cases} \omega_0 &= \omega_{\text{EPW},1} + \omega_{\text{EPW},2} \approx 2\omega_{pe}, \\ \mathbf{k}_0 &= \mathbf{k}_{\text{EPW},1} + \mathbf{k}_{\text{EPW},2}. \end{cases} \tag{3.4.7}$$

Considering the matching conditions in (3.4.7), it is clear that this instability can only occur in the neighbourhood of the quarter-critical density point, where $n_e \approx n_c/4$. As the SRS instability, only the EPWs are involved in the dynamics of the instability. The

damping results in the transfer of energy to both thermal and non-thermal electrons. The growth rate of the instability can be derived in the vicinity of the quarter-critical zone by linearizing the dispersion relation, such that:

$$\gamma_{0,\mathrm{TPD}} = \frac{\mathbf{k}_{\mathrm{EPW},2}\cdot\mathbf{e}_0}{2}\left[\frac{|\mathbf{k}_{\mathrm{EPW},1}|^2 - |\mathbf{k}_{\mathrm{EPW},2}|^2}{|\mathbf{k}_{\mathrm{EPW},1}||\mathbf{k}_{\mathrm{EPW},2}|}\right] v_{os}, \tag{3.4.8}$$

where $\mathbf{e}_0$ corresponds to the polarization vector of the transverse mother wave. From Equation (3.4.8), it can be verified that the growth rate is maximum when the vectors $\mathbf{k}_{\mathrm{EPW},1}$ and $\mathbf{k}_{\mathrm{EPW},2}$ are in the plane ($\mathbf{e}_0$, $\mathbf{k}_0$). The maximum occurs for plasma waves propagating at a 45° angle both to the wave vector and the electric field of the incident wave. In this particular case, the maximum growth rate is given by:

$$\gamma^{\max}_{0,\mathrm{TPD}} = \frac{3^{1/2}}{2}\left(\frac{\omega_0}{2}\right)\left(\frac{v_{\mathrm{os}}}{c}\right). \tag{3.4.9}$$

According to the litterature ([55]), the threshold in terms of laser intensity for absolute TPD in c.g.s. units reads:

$$I^{\mathrm{threshold}}_{L,\mathrm{TPD}} = \frac{\alpha c^4 m_e \omega_0}{8\pi e^2 L}\frac{v^2_{\mathrm{the}}}{c^2}, \tag{3.4.10}$$

where $\alpha = 16.536$ is assumed constant. Equation (3.4.10) shows that $I^{\mathrm{threshold}}_{L,\mathrm{TPD}} \propto (T_e/L)$. Considering typical laser and plasma parameters, with electron temperature in the kilo-electronvolt range, we obtain that the intensity threshold is about 10^{14} W/cm^2, similar to the value obtained for the SRS. Furthermore, TPD is influenced by the polarization of laser light. Under OMEGA conditions, when using a 2D system with p-polarization configuration, TPD tends to be the dominant phenomenon over SRS. However, when utilizing an s-polarized configuration in a 2D setup, only SRS is observed. In practice, L is large when ignition-class lasers are used, decreasing the intensity threshold so that TPD should very present. Nevertheless, there is competition with SRS, and the latter is mostly observed at NIF scale ([56], [57]).

3.4.1.3 Resonant absorption

Resonant absorption emerges as a mechanism for absorbing a transverse wave propagating through an inhomogeneous plasma, and depends strongly on density profile steepness.

In this process, an EM wave of frequency ω travels along a preformed density ramp, where the density increases with the x-coordinate. The parallel wavenumber of the wave, denoted as k_x, is determined by the local EM dispersion relation: $k_x^{EM} = (\omega/c)\big[\cos^2\theta_0 - n_e(x)/n_c)\big]^{1/2}$. Here, n_c represents the critical density, $n_e(x)$ the electron density profile, and θ_0 the incidence angle at zero density.

As the wave encounters regions of higher density, the parallel wavenumber decreases. At the turning point, characterized by $n_e(x) = n_c\cos^2\theta_0$, the wave number reaches zero, leading to the splitting of the EM wave into reflected and evanescent waves. Then, the evanescent wave tunnels through the turning point and reaches the critical surface where $n_e(x) = n_c$. If the EM wave has a polarization component aligned with the density gradient, it induces an oscillating charge separation by accelerating electrons back and forth across the gradient. This oscillation results in the resonant excitation of an EPW.

The EPW excited near its own turning point at $n_e(x) = n_c$ propagates down the density ramp. The phase velocity of the EPW decreases as it encounters lower densities, leading to an increase in Landau damping. The EPW selectively accelerates a small number of electrons towards the higher velocity tail of the distribution, resulting in minimal damping near the critical surface. However, at lower densities where $n_e(x) \leq 2n_c/3$, the EPW accelerates electrons closer to the bulk of the distribution, leading to rapid damping. By the time the phase fronts of the EPW reach densities below $n_e(x) \leq n_c/2$, the original EM energy converted to electrostatic energy at the critical surface is mostly converted into electron kinetic energy.

The EPW accelerates electrons in the direction of its phase velocity, generating a flux of heated electrons directed down the density ramp. In the context of ICF implosions, this flux moves away from the capsule. However, the resulting electrostatic sheath can accelerate the electrons back towards the capsule, resulting in electron refluxing. This refluxing phenomenon preheats the capsule, which hinders compression and ultimately limits the overall yield. Figure 3.6 shows a schematic of resonant absorption.

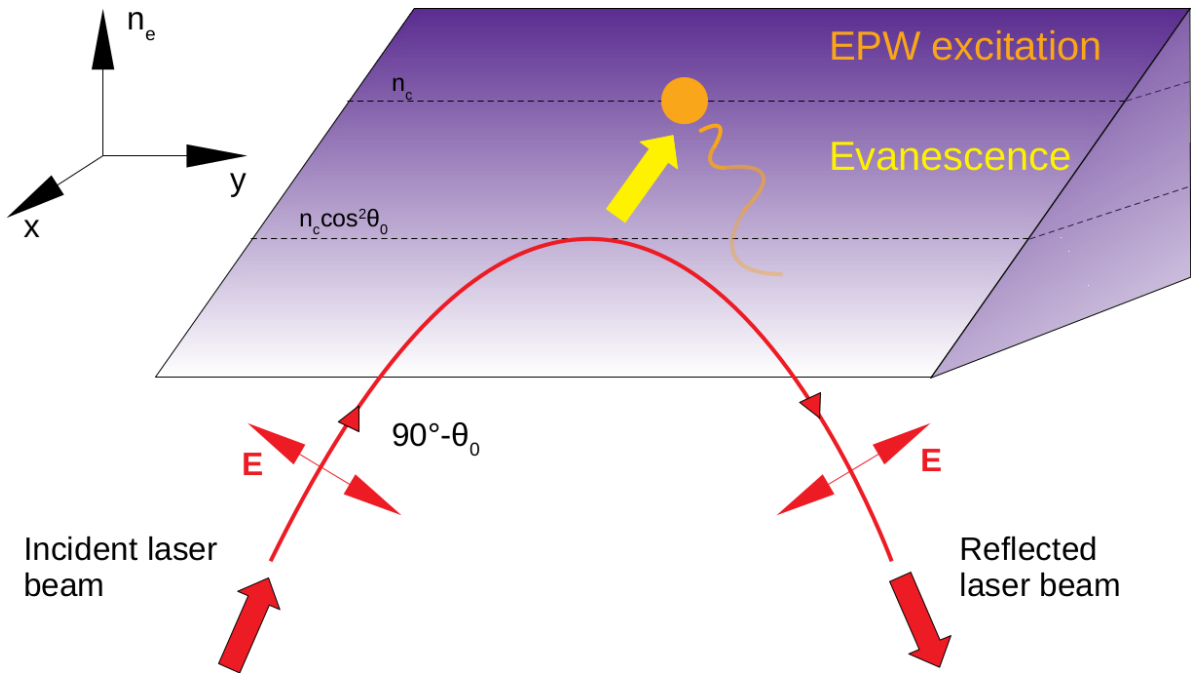

Figure 3.6 – Schematic of the resonant absorption mechanism. An incident EM wave propagates with oblique incidence along a density gradient in the case of p-polarisation. It is reflected at the turning point. The evanescent field resonantly excites an EPW that is backscattered down the density ramp. The interaction between the electron plasma wave and particles leads to the conversion of electrostatic energy into kinetic energy for the electrons. These suprathermal electrons, in the context of ICF, may preheat the target and harm the implosion efficiency.

3.4.2 Main absorption losses

3.4.2.1 Stimulated Brillouin scattering

In the case of Stimulated Brillouin Scattering (SBS) the high amplitude electromagnetic wave with parameters (ω_0 , $\mathbf{k}_0$) is unstable with respect to the excitation of a scattered electromagnetic wave and an ion acoustic wave with respective parameters (ω_s, $\mathbf{k}_s$) and (ω_{IAW}, $\mathbf{k}_{\mathrm{IAW}}$). The mechanism is the same as that of the Raman instability, with the difference being that the perturbation of electron density is due to the existence of the ion acoustic wave and no longer to that of an electron plasma wave. Furthermore, the scattered photons have a probability of propagating forward or backward. When they are backscattered, it increases the plasma reflectivity and thus reduces laser absorption, whereas when they are forward scattered, it diffuses the energy and locally reduces the laser intensity, leading to a subsequent reduction in collisional absorption. Similarly to the previous subsections, the coupling conditions are:

$$\begin{cases} \omega_0 &= \omega_s + \omega_{\mathrm{IAW}}, \\ \mathbf{k}_0 &= \mathbf{k}_s + \mathbf{k}_{\mathrm{IAW}}. \end{cases} \tag{3.4.11}$$

As the IAW has a low frequency, its frequency will be lower than the ionic frequency of the plasma, i.e., $\omega_{\mathrm{IAW}} < \omega_{pi}$, thus there are two electromagnetic waves with relatively close frequencies ($\omega_0 \leq \omega_s$). This implies that this instability can occur anywhere in the underdense plasma ($n_e < n_c$). It is particularly significant for large-scale plasmas. The wave vector $\mathbf{k}_{\mathrm{IAW}}$ and frequency ω_{IAW} of the IAW associated with scattering of a light wave into another light wave propagating at angle θ_s (the angle between the incident and scattered wave) are $|\mathbf{k}_{\mathrm{IAW}}| = 2|\mathbf{k}_0| \sin(\theta_s/2)$, $\omega_{\mathrm{IAW}} = kc_s$ - where $\mathbf{k}_0$ is the wave number of the pump wave and c_s is the ion sound speed.

Most unstable modes are found to be in the backscattering case. If we consider the weak field limit, where $k_{\mathrm{IAW}}^2 c_s^2 \ll 1$, then the largest growth rate is:

$$\gamma_{0,\mathrm{SBS}}^{\mathrm{b}} = \frac{1}{2\sqrt{2}} \frac{k_0 v_{os} \omega_{pi}}{\sqrt{\omega_0 k_0 c_s}}. \tag{3.4.12}$$

Similar to other parametric instabilities, SBS mainly occurs when the laser intensity surpasses a specific threshold value:

$$I_{\mathrm{L,SBS}}^{\mathrm{threshold}}[\mathrm{W/cm^2}] = 5 \times 10^{15} \frac{T_e[\mathrm{keV}]}{L[\mu\mathrm{m}]\lambda[\mu\mathrm{m}]}. \tag{3.4.13}$$

Here, L and T_e correspond to the plasma density scale length and coronal temperature, respectively, expressed in micrometers and kiloelectron-volts (keV). λ_L represents the laser wavelength, also expressed in micrometers. When considering standard ICF parameters, the threshold for SBS is approximately 10^{14} W/cm^2.

3.4.2.2 Cross-Beam Energy Transfer

Equations and examples

CBET is a process occurring when multiple laser beams exchange energy through a shared IAW grating. The interaction between the laser beams and the induced density perturbations can lead to a resonant wave coupling process, which occurs either when the

laser waves have different frequencies, or when they have equal frequencies but in presence of a plasma flow. This situation, that can be seen as induced Brillouin scattering, significantly impacts the symmetry of implosion by transferring power between laser beams, modifying coronal plasma conditions and changing the other LPIs intensity and location. We define the frequency shift Ω, which incorporates the influence of Doppler shift arising from the plasma flow, as:

$$\Omega = \omega_1 - \omega_2 - (\mathbf{k}_1 - \mathbf{k}_2) \cdot \mathbf{V}_p, \tag{3.4.14}$$

where $\mathbf{V}_p$ corresponds to the plasma flow velocity. The frequency detuning is then expressed as $\delta = \Omega - \omega_s$, where it is zero at resonance. Figure 3.7 depicts the geometry of interaction. We assume $\Omega > 0$, indicating that the wave labelled as 1 is the high-frequency (pump) beam, accounting for the Doppler shift. The wave 2 is referred to as the probe beam. We consider top-hat intensity profiles for the different beams. Utilising these notations, the coupled equations governing the evolution of the wave intensities are given by:

$$\begin{cases} \left(\partial_t + 2\nu_1 + \mathbf{V}_{\mathrm{g},1} \cdot \nabla\right) |A_1|^2 &= \omega_1 \dfrac{n_e}{n_c} \Im\left(\dfrac{\Gamma_s}{D_s}\right) |A_1|^2 |A_2|^2, \\ \left(\partial_t + 2\nu_2 + \mathbf{V}_{\mathrm{g},2} \cdot \nabla\right) |A_2|^2 &= -\omega_2 \dfrac{n_e}{n_c} \Im\left(\dfrac{\Gamma_s}{D_s}\right) |A_1|^2 |A_2|^2. \end{cases} \tag{3.4.15}$$

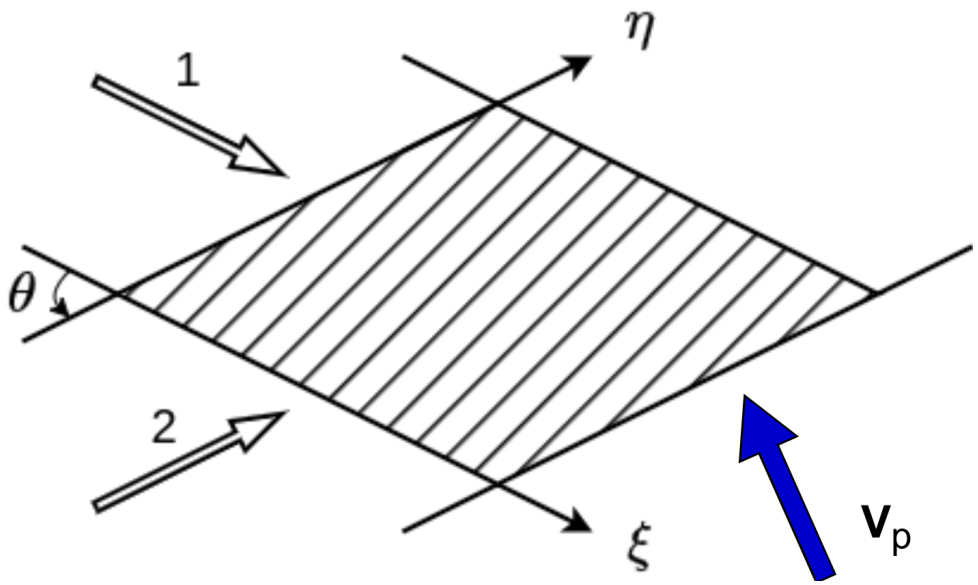

Figure 3.7 – The diagram illustrates the interaction geometry between crossed laser beams within a plasma flow $\mathbf{V}_p$. The beamwidths are uniform, while the angle of intersection between the beams is labelled θ. The vectors η and ξ are used to characterise the propagation directions of beams 1 and 2, respectively. Plasma parameters are arbitrary in the interaction region.

In these equations:

— $\Gamma_s = \left(\dfrac{e}{m v_{\mathrm{the}}}\right)^2 \left(\dfrac{k_s^2 c_s^2}{1 + k_s^2 \lambda_D^2}\right)^2$ denotes the coupling coefficient,

— A_i represents the transverse electromagnetic potential of the wave i, and is defined as the quiver velocity of electrons in the high-frequency electric field, divided by a characteristic speed equal to the electron thermal speed,

— $\mathbf{V}_{\mathrm{g,i}}$ corresponds to the velocity group of wave i,
— ν_i is the damping rate associated with the wave i, and ν_s is the ion-acoustic wave damping rate,
— $D_s = \Omega^2 - \omega_s^2 + 2i\omega_s\nu_s$ is the resonance denominator,
— the fluid approximation is used to model the IAW response.

The interaction geometry is depicted in Figure 3.7. By substituting the expressions for A and n_e in terms of their spatial and temporal dependencies and making the slowly varying envelope approximation, the following equations can be derived:

$$\begin{cases} \partial_\xi A_1 &= -i\left(\dfrac{\omega_{pe}^2}{2\omega_1 V_{\mathrm{g},1}}\right) n_e A_2 \exp\left(i\omega t\right), \\ \partial_\eta A_2 &= -i\left(\dfrac{\omega_{pe}^2}{\omega_2 V_{\mathrm{g},2}}\right) n_e^* A_1 \exp\left(-i\omega t\right), \end{cases} \tag{3.4.16}$$

where ξ and η are characteristic variables that are used to measure distances along the propagation directions of beams 1 and 2, respectively, so that $\mathbf{k}_1 = k_1\boldsymbol{\xi}$, $\mathbf{k}_2 = k_2\boldsymbol{\eta}$.

Steady-state analysis

In steady state, Equations (3.4.16) simplify and the beams interact according to:

$$\begin{cases} \partial_\xi A_1 &= (i\alpha - \beta)\left|A_2\right|^2 A_1, \\ \partial_\eta A_2 &= (i\alpha + \beta)\left|A_1\right|^2 A_2, \end{cases} \tag{3.4.17}$$

where the nonlinear coefficients α and β are defined as the real and imaginary parts of the ion-acoustic response to the ponderomotive force:

$$\begin{cases} \alpha = \dfrac{\omega_{pe}^2\omega_s^2\left(\omega_s^2 - \Omega^2\right)}{2\omega_2 V_{\mathrm{g},2}\left[\left(\omega_s^2 - \Omega^2\right)^2 + 4\nu_s^2\Omega^2\right]}, \\ \beta = \dfrac{\omega_{pe}^2\omega_s^2\nu_s\Omega}{\omega_2 V_{\mathrm{g},2}\left[\left(\omega_s^2 - \Omega^2\right)^2 + 4\nu_s^2\Omega^2\right]}. \end{cases} \tag{3.4.18}$$

In the vicinity of resonance, it can be considered that $\Omega \approx \omega_s$, so that $\Omega^2 - \omega_s^2 \approx 2\omega_s\left(\Omega - \omega_s\right)$, and Equations (3.4.18) can be approximated by:

$$\begin{cases} \alpha \approx \dfrac{-\omega_{pe}^2\omega_s\delta}{4\omega_2 V_{\mathrm{g},2}\left(\delta^2 + \nu_s^2\right)}, \\ \beta \approx \dfrac{\omega_{pe}^2\omega_s\nu_s}{4\omega_2 V_{\mathrm{g},2}\left(\delta^2 + \nu_s^2\right)}, \end{cases} \tag{3.4.19}$$

where $\delta = \Omega - \omega_s$ is the detuning parameter and explicits the "distance" to the matching conditions ($\delta \to 0$). In Figure 3.8, both coefficients α and β are plotted as functions of δ under the condition where $\nu_s/\omega_s \leq 0.1$. These coefficients are scaled relatively to $\omega_{pe}^2\omega_s^2/(4\omega_s\nu_s v_2 v_s)$, which, with the exception of a factor of $|A_1|^2$, represents the spatial growth rate of SBS in events characterized by strong damping. While the accuracy of the approximation for α diminishes as the magnitude of the frequency detuning parameter increases, the approximation for β remains valid across a wide range of frequency detuning values. However, when ν_s/ω_s exceeds 0.1, noticeable disparities arise between the approximate and precise expressions for both coefficients [58]. It is possible to solve Equations (3.4.17) by considering boundary conditions:

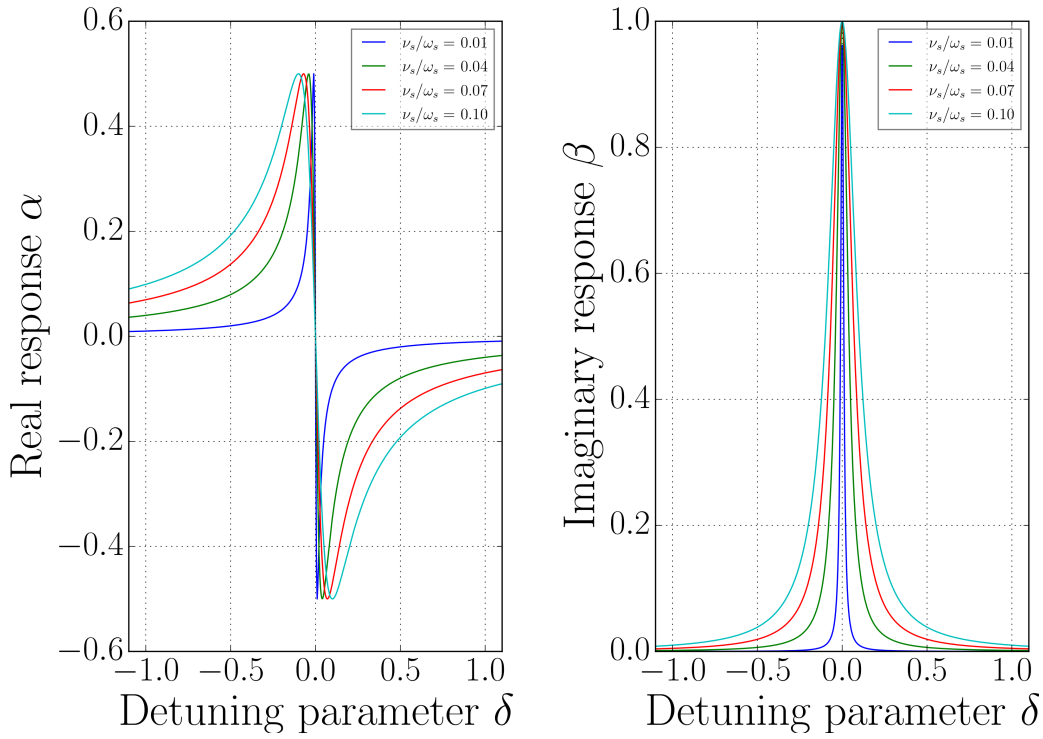

Figure 3.8 – The nonlinear coefficients α and β as described by Equations (3.4.19), are depicted in the plot as functions of the frequency detuning parameter δ for the four scenarios where $\nu_s/\omega_s \leq 0.1$.

$$\begin{cases} A_1(0,\eta) &= A_0, \\ A_2(\xi,0) &= \rho A_0, \end{cases} \tag{3.4.20}$$

and by changing variables, so that:

$$\begin{cases} B_1 &= A_1 \exp\left(-i\alpha \int_0^\xi |A_2|^2 \mathrm{d}\xi'\right), \\ B_2 &= A_2 \exp\left(-i\alpha \int_0^\eta |A_1|^2 \mathrm{d}\eta'\right). \end{cases} \tag{3.4.21}$$

To simplify the analysis, we introduce the following normalized quantities:

- normalised intensity $I_j = |B_j|^2/|A_0|^2$,
- normalised distances $x = 2\beta|A_0|^2\xi$ and $y = 2\beta|A_0|^2\eta$,
- normalised beamwidth $l = 2\beta|A_0|^2 w/\sin\theta$, where w represents the physical beamwidth, and θ forms the intersection angle between the two beams (see Figure 3.7).

These normalised quantities help streamline the calculations and analysis. From Equation (3.4.17), it follows:

$$\begin{cases} \partial_x I_1 &= -I_1 I_2, \\ \partial_y I_2 &= I_1 I_2. \end{cases} \tag{3.4.22}$$

The new boundary conditions are now as such:

$$\begin{cases} I_1(0,y) &= 1, \\ I_2(x,0) &= r, \end{cases} \tag{3.4.23}$$

where $r = |\rho^2|$ is the incident intensity ratio of the beams.
Even though Equations (3.4.22) describe nonlinear beam propagation in two directions,

there is an analytical solution available. To facilitate this, we define:

$$\begin{cases} P_1(x,y) &= \int_0^y I_1(x,y')dy', \\ P_2(x,y) &= \int_0^x I_2(x',y)dx'. \end{cases} \tag{3.4.24}$$

Here, $P_1(x,l)$ represents the power within the cross-section of beam 1 at a distance x from the interaction region's entrance, and $P_2(l,y)$ represents the power within the cross-section of beam 2 at a distance y from the entrance to the interaction region. By combining these equations with (3.4.22), we can derive:

$$\partial_x P_1 = r\left[1 - \exp\left(P_1\right)\right] \tag{3.4.25}$$

$$P_1(x,y) = -\log\left[1 - \exp\left(-rx\right)\left[1 - \exp\left(-y\right)\right]\right]. \tag{3.4.26}$$

$$\begin{cases} I_1(x,y) &= \dfrac{\exp(-y)}{\exp(rx) - 1 + \exp(-y)}, \\ I_2(x,y) &= \dfrac{r\exp(rx)}{\exp(rx) - 1 + \exp(-y)}. \end{cases} \tag{3.4.27}$$

Using Equations (3.4.26) and the relationships $I_1 = \partial_y P_1$ and $I_2 = r\exp(P_1)$, we can further analyse the system.

The left column on Figure 3.9 shows the beam intensity profiles when they cross each other for the scenario where l = 3 and r = 0.01. It appears clearly that the intensity of beam 1 remains relatively constant, while the intensity of beam 2 does not vary significantly with respect to x. In this case (with $rl \ll 1$), Equations (3.4.27) simplify to $I_1 \approx 1$ and $I_2 \approx r\exp(y)$, which aligns with the linearised versions of Equations (3.4.22).

Figure 3.9 right column also displays the beam intensity profiles, but for a situation where $l = 3$ and $r = 0.1$. Here, the intensity profiles exhibit a more pronounced two-dimensional behaviour. Beam 1 experiences depletion as it propagates along the x-direction, while beam 2 undergoes amplification as it travels in the y direction. Consequently, beam 2 experiences faster amplification along the characteristic $x = 0$ compared to its amplification along the characteristic $x = l$, and beam 1 undergoes more rapid depletion along the characteristic $y = l$ than along the characteristic $y = 0$.

Energy conservation along the laser paths can be written by as follows by summing and integrating the two Equations (3.4.24):

$$\begin{aligned} &\int_0^x \int_0^y \left(\partial_{x'} I_1 + \partial_{y'} I_2\right) \mathrm{d}x'\mathrm{d}y' = 0, \\ &\qquad \Leftrightarrow P_2(x,y) - P_2(x,0) = P_1(0,y) - P_1(x,y). \end{aligned} \tag{3.4.28}$$

The power transfer defined as $P_2(l,l) - P_2(l,0) = T(l)$ can then be written as such:

$$T(l) = \log\left[\exp(-rl) + \exp(l)\left[1 - \exp(-rl)\right]\right], \tag{3.4.29}$$

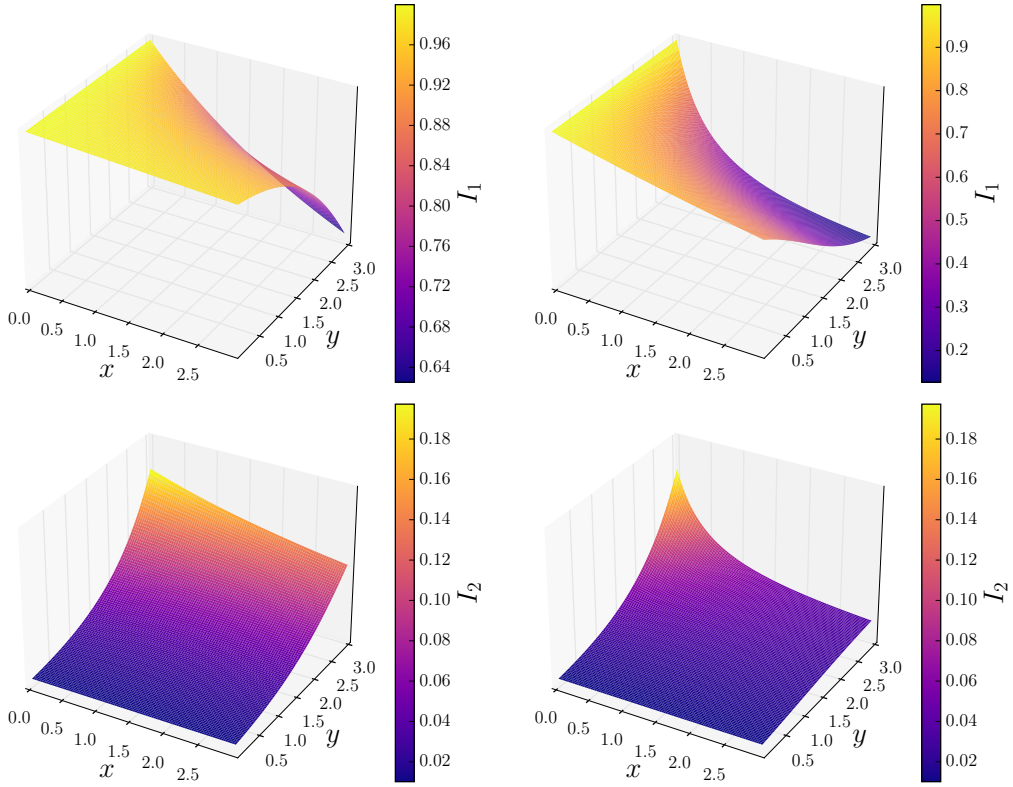

Figure 3.9 – Figure of the beam intensity profiles is represented as a colourmap function of x and y. The top row shows the intensity for laser 1. The bottom row shows the intensity for laser 2. Left column is when $r = 0.01$, right column is when $r = 0.1$. The normalised beamwidth is set to $l = 3$ ($x_{\max}$ and $y_{\max}$ on the plot) for all 4 figures.

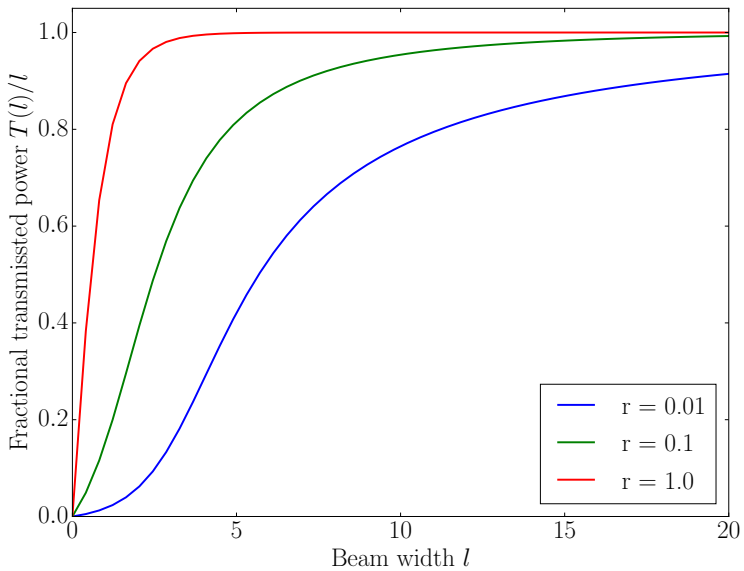

Figure 3.10 – The graph shows the fractional power transfer from beam 1 to beam 2, as given by Equation (3.2.23), plotted as a function of the normalised beamwidth l. It includes three curves representing different values of r, which is the ratio of the incident beam intensities.

The fractional power transfer is represented graphically in Figure 3.10. For values $rl \ll 1$ and $l \approx 1$, the relationship $T(l)$ approaches approximately $rl\,[\exp(l) - 1]$. On the other hand, for $l \gg 1$, $T(l) \to l$: the bigger the cross-sectional distance, the more energy transfer there is.

Despite the intricate evolution of the beams, the power transfer process can be succinctly captured by two dimensionless parameters. The first, denoted as r, encapsulates the relationship between incident beam intensities. The second parameter, l, is contingent on various dimensional factors characterising both the beams and the plasma. It is noteworthy that for different parameters, l can be determined through its proportional relationship with $n_e\lambda_0 I_0 w$ and its inverse proportionality to T_e, while keeping the electron-to-ion temperature ratio constant.

In the context of Equation (3.2.23), which holds true for angular values between 0 and π, the dependence on the beam angles becomes important. As δ approaches 0, $\beta|A_0|^2$ is the spatial growth rate of SBS. In the case of an IAW undergoing Landau damping, this growth rate stays unaffected by the angle θ ([59], [60]). In our scenario, l exhibits an inverse relationship with $\sin\theta$. This implies that the power transfer is more pronounced when the beams are nearly parallel or anti-parallel, allowing for an extended overlap. The role of $\delta \neq 0$ gains significance concerning ν_s and ω_s, both being proportional to $\sin(\theta/2)$. Hence, the power transfer exhibits heightened sensitivity to detuning when beams are nearly parallel and reduced sensitivity when they are nearly antiparallel.

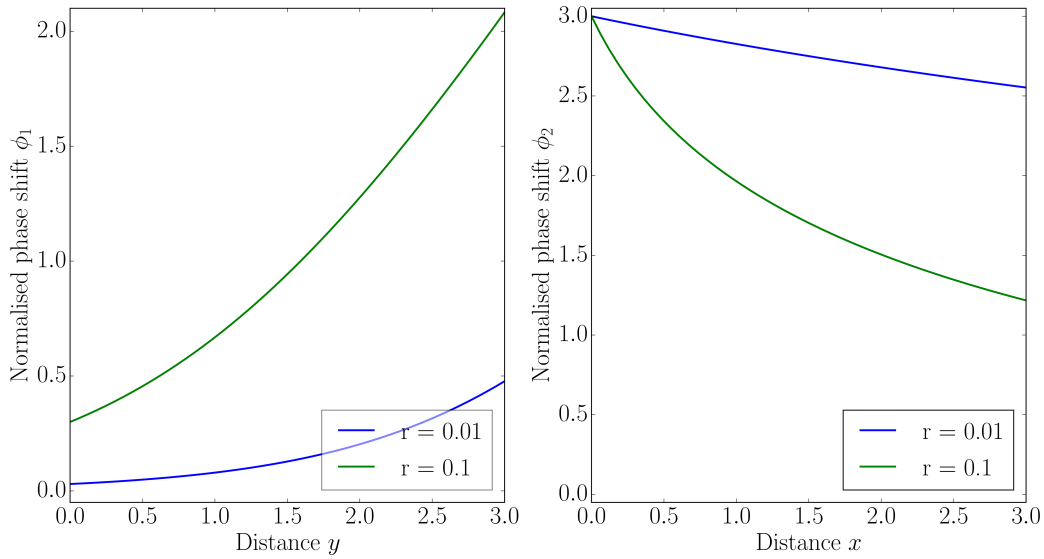

Figure 3.11 – Graphs illustrating the normalised phase shifts, as defined in Equations (3.4.30) for the scenario where the normalised beamwidth $l = 3$, and considering two values of r (the ratio of the incident beam intensities). Blue represent r=0.01, while green lines represent r=0.1. The spatial variation in these phase shifts results in the deflection of the beams.

As $\delta \neq 0$, the interaction between beams 1 and 2 induces phase shifts denoted as ϕ_1 and ϕ_2, respectively. This is deduced from Equations (3.4.21), (3.4.24):

$$\begin{cases} \phi_1(y) &= \dfrac{\alpha P_2(l,y)}{2\beta I_0}, \\ \phi_2(x) &= \dfrac{\alpha P_1(x,l)}{2\beta I_0}, \end{cases} \tag{3.4.30}$$

Normalised phase shifts are plotted on Figure 3.11. For beams of moderate width ($l \approx 1$), the phase change with distance exhibits an approximately linear behaviour, facilitating a straightforward estimation of the deflection angles θ_1 and θ_2. It can be shown that the deflection of both beams shares a common angular direction: counterclockwise when $\delta < 0$ and clockwise when $\delta > 0$. The angle of deflection hinges on the values of both α and β, considering that the fractional power transfer's reliance on l and, consequently, β. Examining Figure 3.8 reveals that the most substantial deflection angle occurs when $|\delta|$ is approximately equal to ν_s: best compromise to maximise α and β in our case, ν_s/ω_s . In scenarios where $\delta = 0$ or $|\delta| = \omega_s$, the beams undergo no deflection.

In the scenario of wide beams $l \geq 1$, the linear phase evolution of beam 1 persists over distance, as indicated. On the other side, the phase progression of beam 2 exhibits strong nonlinearity, making it challenging to accurately assess the beam deflection angle and the distance of focus. Despite these complexities, in such situations, the power transfer from beam 1 to beam 2 is comprehensive, leading to modifications in irradiation symmetry, rendering concerns about beam deflection and focus inconsequential.

The beam deflection angle is more pronounced for beams that are nearly parallel or antiparallel. This phenomenon arises from the fact that nonlinear phase shifts causing beam deflection are directly proportional to the power transfer. Consequently, the deflection angle exhibits greater sensitivity to detuning when beams are almost parallel, whereas it becomes less sensitive when the beams approach antiparallel alignment.

A similar study was performed ([61]) and conducted a thorough three-dimensional examination of the power exchange dynamics between intersecting laser beams, considering arbitrary upstream intensity profiles. The analysis reveals that the power transfer induces shifts in the centroids of the beams, while the phase shifts result in changes to the beam directions and focal lengths. In cases where the beams exhibit hot spots in their upstream intensity profiles, the power transfer is particularly sensitive to the intersection of the associated filaments.

As a conclusion, the significance of CBET lies in its impact on the symmetry of implosion in ICF experiments. In both direct-drive and indirect-drive scenarios, this nonlinear LPI effect introduces dynamic alterations to the irradiation field, which can lead to asymmetries in the drive and deformations in the capsule.

Importance of understanding CBET

CBET is one of the many laser-plasma interaction processes that pose challenges in computational target design. These difficulties arise due to the spatial and temporal scale differences between large-scale hydrodynamical modeling and the rapid, small-scale evolution of wave coupling processes involved in CBET.

In indirect drive laser fusion, [62] were the first to demonstrate that this process could take place at the laser entrance hole (LEH) of ignition hohlraums, where multiple laser beams intersect in a flowing plasma. Subsequently, energy transfer between two crossing laser beams was experimentally observed on the Nova laser facility by [63]. This discovery led to extensive theoretical or numerical investigations ([58], [64]) and further experimental studies ([65], [66]).

More generally, nearly four decades ago, the ICF community realized that simulations based on the Spitzer-Härm heat transport model [31] were overestimating the laser drive. To address this, they proposed limiting the Spitzer-Härm fluxes using an adjusting flux-limiter parameter, denoted as f with values typically in the range of 0.04 to 0.1 (as seen

by [32]). Although this approach lacked a physical rationale, [67] provided reasonably accurate results for experiments conducted on OMEGA over the past decades, including planar shock-timing experiments and implosions using 1-ns square laser pulses at intensities between 10^{14} and 10^{15} W/cm^2.

However, investigations [68] have shown that this fixed or time-dependent f parameter cannot accurately model implosions performed under different conditions, such as using longer square or shaped pulses. The challenge arises from the fact that simulations can be adjusted by varying f to match specific observables, like the absorption fraction, while other observables remain unmatched. To address this issue, the flux-limited model has been replaced with a recently developed nonlocal heat transport model developped by [33]. This new approach employs a solution to the simplified Boltzmann equation without assuming a small mean free path for electrons. Unlike the previous flux-limited model, the nonlocal model offers good agreement across a wide range of experimental conditions, providing a more accurate representation of the simulations.

Nevertheless, simulations performed by [68] were still overpredicting laser absorption on experiments at the OMEGA60 facility by 10%. Simulations incorporating CBET demonstrate excellent agreement with all observed data in implosion experiments involving various laser and target parameters (work performed by [69]). Experiments are not consistently replicated by simulations using flux-limited transport, with or without CBET.

More recently, the *ASTER* radiation hydrodynamics code ([4]) has been enhanced by Colaïtis et al. [5] to include an inline implementation of the *IFRIIT* 3D laser model, designed specifically for this physics. When used in simulations of cryogenic OMEGA implosions, Ref. [6] shows that the *IFRIIT* model demonstrates remarkable accuracy in reproducing essential aspects of the implosions, encompassing the bang time, neutron yield, flow velocity, and direction of two cryogenic shots. Importantly, this precision is achieved without the need for arbitrary parameter adjustments. The model takes various uncertainties into account, including laser pointing and factors related to fuel aging, such as tritium decay, 3He contamination, radiological capsule damage, and laser-induced low modes. Notably, the polarized CBET model employed in the simulations successfully captures the consistent flow direction observed across numerous shots conducted in recent years ([7]).

Recent papers ([6], [70], [71]) explore even more the coupling between the two codes *ASTER+IFRIIT* and has yielded promising and robust results at the OMEGA scale. However, ICF target modeling at the full scale, or the ignition scale, using these 3D tools has been infrequent. Thus, the next crucial step involves applying and validating the coupled code at the ignition scale to explore its capabilities fully.

3.5 Modeling laser propagation in a plasma: the inverse ray-tracing code *IFRIIT*

The *IFRIIT* code [5], named after "Inline Field Reconstruction and Interaction using Inverse Tracing," is a versatile module tailored to compute the interaction of laser light with plasmas at large scales, efficiently meeting the requirements of inline modeling with the 3D eulerian radiative hydrodynamics (RH) code *ASTER*. It is the first time that an Inverse Ray-Tracing (IRT) method was used for laser propagation calculations in a plasma

coupled to a RH code by opposition with the method of Forward Ray-Tracing (FRT) that is usually employed. This model combines IRT techniques with both real-valued geometrical optics (GO) and employs Etalon integrals (EI) to accurately compute laser fields in 3D, including around Fold-type caustics, without the need for limiters or artificial coefficients.

Unlike conventional ray-trace algorithms commonly used in hydrodynamic codes, the IRT approach involves tracing rays from an initial ray surface (such as a lens) to specific observation points within the medium, determining the phase space ray parameters in the process. IRT offers several advantages over traditional rigid-scale estimation techniques. Notably, it eliminates the dependence of field computation on the number of rays per cell, ensuring that every ray contribution to the field at a given point is fully accounted for. Additionally, IRT enables accurate computation of ray phase and amplitude without resorting to averaging processes, making it a robust method for computing ray fields at any location within the medium. Finally, employing IRT offers further benefits. For instance, it facilitates a clear differentiation of the laser field among the different reflected components. This capability enables precise accounting for the self-interaction of the incident and reflected fields of beams through CBET. Additionally, IRT significantly accelerates pump depletion iterations in CBET algorithms by allowing updates only to specific parts of the ray equations.

The *IFRIIT* model uses a geodesic tetrahedron mesh for tracing rays and spherical polar mesh for computing fields [72]. It is adaptively refined, aiming to provide enhanced resolution for the subgrid-scale gradients of laser-related quantities, including fields or permittivity perturbations, while describing the light propagation and CBET interactions. The correct CBET interaction, even at high gains, is achieved without resorting to any numerical artifices, such as limiters, multipliers, or energy renormalization factors. In *IFRIIT*, all quantities are specified at the nodes of the tetrahedron mesh and are approximated to exhibit linear variation within cells. The propagation of rays within the mesh follows the real-valued geometrical optics model [73]:

$$\begin{aligned} \frac{\mathrm{d}\mathbf{r}}{\mathrm{d}\tau} &= \mathbf{p}, \\ \frac{\mathrm{d}\mathbf{p}}{\mathrm{d}\tau} &= \frac{1}{2}\nabla\epsilon'(\mathbf{r}), \end{aligned} \tag{3.5.1}$$

where r is the position of the ray, $\mathbf{p}$ is the ray momentum, τ is a parametric coordinate related to the ray arc-length s by the differential relation $\mathrm{d}\tau = \mathrm{d}s/\sqrt{\epsilon'}$, and ϵ' is the real part of the permittivity of the medium. The ray field u is obtained by integrating the ray phase ψ'' along the ray trajectory and computing the ray amplitude term A:

$$\begin{aligned} u &= A\exp\left[ik_0\psi\right], \\ \psi''(\tau) &= \int_0^\tau \epsilon''(\mathbf{r}(\hat{\tau}))\mathrm{d}\hat{\tau}/2, \\ A(\tau) &= A(0)\left|\frac{D(0)}{D(\tau)}\right|^{1/2}, \end{aligned} \tag{3.5.2}$$

where ϵ'' is the imaginary part of the permittivity, D is the determinant of the Jacobian of the coordinate change from ray phase space to real space (for more details, refer to [5]), and only the imaginary part ψ'' of the phase is used to compute the field amplitude

in the real-valued geometrical optics formulation. The field computation resolution is conducted within the IRT framework. Instead of tracing rays forward from a lens plane into the plasma, all the rays from all beams that reach each node of the *IFRIIT* mesh are identified, using non-linear multidimensional Newton methods [74]. This approach enables the decoupling of the computation of term A, which is computationally intensive, from the phase integral term ψ'', which only requires knowledge of the ray trajectories and ϵ''. Utilizing IRT allows for accurate and efficient 3D calculations in the spherical ICF geometry while maintaining inline capabilities. After computing the field, which includes contributions from absorption and nonlinear couplings, the heat source term $\epsilon''|u|^2$ is calculated and then interpolated back into the *ASTER* nodes for the subsequent hydrodynamics step.

The process of coupling *IFRIIT* with the 3D radiative hydrodynamics code *ASTER*, developed at the LLE, is described by [72]. Both codes operate on separate grids and establish communication through interpolation. *IFRIIT* employs a dedicated laser grid optimized for its computations, allowing the use of distinct parallelization methods for each code. Figure 3.12 shows the general principle of the grid coupling *ASTER+IFRIIT*.

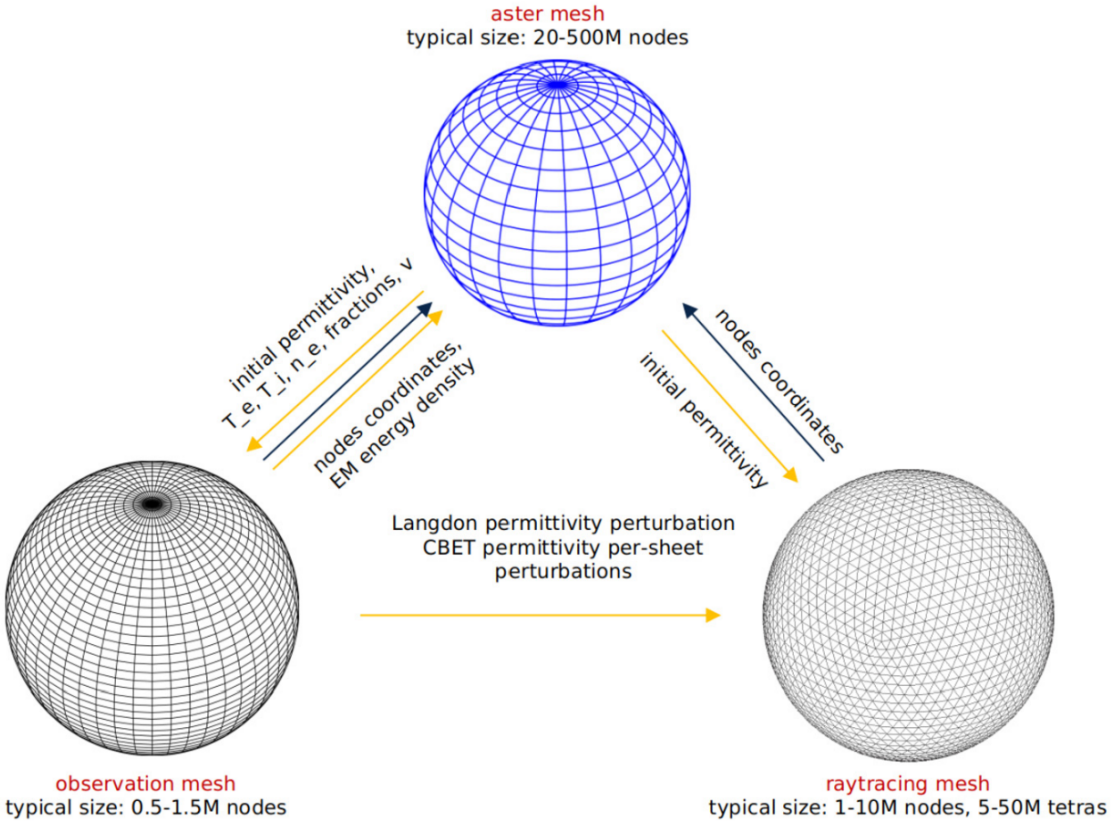

Figure 3.12 – Figure courtesy of A. Colaïtis [72]. The communications between the *ASTER* (blue grid) and *IFRIIT* (black grids) involves a grid coupling principle with distinct mesh arrangements. The *ASTER* mesh, designed as a high-resolution polar grid, serves to solve radiative hydrodynamics equations. In contrast, *IFRIIT* utilizes a spherical geodesic grid as the raytracing mesh, responsible for tracing rays, while the observation mesh, also from *IFRIIT*, takes the form of a polar mesh where field computations occur. Physical quantities like permittivity, plasma temperatures (T_e and T_i), electron density (n_e), plasma velocity (V_p), and material fractions (f) are defined on the observation mesh and are interpolated from the *ASTER* mesh. These quantities play a vital role in calculating the Langdon effect, CBET coupling coefficients, and fields. The plasma permittivity is defined on the raytracing mesh, also obtained through interpolation from the *ASTER* mesh, enabling resolution of the trajectory equations. Moreover, permittivity perturbations from the Langdon effect and CBET, computed on the observation mesh, are further interpolated onto the raytracing mesh to integrate the phase equation. Finally, the EM energy density, acquired at the nodes of the observation mesh, is back-interpolated at the cell vertices of the *ASTER* mesh. The resulting values are then tri-linearly integrated from the vertices into the cell volume. Information exchange between the three grids during the *IFRIIT* operation is depicted with arrows. Notably, only exchanges to and from the *ASTER* mesh involve MPI communications. Additionally, due to block decomposition of the *ASTER* mesh, communications with *IFRIIT* are limited to specific ranks only. Yellow arrows highlight the interpolation steps undertaken throughout the process.

Chapter 4

Role of CBET in solid sphere ignition scale polar direct drive experiments at the National Ignition Facility

4.1 Motivations

In DD ICF [3], [16], [48], high power laser beams are used to implode a spherical shell constituted of gaseous DT fuel surrounded by solid DT and a plastic ablator. In the central hot spot scheme, the mechanical work communicated to the gas prior to target stagnation ignites the DT gas, creating a thermonuclear burn wave in the solid DT fuel and providing significant energy release and gain. Alternative schemes, such as shock ignition (SI) [21], [22], [75], [76], decouple the compression and ignition phases in order to improve energy gain [77], and scheme robustness.

For such laser intensities, the interaction parameter $I\lambda_L^2$ exceeds the threshold value of 10^{14} W µm^2/cm^2 (usually, ICF lasers operate at a wavelength $\lambda_L = 0.351$ µm). The laser-plasma interaction becomes prone to numerous couplings between electromagnetic and plasma waves [78], [79]. Most of these additional processes have non-linear behaviours and are in general harmful to fusion-related implosions. Among these couplings, the overlap between several laser waves in the plasma produces ponderomotive beatings able to drive IAWs. An energy exchange through diffraction on a commonly excited IAW electron density perturbation is likely to occur. This three-wave interaction is commonly known as CBET. [58], [62], [80]–[82].

The dominant absorption mechanism in ICF implosion experiments is inverse bremsstrahlung [54] (also referred to as collisional absorption). It mainly takes place in a close region where the electron density n_e is lower than the laser critical density $n_c \approx 9.0 \times 10^{21}$ cm^{-3}.

On the other hand, CBET, being a type of stimulated Brillouin scattering, may occur in the whole volume of the underdense plasma ($n_e \leq n_c$). It is therefore an efficient process in long scale-length plasmas, which is the case for NIF ICF experiments. CBET is especially prominent in the polar-direct-drive (PDD) [57], [83]–[85] geometry used on NIF to approach DD ICF. Because of this scattering phenomenon, laser beams fail to penetrate deeply enough into the plasma causing a significantly reduced laser-target coupling and

an enhancement of low mode asymmetries [6], [71]. Beam overlap is large and energy exchange between beams lead to large-scale modulations to the laser drive.

Recently, an inverse-ray tracing laser model without *ad hoc* parameters, *IFRIIT* [5], [72], specifically designed for DD ICF was implemented inline in the 3D radiative hydrodynamics code *ASTER* [4], [52]. CBET was efficiently modeled in *IFRIIT* and the coupling between the two codes shows promising and robust results at the reduced OMEGA scale [6], [70], [71].

In this context, a series of experiments [57] was performed at the National Ignition Facility (NIF) [1] to diagnose energy coupling in PDD using platic solid sphere targets. These experiments aim to study the efficiency of the laser energy coupling to a spherical target with beam intensities close to the standard SI regimes. These solid spheres offer the advantage of quantifying energy coupling without the challenges from hydrodynamic instabilities of thin-shell implosions or kinetic effects in exploding pushers. NIF PDD implosions measured the energy-coupling in a series of shots up to 3×10^{15} W/cm^2 peak intensity with a 5 to 7-ns-long shaped pulse. Similar experiments on OMEGA with scaled solid spheres were performed to test the scaling arguments of PDD implosions from OMEGA to the NIF [86]–[88]. Good agreement was obtained between the measured data (shock trajectories and shock collapse) with the trajectories from 2D *DRACO* [89] radiation-hydrodynamics simulations using CBET and non-local heat-transport models [32], [33], [90]. However, these models at the NIF scale were manualy adjusted to reproduce the experimental data (with several ad-hoc parameters on the laser profile and CBET coefficient), and hence cannot be considered to be robust for that scale. In addition, more detailed quantities such as the angular dependence of scattered light is not reproduced correctly. In particular, this prevents more general studies of the ICF concept at these scales and in presence of large amounts of CBET (which is notably the case of SI). Conversely, *IFRIIT* has no free parameters in its CBET modeling, due to novel algorithms implemented specifically to that end. *ASTER/IFRIIT* has been well validated at OMEGA scale and should now be applied to the NIF scale.

4.2 Polar direct drive

The more energetic energy laser facilities, such as the National Ignition Facility (NIF)[1] and Laser Mega-joule (LMJ)[91], are designed with beam ports in the polar regions of the target chamber, primarily for indirect drive inertial confinement fusion (ICF). In this approach, laser energy is directed onto the interior of a cylindrical target, generating x-rays that drive an implosion capsule toward conditions suitable for ignition[92]. Achieving uniform drive throughout the implosion is a crucial challenge in this process[93]. The NIF, utilizing indirect drive, has recently achieved thermonuclear ignition [2], [94]. To transition into the energy production regime, it is imperative to enhance fusion energy output. This necessitates improved coupling of laser energy to the target. While direct drive (DD) achieves higher laser-to-target coupling [48], it imposes strict conditions on laser driver uniformity. DD facilities now have the capability to attain deviations in drive symmetry below 1%, meeting the requirements for high-performance implosions.

The NIF has 192 laser beams arranged into groups of 4, called quads. Each quad enters trough a different port on the target chamber. These quads are arranged into groups at equal angle from the poles: $\theta_p = \{23.5°, 30.0°, 44.5°, 50.0°\}$ which are described

as cones. Top and bottom hemisphere of the chamber are symmetric, with 4 cones each. The facility layout is optimised for indirect drive, including port locations and beam spots.

Polar direct drive (PDD) has emerged as a method for conducting DD experiments at mega-joule laser facilities [83], [95]. PDD configurations vary widely, but a common strategy involves redirecting laser beams toward the target equator to achieve a more uniform distribution of energy. Figure 4.1 illustrates the beam pointing of PDD.

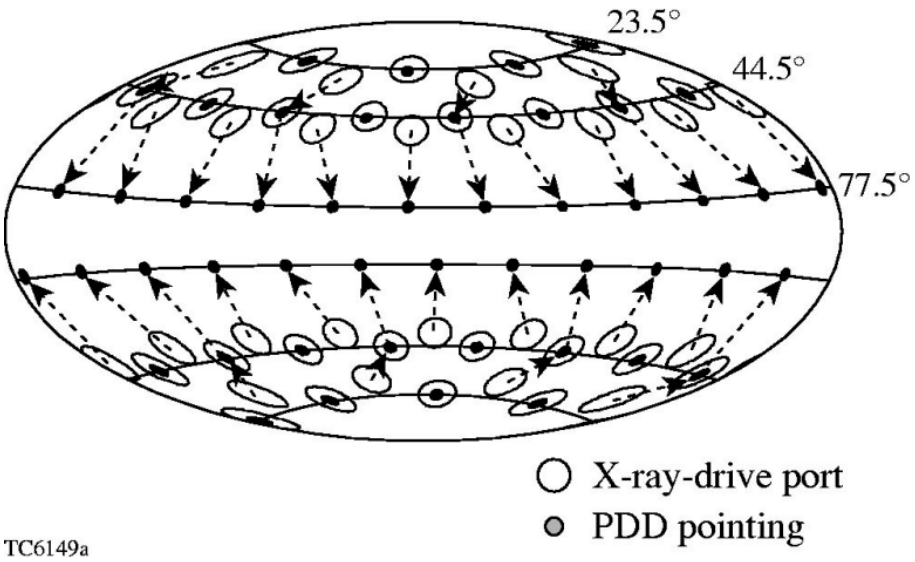

Figure 4.1 – Schematic of the PDD geometry at the NIF experimental chamber. PDD repoints of some laser beams toward the target equator. This figure shows the beams being directed to the direct-drive positions corresponding to three rings of beams incident upon the target in each hemisphere. Image taken from Ref. [83].

Given the substantial laser energies at disposal, PDD has demonstrated utility as a technique for investigating high energy density physics [96], [97], LPIs [98], [99], hydrodynamic scaling [100], and reliable neutron production [101]. However, achieving optimal ICF implosions with PDD is currently a challenge due to the difficulty in maintaining uniform drive. In this chapter, the focus shifts to solid plastic targets, often doped or deuterated, providing an easily diagnosable platform for experiments related to laser-target coupling and shock propagation in PDD.

4.2.1 Experimental setup description

The aim of these NIF experiments (N190204-003 and N210519) is to study the coupling efficiency of laser energy to an imploding spherical target in a regime towards SI. Laser parameters are given for both experiments in Table 4.1 and laser pulses are showed in Figure 4.2.

These consist in a spherical-solid target being illuminated by 184 NIF beams in a PDD configuration. A copper backlighter foil shot by one laser quad is used to obtain x-ray radiographies to track the shock position in time. The shock-trajectory was recorded during and after the main drive over a 3 ns time window with a 57.9 kJ pulse.

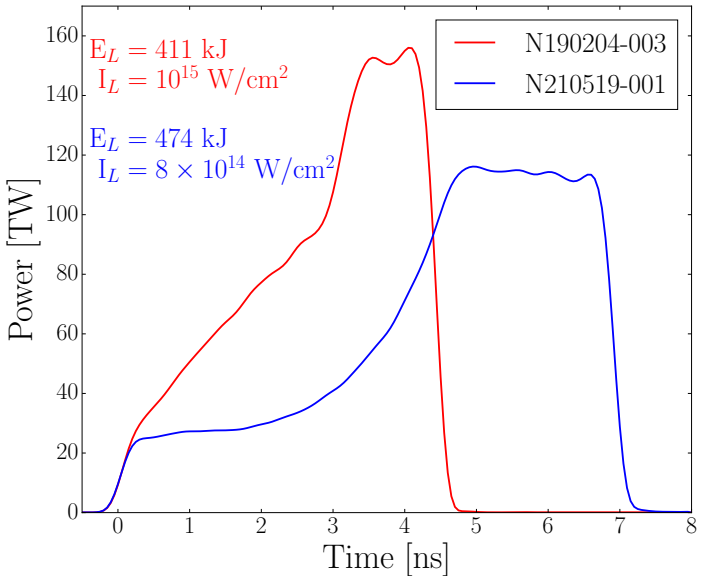

Figure 4.2 – Average solid target pulses with their respective energy and peak intensity. Red is for shot N19204-003 and blue is for shot N210519-001.

Table 4.1 List of experimental parameters for both shots: the total laser energy E_L in kJ, the peak power used during the spike P_L in TW, the peak laser intensity estimated at the initial target radius I_L in units of 10^{14} W/cm^2, the duration of the laser pulse t_L in ns, the target radius R in mm, and the mixture of the target. Subscripts "i" and "o" denote for "inner" and "outer".

Shot number	E_L [kJ]	P_L [TW]	I_L [10^{14} W/cm^2]	t_L [ns]	R [mm]	Mixture
N190204-003	411	150	10.0	5	1.0+0.1	CD_i+CH_o
N210519-001	474	120	8.0	7	1.063	CH

An extra quad is repointed in order to accommodate the target stalk (100 µm diameter large). Full-aperture backscattering system (FABS) [102] diagnostics are used for both experiments. SBS appears to be the primary source of backscattered energy, occurring mainly during the spike and located around the equator. The filter-fluorescer diagnostic system (FFLEX) [103] allows to characterise suprathermal electrons. Figure 4.3 shows a schematic of the experimental setup.

The plasma conditions of these shots are similar to ignition designs for the NIF [104]. The electron temperature is $T_e \sim 3.2$ keV and the scale-length reaches ~ 330 μm at the poles and ~ 400 μm at the equator. Data were measured at quarter critical ($n_e = n_c/4$) and at the middle of the laser spike.

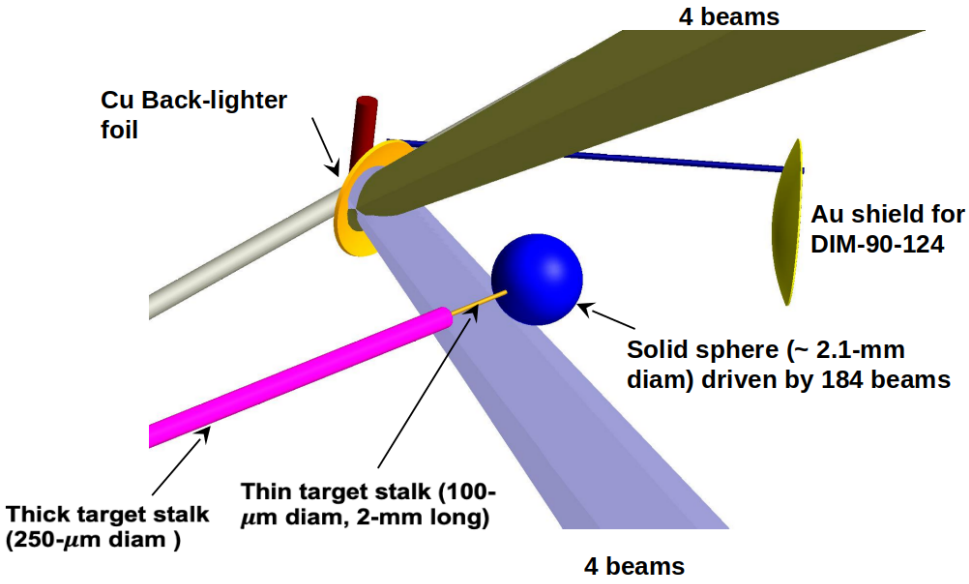

Figure 4.3 – Schematic of the experimental setup for the SSS shots.

4.3 Characterisation of 10 mm defocused NIF laser quads in vacuum

Simulations are performed with the *ASTER/IFRIIT* coupled code. In the following results, we modelled the employed quad splitting configuration - all 184 beams are individually simulated. In the experiment, the beams are 10 mm defocused. Experimental data was obtained by extracting the cross-sectional area enclosing 90% of the quad power. When defocusing a laser spot up to $d = 10$ mm, the area and shapes are very different as seen in Figure 4.4.

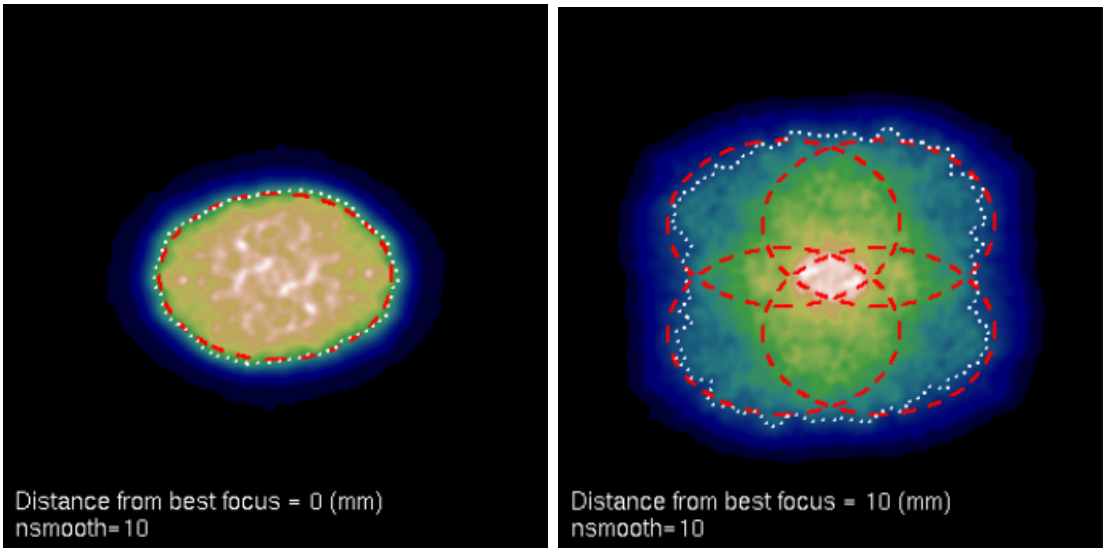

Figure 4.4 – Illustration of a laser spot for a cone with polar angle $\theta_p = 23.5^\circ$ at $d = 0$ mm (left) and $d = 10$ mm (right). Both images are on the same spatial scale. Image courtesy of T. Chapman from LLNL.

There is a need to characterise correctly the spot shapes with defocus using *IFRIIT*. To make it easier, we first rotated along the $x-$axis the NIF quads located at the polar angle

$\theta_p = 23.5°, 30.0°, 44.5°$, and $50.0°$ (angles of the beam ports used during the experiment). In this way, beams are virtually travelling only along the $x-$axis and the spot surface can be studied in the $z-y$ plane only for specific slices at a given x, which is the distance from best focus ($x = 0$ is at best focus). x is also analogous to the defocus. For a given defocus d, we will scan the slice at the same given value of x. In our simulation, we adopt a systematic approach to extract the surface of the spot. In our simulation methodology for spot surface extraction, we follow a structured process.

Initially, an offline simulation is conducted using the ASTER/IFRIIT framework to analyze the spot. This involves examining the power distribution within the spot domain and determining its size. The power values are then organized to identify the portion encompassing 90% of the total power. Subsequently, this calculated value is compared to experimental data, and any inconsistencies lead to adjustments in the $1/e$ radius of the beams using the formula specified in equation 4.3.1..

This method will help us to characterise the spot shapes with the addition of defocus. To try and match the experimental data, the $1/e$ radius of the super Gaussian beams, σ [mm], are modified according to the following formula:

$$\sigma_\alpha = \sigma_{0,\alpha}(1 + d\beta), \tag{4.3.1}$$

where α denotes for the x or y axis of the beam, d corresponds to the the defocus in mm and β is a fitting factor ($\beta = 0.30/50, 0.40/50, 0.80/50$, and $0.95/50$) determined for each different cone polar angle ($\theta_p = 23.5°$, $30.0°$, $44.5°$, and $50.0°$).

The final results are shown in Figure 4.5. Top images show the spatial distribution of the electromagnetic field in the Z-Y plane at $x = 10$ mm for a quad located in the ring at $\theta_p = 50°$. The colormap is employed here as an indicative tool. Left image is in the case where there is no defocus, right image is obtained when applying the fitting formula (4.3.1) for defocus. The differences are noticeable: with the defocus module, laser spot tend to overlap more and create a bigger surface enclosing 90% of the total power. Bottom figure shows the evolution of the area enclosing 90% of the quad power for all the different cones (from $\theta_p = 23.5°$ in yellow to $\theta_p = 50.0°$ in orange). The curves are fitted functions from the experimental data which are given by:

$$\mathcal{A}_{\theta_p}(d) = \mathcal{A}_{\theta_p,0} + ad + bd^2 + cd^3, \tag{4.3.2}$$

where $\mathcal{A}_{\theta_p}$ corresponds to the area enclosing 90% of the total power of the quad located at the θ_p cone for a given defocus/distance from best focus d, $\mathcal{A}_{\theta_p,0}$ corresponds to the area enclosing 90% of the total power of the quad located at θ_p cone at best focus. a, b and $c \in \mathbb{R}$ are parameters which are specific to each θ_p cone. Note that $a, b > 0$, when $c < 0$. Our results match very closely with the experimental data as the points follow the fits. These are then used to perform our SSS simulations.

4.4 3D CBET radhydro simulation analysis of the SSS shots

4.4.1 Hydrodynamics comparison

4.4.1.1 High intensity shot: N190204-003

In this PDD experiment, a 1100 µm radius deuterated plastic target was irradiated by 184 laser beams having a total energy of 411 kJ with a peak intensity of 1.0×10^{15} W/cm^2

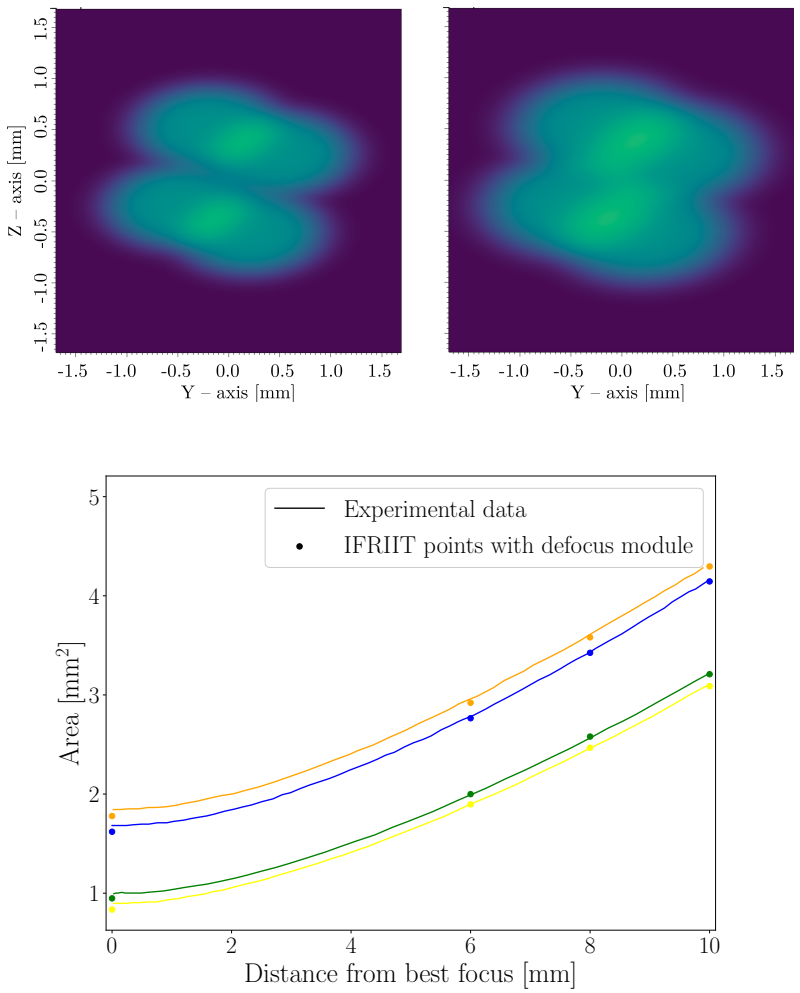

Figure 4.5 – (top) A slice of the laser field at $x = 10$ mm for a quad at $\theta_p = 50°$ in the case where defocus was (right) and was not accounted for (left). (bottom) Evolution of the area enclosing 90% of the total quad power as a function of distance from best focus. It is a validation of the NIF spots characterisation with defocus. Colours are for the different cone rings. Yellow is for 23.5°, green is for 30.0°, blue is for 44.5° and orange is for 50.0°.

(see Table 4.1). 3D simulations with and without CBET are performed. Measured laser pulses are used for the simulations.

As shown in Figure 4.7 (top), the instantaneous absorption fraction without CBET is of 98%. The lasers in the PDD reach the target with a non-normal incidence angle. Specifically, the laser beams pointing closer to the equator have a higher incidence angle than the ones around the poles, leading to non-symmetrical laser drive. Specifically, more energy is delivered to the equator region, as can be seen in top right figure 4.7. The density of the target is higher toward the equator, resulting from higher ablation pressure caused by increased laser absorption.
On the other hand, adding the effect of CBET shows a large impact in absorption fraction both spatially and temporally (see bottom figure 4.7). The bottom left plot shows that the laser absorption ratio drops to 70% during the laser spike. In addition, the spatial absorption distribution has changed and is still not homogeneous. In this case, the laser energy is predominantly absorbed at the poles, where the laser intensity is lower and where beam overlap is less significant due to the PDD geometry. CBET alters the shape

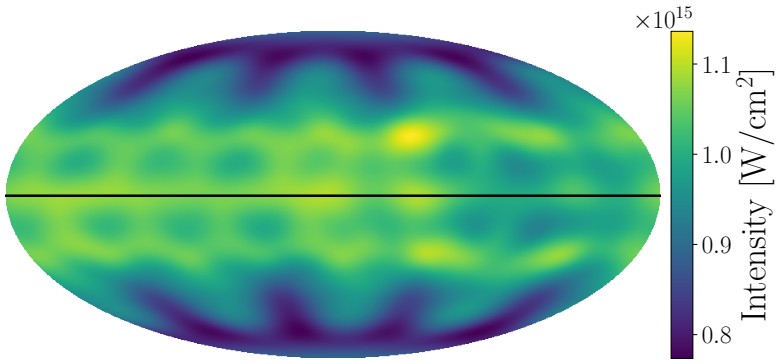

Figure 4.6 – Mollweide projection of the irradiation map for the CH+CD target at the beginning of the laser pulse using the measured beam powers and the pointings of the experiment at 3.6 ns.

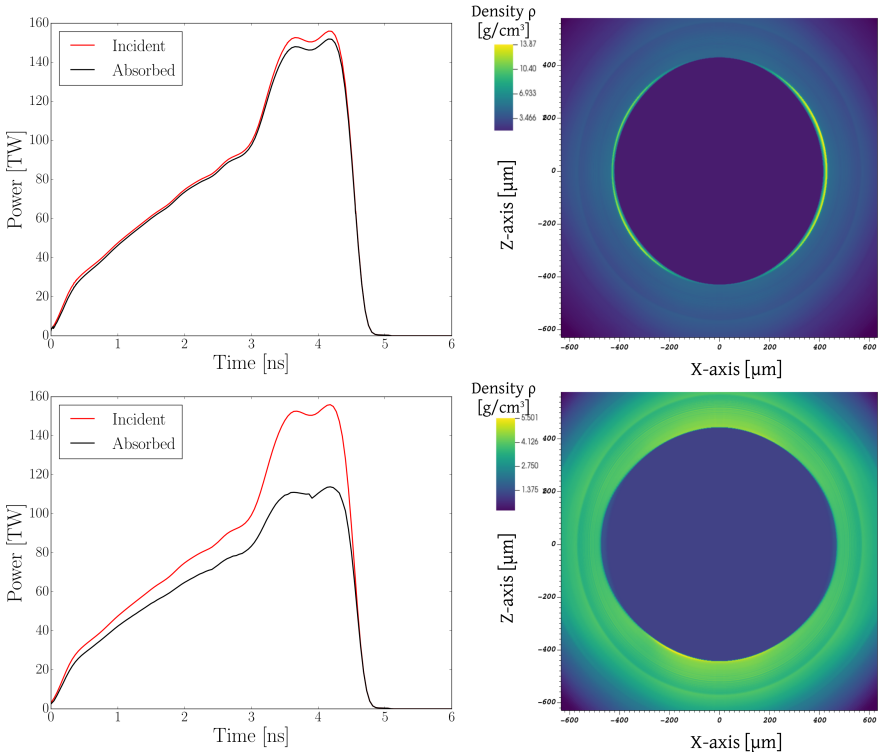

Figure 4.7 – Incident and absorbed laser power as a function of time (left), and a polar slice of the target (right) showing the maximum density location in bright yellow for the high intensity shot at 8.0 ns without and with CBET considered (top and bottom).

of the imploding shock to more oblate and affects the average speed of the shock, slowing it down. At 8.0 ns, the maximum density value has been divided by 2.5 in comparison to a non-CBET case.

In Figure 4.8, the experimental and simulation shock fronts are represented versus time. Both experimental and simulation data relatively agree on the shock velocities. Indeed, as seen in Figure 4.7 bottom, the absorption mainly occurs around the poles, inducing a higher compression and thus a higher shock front velocity in this area. Unfortunately, the pinhole imagers did not catch a shock flash from the N190204-003 shot. The diagnostic window detection corresponds to the grey-hatched surface. Shocks in the

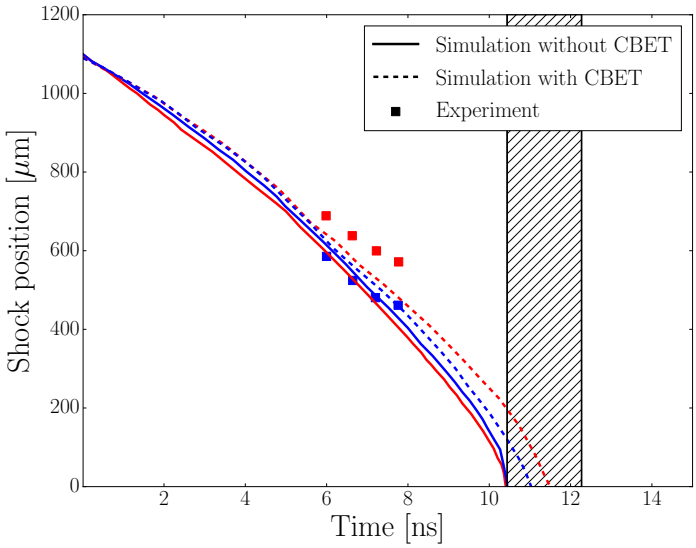

Figure 4.8 – Equatorial (red) and polar (blue) shock positions versus time. Experimental data are represented with squares, *ASTER/IFRIIT* data with plain lines. The imploding target is backlit with a 9 keV Zn source, allowing to radiograph the shock front. The pinhole imager detection window in DIM 90-124 and DIM 0-0 corresponds to the hatched surface. These diagnostics did not catch a shock flash from the low intensity shot N190204-003.

CBET simulation all converge at the center while being under the detection zone. This either means that the experimental shock reaches the center of the target after the end of the diagnostic window, which is not consistent with the simulation results, as both equatorial and polar shock collapse during the diagnostic window; or that the experimental X-ray flash is below the diagnostic detection threshold. Conversely, the simulation without CBET matches neither the measured shock front nor the collapse time. In this experiment involving deuterated solid targets, higher densities and pressures achieved at shock convergence could potentially create the conditions conducive to fusion, resulting in an x-ray flash. In N190204-003, however, while the x-ray flash serves as a valuable diagnostic tool, its observation was not recorded. The experimental data of this shot is not sufficient to draw any conclusions. To continue, we proceed with the analysis of a lower intensity shot: N210519-001.

4.4.1.2 Low intensity shot: N210519-001

For this experiment, a 1063.4 µm radius plastic target is theoretically irradiated by 184 laser beams having a total energy of 474 kJ with a peak intensity of 8.0×10^{14} W/cm^2 (see Table 4.1). During the experiment one quad was off, and only 180 laser beams actually shot on target. 3D simulations with and without CBET are performed with the 180 laser beams. The measured laser pulses are used for the simulations.

Figure 4.11 (left) shows a raw gated x-ray image [105] of the N210519-001 shock at 7.02 ns. These raw radiographies are then fitted with transmission models to reconstruct early backlighter profiles in early time shots. Right figure shows the N210519-001 simulation and has a similar shape but at a later time, 9.0ns.

The absorption fraction without CBET is at 96.5% in average as shown in Figure 4.10 (top). Using Figure 4.12, we track the shock trajectory via the flow diagram (left figure)

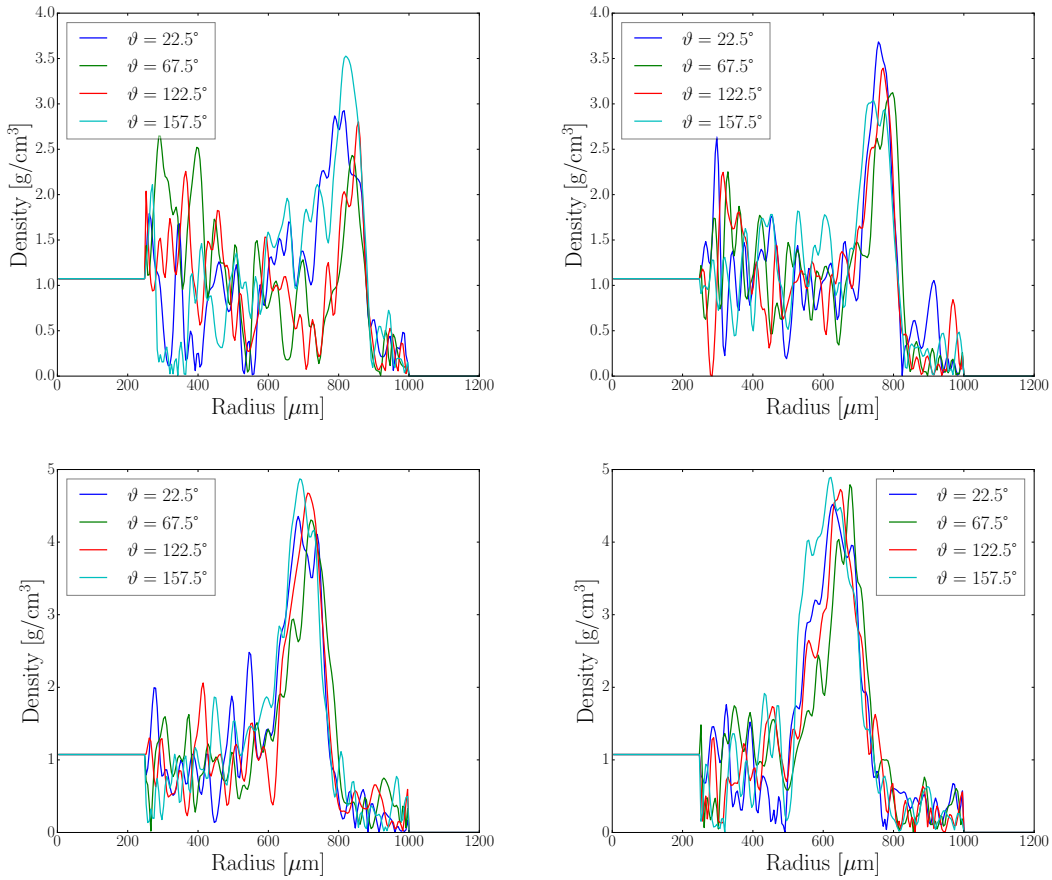

Figure 4.9 – Experimental angular density versus radius plots are depicted at time intervals of $t = 5.1, 6.1, 7.1$, and 8.1 ns, progressing from the top left to the bottom right, for every positive azimuthal angle. To enhance clarity, curves for negative angles are omitted. The density plots presented in Figure 4.14 are averaged across all ϑ angles at each time step.

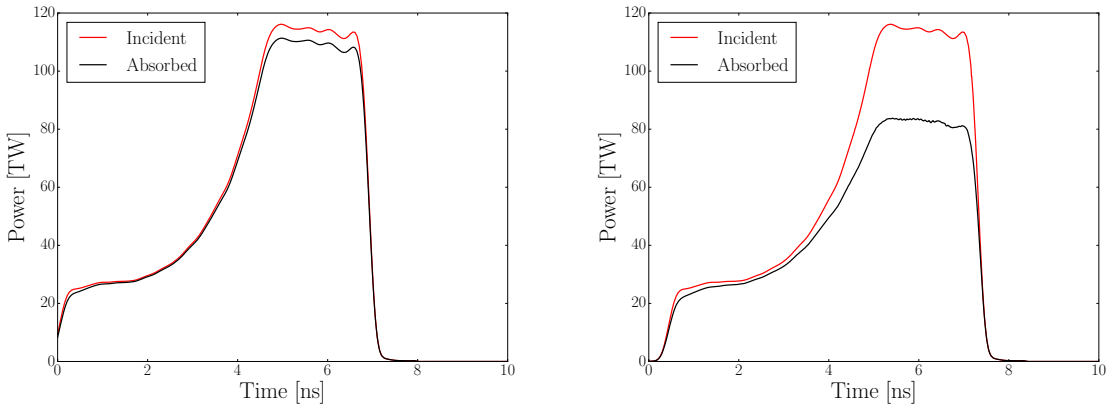

Figure 4.10 – Incident and absorbed laser power as a function of time without and with CBET considered (top and bottom) for the N210519 shot.

and determine its collapse time at the target center by observing the sharp increase in density upon shock arrival. The resulting density-versus-time plot (right figure) at the target center showcases the timing of the X-ray flash relative to shock trajectories. This analysis, demonstrated for a polar shock, is also equally applied to the equatorial region.

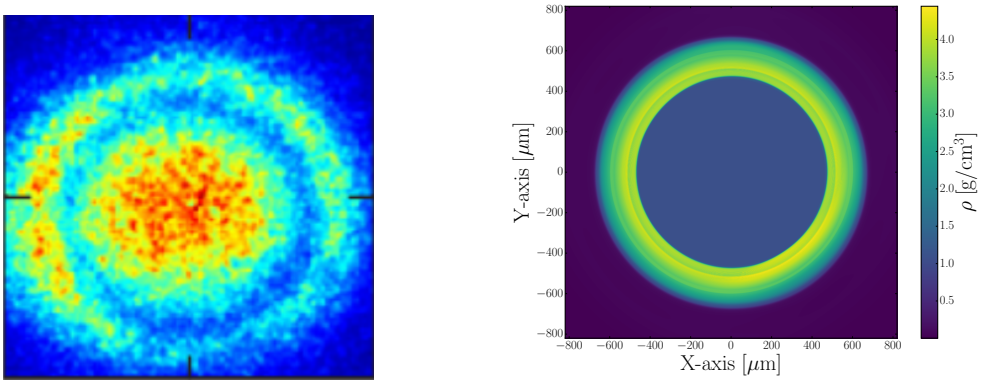

Figure 4.11 – (left) A gated x-ray image of N210519-001 experiment at 7.02 ns. The elliptical shape of the ingoing shock is visible as the dark blue region. (right) Density slice from 3D CBET simulation of N210519-001 at 9.0 ns.

Bang time occurs when the main shock reaches the target centre and the density suddenly increases at 12.5 ns.

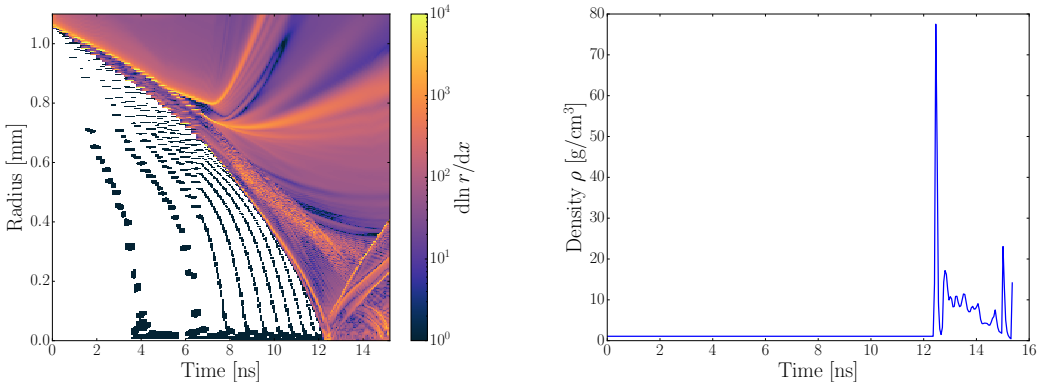

Figure 4.12 – Flow diagram of the N210519-001 shot, shown using a polar slice (left), alongside the temporal evolution of material density at the target center (right). These plots are helpful in tracking shock positions and determining bang time.

As for N190204, when CBET is considered, the total power absorbed by the target drops significantly, here to an instantaneous value of 79.6% (and 72.2% during the spike). It can be seen in Figure 4.13 that both polar and equatorial shocks seem to travel into the target at almost the same speed, collapsing at the center at respectively 12.5 and 12.7 ns. This is in average 200 ps sooner than expected, as the X-ray flash was detected at 12.84 ns according to the experimental data, but still is a solid result as the difference can be explained by the use of specific parameters that were used (see Table 4.2).

The evolution of the radial solid sphere density for different time steps is shown in Figure 4.14. Experimental data is shown with dashed lines and reconstructed from x-ray radiographs. Density profiles are extracted at several azimuthal intervals (see Figure 4.9) and interpolated applying an Abel inversion for a full 2D reconstruction [106]. First, we notice that there is a discrepancy between the experimental and simulation absolute values. For the experiment, the maximum density starts around 2.8 g/cm^3 at 5.1 ns when it increases to 4.2 g/cm^3 at 8.1 ns. On the other hand, the maximum density obtained from

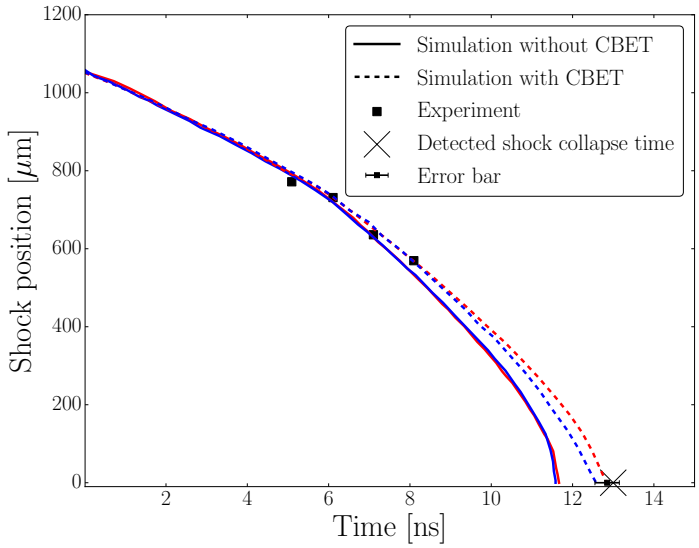

Figure 4.13 – The equatorial and polar shock positions derived from the 3D *ASTER/IFRIIT* simulation are depicted by red and blue curves, respectively. Experimental data is illustrated by dark squares, which are integrated across azimuthal angles and averaged over various polar angles of the diagnostic (ranging from ± 22.5° to 157.5°). The trajectory was captured using a pinhole imager on an x-ray framing camera, with a temporal resolution of 100 ps and a spatial resolution of 30 mm. The dark cross showcases the detected shock collapse time during the experiment.

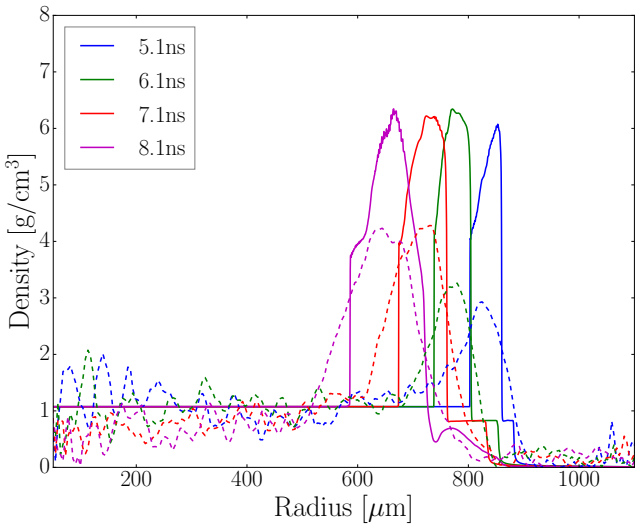

Figure 4.14 – Coloured lines give the angularly averaged density of the plastic target. Each color corresponds to a different time. Experimental data is represented with dashed lines and is reconstructed from radiographs. The position of the experimental shock front is obtained where $\rho = (\rho_0 + \rho_{\max})/2$, with $\rho_0 = 1.074$ g/cm^3 the initial density and $\rho_{\max}$ is the maximum density at each time step. The solid lines show the simulation data. The simulation shock front is obtained where the density gradient becomes infinite.

the *ASTER/IFRIIT* simulation increases very little over time, starting at 6.0 g/cm^3 at 5.1 ns and going up to 6.3 g/cm^3 at 8.1 ns. The experiment takes longer to reach maximum

density compared to simulations, and spike density appears to be lower. The opacity tables used may explain some of the disagreement for the absolute value. Nevertheless, the relative behaviour is still informative as shock positions remain relevant, and show a reasonable match with simulations.

Note that the density from the centre of the target to the shock front tends towards the initial value of the plastic ρ_0 for both experiment and simulation. Figure 4.14 also shows the shock front position/time delay between the experiment and the simulation. Both simulated and experimental shock positions match very closely from 5.1 to 8.1 ns, which gives more credit to Figure 4.13 results.

4.4.2 Offline calculations of N210519-001

Table 4.2 List of offline simulations with *IFRIIT* modifications at 6 ns. The initial parameters used in the 3D *ASTER/IFRIIT* simulation are shown in the first row. CBET Langdon (CBET-L) effect and CBET polarized (CBET-p) were not initially used. A 1.5% IAW saturation value is used, which is lower than expected in NIF experiments [107], meaning that we consider no saturation here. The Coloumb logarithms used are derivated in Lee and More [108]'s and Turnbull, Katz, Sherlock, *et al.* [109]'s papers. The two last rows are performed without CBET and are shown to highlight the laser absorption differences between a CBET and non-CBET simulation.

CBET	CBET-L	CBET-p	L-effect	IAW sat.	Target	Log Λ	$f_{\text{abs}}(\%)$
ON	OFF	OFF	ON	0.015	CH	[108]	**72.24**
ON	OFF	OFF	ON	0.015	""	[108][1]	73.52
ON	OFF	OFF	ON	0.015	""	[109], [110]	71.09
ON	OFF	OFF	ON	0.015/4	""	[108]	72.24
ON	ON	OFF	ON	0.015	""	""	73.77
ON	OFF	ON	ON	""	""	""	68.92
ON	OFF	OFF	OFF	""	""	""	78.21
ON	OFF	OFF	ON	""	Exact[2]		
OFF	OFF	OFF	ON	""	CH	""	95.87
OFF	OFF	OFF	OFF	""	""	""	99.08

Additional offline calculations of the laser spike interaction in N190204-003 at 6 ns were made using hydrodynamics profile from the *ASTER/IFRIIT* simulation. These additional simulations were performed to explore if additional adjustments could significantly alter the absorption (see Table 4.2). In the initial simulation (first row of Table 4.2), considering only CBET and the Langdon effect, which assumes that laser-heated electron distribution functions become super-Gaussian [111], the laser absorption fraction reaches 72.24% at the laser peak intensity. The third row corresponds to the consideration of alternate model for the coulomb logarithm [109]. In this case, we account for the Langdon effect; a laser-frequency (rather than plasma-frequency) dependance in the Coulomb logarithm; and a correction factor due to ion screening effects. Additional details used in third row and in a combination of the fifth and sixth rows show promising results as they both reduce the absorption fraction by a seemingly small enough amount to match the

1. Ionization factor Z slightly modified in comparison to [108]
2. 47.83%C, 51.26%H, 0.48%F, 0.23%N, 0.20%O

data. The mentioned cases respectively account for the Langdon effect on the CBET gain, which increases laser absorption, and for polarized CBET effects. Indeed, CBET is very sensitive to the polarization of the interacting beams and can, in turn, strongly modify each beam's polarization ([70], [71]). These polarization effects can significantly influence CBET in a multi-beam configuration (at it is the case here), and even interactions that are off-resonant can exert a substantial impact on resonant energy transfer [112], thus reducing the laser absorption.

With all the different tests operated, the parameter changes modify little the absorption ratio: $68.92\% \leq f_{abs} \leq 73.77\%$.
We then used absorption laser profiles extracted from the 3D *ASTER* simulations into the 1D *CHIC* code. We can still use these results from offline simulations to estimate the bang time using 1D *CHIC* [35] calculations. According to these simulations, we expect the shock collapse time to lie within the error bar shown in Fig. 4.13. This error bar is obtained from the sensitivity of 1D *CHIC* simulations due to adding and removing certain laser-plasma interaction related packages in *IFRIIT*. The experimental results is well reproduced by the simulation and is within the uncertainty.

Additionally, we also experimented with adjustments such as modifying the EOS and varying the flux limiter value for electron transport, as well as implementing the SNB [33] non-local thermal electron transport model using *CHIC* code. However, these modifications did not yield significant additional changes.

4.4.3 Backscattered light comparison

We now compare the detail of the scattered light in N210519-001 in order to provide additional constraints on the comparison with the experiment. To reconstruct the scattered light intensity on the chamber wall, diagnostic rays are propagated in the plasma once the CBET coefficient calculation is converged. The rays are then propagated from the outer boundary of the simulation domain up to the spherical chamber wall, which gives a spherical map where ray powers are known at discrete points in space. A Delaunay Triangulation Field Estimator (DTFE) is then used to compute the laser intensity from the distribution of ray powers, similarly to what is presented for the case of DTFE planar geometry in Ref. [114]. To do so, we perform offline calculations at different time steps: every 1 ns. For each time step, we extract the scattered intensity map over the chamber wall as a function of longitude and latitude (ϑ and φ). We then compute the intersection between our wall intensity map and the diagnostic data. Thus accessing to the power going through the FABS/SLTD diagnostic apertures for each time step. For each diagnostic, to obtain kJ/sr, we integrate over the time interval and divide by the corresponding solid angle.

A map of the backscattered light over the wall chamber is shown in Fig. 4.15 (top). The amplification contribution from all quads to scattered light is computed and allows to reproduce synthetic FABS and SLTD diagnostics. The light is mainly scattered within a 30°-45° range. This can be seen in Fig. 4.15 (right). Data points obtained with the *DRACO* code [113] are shown, and reveal a strong disagreement for angles close to the pole, and in the absolute values. Whereas *DRACO* seems to overpredict the amount of lost energy, with about twice as much backscattered energy as captured by the experi-

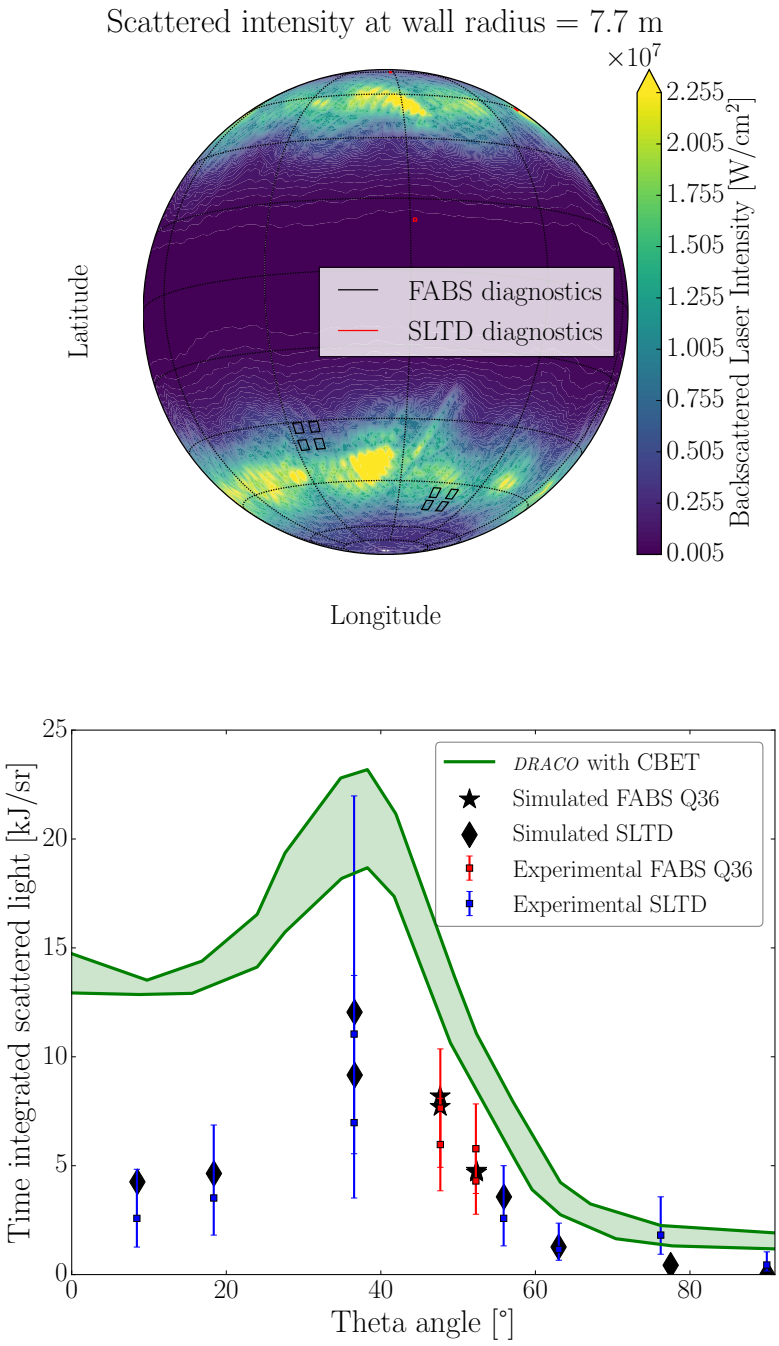

Figure 4.15 – Orthogonal projection of the backscattered laser intensity on the chamber wall at $t = 100$ ps (top). The black and red squares represent the position and surface of the diagnostics. Time integrated backscattered light as a function of the theta/latitude angle (bottom) is also shown. Angles are displayed from 0 to 90 degrees as the system is symmetrical to the equator. The plain crosses represent offline simulation points and the squares associated with their respective error bars are the experimental data points. The colors, red and blue, respectively stand for the FABS and SLTD. The green filled curve corresponds to the maximum and minimum scattered light from the pole at each angle. It is obtained thanks to the code *DRACO* [113] which takes account of CBET thanks to a laser pulse multiplier based model for the absorption.

ment, *ASTER/IFRIIT* appears to give the correct amount of backscatterd laser energy. All the plain crosses match the experimental data, lying within the errors bars, and with the correct trend, giving also correct data points for angles close to the pole and equator. In addition to the different geometry (*DRACO* is 2d axysymmetric), CBET models also differ in their formulation, notably for the lack of caustic field modelling in *DRACO*. The CBET-model accounted in *IFRIIT* seems to give the correct laser absorption (within the error bars), and a correct bang time even though a small discrepancy remains, also in agreemet with results obtained at OMEGA scale [6], [70], [71].

The small discrepancy suggests that other unaccounted hydrodynamics related effects may play a role and modify the shock velocities. Hot electrons are thought to be one of the explanations. For SI, it was predicted that hot electrons could improve the drive efficiency and accelerate the shocks [76], [115]. FFLEX experimental data shows that for N190204-003, with a laser peak intensity $I_L = 10^{15}$ W/cm^2 similar to N210519, the hot electron population has an energy equal to 1.7 % of the total laser energy and a temperature $T_h = 46$ keV. As *ASTER* does not have a hot electrons module, 1D *CHIC* simulations were performed to estimate their effect [116]. According to the experimental data and these simulations, using the same hot electron population with a 1 ns temporal width peaking at 5.75 ns (middle of the laser peak intensity), it speeds up the shock and reaches the center of the target $\approx$ 200 ps earlier. Nevertheless, 1D simulations tend to overestimate the impact of hot electrons. Also, in the NIF solid target experiment, there is uncertainty in the measurement of the hot electron population. The effect of HEs on the shock velocity in these experiments was investigated to be of the order of $\sim$ 200 ps in Ref. [99]. However, these simulations may overestimate the HE effect due to neglecting large-angle collisions ([117], [118]) and a more robust method as implemented in Refs. [117], [118] could be considered and added to *ASTER*.

4.5 Conclusions

The CBET-model implemented in *IFRIIT* coupled inline with *ASTER* has been studied at the ignition/NIF scale by comparing shock positions and scattered light maps in solid-sphere coupling experiments. The laser absorption in the coupled code matches the experimental results from the FABS and SLTD. The shock time collapse remains slightly off, but can be improved by using a more detailed and complete model for CBET that is already included in *IFRIIT* (polarized CBET + Langdon effect on CBET), that decreases the laser absorption. These additional phenomena were not first included for computational time concerns (indeed polarized CBET demands 4 $\times$ more computer resources than CBET alone). Finally, the use of a different model for Coulomb logarithm could play a large role in laser absorption as was proposed in Ref. [109]. This model accounts for Langdon effect, screening corrections and a Coulomb logarithm depending on the laser frequency rather than the plasma frequency and has alrady shown accurate results when compared to measurements performed on OMEGA. Building on these results, the *ASTER-/IFRIIT* code can be used to study the physics of SI for ICF at full scale with confidence.

Chapter 5

Study of innovative beam ports arrangement geometries to assist in the design of future direct-drive laser facilities

5.1 Motivations

The study of laser irradiation homogeneity for ICF is crucial for achieving efficient and reliable fusion reactions. In direct-drive ICF experiments, high-power laser beams are directed onto a fuel target initiating fusion reactions through compression and heating. However, any non-uniformity in laser intensity across the target surface can lead to asymmetrical compression, causing instabilities and reducing fusion yields. Optimising laser irradiation homogeneity is thus essential for enhancing fusion performance and achieving ignition. Detailed studies on laser energy distribution, spatial and temporal variations, and their effects on target compression are necessary to develop strategies for improving fusion efficiency and mitigating challenges associated with non-uniform irradiation. Additionally, the study of laser beam port geometries in ICF is vital for delivering high-power laser energy efficiently to the target. Additionally, optical smoothing techniques play a crucial role in high-power laser systems by serving as precise instruments for fine-tuning the properties of laser beams. Their primary function is to attenuate nonlinear LPIs and mitigate hydrodynamic instabilities, thus ensuring the stability of the target.

Optical components are also used to control and shape laser beams, influencing factors such as beam alignment, focal spot size, and energy distribution. Scientists aim to optimise beam port designs to minimise energy losses, mitigate instabilities, and ensure uniform irradiation of the target surface, thereby advancing the precision and reliability of laser-driven fusion experiments towards the goal of sustainable fusion energy production. Future direct drive facilities will necessitate thorough consideration of all these diverse irradiation aspects to ensure optimal operation and performance.

So far, beam arrangement studies delved into the direct-drive illumination schemes were mainly emphasising geometrical aspects [8]–[10]. Yet, ensuring even illumination on a fuel pellet remains a key challenge in ICF, and experimental errors may be the main source of inhomogeneities [11], [119]. The quality of an illumination can be described by

the root-mean square deviation:

$$\sigma^2_{\text{rms}} = \frac{1}{4\pi\langle I\rangle^2}\int |I(\theta,\phi) - \langle I\rangle|^2 \mathrm{d}\Omega, \tag{5.1.1}$$

which represents the angular nonuniformity of a laser intensity distribution, $I(\theta,\phi)$, on a sphere. We define also the average intensity $\langle I\rangle = \int I(\theta,\phi)\mathrm{d}\Omega/4\pi$. To achieve ignition and high gain, a high illumination uniformity of about 1-2% rms is generally required [120], [121].

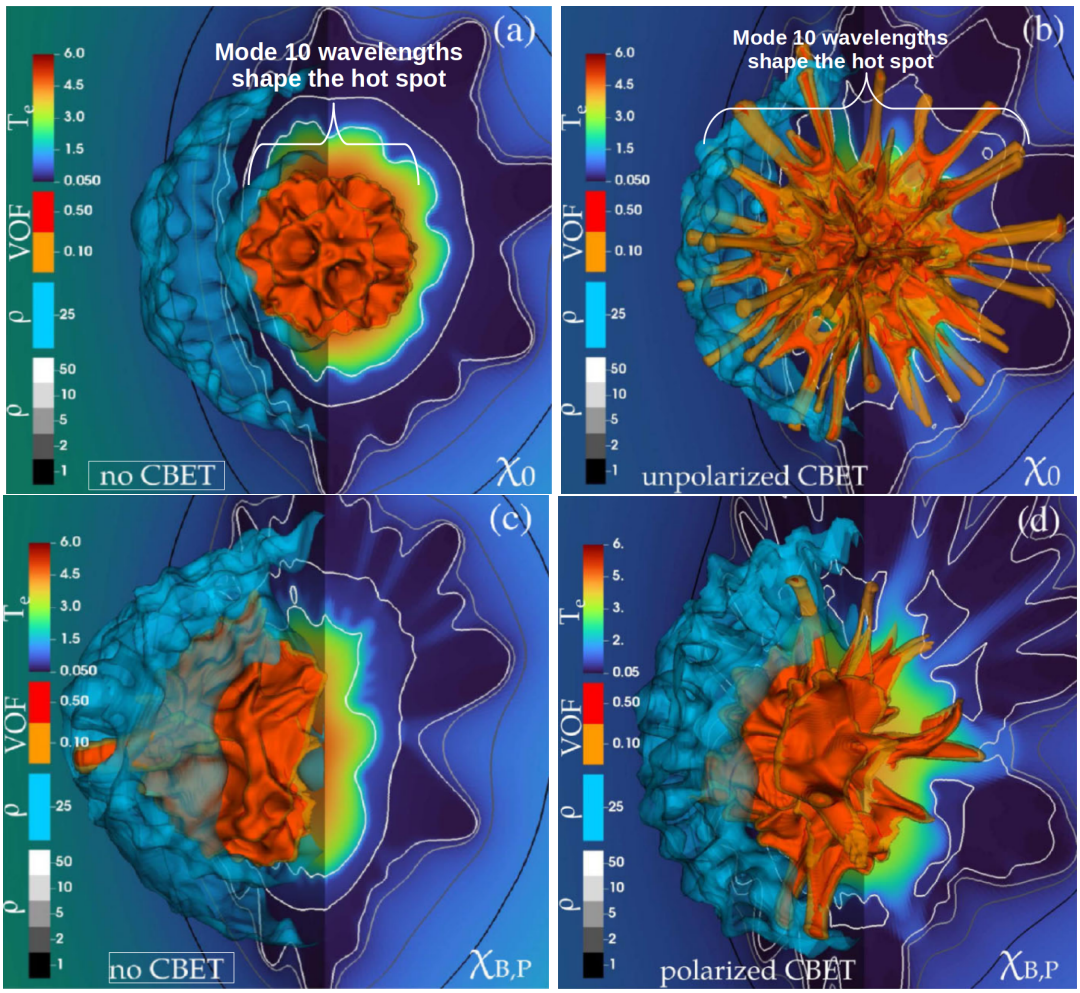

Figure 5.1 – Target hot-spot electron temperature (colored background, kilo-electron-volts), 10% and 50% volume fraction of DT gas (orange and red volume contours, respectively), 25 g/cc density isovalue (light blue volume contour), and 1, 2, 5, 10 and 50 g/cc isocontours (black to white contour lines). χ_0 corresponds to an idealised case with no system errors. $\chi_{B,P}$ uses beam mispointing and power imbalance measures. Figures were taken at bang time for shot 94343. Figures courtesy of A. Colaïtis [122].

Currently, the largest direct-drive laser facility is located at the Laboratory for Laser Energetics (LLE), Rochester, USA. The laser system, OMEGA (Ω60) operates with 60 laser beams in the 30-kJ range. In experiments, due to the limited number of beams, CBET and additional systematic experimental errors, uneven laser irradiation on the target surface results in an irregular shell compression, leading to a decrease in implosion

performance, or even worse, to the puncturing of the target in-flight. To give an example, shot 94343 was realised with close to current best Ω60 laser performances, meaning minimal systematic errors. The implosion for shot 94343 was carried out in a standard setup for Ω60. Both experimental and simulation results agree on showing that the target is punctured due to high low-modes (long wavelength) amplitudes (see figure [122], with simulations matching observables for flow at stagnation. It can be seen in Figure 5.1(c-d) how such system errors can drastically modify the hot spot shape. Effectively controlling and mitigating low-modes perturbations is a critical step towards enhancing implosion performance, particularly in direct-drive [123], [124]. These low modes induced by systematic errors can never be eliminated entirely.

In this chapter, we present studies about the irradiation and low-mode perturbations in 3D at MJ scale (also called "ignition" or NIF scale). While the stability of direct-drive targets to low mode was analysed in the past on the basis of 2D simulations, only 3D simulations can capture correctly the effects of beam imbalance, beam mispointing and target offset errors. We first perform optimisation studies of innovative chamber designs [72], [119], [125] (where the beam ports are arranged differently) using a solid sphere illumination thanks to the inverse-ray-tracing code *IFRIIT*. We sample and select free parameters – the super-gaussian order and the spot size of the laser that reduce the most the initial laser perturbations on target. Robustness to systematic low-mode asymmetries is then evaluated between the chamber geometries using gaussian sampling and statistical methods. We also assess how the in-flight stability of the target is affected for different ignition schemes.

5.2 Designs overview

Three beam port geometries are used for this study. These geometries give different approaches to pave a sphere in a regular manner. After describing the method for each, we select for each design a chamber with ~ 70 beams for comparison.

5.2.1 Charged particle method design

The charged particle method [119], [126] (CPM) is mostly a simple numerical method which achieves highly uniform illumination. It does not rely on geometrical aspects, like Platonic or Archimedean solids, and is applicable for a fictitious number of beams. The method works by randomly distributing N_b charged particles over the surface of a sphere. Each particle will repel each other with a Coulomb force, according to the following dimensionless equation of motion:

$$\frac{\mathrm{d}^2\hat{\mathbf{r}}_i}{\mathrm{d}t^2} = \sum_{j=1(j\neq i)}^{N_B} \frac{\hat{\mathbf{r}}_i - \hat{\mathbf{r}}_j}{|\hat{\mathbf{r}}_i - \hat{\mathbf{r}}_j|^3} - \frac{\mathrm{d}\hat{\mathbf{r}}_i}{\mathrm{d}t}, \tag{5.2.1}$$

The last term of Eq. 5.2.1 acts as a damping term stabilising the system. The goal here is to find the lowest potential energy of the N_b-body system at $t \to \infty$, when the potential energy variation between two succeeding time-steps is lower than 10^{-15}. The beam ports locations are then extracted from the resulting N_b triplet coordinates. In summary, the beam ports locations are obtained via a self-organizing system solving a N_b-body problem, that does not depend on the initial configuration.

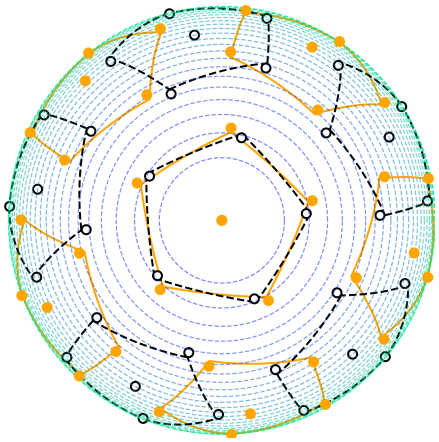

Figure 5.2 – Perspective view of a unit sphere with the M72 geometry. Orange filled circles and dark empty circles respectively denote northern and southern hemisphere beam ports location. Coloured lines represent latitudes for better perspective. Points are projected on the equatorial-plane normal to the view axis ($z-$axis). The laser beams are pointing towards the chamber center.

Generally, uniformity improves with N_b, however there are some cases which have exceptional uniform illumination. These configurations are called M24, M48, and M72, where the notation "MX" stands for the configuration obtained with $N_b = \mathrm{X}$ charged particles. They show local minima of the irradiation nonuniformity (Fig.8 in [119]). In this work, our results are focused on M72. Its structure is particularly symmetric such that the (θ_i, ϕ_i) data points can be expressed in a compact manner as follows:

$$\mathrm{M72}\ \begin{cases} \theta_{i+7m+14\ell} = (-1)^m\theta_i + 180m, \\ \phi_{i+7m+14\ell} = (-1)^m\phi_i + 88.8328m + 72\ell, \\ i = 1, 2, \ldots, 7, \quad m = 0, 1, \quad \ell = 0, 1, 2, 3, 4, \\ (\theta_{71}, \phi_{71}) = (0, 0), \quad (\theta_{72}, \phi_{72}) = (180, 0). \end{cases} \tag{5.2.2}$$

The majority of patterns derived from the CPM exhibit the benefit of lacking pairs of points that are antipodes of each other. This characteristic is highly advantageous for optical system protection. Figure 5.2 shows the arrangement found for beam ports using the CPM. A very high symmetric pattern can be seen as the beam ports form 12 pentagons with an extra beam port at their center. The centres are equidistant to the vertices forming the corresponding pentagons. Note that there is no other regular manner to link the beam ports between each other: each point is equidistant to either one or five other points. The advantage in this method is its simplicity as, being an N_b-body problem, an odd number of beams can be investigated, and can be applied for any arbitrary N_b, in contrast to configurations based on geometrical aspects.

5.2.2 Spherical t-sphere design

Ref. [125] proposes a new class of beam configurations for symmetric-direct-drive inertial confinement fusion laser systems. These configurations are based on spherical t-designs that are studied in spherical design theory in mathematics [127]. According to [120], an important strategy to keep in mind in designing an irradiation system is to remove all spherical modes below a certain number. The spherical t-designs apply this method, eliminating all modes $l \leq t$. Such a design consist of a set of points $p = 1, ..., N_b$ on a unit sphere with coordinates $(x_p, y_p, z_p) = (\sin\theta_p\cos\phi_p, \sin\theta_p\sin\phi_p, \cos\theta_p)$ that satisfy:

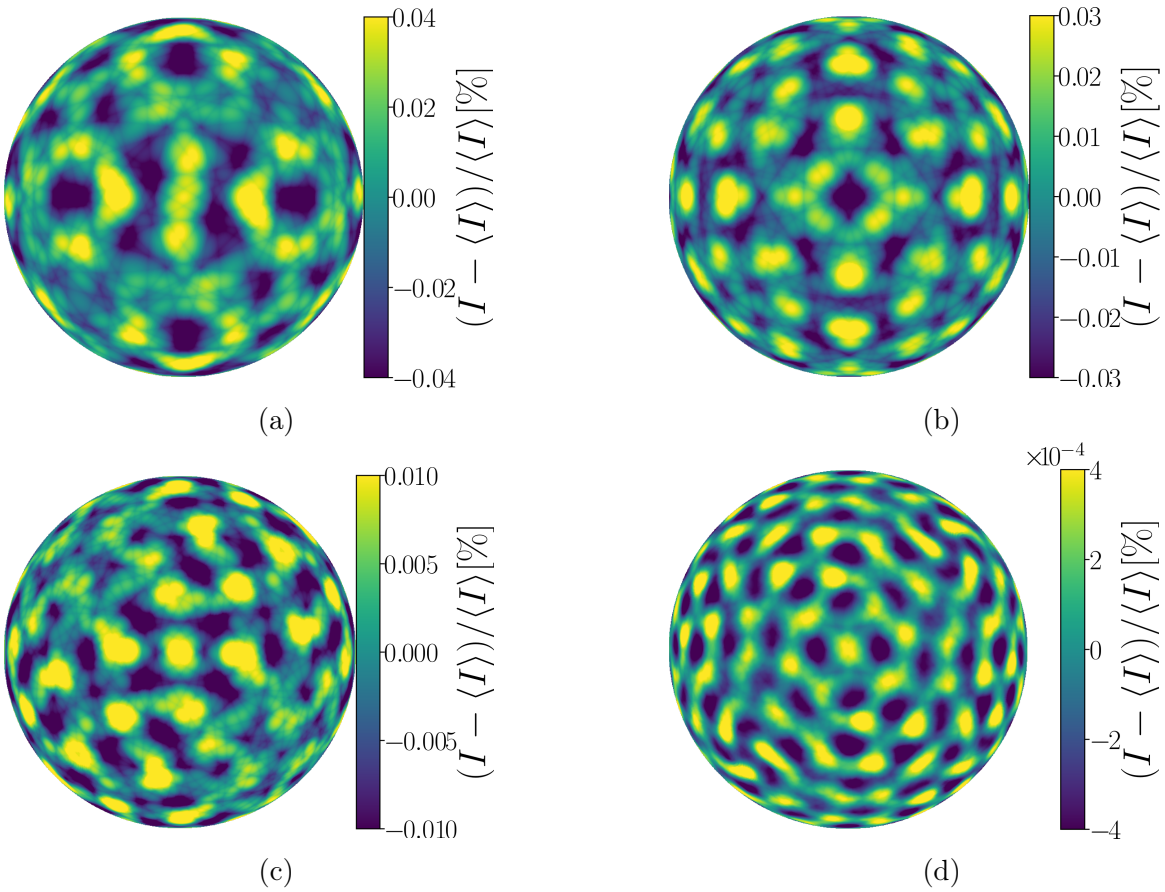

Figure 5.3 – Orthogonal projections of intensity distributions for designs $T72$ (a), $13t96$ (b), $14t108$ (c), $21t240$ (d). The more laser beams, the higher is the peak mode and the better is the irradiation uniformity.

$$\frac{1}{N}\sum_{p=1}^{N_b} x_p^a y_p^b z_p^c = \frac{1}{4\pi}\int x^a y^b z^c \, \mathrm{d}\Omega, \tag{5.2.3}$$

where $(x, y, z) = (\sin\theta\cos\phi, \sin\theta\sin\phi, \cos\theta)$ and powers a, b, c are integers satisfying $a + b + c = k$, with $k = 1, 2, , ..., t$. To fulfil this criteria, a certain condition on the number of beams N_b can be found. For N_b large enough, it yields:

$$N_b \geq t^2/2 \tag{5.2.4}$$

Examples will follow with $N_b = 12m$, with $m = 1, 2, 3, ...$ increasing up to $N_b = 240$. For $t = 11$, it results that $N_b = 72$.

Future ICF laser systems designed for direct-drive configurations will aim to enhance uniformity by increasing the t in t-designs with the minimal number of beams N_b. As t increases with the number of beams as $t \propto \sqrt{2N_b}$, the pursuit of t-designs with the smallest N_b for a given t represents a fundamental challenge within the spherical design theory.

Figure 5.3 shows the intensity distributions for four spherical designs. The $N_b = 12m$ configurations with higher number of beams have intrinsic symmetry groups and show symmetric intensity distribution patterns. Observe the significant decrease in the

amplitude of nonuniformity with the parameter t, as indicated by the colorbar ranges in Fig. 5.3.

In this manuscript, the design called '11t72' is the only spherical t-design to be studied more deeply. This choice is made due to its realistic number of laser beam ports, slightly exceeding that of the Ω60 facility. It will be denoted T72.

5.2.3 Icosahedron design

At this time, irradiation systems for direct-drive have been designed according to the topological structures of the 13 Archimedean solids [128] which are highly symmetrical. The Ω60 chamber geometry is one of them. This polyhedron is constructed from an icosahedron, with the 12 vertices truncated (cut off) such that one third of each edge is cut off at each of both ends. This creates 12 new pentagonal faces, and replaces the original triangular faces with 20 regular hexagons.

Another way to pave a sphere is to start again with an icosahedron and form a geodesic

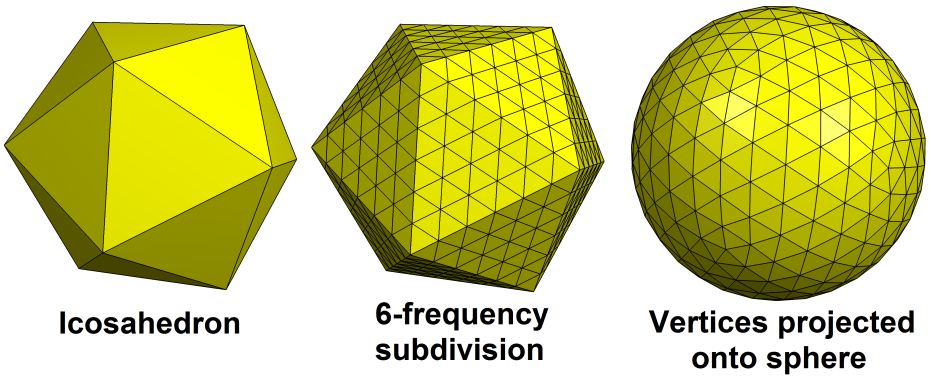

Figure 5.4 – Example of a geodesic icosahedron (120 faces) via the subdivision of an initial icosahedron. Image taken from Wikimedia Commons.

polyhedron. This way a new class of high-performing beam configurations can be achieved. Geodesic icosahedra constitute a category of polyhedra generated through the subdivision of icosahedron's faces and the projection of the resultant vertices onto the surface of a sphere. Geodesic polyhedra are a good approximation of a sphere [129]. They result in a beam chamber with $20 \times N_{\text{sub}}$ laser beams arranged in a highly symmetrical way. In this manuscript, we focus only on a geodesic icosahedron with 80 faces (each of the initial triangular faces is subdivided into 4 smaller triangles). This geometry is denoted as 'I80'. This geometry allows a realistic number of laser beam ports, slightly exceeding that of the Ω60 facility that is comparable to the other geometries. The subdivision process is shown in figure 5.4.

5.3 Initial optimisation study

5.3.1 Spherical harmonics decomposition of the laser intensity on target

We have selected 3 different chamber geometries that are based on different considerations and feature similar number of beams. As these systems exhibit spherical symmetry,

it can be useful to use spherical harmonics to describe the laser intensity on target. The spherical harmonics decomposition of the normalised laser intensity can be written as:

$$\begin{aligned} f(\theta,\phi) &\simeq \sum_{l=0}^{l_{\max}} \sum_{m=-l}^{+l} C_{lm} Y_{lm}(\theta,\phi), \\ C_{lm} &= \iint f(\theta,\phi) Y^*_{lm}(\theta,\phi)\sin(\theta)\mathrm{d}\theta\mathrm{d}\phi, \end{aligned} \tag{5.3.1}$$

with Y_{lm} the spherical harmonics basis vectors, C_{lm} its corresponding coefficients and l, m integers. For a given value of l, there exist $2l+1$ independent solutions of this form, one for each integer m with $-l \leq m \leq l$. We can also define the rms deviation for a single mode l (σ^l) and the total rms (σ^*_{tot}) of a laser intensity distribution over a sphere:

$$\begin{aligned} \sigma_l &= \sqrt{\frac{1}{4\pi} \sum_{m=-l}^{+l} C_{lm} C^*_{lm}}, \\ \sigma^*_{\mathrm{tot}} &= \sqrt{\sum_{l=0}^{l_{\max}} \sigma_l^2}. \end{aligned} \tag{5.3.2}$$

These equations are equivalent to Equation (5.1.1). They will help us determine the uniformity of a specific design The maximum $l-$mode is determined by the area of the size of the smallest polygonal on the solid, with respect to the total area (4π).

5.3.2 Relevant laser parameters to scan: super-gaussian order and laser radius at $1/e$

The *IFRIIT* ray-tracing code is used offline (i.e. with no hydrodynamic evolution) on ignition scale targets (mm-size). It is assumed that the laser beams are associated with a set of irradiation parameters and all the beam axis are directed towards the sphere center. A three-dimensional numerical tool has been developed to assess the uniformity of the capsule illumination based on spherical harmonics decomposition. These calculations account only for the direct illumination of the capsule without refraction. Thus, these results only apply during the first stages of the laser pulse when the laser imprints its irradiation defects on the target. It corresponds to the time at which the target is most sensitive to high and low mode asymmetries. A given irradiation scheme is characterised by its own intrinsic nonuniformity, which is a function of the laser power profile [130]. For each design, it is therefore mandatory to first minimise the intrinsic nonuniformity.

Many laser parameters exist, and it is necessary to limit the number of possible combinations to a manageable number. Thus, a first approach is to consider and select different laser spatial profiles. For more simplicity, we consider a super-gaussian shape shape for the laser spots, where the spatial laser intensity $I(x,y)$ follows:

$$I(x,y) = I_0 \exp\left[-\left(\frac{\sqrt{x^2+y^2}}{R_{\mathrm{las}}}\right)^{S_G}\right], \tag{5.3.3}$$

Table 5.1 optimised geometry designs with their respective laser parameters and associated minimum RMS.

Design	$\sigma^*_{\text{tot}}(\%)$	Beam-target intersection (%)	S_G	R_{las}/R (%)
Ω60	0.456	99.6	5.2	72.9
$M72$	0.047	99.6	4	70
$\boldsymbol{T72_2}$	**0.023**	**98.2**	**2**	**50**
$T72_4$	0.029	98.8	4	75
$I80$	0.125	95.3	3	75

with I_0 the peak laser intensity, and we consider that $I_0 = 1$ TW for each laser beam. The x and y axis are orthogonal axis in the focal plane of each beam, so that $I(0,0) = I_0$ and peak intensity is reached at the centre.

An optimisation study can then be performed on a restricted data space, with $S_G = \{1,2,3,4,5,6,7\}$ and $R_{\text{las}} = \{40,45,50,...,100\}$ % R (R, the initial target radius). Thus, the number of simulations is $N = \#S_G \times \#R_{\text{las}} = 7 \times 13 = 91$ per each geometry design. For each of these simulations, we make use of the spherical harmonics decomposition of the laser field on a so-called 'solid' sphere, *i.e.* no plasma and no target shine through. Then, the total rms irradiation nonuniformity σ^*_{tot} is calculated as the square-root of the sum of each Legendre mode amplitude. The lower σ^*_{tot}, the more uniform the studied design. This method is equivalent to calculate the standard deviation of the laser intensity over the surface of a solid sphere as written in Equation (5.1.1). Once done, we can compare rms and select the lowest for further study. To summarise, for each design we use two beam spatial parameters (S_G, R_{las}) that minimises the intrinsic nonuniformity σ^*_{tot}, resulting in the most uniform initial laser irradiation on target with a specific design.

5.3.3 Results of the scan

In Figure 5.5, the results of the scan are presented. With this plot, we can estimate and find the optimum laser spatial parameters to minimise the intrinsic non-uniformity of a design. Figure 5.5 (a) shows that for M72, the two parameters that give the most uniform illumination on target are in the area where $S_G \simeq 3-4$ and $R_{\text{las}} \simeq 65-75\%$ R. In the case of $I80$, Figure 5.5 (c) explicitly shows that the most beneficial parameters lie within the range $S_G \simeq 3-4$ and $R_{\text{las}} \simeq 70-85\%$ R. The spherical t-design $T72$ shows a different behaviour (see Figure 5.5 (c)). There seems to be two different minima with very different laser parameters. The first one lies in a very narrow space where $S_G = 2$, and $R_{\text{las}} \simeq 50-55\%$. The second one lies within the range where $S_G \simeq 4-6$ and $R_{\text{las}} \simeq 75-85\%$ R, which is more similar to the other designs. Having very different laser spatial parameters, these two configurations are studied along this manuscript and are denoted respectively as $T72_2$ and $T72_4$.

Table 5.1 shows the optimised parameters minimizing the rms for the different geometries, alongside typical Ω60 parameters and rms. If we compare Ω60 with the best performing design, $T72_2$ shown in bold characters, we can see that with only 12 more laser beams than Ω60, we succeed to divide the rms by 20, so that $\sigma_{\text{tot, }T72_2}/\sigma_{\text{tot, }\Omega60} \approx 0.05$. We aim for an irradiation uniformity of 1% to 2% which should not be exceeded [120], [121]. Here, all geometry designs lie below the threshold value as $0.023\% \leq \sigma^*_{\text{tot}} \leq 0.125\%$.

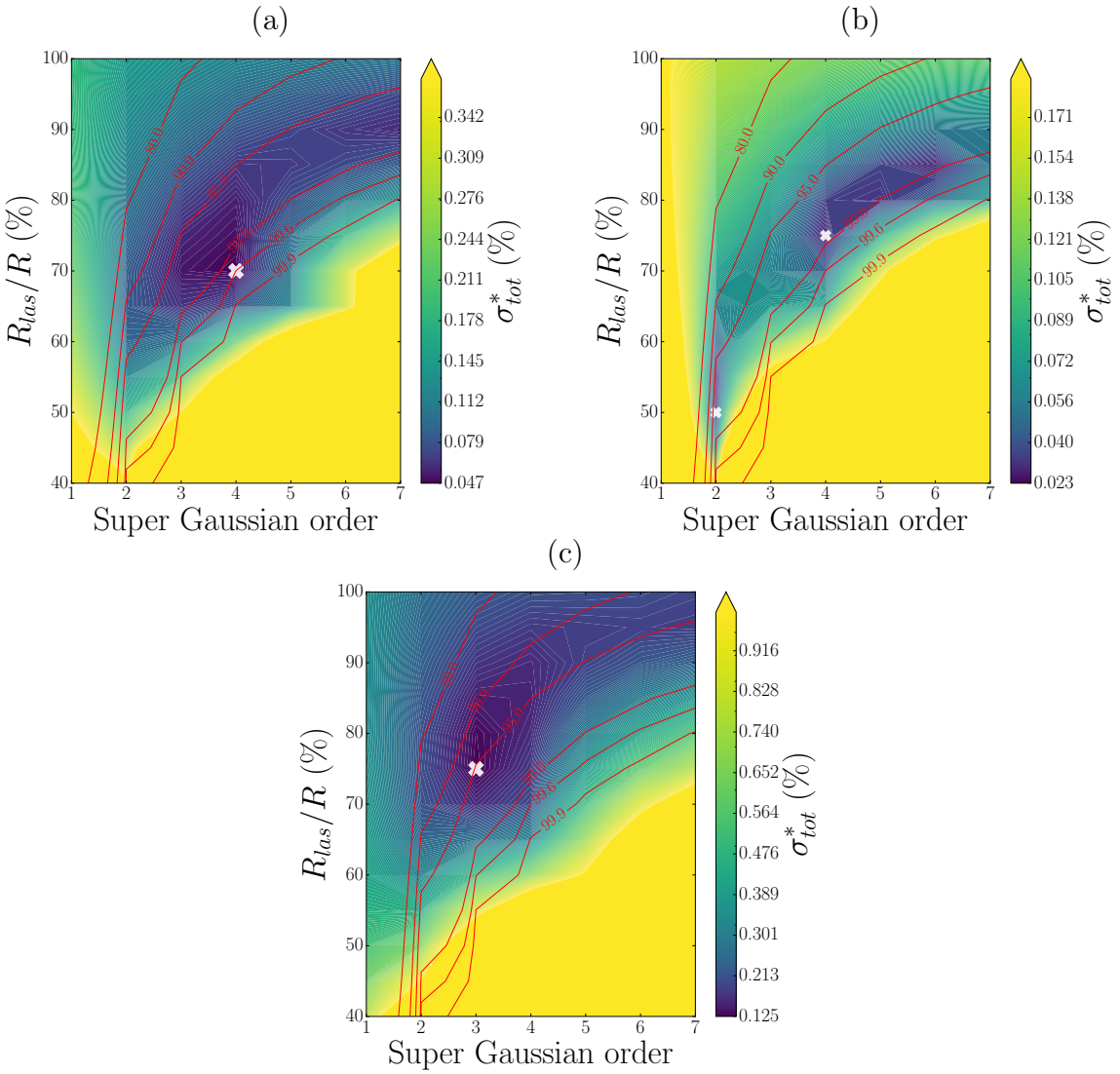

Figure 5.5 – Contour plots showing the optimisation study for M72 (left), $T72$ (middle), $I80$ (right). The colorbars range from the minimum $\sigma^*_{\text{tot,min}}$ to $8\sigma^*_{\text{tot,min}}$ for each specific design. Points above maximum are displayed as the colour corresponding to the maximum on the colorbars. Optimised points reported in Table 5.1 are shown here with white cross markers. The red lines correspond to contours of beam-target intersection in percentage.

The design with the most beams, $I80$, shows less promising results as its optimised rms is at least three times larger than any other geometry designs (it is even four to five times larger than $T72_2$ and $T72_4$). This is due to the fact that CPM and spherical t-design are based on minimisation and mathematical approaches rather than only considering iterative division of the faces of a platonic solid. Local minima, as seen in the CPM for configurations with $24 \times n$ beam ports (n a positive integer), can emerge from these methods [119].

Top Figure 5.6 shows the different irradiation patterns between $\Omega 60$ (left) and $T72_2$ (right). One can notice that $\Omega 60$ has very symmetric irradiation structures of a medium range (top left). These are significant of $\Omega 60$'s mode $l = 10$ that is completely imposed by the truncated dodecahedron geometry. The associated spherical harmonics decomposition shows that the Legendre mode $l = 10$ is predominant, peaking at an amplitude $\sigma_{10} \geq 0.4\%$. As a result, this mode completely imposes its amplitude to the total RMS

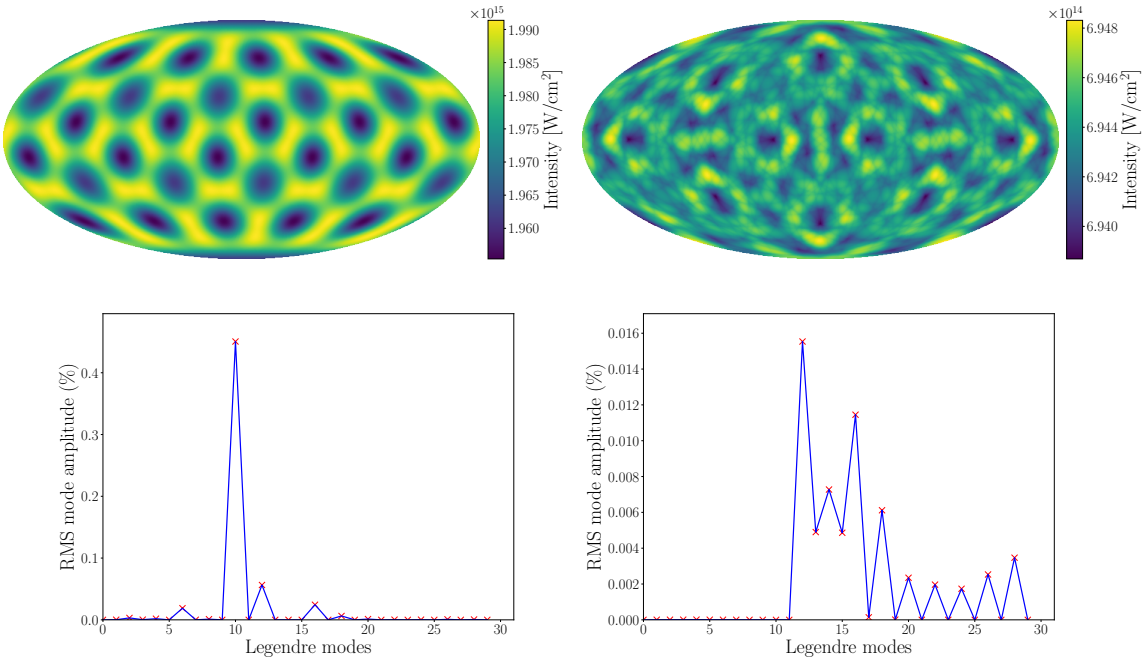

Figure 5.6 – Comparison between Ω60 (left) and $T72_2$ (right) irradiation maps with their corresponding spherical harmonics decomposition.

as we have $\sigma_{\text{tot, }\Omega 60} \simeq 0.456\%$. On the other hand, if we analyse $T72_2$, one can notice that there are smaller structures in its irradiation pattern. This is a characteristic of medium/high modes to have such small wavelengths and this is what appears once we look at the the spherical harmonics. First, one very noticeable aspect is that the spherical t-design strategy works as all modes from mode $l = 0$ to mode $l = 11$ included are completely removed, their amplitude is negligible. The maximum amplitude is reached for mode $l = 12$ with a peak amplitude of $\sigma_{12} \simeq 0.016\%$, which is much lower than mode $l = 10$ of Ω60. The other successive modes also have a non-negligible amplitude but remain below $\sigma_l \leq 0.010\%$, so that in the end $\sigma_{\text{tot}} = 0.023\%$. From an idealistic point of view then, considering no source of experimental errors whatsoever, the $T72$ designs seem to be the best suited for the next direct drive facilities.

Nevertheless, we can have a look on the $T72_2$ design for 2 different cases and see the behaviour of the illumination patterns: a first case with a very small mispointing error of $\Sigma_{BM} = 10^{-3}\%\ R$ and a second with a larger mispointing error of $\Sigma_{BM} = 4.0\%\ R$. With beam mispointing, lasers do not intersect the target exactly where they are supposed to and so the irradiation pattern is modified and homogeneity is compromised. In Figure 5.7 are shown the irradiation maps and spherical harmonics decomposition for the two different cases of $T72$ previously just discussed. The case with small mispointing is displayed on the left, and the case with more significant mispointing error is displayed on the right. If we analyse the figures for the low mispointing error case (left), we do not see not much difference with the previous Figure 5.6 (right), in particular comparing the irradiation maps. Irradiation pattern and minimum and maximum intensities remain identical. Nonetheless, one can start to see a small difference by looking at the spherical harmonics decomposition (bottom left). Indeed, it shows low modes ranging from $l = 1$ to $l = 6$ roughly that are starting to appear. Their amplitude at such mispointing error is still very low (does not exceed 0.001%) but is noticeable. The total RMS remains

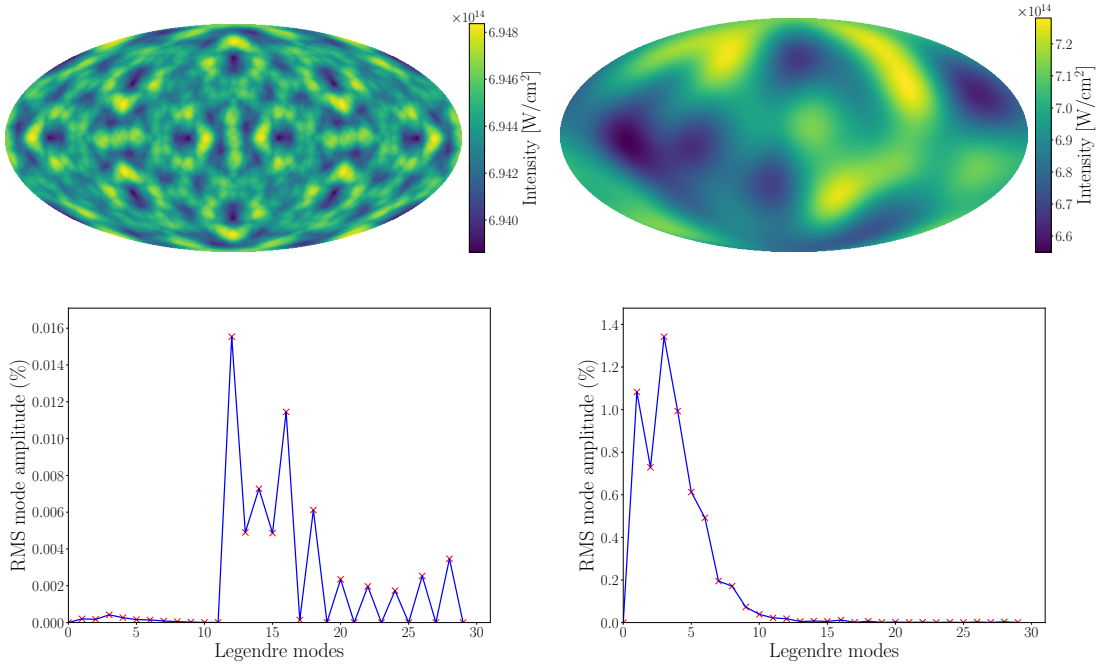

Figure 5.7 – $T72_2$ design in case where $\Sigma_{\text{BM}} \approx 10^{-3}\%\ R$ (left) and where $\Sigma_{BM} \approx 3.9\%\ R$. It results in an appearance of Legendre modes $l \leq 10$ that grow rapidly with mispointing error.

the same, $\sigma_{tot} = 0.023\%$. On the other hand, the right figures 5.7 with $\Sigma_{\text{BM}} \approx 3.9\%\ R$ show a very different behaviour. First, irradiation patterns are drastically different. Long wavelength structures are very visible (large dark blue and bright yellow zones) and are caused by low modes. Moreover, minimum and maximum intensities have been extended. In the idealized case, extreme values of the intensity were $\min(I) = 6.939 \times 10^{14}$ W/cm^2 and $\max(I) = 6.948 \times 10^{14}$ W/cm^2. Now, we have $\min(I) = 6.550 \times 10^{14}$ W/cm^2 and $\max(I) = 7.281 \times 10^{14}$ W/cm^2. These values indicate a loss in laser homogeneity. This is very visible when we analyse the spherical harmonics decomposition. On the bottom right of Figure 5.7, we can notice a whole range of low, high-amplitude Legendre modes between $l = 0$ and $l = 10$. These modes reach amplitudes above $\sigma_l \geq 1\%$ for $l = 1, 3, 4$ and we even have $\sigma_{1 \leq l \leq 7} \geq 0.2\%$. The original spherical harmonics decomposition is not recognisable in the new system as it is fully dominated by the low modes. A question that we should ask now is how these persistent system errors can modify the irradiation of the target? How robust are the selected designs to experimental errors?

5.4 Systematic errors: source of low modes

Based on the previous results alone, the t-sphere design appears superior. However, experimental errors like beam mispointing (BM), target offset (TO), and power imbalance (PI) are known to be source of nonuniformity and unavoidable. These imperfections tend to deteriorate the illumination uniformity with respect to the theoretical minimum σ^*_{tot}. High system errors Σ_{sys} would lead to important implosion asymmetries and neutron yield reduction. As such errors can lead to low-mode asymmetries, it is necessary to asses the robustness of these designs to system errors.

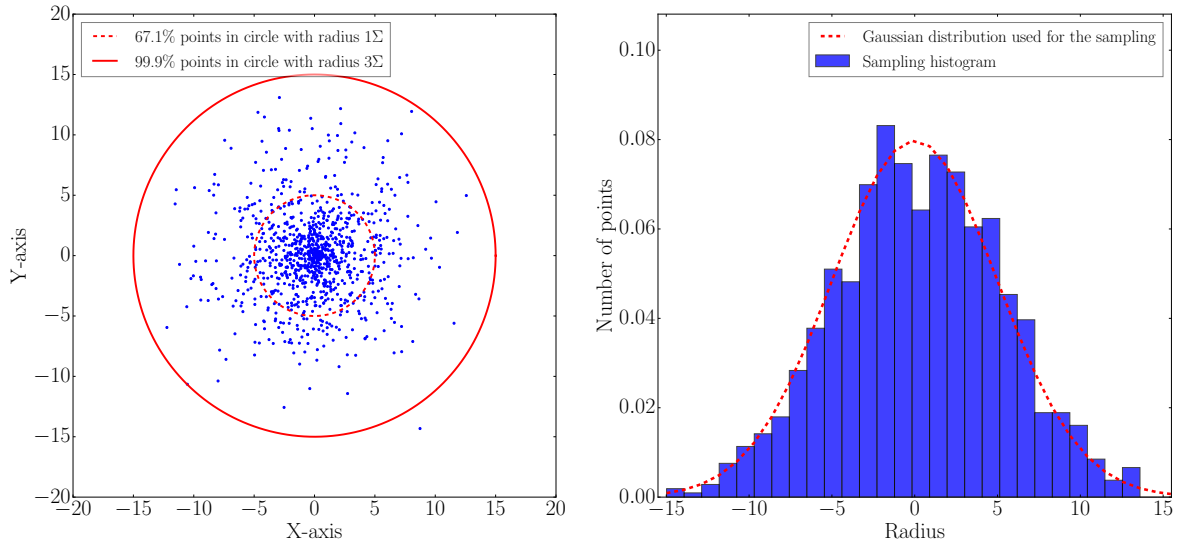

Figure 5.8 – Scatter plot representing the Gaussian sampling for the beam mispointing coordinates (X, Y) at the laser focal plane using 1000 blue points. The mean and variance used were: $\mu_x = \mu_y = 0.0$, and $\Sigma_x = \Sigma_y = \Sigma_{\text{BM}} = 5.0$. 67.1% (99.9 %) points are respectively located within the red solid (dashed) circle of radius $R = 1\Sigma$ ($R = 3\Sigma$). This corresponds roughly to the empirical rule where Pr is the probability function, X is an observation from a normally distributed random variable where μ_0 is the mean of the distribution and Σ_0 is its standard deviation: $Pr(\mu_0 - 1\Sigma_0 \leq X \leq \mu_0 + 1\Sigma_0) \approx 68.27\%$ and $Pr(\mu_0 - 3\Sigma_0 \leq X \leq \mu_0 + 3\Sigma_0) \approx 99.73\%$.

5.4.1 Gaussian statistical sampling method for beam mispointing, target offset and power imbalance

In order to mimic the errors that are systematic in experimental conditions, we will proceed to a statistical Gaussian sampling of these errors. As an example, we chose to detail the beam mispointing error sampling method. An illustration explaining how the method works is shown in the figure 5.8. For each laser beam:

— transform into the coordinate system of the focal plane of the laser beam,
— select (X, Y) mispointing coordinates randomly according to a Gaussian sampling $(\mu, \Sigma_{\text{BM}})$,
— run a solid sphere illumination calculation with the additional errors,
— perform the spherical harmonics decomposition of the laser irradiation,
— determine the total RMS of the irradiation.

In order to achieve a statistically representative sample, this procedure is repeated several hundreds of times, so that we can average the rms and divide the error per $\sqrt{N}$, N being the number of simulations. Indeed, we can then determine the average total RMS for a specified input variance Σ error and for a specific design. The uncertainty s on the average total RMS $\overline{\sigma}_{\text{tot}}$ decreases with the total number of simulations N performed as such:

$$s(\overline{\sigma}_{\text{tot}}) = \frac{s(\sigma_{\text{tot}})}{\sqrt{N}}. \tag{5.4.1}$$

This step is critical to get relevant results as, while the variance Σ_{BM} increases, the Gaussian distribution widens and so more data points are needed to represent correctly

the sampled area. Thus, more simulations need to be performed to obtain a correct uncertainty on the final results. This method is also used for other laser parameters and is aswell used for target offset (in 3D), and power imbalance (in 1D, but making sure that sampled negative values of power are discarded) for this manuscript.

5.4.2 Results of the sampling

The samplings are performed as such: every 0.1% from 0%R to 0.5%R and then every $\sim$ 0.56%R from $\sim$ 0.56%R to $\sim$ 3.89%R, with R the target radius. In Figure 5.9, we present illustrative examples of spherical harmonics decompositions for two distinct designs, namely $T72_2$ and $\Omega 60$, under a specific beam mispointing error of $\Sigma_{\mathrm{BM}} = 4.0\%$. This visualization serves as a representative depiction, showcasing the variability in irradiation patterns using gaussian samplings.

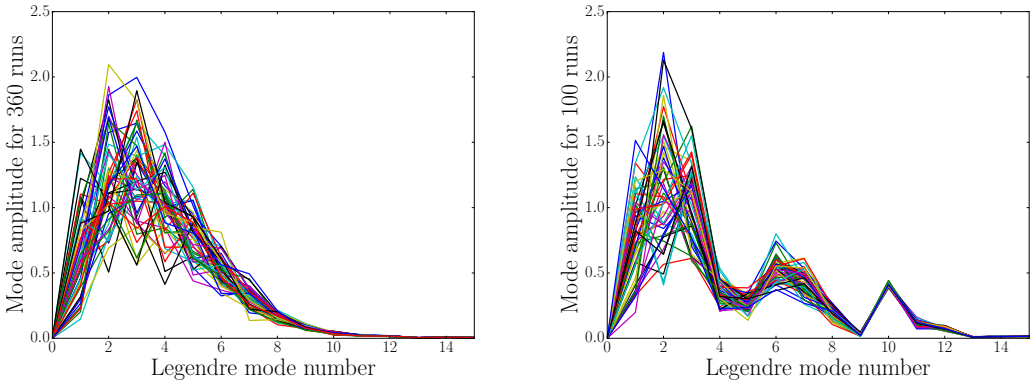

Figure 5.9 – Spherical harmonics decomposition of the laser intensity for $T72_2$ (left) and $\Omega 60$ (right) designs. The two plots represent a characteristic reduced sample of 50 simulations. They are both studied for a mispointing error $\Sigma_{BM} = 4.0\%\ R$.

From these plots, it is possible to extract the average spherical harmonics decomposition for a design corresponding to a specific error Σ_{BM}. This is shown in top figure 5.10. The colourmap system goes from dark blue to bright yellow, blue being close to the ideal case with a little mispointing error ($\Sigma_{\mathrm{BM}} \approx 10^{-3}\%\ R$), and yellow showing the most imprecise case considered ($\Sigma_{\mathrm{BM}} \approx 4.0\%\ R$).

A more precise example is given in figure 5.10 (bottom). The contour shows the evolution of the spherical mode amplitude with respect to the mispointing error. The appearance of small modes $l \leq 10$ and growth of these is highly visible, for both designs $T72_2$ and $\Omega 60$, and fully dominate the initial spherical harmonics decomposition. The decomposition broadens and the modes reach higher amplitudes with the increase of Σ_{BM}. For $T72_2$, as an average over a thousand simulations, the peak amplitude is reached for mode $l = 3$ with $\sigma_l \approx 0.750\%$, when it was equal to zero in the idealised case with the theoretical pointings. Between $l = 1$ and $l = 6$, we have $\sigma_{1\leq l\leq 6} \geq 0.3\%$. For $l \geq 8$, we eventually have $\sigma_{l\geq 8} \leq 0.1\%$ but with another local peak for $l = 12$, remaining the same as previously. For $\Omega 60$, the same behaviour occurs. When in Figure 5.6, there was a local minima for $l = 6$, with $\sigma_{l=6} \leq 0.05\%$, we now observe a substantial increase of the amplitude with Σ_{BM}. The $\sigma_{l=6}$ peaks at 0.2% and the modes around also start to grow, notably $\sigma_{1\leq l\leq 3} \geq 0.3\%$ (with a maximum reached for $l = 2$, $\sigma_2 \approx 0.5\%$), and

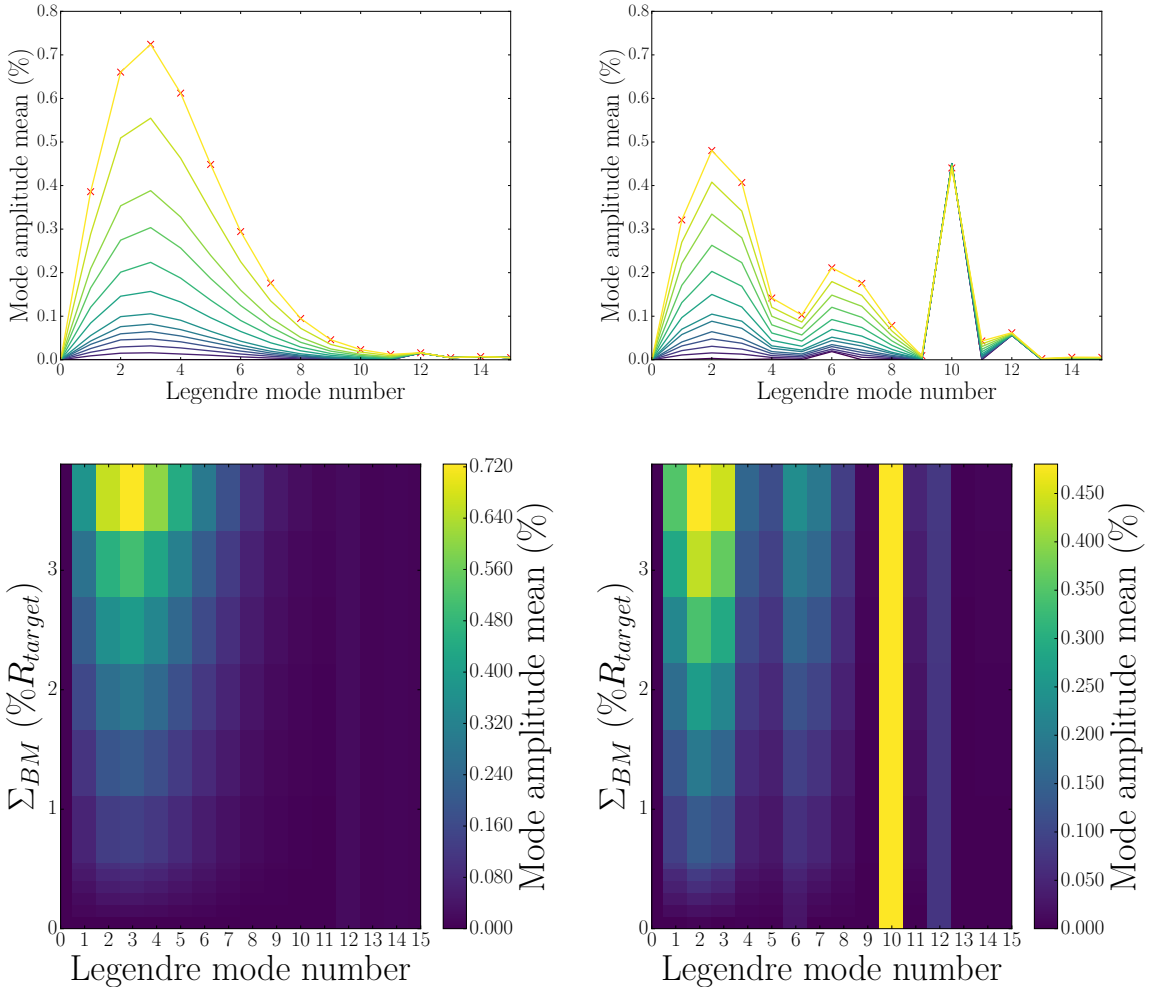

Figure 5.10 – $T72_2$ and Ω60 design plots are respectively shown on the left and on the right. (Top) Spherical harmonics decomposition of the laser intensity. The amplitudes are averaged among all the simulations. (Bottom) Contour plot showing the evolution of the mode amplitude mean for the Legendre mode numbers l as a function of Σ_{BM}. For both plots, Legendre modes range from $l = 1$ to $l = 15$, and the beam mispointing error is increased up to $\Sigma_{\mathrm{BM}} = 4.0\%$ (curve shown with red markers on top).

$\sigma_{6\leq l\leq 7} \approx 0.2\%$. What is remarkable is also the fact that the mode $l = 10$ remains similar ($\sigma_{l=10} \approx 0.46\%$) even when reaching such high mispointing errors like $\Sigma_{\mathrm{BM}} \approx 3.9\%$. It seems that all the modes below the lowest dominant mode of the initial configuration appear and grow with the systematic error. It is at least notable for $T72_2$ and Ω60, where both configurations see respectively their lowest dominant mode $l = 12$ and $l = 10$ unchanged, whereas an important variety of lower modes increases in amplitude.

Table 5.2 Summary of shot characteristics and low-mode system amplitude for the simulated experiment. Obtained from Reference [122].

Shot number	**Date**	**E$_{las}$** [kJ]	**R** [μm]	**Offset** [μm]	**Pointing** $l = 1$ [% rms]
94343	09/07/2019	27.7	491	3.5	1.26

5.4.3 Comparison to typical best laser performers at Ω60

In Figure 5.11, the growth of σ_{tot} with respect to the previously mentioned systematic errors known in typical DD ICF experiments Σ_{BM}, Σ_{TO} and Σ_{PI} is shown for all the studied designs ($M72$, $T72$, $I80$, and Ω60). These are compared directly to shot 94343 which is a cryogenic implosion implosion typical of the best laser performances at Ω60 obtained with low offset, pointing and balance error [124]. The findings from this experiment are documented in Table 5.2. The study utilized all 60 available beams, SG5 phase plates, and a distributed polarization rotator (DPR) system. Additionally, the experiment incorporated smoothing by spectral dispersion (SSD), a technique that temporally shifts the speckle pattern. The DPR +SSD system plays a crucial role to increase contrast, reduce the impact of high-frequency imprint from the laser and mitigate instability growth [6].

Two important conclusions can be obtained from Figure 5.11. First, it is crucial to optimise correctly the irradiation system with the beam patterns to obtain σ^*_{tot} as low as possible in the idealised case where system errors are nonexistent $\Sigma_{\text{err}} \to 0$ or at least $\Sigma_{\text{err}} \ll 1$ %. This can be seen in both left and right Figures as the idealised rms nonuniformities have different values for each design that were reported in the previous Table 5.1. In this idealised case, $T72$ designs show the more promising results. Second, it is also very important to see that above a certain critical value of Σ, some designs that were promising suffer the worst due to system errors. Even though, the t-sphere design $T72_2$ starts with the lowest theoretical rms value, it is not systematically the more robust to experimental errors. If we compare all designs with system errors that typically are expected at Ω60, it emerges that $I80$ is actually the more robust to system errors. For example, for a typical mispointing error encountered at Ω, $\sigma^{I80}_{\text{tot}} \approx 1.0\%$, when it exceeds 2% for $T72_2$ and it is $\geq 1.2\%$ for all other designs. For target offset, it is less clear which design shows best robustness at typical errors encountered at Ω. They all show close results as Σ_{BM} is low. On the other hand, when we consider power imbalance, $I80$ shows again the most promising results. At $\Sigma_{\text{PI}} = \Sigma^{\Omega 60}_{\text{PI}}$, we have $\sigma^{I80}_{\text{tot}} \approx 0.75\%$ and $\sigma^{T72_2}_{\text{tot}} \approx 1.2 - 1.3\%$. The other designs have values between these two extremes. Nevertheless, the performance of $T72_4$, despite having fewer beams compared to $I80$, presents intriguing results, displaying similar outcomes for typical errors observed in Ω60. It is noteworthy that achieving very-high irradiation uniformity in an idealised scenario, where $\sigma_{\text{tot}} \ll 1.0\%$ as $\Sigma_{\text{err}} \to 0$, may not guarantee efficiency if the system encounters experimental imperfections surpassing a critical value $\Sigma^{\text{crit}}_{\text{err}}$. Under such circumstances, the total rms can be estimated using $\sigma_{\text{tot}} \propto \Sigma_{\text{err}}/\sqrt{N_b}$. This estimation is illustrated in Figure 5.11, taking $\Sigma_{\text{BM}} = \Sigma^{\Omega 60}_{\text{BM}} \approx 3.56\%$ and $N_b = 72$, resulting in $\sigma_{\text{tot}} \approx 0.84$. This estimation closely aligns with the values obtained by our designs, notably $I80$, $T72_4$, and $M72$ (utilising $N_b = 80$ yields similar outcomes). When we observe the logarithm-scale plots, these designs follow similar trends for $\Sigma_{\text{err}} \geq 1\%$, despite having very different intrinsic rms nonuniformities.

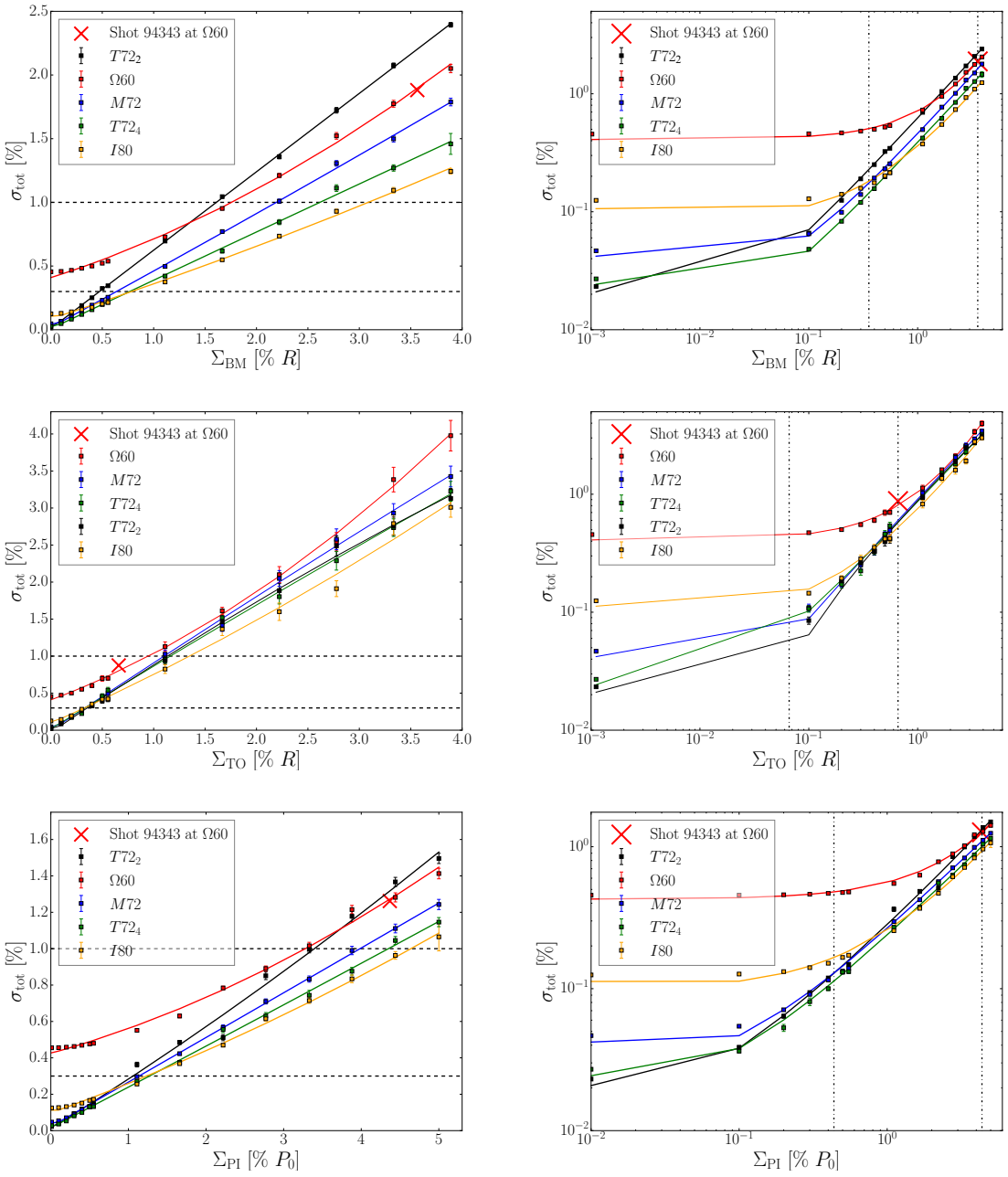

Figure 5.11 – Scatter plot of σ_{tot} versus their respective systematic errors Σ_{BM} (top), Σ_{TO} (middle), and Σ_{PI} (bottom) for all designs. The left figures are in linear scale, the right figures are in log-scale. Fitted curves are plotted to help data visualisation. Each dot is represented with its error bar along the y-axis. Error bars are small because numerous calculations were performed for each data point. The red cross indicate the solid-sphere illumination of shot 94343 which is a shot with low experimental errors at Ω60. Dashed horizontal lines in the left figures show constant values $\sigma_{\text{tot}} = 0.3\%$ and 1.0%. Dashdotted vertical lines in the right figures show $\Sigma_{\text{err}}^{\Omega 60}/10$ values.

Moreover, when aiming for a total RMS error of $\sigma_{\text{tot}} = 1\%$, which design provides the highest Σ, indicative of greater robustness? Conversely, when striving for even higher irradiation quality with $\sigma_{\text{tot}} = 0.3\%$, which design exhibits more resilience? By examining specific values of σ_{tot} using the horizontal dashed lines in the left figures, we find that at $\sigma_{\text{tot}} = 1\%$, the $I80$ design allows for the largest Σ: it is therefore the most robust option. Conversely, for a target of 0.3% total RMS, both $T72_4$ and $I80$ demonstrate nearly identical results. Furthermore, upon inspecting the vertical dash-dotted lines in Figure 5.11, which represent system errors $\Sigma^{\Omega 60}$ typical of $\Omega 60$, we observe that the $I80$ design yields the lowest σ_{rms}. For improved performance with $\Sigma^{\Omega 60}/10$, the $T72_4$ configuration emerges with the lowest σ_{tot}.

We have seen that a quantitative analysis of uniformity degradation delves into 4 factors: the number of beams, beam patterns, laser spatial profile and the system errors. The findings reveal that the enhanced sophistication of only one of these aspects does not inherently lead to improved irradiation performance. Rather, for a high level of irradiation uniformity, a simultaneous control approach including all factors is required. A high level of drive uniformity with a low rms value, approximately $\sigma_{\text{tot}} \approx 1.0\%$, is feasible. This involves effectively controlling the beam profile and simultaneously minimising system imperfections, maintaining $\Sigma_{\text{err}} \leq 1.0\%$.

However, the laser spatial parameters were initially selected based on the idealized case, assuming $\Sigma_{\text{sys}} = 0$. Exploring alternative combinations of R_{las} and S_G might offer opportunities to enhance drive uniformity on the target. The next step involves choosing laser parameters while accounting for system errors.

5.4.4 Optimising spatial laser parameters including system errors

In the previous section, we optimised the laser profiles in an idealised case, with no error sources. We chose now to optimise the laser spatial parameters with fixed Σ_{err} estimated from shot 94343 at $\Omega 60$. Nevertheless, due to lack of computational time, we cannot scan the whole same parameter space as we need statistics to obtain meaningful results. Indeed, for a single point (S_G, R_{las}/R), with system errors included, at least several hundreds of simulations are needed. We then decide to scan only the area around the initial best parameters that were found in Table 5.1. We proceed with the same gaussian sampling method for each of the points. We used $\Sigma_{\text{BM}} \approx 3.57\%R$, $\Sigma_{\text{TO}} \approx 0.71\%R$, $\Sigma_{\text{PI}} 4.37\%P_0$. Results are shown in Table 5.3.

The scattered points represent the total rms σ_{tot} in a reduced parameter space (S_G, R_{las}/R) for the $T72$ (a-b), $M72$ (c) and $I80$ (d) designs. The white crosses show which point was considered as to give the optimised laser parameters for each design in the initial study. The different parameters of the points shown in figure 5.12 are shown in the table 5.3.

In bold are written the initial points considered as optimised in the study with no system errors, as expected from the low-level perturbations considered. These points are also represented with white thick crosses in figure 5.12. In red are highlighted the different configurations that have $\sigma_{\text{tot}} \leq \sigma_{\text{tot}}^{\Omega 60} \approx 2.7\%$ within the error bar (obtained thanks to shot 94343 considering only offset and beam mispointing, should be even higher when including power imbalance). The beam-target intersection is not affected much when adding system errors, as they remain almost the same as in the initial study.

The insights observed from the table highlight the advantageous impact of reducing the super Gaussian order and increasing the $1/e$ radius of laser beams on laser irradiation.

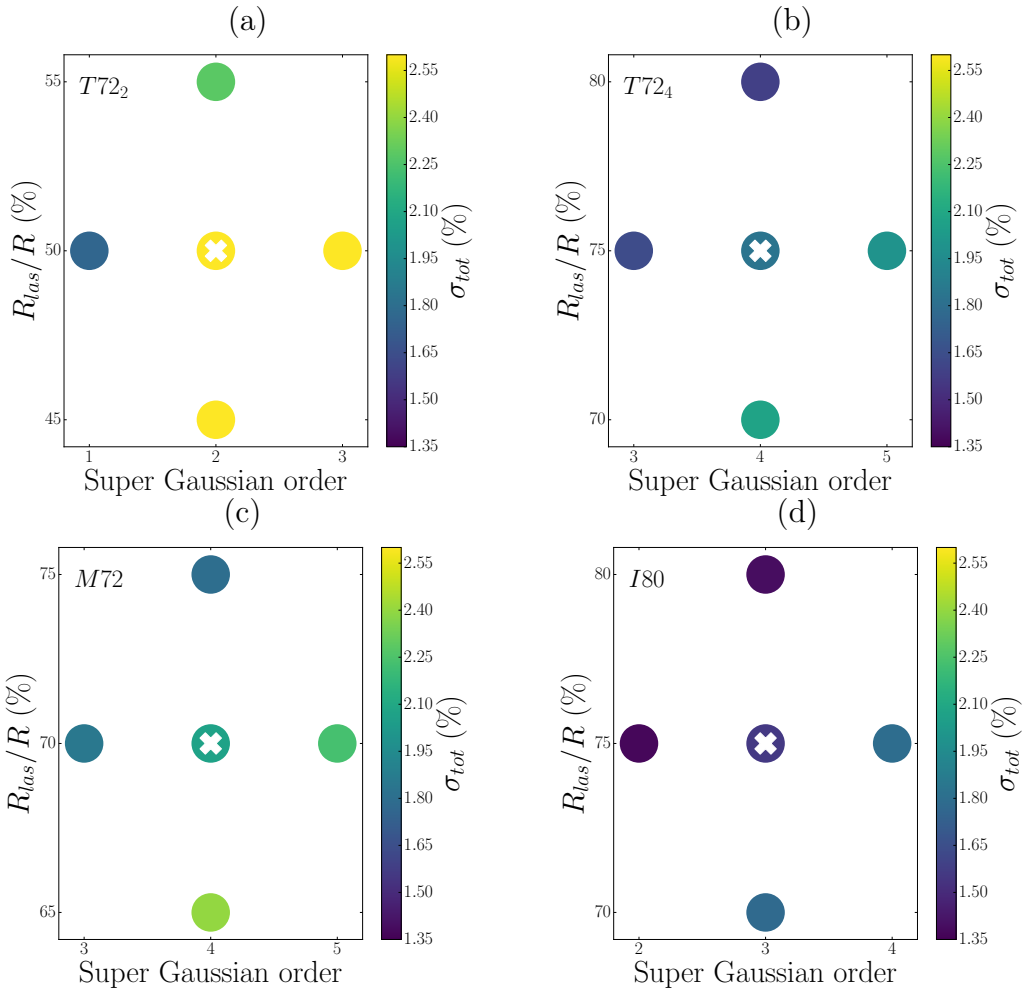

Figure 5.12 – Scatter plots showing the optimisation study for $T72_2$ (a), $T72_4$(b), $M72$ (c) and $I80$ (d). All designs show a colorbar ranging from $\sigma_{\text{tot,min}} = 1.35\%$ to $\sigma_{\text{tot,max}} = 2.60\%$, which is the total RMS of shot 94343 at Ω60 with offset and power imbalance. Points in bright yellow overcome this threshold. The white crosses represent the initial point with the best laser parameters shown in Table 5.1.

This strategy proves beneficial by decreasing the total rms. When the laser spot size (the super gaussian order) is increased (decreased), the beams become wider, favouring increased overlap and consequently greater homogeneity. However, a trade-off exists, as larger beams reduce the beam-target intersection — the region where laser light effectively illuminates the target without missing it. It is important to note that refraction and other laser-plasma instabilities are not factored into this calculation. For example, shot 94343 at Ω60 shows a beam-target intersection of 99.6%. Despite this, experiment and simulations indicate an average estimated laser target coupling of $f_{\text{abs}} \approx 74\%$ [131]. This is due to losses from refraction, LPIs, and specifically CBET. Maximizing the beam-target intersection is a priority, as even small losses in this parameter can significantly impact the laser-target coupling energy. Additionally, configurations with high drive efficiency can be achieved by employing more localized beams with either small $1/e$ radius or large super Gaussian order laser beams. We also note that because smaller beams produce less overfill of the in-flight critical surface, they also help in mitigating CBET efficiently [132].

It is crucial to strike a balance, aiming to maximise the beam-target intersection, using the approximation that our design will suffer similar f_{abs} drops due to LPIs and refrac-

Table 5.3 Sampled data around the initially optimised point (in bold), with their respective total RMS, beam-target intersection and laser parameters. In red are shown the configurations that have higher beam-target intersection ($> 99.6\%$) and a lower σ_{tot} ($< 2.6\%$) than shot 94343 at Ω60 for shot 94343.

Design	$\sigma_{\text{tot}}(\%)$	Beam-target intersection(%)	S_G	R_{las}/R (%)
$M72$	1.85 ± 0.02	97.3 ± 0.2	3	70
	2.40 ± 0.02	99.8 ± 0.2	4	65
	2.07 ± 0.02	**99.5 ± 0.2**	**4**	**70**
	1.80 ± 0.02	98.8 ± 0.2	4	75
	2.23 ± 0.02	99.9 ± 0.1	5	70
$T72_2$	1.76 ± 0.01	59.4 ± 0.1	1	50
	3.2 ± 0.2	99.2 ± 0.2	2	45
	2.69 ± 0.02	**98.2 ± 0.2**	**2**	**50**
	2.28 ± 0.02	96.2 ± 0.2	2	55
	3.48 ± 0.02	99.9 ± 0.1	3	50
$T72_4$	1.63 ± 0.01	95.2 ± 0.2	3	75
	2.08 ± 0.02	99.5 ± 0.3	4	70
	1.83 ± 0.02	**98.6 ± 0.3**	**4**	**75**
	1.59 ± 0.02	97.1 ± 0.3	4	80
	1.99 ± 0.02	99.7 ± 0.2	5	75
$I80$	1.37 ± 0.02	83.1 ± 0.2	2	75
	1.78 ± 0.02	97.3 ± 0.2	3	70
	1.56 ± 0.01	**95.2 ± 0.3**	**3**	**75**
	1.39 ± 0.01	92.5 ± 0.2	3	80
	1.79 ± 0.02	98.8 ± 0.3	4	75
	1.98 ± 0.02	99.4 ± 0.2	4	70

tion, while simultaneously minimising the total rms - ideally surpassing the performance achieved by Ω60. This compromise ensures an optimal configuration that enhances both homogeneity and laser-target coupling efficiency.

In the right half of Figure 5.13, the evolution of the total rms concerning the $1/e$ radius of the laser and the super gaussian order is depicted, accounting for pointing, offset, and balance errors of $I80$ design. The white points in the left figure denote the sampled positions, and their specifications are detailed in the final row ($I80$) of Table 5.3. An intriguing addition is marked in the bottom right corner ($S_G = 4$, $R_{\text{las}}/R = 70\%$). This particular combination holds significant merit as it achieves a remarkable laser-target intersection value (approximately 99.6%) and exhibits a higher degree of illumination homogeneity compared to Ω60 ($\sigma_{\text{tot}}^{I80} = 1.98 \pm 0.02\%$, surpassing $\sigma_{\text{tot}}^{\Omega 60} \approx 2.7\%$). We can even further reduce the total rms ($\approx 1.79\%$) and still achieve considerably important laser-beam target intersection ($\approx 98.8\%$) when using $S_G = 4$ and $R_{\text{las}}/R = 75\%$ for $I80$. The other designs ($M72$, $T72_4$) can also offer good results but are not considered as promising as the $I80$.

An interesting observation emerges when comparing different designs with the same number of beams, identical super gaussian order, and matching R_{las}/R. Taking a closer look at $M72$ and $T72_4$ under the influence of system errors, we find two points that share the same spatial laser parameters ($S_G = 4$, $R_{\text{las}}/R = 70\%$, and $S_G = 4$, $R_{\text{las}}/R = 75\%$).

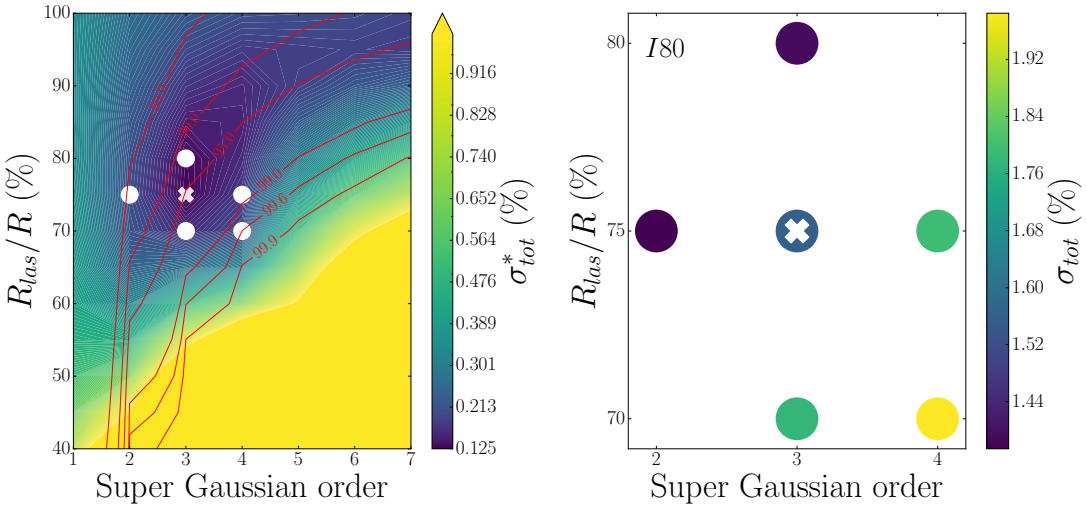

Figure 5.13 – Contour plot of the $I80$ design (left) as shown in Figure 5.5 (c). On the right, we show a scatter plot of the bew optimisation study for $I80$. Points on the left figure above the maximum of the colorbar are shown as maximum.

Specifically, $M72_4^{70}$ and $T72_4^{75}$ exhibit total rms values of approximately 1.80% and 1.83% respectively, along with beam-target intersections of about 98.8% and 98.6% respectively. However, it is noteworthy that their initial idealised rms values were significantly lower at 0.03% and 0.05% respectively. As mentioned earlier, beyond a critical value, system errors become a predominant source of inhomogeneity, causing the total rms to scale directly with the system error and the number of beams.

5.4.5 Conclusion

We have proposed a study on irradiation quality with three different beam port geometries. The aim is to assist in the design of future direct-drive laser facilities. These designs are denoted as $M72$, $T72$, and $I80$.

In this section, we found it imperative to optimise the irradiation system alongside the beam pattern. However, once the system surpasses a critical error value, the total rms demonstrates a linear increase with the system error: $\sigma_{\text{tot}} \propto \Sigma_{\text{err}}/N_b$. Our findings indicate that the $I80$ design appears to be more robust in the face of typical $\Omega 60$ system errors. Additionally, the general trend suggests that enlarging the laser spot size enhances laser illumination homogeneity, albeit at the expense of the beam-target intersection. Considering a $\sigma_{\text{tot}} = 1\%$ threshold error, the $I80$ consistently offers higher irradiation uniformity. At $\sigma_{\text{tot}} = 0.3\%$, both $T72_4$ and $I80$ compete with very similar results. For typical system errors $\Sigma_{\text{err}}^{\Omega 60}$, it is found that $I80$ is the most robust design. For system errors ten times smaller, it is seen that $T72_4$ achieves higher illumination quality.

In conclusion, the $I80$ design offers promising prospects for achieving a beam-target intersection akin to $\Omega 60$, coupled with a nearly 1% reduction in total rms compared to $\Omega 60$, achieved by minor adjustments to the initially optimised laser spatial parameters. Our next steps involve investigating low-mode asymmetries in comprehensive 3D implosions using this optimised design. Additionally, we plan to delve into the correlation between system errors and target performance, evaluating various ignition schemes such as shock

ignition and standard ignition for a specific design. A future study should check the proposed relationship between beam-target intersection, increased refraction/CBET and lower f_{abs}. This work could also be expanded to evaluate sensitivity to variation in beam spots.

5.5 1D radhydro simulations for standard ignition and shock augmented ignition using *CHIC*

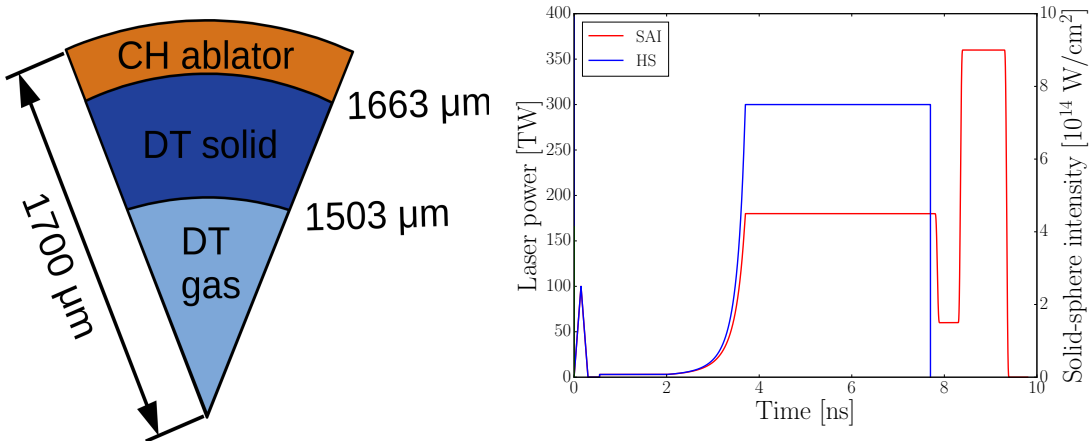

Figure 5.14 – Target (left) and laser profiles (right) used for the 3D hydrodynamic simulations. HS designs are in blue, SAI are in red.

To estimate the impact of system errors on target performance, we have chosen two distinct ignition schemes: standard hot-spot ignition (HS) and SI. These two schemes currently seem to be the most promising for DD ICF.

In these designs, we opt for a drive energy of approximately 1.3 MJ, positioning them within the regime conducive to ignition. The 1.3 MJ scale HS design represents a single picket version, inspired by the proposals outlined in section III.A of Reference [48]. From this reference, we also derived a SI design for comparative analysis.

In our analysis for each design, we leverage the 1D CHIC hydrodynamic code to conduct a comprehensive scan of laser power and timing. This scan aims to identify the ignition threshold window, as illustrated in Figure 5.15. Through this process, we can determine the power threshold (refer to Table 5.4), ascertain the maximum target gain, and establish the optimal pulse timing. Subsequently, the pulse configurations are slightly adjusted for the 3D *ASTER/IFRIIT* simulations to refine shock timing and adapt to the three-dimensional scenario. It is worth noting that the SI design employed here incorporates an ignitor spike with much lower intensity than usual for SI, shifted outside the compression pulse. This concept aligns with the framework formalized in Reference [133] and is commonly referred to as shock-augmented ignition (SAI).

SAI introduces a dip between the compression plateau and the power spike, strategically cooling down the plasma. This cooling enables the generation of a strong shock while maintaining the laser intensity below current SI schemes. Compared to SI, SAI's lower intensity requirements have the potential to significantly reduce laser-plasma instabilities, enhancing laser coupling and mitigating hot-electron preheat. However, recent findings [132] indicate that SAI designs still necessitate significant bandwidth due to the cooling

Table 5.4 Presented here is a summary of the design parameters employed for the ignition study: laser energy E_L, peak solid-sphere laser intensity I_L, peak laser power P_L, implosion velocity at coast time $\mathrm{U_{imp}}$ - measured before the strong shock for SI, in-flight aspect ratio at coast time $\mathcal{A}_{if}$ - the time between peak ablation pressure and implosion bang-time, convergence ratio averaged over the fuel convergence ratio $\mathrm{C}_{d,\mathrm{ave}}$, maximum target gain $\mathcal{G}$ and maximum neutron yield. These parameters serve as essential metrics for the study, providing a comprehensive overview of the design characteristics and performance considerations.

Case	E_L [MJ]	I_L [10^{14} W/cm^2]	P_L [TW]	v_{imp} [km/s]	$\mathcal{A}_{if}$	$\mathrm{C}_{r,\mathrm{ave}}$	$\mathcal{G}_{\mathrm{max}}^{\mathrm{window}}$	Yield
HS	1.37	8.3	275	420	10	9	98	1.45×10^{19}
SAI	1.22	9.9	300	250	11	10.5	144	1.74×10^{19}

of the plasma during the power dip, leading to an increase in CBET gain. Notably, the re-heating of the plasma during the ignition spike is found to be insufficient to counteract this effect.

The target and pulses used to study the two schemes are shown in Figure 5.14.

5.5.1 Ignition window with α particle deposition

In the 1D CHIC simulations for these designs, we conducted multiple cases by modifying parameters such as peak power, exponential-like rise for HS, or spike launching time for SAI. Through this approach, we identified the ignition window for each target, as presented in Figure 5.15. The parameter space scan included the plateau (spike) launching time from 3.5 to 7.3 ns (7.0 to 10.0 ns) and the plateau peak power from 200 to 300 TW for both schemes.

In the top part of the figure, the colorbar represents the total number of neutrons created by the end of each simulation on a logarithmic scale. The bottom part illustrates the total thermonuclear energy released at the end of a simulation for HS (left) and SAI (right). Contours in red solid lines represent the energy gain (ranging from 20 to 80 or 120 depending on the scheme) defined in (1.3.1). For HS, the maximum gain is 98, while for SAI, it reaches 145. These are simulations with a 4% flux limiter, and we consider that CBET has been fully mitigated.

Observing the bottom figures, we notice that to achieve $\mathcal{G} \geq 20$, the two methods offer different advantages. HS demonstrates more robustness concerning plateau launching time. If we consider the horizontal dashed line at $P_L = 275$ TW (where the maximum gain is reached), the range where $\mathcal{G}_{\mathrm{HS}} \geq 20$ lasts for almost 3 ns. This window is nearly the same for $\mathcal{G}_{\mathrm{HS}} \geq 40$ on the same horizontal line.

On the other hand, for SAI, considering a horizontal line at $P_L = 250$ TW (where the maximum gain is reached), the behaviour is different. This time, the window where $\mathcal{G} \geq 20$ ranges from 8.0 to 9.5 ns, resulting in a window width of only 1.5 ns, which is half as much as in the HS case. This disadvantage of SAI compared to HS is simply caused by the increased sensitivity to shock timing of this scheme.

Additionally, if we consider a vertical line passing through the maximum gain (shown by the red cross), it is the HS scheme that is more sensitive to peak power. At 6.7 ns, a peak power ≥ 250 TW is needed to obtain $\mathcal{G}_{\mathrm{HS}} \geq 20$. Conversely, for the SAI scheme, the maximum gain is reached when the spike is launched at 9.0 ns. In this case, a spike with power $P_L \geq 205$ TW will result in an implosion with an energy gain $\mathcal{G} \geq 20$. SAI

is sensitive to spike and shock timing, but if the shock is timed correctly, then increasing spike power does not increase laser energy as fast as for HS, this leading to higher gains for lower peak powers.

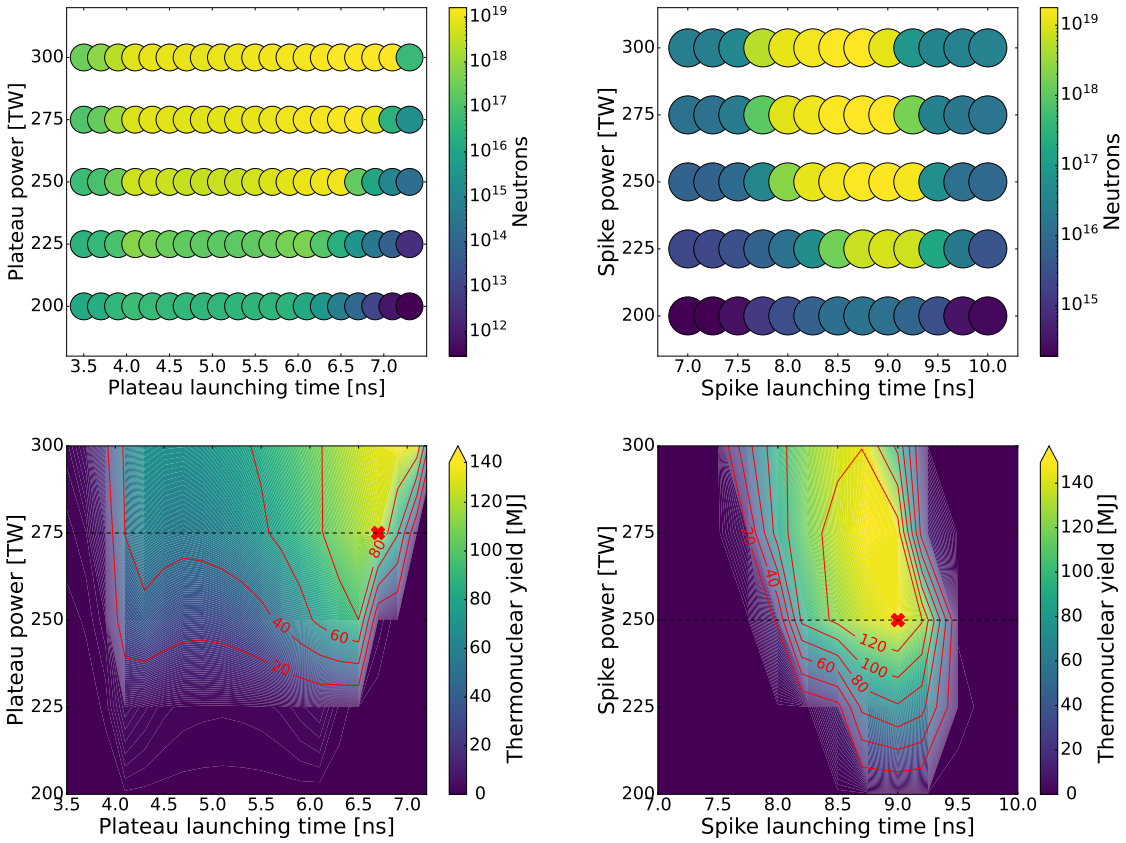

Figure 5.15 – Ignition windows for a standard ignition case (left) and a shock augmented ignition case (right) [133]. At the top, the total number of neutrons created at end of the simulations is shown. The amount of neutrons produced in high gain scenarios is around 1.5×10^{19}. At the bottom, red curves are contour plots showing the energy gain, and the red cross shows the maximum gain reached for both schemes. Results are obtained via 1D *CHIC* simulations of an ignition scale target (1700 μm radius DT cryogenic pellet, see Figure 5.14).

To conduct 3D *ASTER* simulations comparing the robustness of HS and SAI to system errors, we acknowledge that *ASTER* does not incorporate burn physics modules. Therefore, to estimate the performance of a design, we plan to compare 3D results with 1D *CHIC* results by removing all burn physics packages. This approach will allow us to evaluate the behaviour of the designs in 3D simulations while leveraging the 1D *CHIC* results as a reference for performance estimation.

Finally, we should note here that various different optima may be found for HS and SAI by varying more parameters in the laser pulse, so we cannot conclude strongly on maximum gains for SAI versus HS. Rather than that, we are more interested in scheme robustness given a similar adiabat.

We also show in Figure 5.16 the thermodynamic paths of the hot spot in the $(\langle \rho_h R_h \rangle, \langle T_h \rangle)$ plane for HS and SAI designs using 1D *CHIC* simulations and the target/pulses shown in Figure 5.14. These figures serve as a means of comparison with 3D *ASTER* simulations for later.

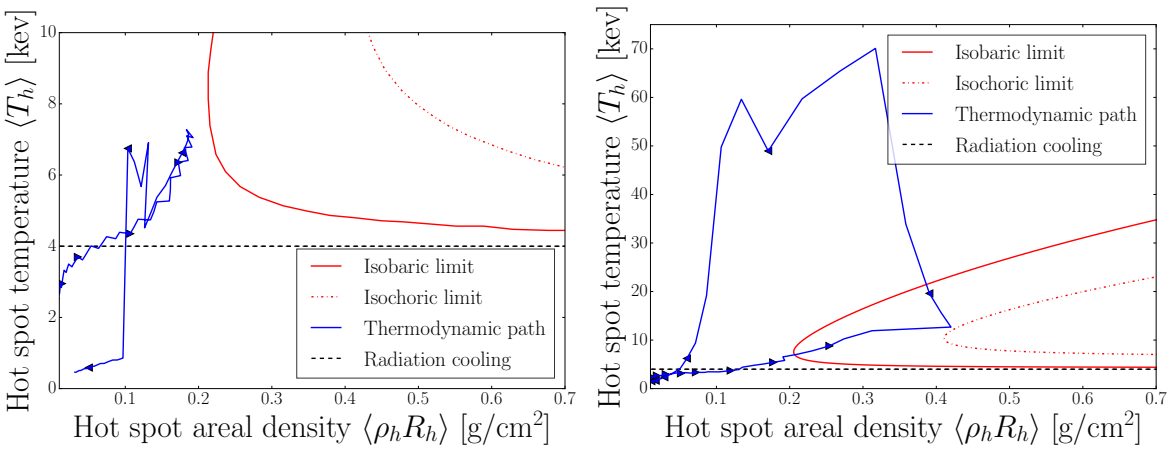

Figure 5.16 – 1D *CHIC* thermodynamic diagrams for HS (left) and SAI (right) using the laser pulses shown in Figure 5.14 and α-particle energy deposition. Red solid (dotted-dashed) lines show the isobaric (isochoric) limit. The scattered triangles show the direction of the hot spot in time.

5.5.2 Ignition criteria detection without α particle deposition

3D low mode simulations will be performed with *ASTER*, which does not include burn physics. In order to relate the *ASTER* results to ignition performances, we conduct a second 1D parameter scan but without $\alpha-$particles energy deposition.

In that case, no energy is deposited by the alphas in the surrounding matter, and self-heating cannot occur, but we can still track a no-α number of neutrons produced. The results of this study are presented in Figure 5.17, where the total number of neutrons is displayed for HS (left) and SAI (right). For HS, the maximum neutron yield $Y_n^{\mathrm{HS}} = 3.7 \times 10^{16}$ is considered as the optimal yield. In the case of SAI, the maximum number of neutrons is $Y_n^{\mathrm{SAI}} = 2.9 \times 10^{16}$. Without burn physics, HS produces more neutrons than SAI. This difference can be attributed to the fact that standard hot spot ignition can be modeled via an isobaric configuration ($p_h = p_c$). In an isobaric configuration, the hot spot lifetime is maximized as the system remains stable. In the SAI scheme, the pressure in the hot spot is higher ($p_h > p_c$), leading to earlier expansion and a reduced number of reactions due to additional mechanical power losses in the hot spot. This characteristic is common to all alternative, non-isobaric schemes. The most challenging case is observed in fast ignition, particularly the isochoric hot spot, as depicted in Figure (b) 5.18. The self-heating condition is more demanding in the isochoric case, as illustrated in Figure 2.14, which represents the self-heating conditions in the $(\rho_h R_h, T_h)$ plane for both isochoric and isobaric conditions. The self-heating line for the isochoric case is higher than the isobaric one. Without burn, it is even more challenging to exceed the ignition limit, explaining why SAI produces fewer neutrons in a no-α scenario.

Bottom Figure 5.17 shows the evolution of the Yield Over Ideal (YOI) in percentage, which is defined as the the ratio between the neutron yield and maximum neutron yield of the ideal case, over the parameter space. Dashed red lines show represent contour plots of the YOI for given values: 25%, 50% and 75%. From the plots, we see that HS is less restrictive than SAI as the contour plots have bigger areas. If we consider the time duration Δt, where we have YOI > 25 % at 300 TW, we have $[\Delta t]^{\mathrm{HS,\ 25\%}}_{\mathrm{300TW}} > 3.5$ ns. For a power spike with the same amplitude in SAI, we have $[\Delta t]^{\mathrm{SAI,\ 25\%}}_{\mathrm{300TW}} = 2.5$ ns. For 50% and 75% contour plots, the same can be done. We have: $[\Delta t]^{\mathrm{HS,\ 50\%}}_{\mathrm{300TW}} > 3.5$ns, $[\Delta t]^{\mathrm{HS,\ 75\%}}_{\mathrm{300TW}} = 2.6$

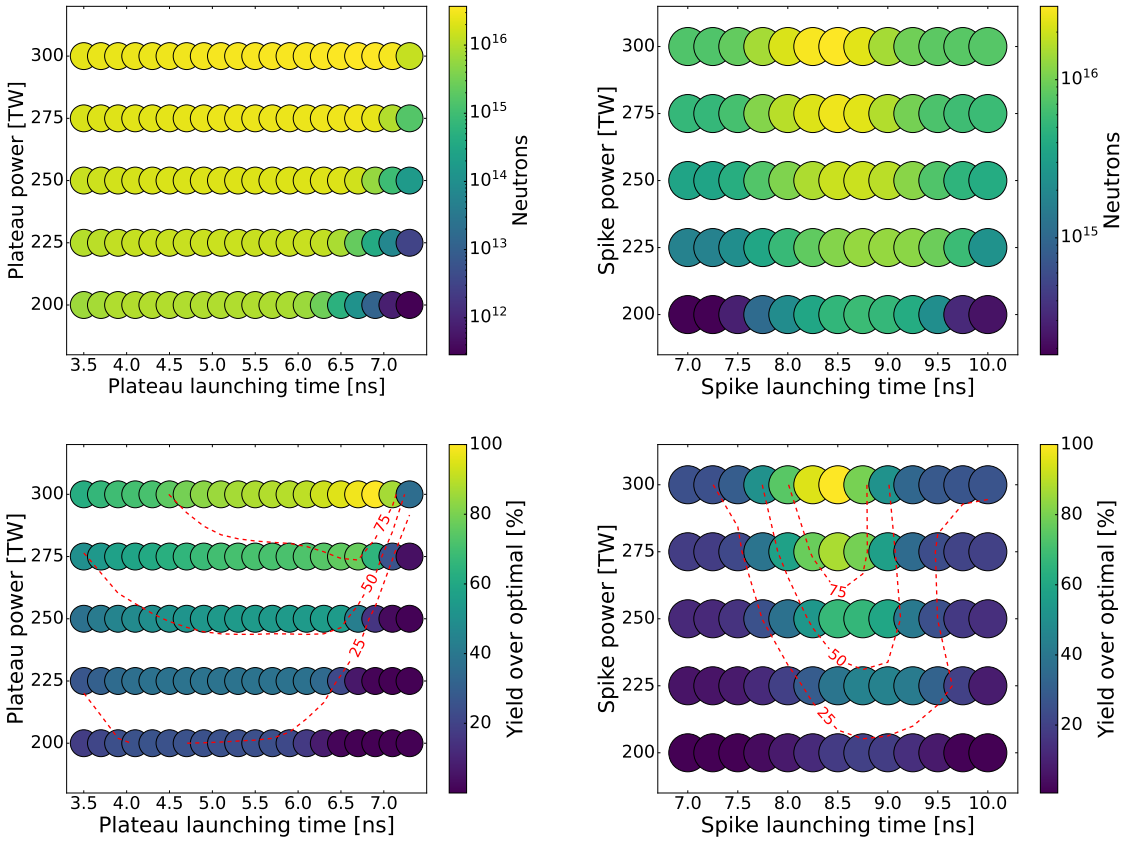

Figure 5.17 – At the top, we show a scatter plot of the total number of neutrons produced for HS (left) and SAI (right). At the bottom is shown the Yield Over Ideal (YOI) in percentage, defined as the ratio between the neutron yield and the maximum neutron yield of the optimised case. Dashed red lines show contour plots of the YOI (in %) for YOI $= \{25, 50, 75\}$ %. These simulations are performed without burn physics.

ns and $[\Delta t]^{\text{HS, 50\%}}_{\text{300TW}} = 1.25$ ns, $[\Delta t]^{\text{HS, 25\%}}_{\text{300TW}} = 0.75$ ns. The different results are shown in the following Table 5.5:

Table 5.5 Neutron production results for the 1D simulations without burn physics. The hot spot in HS lasts longer, producing more neutrons and the yield has a wider range of time.

Case	Yield [$\times 10^{16}$]	Δt [ns] at $P_L = 300$ TW		
		25% YOI	50% YOI	75% YOI
HS	3.70	> 3.5	> 3.5	2.6
SAI	2.91	2.5	1.25	0.75

Without alpha deposition, we see a strong indication that HS is more stable as it offers wider contour plots for all the different YOI values, and a higher maximum yield.

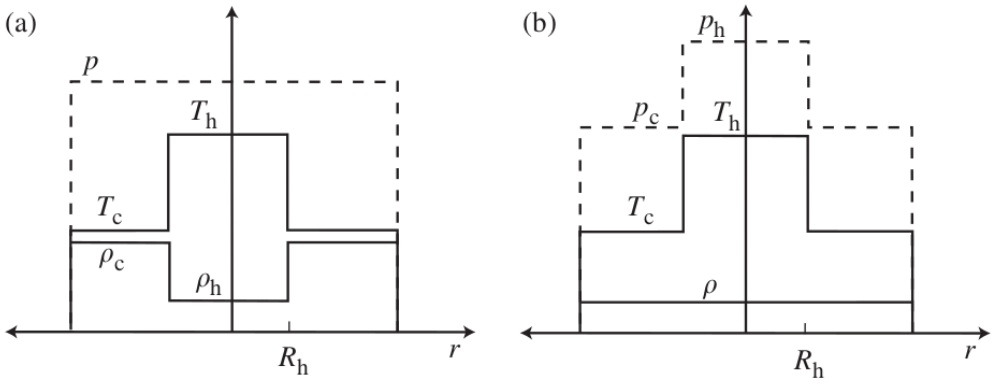

Figure 5.18 – The model configurations for the compressed fuel at ignition are illustrated through two setups. (a) This configuration maintains constant pressure during the assembly process, and it features a central hot spot. (b) Isochoric assembly with central hot spot: in this configuration, the assembly is carried out under constant density, with a central hot spot. The radial profiles of temperature (T), density (ρ), and pressure (p) are provided for both configurations. These profiles offer insights into the distribution and behaviour of these key parameters within the compressed fuel at ignition.

5.6 3D radhydro simulations aiming to compare standard and shock ignition robustness to target offset using the coupled code *ASTER/IFRIIT*

Now that we have an analysis of the target performances using 1D *CHIC* simulations, we aim to conduct 3D *ASTER/IFRIIT* hydrodynamics simulations. HS and SAI will be compared in the first place in an idealised case, considering no system errors. In a second step, additional simulations will be performed with linearly increasing offset. The goal here is to compare ignition scheme robustness to system errors to select which should be preferred for IFE using a specific optimised chamber geometry design. The target and pulses used are shown in Figure 5.14.

5.6.1 3D idealised simulations

In these idealized 3D simulations, we have selected a specific beam chamber geometry known as $M72$. As demonstrated earlier, this geometry exhibits excellent irradiation performance, surpassing even Ω60 , with a comparable beam-target intersection (refer to Table 5.3). In these simulations, we do not account for phenomena such as CBET or other LPIs.

We present in Figure 5.19 2D density slices for HS (left) and SAI (right) schemes. The red contours correspond to the volume fraction of DT gas which gives insights on the hot spot dimensions and shape. On top are shown the slices at a tenth of peak neutron production, and at the bottom at peak neutron production. Both schemes present similar hot spot shapes and sizes. First, we notice differences in the structure of the layers surrounding the hot spot. At the bottom, low mode perturbations can be seen, in particular for the HS case. The wavelengths of these perturbations are large enough to be visible but not to puncture the target. In SAI, the perturbations are much lower. This is because the implosion velocity of these two designs are relatively different. In the HS

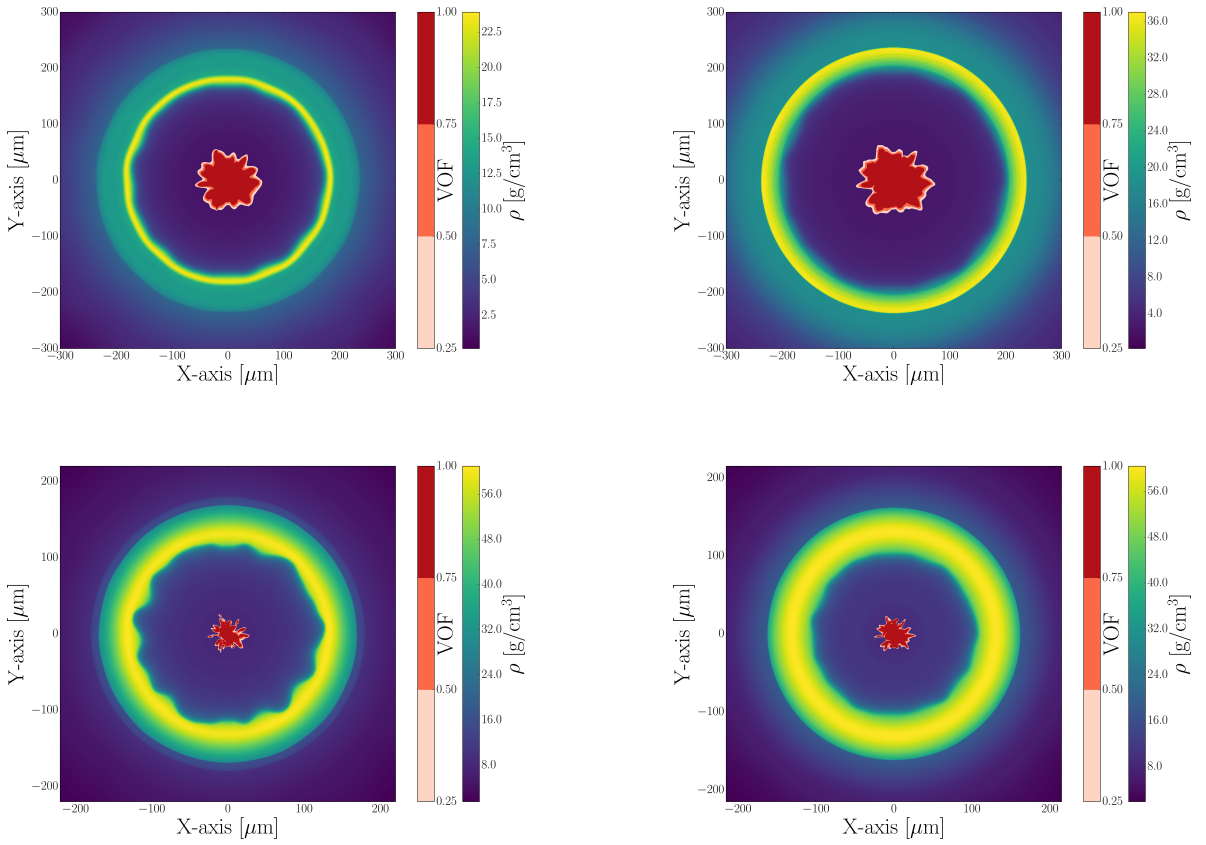

Figure 5.19 – 2D density slices of both HS (left) and SAI (right) schemes at a tenth of peak neutron production, $t_{10\%}^{\mathrm{HS}} = 8.80$ ns and $t_{10\%}^{\mathrm{SAI}} = 10.19$ ns (top) and at peak neutron production (bottom), $t_{\mathrm{peak}}^{\mathrm{HS}} = 9.12$ ns and $t_{\mathrm{peak}}^{\mathrm{SAI}} = 10.43$ ns. Red contours show the volume fraction of DT gas, highlighting the hot spot shape.

design, we have $v_{\mathrm{imp}}^{\mathrm{SAI}} = 420$ km/s, and $v_{\mathrm{imp}}^{\mathrm{HS}} = 250$ km/s for the SAI design. Considering Equation (2.6.14), the higher the implosion speed, the higher is the acceleration and the deceleration of the shell, meaning that the RTI growth-rate increases. Also, SAI seems to offer a thicker and more homogeneous shell than HS thanks to a slower implosion. Both schemes have relatively similar hot spot temperature: $T_i \approx 2$ keV at peak neutron production. The neutron yield values are $Y_n^{\mathrm{HS}} = 2.14 \times 10^{16}$ and $Y_n^{\mathrm{SAI}} = 1.20 \times 10^{16}$. For both cases the number of neutrons is reduced compared to an idealised 1D scenario (see Table 5.5).

Figure 5.20 shows thermodynamic paths of the hot spot in blue for both schemes HS (left) and SAI (right) in the $(\rho_h R_h, T_h)$ plane. The three scattered points represented in cyan, magenta, and yellow are crucial markers around the stagnation phase of the target. These points correspond to specific times: one-tenth of the peak neutron production, the moment of peak neutron production, and the instance of peak areal density in the hot spot. In both ignition schemes, the trajectories do not intersect with the hot-spot self-heating thresholds, whether isochoric or isobaric. This stands in contrast to the scenario depicted in Figure 5.16, particularly the right part, which illustrates the trajectory of a self-heating hot spot under an α-particle deposition scenario for the SAI scheme. In Figure 5.20, the hot spot is not hot enough and is cooled due to radiations - in particular electron bremsstrahlung losses, which is the dominant radiation mechanism at temperatures of a few keV. The evolution of the hotspot characteristics is assessed in a $(\rho R, T)$ diagram. The hotspot averaged areal density $\langle \rho_h R_h \rangle$, the averaged temperature $\langle T_h \rangle$ and the mass

of the hot spot M_h are defined as [134]:

$$\begin{aligned}\langle \rho_h R_h \rangle &= \int_0^{R_h} \rho(r) \mathrm{d}r, \\ \langle T_h \rangle &= \frac{3}{R_h^3} \int_0^{R_h} T_h r^2 \mathrm{d}r, \\ M_h &= \frac{4\pi}{3} \frac{(\rho_h \rho_h)^3}{\rho_h^2} \approx \frac{4\pi}{3} \frac{\langle \rho_h R_h \rangle^3}{\langle \rho_h \rangle^2}.\end{aligned} \tag{5.6.1}$$

where R_h is the hot spot radius, defined as $R_h = R\,(T_i = T_i(0)/10)$, with $T_i(0)$ being the ion temperature at the center of the target.

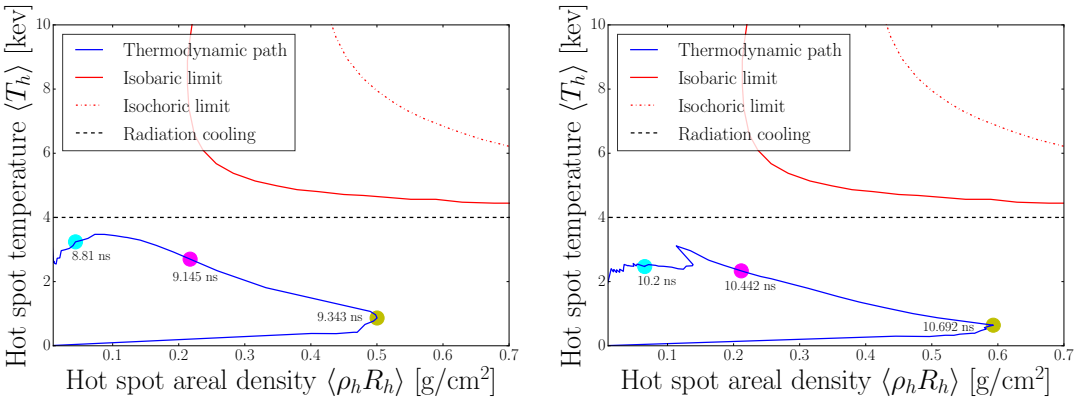

Figure 5.20 – Thermodynamic diagram of the hot spot in the $(\langle \rho_h R_h \rangle, \langle T_h \rangle)$ plane for HS (left) and SAI (right) schemes. Red solid (dotted-dashed) lines show the isobaric (isochoric) limit. Cyan, magenta and yellow dots show respectively the points at a tenth of peak neutron production, at peak neutron production and at peak areal density of the hot spot.

Similar results can be found for the 1D optimised *CHIC* simulations - the hot spots do not cross the ignition thresholds when no alpha-particles deposit their energy.

The most significant difference is observed in the areal density of the SAI scheme, which is significantly higher at the moment of maximum compression of the hot spot (indicated by the yellow dot in Figure 5.20). However, the hot spot temperature is notably low, falling below 1 keV. This decrease in temperature can be attributed to the increased hot spot radius. The loss mechanisms discussed in Section 2.5.2.4 cool the hot spot. The process of electron conduction can heat a thin layer of the surrounding cold matter, causing it to heat up and ablate. As a result, the mass of the hot spot increases over time. In some cases, it may happen that a hot spot initially cools, while its mass and $\langle \rho_h R_h \rangle$ increase. However, without the energy deposition from α-particles, the temperature cannot rise sufficiently for self-heating to occur. For clarity, the properties of the hot spot at these three times are provided in Table 5.6. The absorption fraction of the laser light on target is $f_{\mathrm{abs}}^{HS} = 96.2\%$, and $f_{\mathrm{abs}}^{SAI} = 92.2\%$. For SAI, during the spike, the fast increase to higher powers and intensities reduces the absorption fraction due to higher temperatures.

5.6.2 Target offset effects

We conduct a set of simulations with different target offsets, TO $\in \{9.45, 18.90, 28.35, 37.80, 75.60, 151.20\}$ μm, which correspond to TO $\in \{0.56, 1.11, 1.67, 2.22, 4.45, 8.89\}\%R$.

Table 5.6 Here is a summary of the properties of the hotspot in the HS scheme (left) and the SAI scheme (right) at the times indicated by colour in Figure 5.20. $\langle \rho_h R_h \rangle$ represents the averaged hot spot areal density, and $\langle T_h \rangle$ represents the averaged hot spot temperature. It is essential to note that, due to these definitions, $\langle \rho_h \rangle R_h \neq \langle \rho_h R_h \rangle$.

Case	Time [ns]	$\langle \rho_h R_h \rangle$ [g/cm^2]	$\langle T_h \rangle$ [keV]	$\langle \rho_h \rangle$ [g/cm^3]	R_h [μm]	M_h [mg]	Y_n [$\times 10^{16}$]
HS	8.81	0.04	3.24	16.10	171.50	1.35×10^{-3}	2.14
	9.15	0.22	2.70	61.25	128.50	1.14×10^{-2}	
	9.34	0.50	0.87	14.96	193.80	2.34	
SAI	10.20	0.07	2.47	27.57	147.52	1.55×10^{-3}	1.20
	10.44	0.21	2.33	58.21	117.78	1.17×10^{-2}	
	10.69	0.59	0.64	15.21	188.13	3.78	

These offsets are expected to modify negatively the target performance. We will study how the hot spot and the neutron production are impacted by these modifications.

Neutron yield scaling

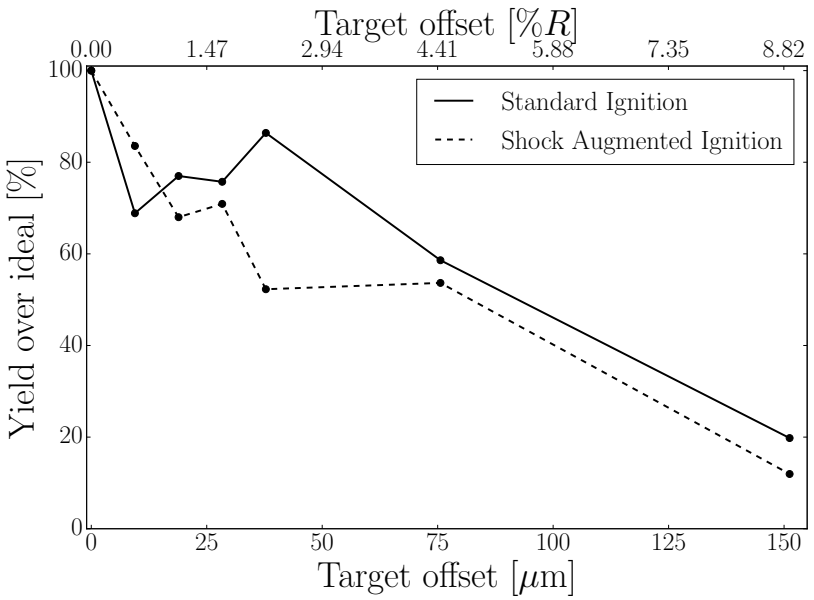

Figure 5.21 – Evolution of the neutron yield YOI as a function of the target offset. HS is shown in black solid lines and SAI is shown is black dashed lines. Neutron yields Y_n with no offset are shown in Table 5.6.

Figure 5.21 illustrates the yield over ideal (YOI) as a function of target offset for HS and SAI schemes. A small offset in both schemes results in a significant drop in neutron production. At a target offset of 9.45 μm (~ 0.56 % R), HS experiences a yield reduction, so that $\mathrm{YOI}^{\mathrm{HS}}_{0.56\%} = 68\%$, while SAI shows $\mathrm{YOI}^{\mathrm{SAI}}_{0.56\%} = 85\%$. Subsequently, HS's neutron yield increases to 86% for a target offset of 37.80 μm ($\sim 2.22\% R$). In contrast, SAI continues to decrease, reaching $\mathrm{YOI}^{\mathrm{SAI}}_{2.22\%} = 52\%$, plateauing with $\mathrm{YOI}^{\mathrm{SAI}}_{4.45\%} = 54\%$, and finally dropping significantly when the target offset reaches 151.20 μm ($\sim 8.89\% R$), with $\mathrm{YOI}^{\mathrm{SAI}}_{8.89\%} \approx 12\%$. On the other hand, from 37.80 μm ($\sim 2.22\% R$) to 151.20 μm

($\sim 8.89\%R$) target offset, HS's YOI decreases almost linearly (although only three data points are available) with the target offset, dropping to $\text{YOI}^{\text{HS}}_{151.20} \approx 20\%$.

In summary, for very low offset errors ($\Sigma_{\text{TO}} < 9.45\mu\text{m} \approx 0.56\%R$), SAI is more robust, exhibiting a higher yield ($\text{YOI}^{\text{HS}}_{\leq 0.56\%} > \text{YOI}^{\text{SAI}}_{\leq 0.56}$). For higher and intermediate offsets ($18.90\mu\text{m} \leq \Sigma_{\text{TO}} \leq 75.60\mu\text{m}$ or $1.11\%R \leq \Sigma_{\text{TO}} \leq 4.45\%R$), HS demonstrates more robustness to offset. For superior offsets, despite a lack of data points, both schemes exhibit similar results, decreasing with comparable slopes. Considering typical Ω60 offset errors ($\Sigma_{\text{TO}} \approx 0.56\%R$), SAI is expected to be more robust. However, a target offset accuracy of 10 μm in an ignition scale facility may not be realistic. Said differently, target offset accuracy may not scale linearly with the scale of a larger experimental required to drive the larger target.

Finally, a comparison between Figures 5.21 and 5.17 is provided. In both configurations, alpha particles are effectively excluded from the simulations. In Figure 5.21, when the SAI scenario shows a 50% (YOI-no-alpha) with a target offset between about $2\%R$ and $4.4\%R$, it can be compared to the 50% YOI no-alpha contour seen in the bottom-right quadrant of Figure 5.17. Looking at the simulations corresponding to this contour in Figure 5.15, where alpha particle effects are active, reveals a significant yield loss of nearly 40%. While this estimate is rough, it gives us a sense of the actual yield reduction.

We now analyse the behaviours of the target offsets in order to understand the yield scaling.

Spherical harmonics decomposition

In Figure 5.22, we present the evolution over time of the mode 1 (top) and mode 2 (bottom) amplitudes for both HS (solid lines) and SAI (dashed lines). Different colors represent various simulations with different offsets. The left side shows the plots in a linear scale, while the right side depicts the figures in a logarithmic scale.

From the right figures, we observe the exponential growth of the modes with time. Additionally, the peak amplitude of the modes shifts towards earlier times with increasing offset. Moreover, the higher the offset, the higher the peak amplitude of the modes. For instance, for HS, the mode 1 ρR amplitude is less than $10^{-3}\%$ at peak neutron production ($t \approx 9.15$ ns) with no offset. However, it peaks at approximately 15% at peak neutron production ($t \approx 8.9$ ns) for an offset $\Sigma_{\text{BM}} = 8.89\ \%R$. Similar trends can be observed for all other offsets and designs.

From the logarithmic plots, the impact of system errors on the initial quality of laser irradiation becomes evident. At $t = 0$ ns, for offsets greater than 1.67 $\%R$, the initial ρR mode 1 amplitude has increased by at least a factor of 100, and even by 10^4 for the highest offsets. The trends are consistent for different offsets, indicating that the initial irradiation significantly determines the implosion quality. Both left and right figures for mode 1 agree on showing the exponential increase of the ρR mode 1 amplitude over time.

Lastly, it appears that doubling the offset roughly doubles the mode 1 amplitude at a specific time for a given design. For example, for HS at $\Sigma_{\text{BM}} = \{2.22, 4.45, 8.89\}$ μm, the σ_1 values are $\{3.4, 7.1, 14.8\}\%$ at a tenth of peak neutron production. At peak neutron production, for the same target offset errors, the σ_1 values are $\{3.8, 8.1, 19.2\}\%$. Similar observations can be made for SAI, yielding comparable results.

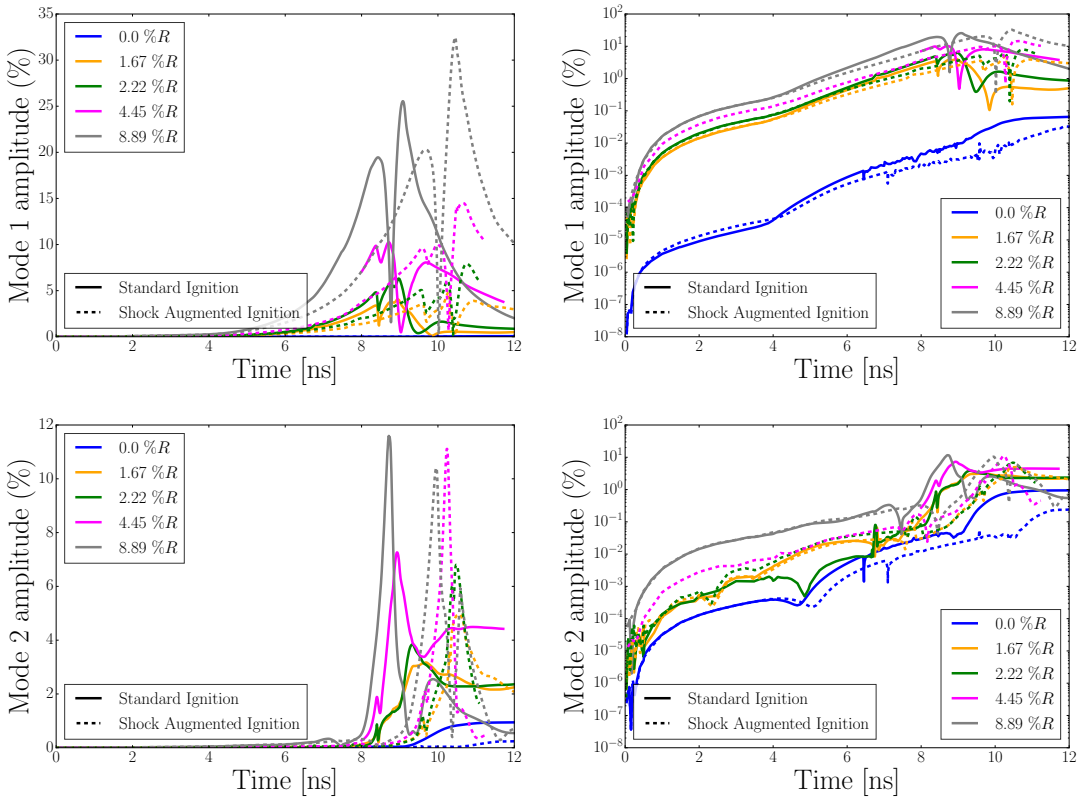

Figure 5.22 – ρR mode 1 (top) and mode 2 (bottom) amplitude evolution as a function of time for HS and SAI schemes and various target offsets. Solid lines are the HS and dashed lines are for SAI. Colored lines are for the different offsets. Left is in linear scale and right is in logarithm scale.

In the bottom figure, the ρR mode 2 amplitude is displayed. It is observed that mode 2 also increases over time with increasing offset, but the differences are less pronounced. System errors, particularly target offset, strongly induce mode 1 amplitude increase, as it favors one specific direction (aligned with the offset). Higher modes do not exhibit significant changes with the modification of the offset.

Examining the left linear scale in Figures 5.22, we observe that the maximum mode amplitudes ($l = 1$) are comparable for both HS and SAI. It is noteworthy that the mode amplitude for SAI consistently remains below that of HS. This difference can be attributed to the lower implosion velocities associated with SAI, resulting in a slower growth of its mode amplitudes compared to HS. As the offset increases, the distinction between HS and SAI becomes less evident, with their maximum amplitudes gradually becoming more comparable.

This discussion on $l = 1$ mode evolution does not help explain the discrepancies found in hot spot performances.

Hot spot degradation

The thermodynamic diagrams in Figure 5.23, illustrating the hot spot behaviour in the $(\langle \rho_h R_h \rangle, \langle T_h \rangle)$ plane for HS (left) and SAI (right) schemes, reveal important insights. The solid-coloured curves represent simulations with different offsets, and the blue curve corresponds to the reference case with no offset.

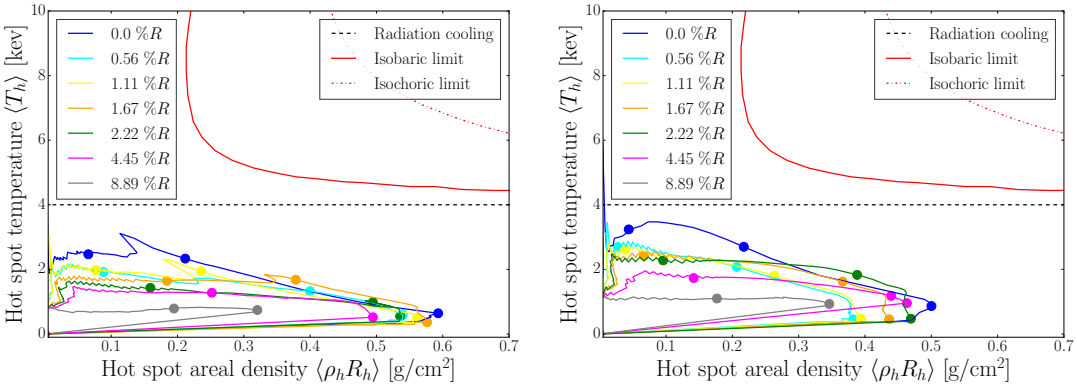

Figure 5.23 – Thermodynamic diagram of the hot spot in the $(\langle\rho_h R_h\rangle, \langle T_h\rangle)$ plane for HS (left) and SAI (right) schemes and for various target offsets. Red solid (dotted-dashed) lines show the isobaric (isochoric) limit. Scattered dots show respectively the points at a tenth of peak neutron production, at peak neutron production and at peak areal density of the hot spot.

In both figures, a consistent decrease in the average hot spot temperature ($\langle T_h\rangle$) is observed at all times. This temperature reduction is evident for all cases, even at the smallest offset values. As the offset increases, the average temperature of the hot spot decreases. For instance, at $\Sigma_{\mathrm{TO}} = 0.56$ $\%R$, the temperature drops by approximately 0.5 keV for both SAI and HS. This behaviour may be associated with the convergence ratio depicted in Figure 5.24. The target convergence ratio C_d systematically decreases with the offset. As the hot spot temperature scales quadratically with C_d (see Equation (2.5.33)), this trend could account for the observed temperature reduction.

Additionally, in this figure, a correlation is observed between the convergence ratio C_d and neutron yield observed in Figure 5.21, as both figures follow very similar trends, especially when normalizing the convergence ratio by its maximum initial value with no offset (right Figure 5.24).

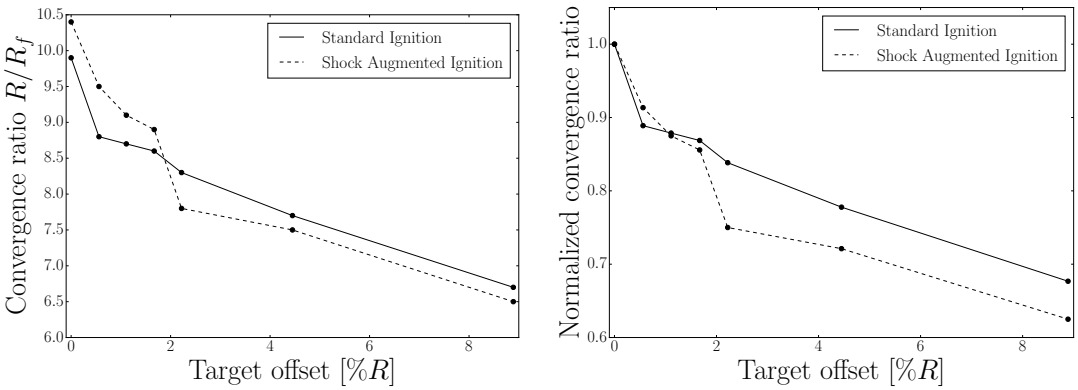

Figure 5.24 – Evolution of the target convergence ratio C_d as a function of the target offset. Solid black lines are for the HS design and dashed black lines are for the SAI. Right figure corresponds to the normalized convergence ratio showing the drop with the target offset.

The behaviour of the averaged hot spot areal density ($\langle\rho_h R_h\rangle$) is distinctive for each scheme. For HS, it initially decreases with lower offsets, reaching $\langle\rho_h R_h\rangle \approx 0.39$ g/cm^2

at $\Sigma_{\text{TO}} = 0.56\%R$. It then increases back to around $\langle \rho_h R_h \rangle \approx 0.47$ g/cm^2 until $\Sigma_{\text{TO}} = 2.22\%R$. Subsequently, it gradually decreases again, reaching $\langle \rho_h R_h \rangle \approx 0.46$ g/cm^2 at $\Sigma_{\text{TO}} = 4.45\%R$, followed by a significant drop to $\langle \rho_h R_h \rangle \approx 0.35$ g/cm^2 at $\Sigma_{\text{TO}} = 8.89\%R$.

For SAI, the behaviour of $\langle \rho_h R_h \rangle$ is distinct from HS. It initially decreases with lower offsets, reaching $\langle \rho_h R_h \rangle \approx 0.54$ g/cm^2 at $\Sigma_{\text{TO}} = 0.56\%R$. It then increases to around $\langle \rho_h R_h \rangle \approx 0.58$ g/cm^2 until $\Sigma_{\text{TO}} = 1.67\%R$. Subsequently, it gradually decreases again, reaching $\langle \rho_h R_h \rangle \approx 0.54$ g/cm^2 at $\Sigma_{\text{TO}} = 4.45\%R$, followed by a significant drop to $\langle \rho_h R_h \rangle \approx 0.33$ g/cm^2 at $\Sigma_{\text{TO}} = 8.89\%R$. For more clarity, in Figure 5.25, we pick a time (a tenth of peak neutron production) and we show the evolution of the $\langle \rho_h R_h \rangle$ and $\langle T_h \rangle$ as a function of the target offset for both ignition designs. It essentially shows that the hot spot temperature decreases with the offset, and the hot spot reaches higher areal densities at a tenth of peak neutron production.

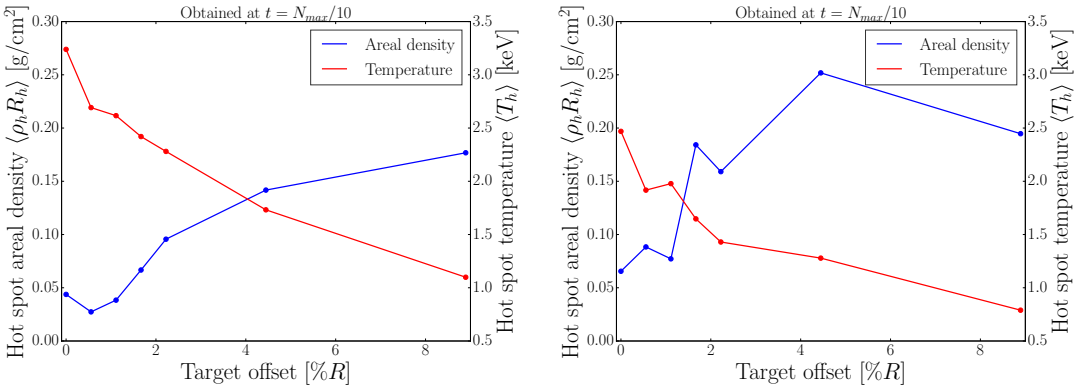

Figure 5.25 – Evolution of the averaged hot spot areal density density (blue) and temperature (red) for HS (left) and SAI (right) at a tenth of peak neutron production while increasing the target offset.

In the extreme case of $\Sigma_{\text{TO}} = 8.89\%R$, which exhibits poor target performance (low temperature, areal density, neutron yield, and high mode amplitudes), it is suggested that the target has been punctured. Such high system errors should be avoided definitively.

These observations provide valuable information about the impact of target offsets on the thermodynamic properties of the hot spot in both HS and SAI schemes.

5.7 Conclusions

In the study of ICF spherical implosions, the quality of irradiation plays a crucial role, particularly in the early stages of the implosion process. Small defects in the irradiation pattern can lead to the generation of low-modes in the spherical harmonics decomposition of the laser intensity. These low-modes are detrimental as they have the potential to significantly impact the performance of the target and may even prevent successful ignition.

To address this issue, our investigation focused on three different chamber geometry designs: the charged particle method $M72$, the spherical t-design $T72$, and the triangulated icosahedron $I80$. For each of these designs, we conducted idealised optimisation studies, where we systematically modified various spatial laser parameters, such as the super Gaussian order and the $1/e$ radii of the lasers. The goal was to identify the optimal

set of parameters for each design that would result in the most uniform laser irradiation on a solid sphere target (see Table 5.1).

It is important to note that in this initial study, we did not account for experimental errors. Subsequently, using the *IFRIIT* code, we performed solid-sphere illuminations to assess the sensitivity of these designs to system errors. Upon further investigation and the inclusion of experimental errors typically observed at the Ω60 laser facility, we found that the $I80$ design exhibited the most robust results. This suggests that, among the considered chamber geometries, $I80$ is more resilient to variations and uncertainties introduced by experimental conditions. This insight is valuable for designing and optimising ICF experiments, especially in scenarios where experimental errors play a significant role.

Continuing our investigation, we delved into the robustness of different ignition schemes, namely standard hot spot ignition (HS) and shock augmented ignition (SAI), under the influence of experimental errors. This study focused on a specific beam chamber geometry design. Employing both 1D and 3D radiative hydrodynamics simulations, facilitated by the *CHIC* and *ASTER* codes, respectively, we characterized the typical optimal ignition-scale target performances, assuming no system errors.

To assess the impact of experimental errors, we systematically increased the target offset, aiming to identify the point at which target performances became so degraded that the compression was considered as punctured. Notably, for low offset errors similar to those encountered at the Ω60 facility, the SAI approach exhibited superior hot spot performances. However, for target offsets greater than or equal to $1\%R$, HS demonstrated more robustness to target offset variations. This was evidenced by higher neutron yields, elevated averaged hot spot temperatures, and a longer-lived hot spot in the HS scheme under such conditions. We further approximated that with a target offset ranging between 2% and 4.4%, the neutron yield for the SAI configuration would experience a reduction of around 40%.

It is crucial to acknowledge that the absence of α-particle energy deposition in these simulations may influence the results. The SAI scheme showed a higher hot spot areal density. This could potentially lead to the hot spot capturing a larger fraction of the α-particles, suggesting that α-particles could deposit their energy more effectively within the hot spot and surrounding layers, increasing the chances of heating up and possibly achieving ignition. Therefore, the consideration of α-particle energy deposition may alter the comparative robustness of the two ignition schemes under certain conditions.

Chapter 6

Conclusion

The understanding of low modes and laser-target coupling play crucial roles in the study of inertial fusion energy. The validation of state-of-the art 3D radiative hydrodynamics codes is then necessary. In this context, examining the CBET models becomes an essential aspect, ensuring accuracy in simulations and contributing to the design of future direct-drive facilities. Additionally, investigating laser homogeneity on target is imperative for understanding its impact on the overall system. On this basis, the objectives of this Ph.D. were the following:

- **Assessing the accuracy of the CBET linear kinetic model and laser coupling in the 3D radiative hydrodynamics coupled code *ASTER/IFRIIT* at the ignition scale**. The coupling between the two codes already showed promising and robust results at the reduced OMEGA scale. *ASTER/IFRIIT* is now tested at the NIF scale in the characteristic case of specific laser geometries and laser intensities close to the SI regime where CBET is prominent.

- **Optimisation of novel beam chamber geometries for the future direct-drive facilities at the ignition scale**. Using the inverse ray-tracing code *IFRIIT* to illuminate solid spheres, innovative geometries are compared to study their robustness to persistent experimental errors. It aims to identify which geometries give the optimum laser irradiation for direct-drive ICF.

- **Characterisation of two ignition schemes robustness to experimental errors at the ignition scale**. Using the 3D radiative hydrodynamics *ASTER/IFRIIT* coupled code, simulations with standard hot spot and shock ignition schemes at the ignition scale using optimised beam chamber geometries are performed. The investigation of target and hot spot performances while increasing experimental errors for both schemes is studied.

6.1 Assessing the accuracy of the CBET linear kinetic model and laser coupling in the 3D radiative hydrodynamics coupled code *ASTER/IFRIIT* at the ignition scale

In DD ICF, high power laser beams are used to implode a spherical shell constituted of gaseous DT fuel surrounded by solid DT and a plastic ablator. In the central hot spot scheme, the mechanical work communicated to the gas prior to target stagnation ignites the DT gas, creating a thermonuclear burn wave in the solid DT fuel and providing significant energy release and gain. Alternative schemes, such as shock ignition (SI), decouple the compression and ignition phases in order to improve energy gain, and scheme robustness.

For such laser intensities, the interaction parameter $I\lambda_L^2$ exceeds the threshold value of 10^{14} W µm^2/cm^2 (usually, ICF lasers operate at a wavelength $\lambda_L = 0.351$ µm). The laser-plasma interaction becomes prone to numerous couplings between electromagnetic and plasma waves. Most of these additional processes have non-linear behaviours and are in general harmful to fusion-related implosions. Among these couplings, the overlap between several laser waves in the plasma produces ponderomotive beatings able to drive IAWs. An energy exchange through diffraction on a commonly excited IAW electron density perturbation is likely to occur. This three-wave interaction is commonly known as CBET.

CBET, being a type of SBS, may occur in the whole volume of the underdense plasma ($n_e \leq n_c$). It is therefore an efficient process in long scale-length plasmas, which is the case for NIF ICF experiments. CBET is especially prominent in the polar-direct-drive (PDD) geometry used on NIF to approach DD ICF. Because of this scattering phenomenon, laser beams fail to penetrate deeply enough into the plasma causing a significantly reduced laser-target coupling and an enhancement of low mode asymmetries. Beam overlap is large and energy exchange between beams lead to large-scale modulations to the laser drive.

Recently, an inverse-ray tracing laser model without *ad hoc* parameters, *IFRIIT* [5], [72], specifically designed for DD ICF was implemented inline in the 3D radiative hydrodynamics code *ASTER* [4], [52]. CBET was efficiently modeled in *IFRIIT* and the coupling between the two codes shows promising and robust results at the reduced OMEGA scale.

In this context, a series of experiments was performed at the NIF to diagnose energy coupling in PDD using plastic solid sphere targets. These experiments aim to study the efficiency of the laser energy coupling to a spherical target with beam intensities close to the standard SI regimes. These solid spheres offer the advantage of quantifying energy coupling without the challenges from hydrodynamic instabilities of thin-shell implosions or kinetic effects in exploding pushers. Similar experiments on OMEGA with scaled solid spheres were performed to test the scaling arguments of PDD implosions from OMEGA to the NIF. Good agreement was obtained between the measured data (shock trajectories and shock collapse) with the trajectories from 2D *DRACO* radiation-hydrodynamics simulations using CBET and non-local heat-transport models. However, these models at the NIF scale were manually adjusted to reproduce the experimental data (with several ad-hoc parameters on the laser profile and CBET coefficient), and hence cannot be consid-

ered to be robust for that scale. In addition, more detailed quantities such as the angular dependence of scattered light is not reproduced correctly. In particular, this prevents more general studies of the ICF concept at these scales and in presence of large amounts of CBET (which is notably the case of SI). Conversely, *IFRIIT* has no free parameters in its CBET modelling, due to novel algorithms implemented specifically to that end. *ASTER/IFRIIT* has been well validated at OMEGA scale and was applied to the NIF scale in this work.

Our initial focus was on validating the *ASTER* radiation hydrodynamics (radhydro) and the *IFRIIT* model in general. This comprehensive model incorporates CBET, laser transport, and absorption calculations. While the PDD experiments inherently involve CBET, our validation effort extends beyond CBET alone. This validation is crucial for assessing the accuracy of hydrodynamics and coupling in general, providing a solid base for their application in ignition-scale bandwidth studies but also subsequent solid-sphere illuminations and 3D implosion ignition scale simulations.

The characterization of the 10 mm defocused NIF beam spots used in the SSS experiments was incorporated into *IFRIIT* to provide a more detailed description of the laser beams. The CBET model implemented in *IFRIIT*, coupled inline with *ASTER*, was thoroughly investigated at the ignition/NIF scale. This involved comparing shock positions and scattered light maps in solid-sphere coupling experiments. The laser absorption in the coupled code was validated against experimental results from FABS and SLTD. While the shock time collapse exhibited some deviation, further improvements were identified by incorporating a more detailed and comprehensive model for CBET in *IFRIIT*, encompassing polarized CBET and the Langdon effect on CBET. Although this more advanced model demands greater computational resources (four times that of CBET alone), it enhances accuracy because it describes the transport and rotation of laser polarization in the plasma, its effect on CBET coupling and the effect of CBET itself on polarization. Additionally, the use of a recent model for Coulomb logarithm, accounting for Langdon effect, screening corrections, and a Coulomb logarithm dependent on laser frequency rather than plasma frequency, has shown promise in laser absorption. This model has demonstrated accurate results in comparison to measurements performed for numerous OMEGA shots, particularly at low plasma densities ($n_e \leq 0.05\ n_c$). With these advancements, the *ASTER/IFRIIT* code stands as a robust tool for confidently studying the physics of shock ignition for ICF at full scale.

6.2 Optimisation of novel beam chamber geometries for the future direct-drive facilities at the ignition scale

A decade of experiments at the National Ignition Facility has demonstrated the credibility of inertial confinement fusion as a viable approach to energy production, surpassing the ignition regime [2]. However, the indirect-drive method, while successful, may not be ideal for high-gain implosions and reliable energy production. The direct-drive ignition approach is favored due to its simpler target designs and enhanced energy coupling, making it a promising candidate for energy production. Unfortunately, there is currently no ignition-scale laser facility configured for the standard direct-drive approach. Integrated direct-drive experiments have primarily focused on understanding physics at reduced scales, aiming to justify and demonstrate the necessity and feasibility of constructing an international direct-drive laser facility. While direct-drive offers better energy

coupling than the indirect-drive method, achieving high irradiation homogeneity remains challenging due to the limited number of beams.

To address this issue, our investigation focused on three different chamber geometry designs: the charged particle method $M72$, the spherical t-design $T72$, and the triangulated icosahedron $I80$.

The *IFRIIT* code is employed offline to assess uniformity on ignition-scale targets. The tool assumes laser beams associated with each direction of irradiation, all directed toward the sphere center. This 3D numerical tool evaluates capsule illumination uniformity, accounting only for direct illumination without refraction during the initial nanoseconds of the laser pulse. Each irradiation scheme is characterized by intrinsic nonuniformity, depending on the laser spatial power profile (super-gaussian order and $1/e$ radius of the laser spot). The study aims to scan the parameter space to find the minimum this intrinsic nonuniformity for each design before analyzing additional factors such as the number of beams, beam patterns, laser shaping, and system errors.

The results highlight the importance of a comprehensive control approach that addresses all these factors for optimal irradiation uniformity. It is shown that enhancing one aspect alone does not guarantee improved performance; instead, simultaneous optimisation of all factors is crucial. Achieving optimal uniformity requires controlling beam profiles and minimising system imperfections simultaneously. A high level of uniformly irradiated beams with a low rms value (approximately $\sigma_{\text{tot}} \approx 0.5\%$) is achievable through this synergistic approach, maintaining $\Sigma_{\text{err}} \leq 1.0\%$.

Upon deeper exploration and the consideration of experimental errors commonly encountered at the $\Omega 60$ laser facility, it became evident that the $I80$ design showcased the most robust outcomes. This implies that, among the examined chamber geometries, $I80$ exhibits greater resilience to fluctuations and uncertainties introduced by experimental conditions. This understanding holds substantial value for the design and optimisation of ICF experiments, particularly in situations where experimental errors significantly influence outcomes.

The study concludes that designs $I80$ and $T72_4$ exhibit greater robustness compared to others under typical $\Omega 60$ system errors. However, further optimisation considering system errors is required. The analysis also suggests that the $I80$ design is more robust in the face of typical $\Omega 60$ system errors, and enlarging the laser spot size tends to enhance illumination homogeneity to the expense of beam-target intersection.

In summary, optimising the irradiation system alongside the beam pattern is crucial. The $I80$ design, in particular, shows promise for achieving a high beam-target intersection comparable to $\Omega 60$ while maintaining lower RMS (approximately 1% lower than $\Omega 60$).

6.3 Characterisation of two ignition schemes robustness to experimental errors at the ignition scale

In the examination of ICF spherical implosions, the quality of irradiation emerges as a critical factor, especially during the initial stages of the implosion process. Even minor imperfections in the irradiation pattern can result in the generation of low-modes within the spherical harmonics decomposition of the laser intensity. The presence of these low-modes is highly detrimental, as it has the capacity to substantially degrade

the performance of the target and, in severe cases, hinder the achievement of successful ignition.

Building on our investigation, we delved into the resilience of different ignition schemes — standard hot spot ignition (HS) and shock augmented ignition (SAI) — when subjected to the influence of experimental errors. This comprehensive study focused on a specific beam chamber geometry design. Leveraging both 1D and 3D radiative hydrodynamics simulations, using the *CHIC* and *ASTER* codes, respectively, we characterized the typical optimal ignition-scale target performances while assuming no system errors.

To gauge the impact of experimental errors, we systematically increased the target offset, aiming to pinpoint the threshold at which target performances degraded to the point of considering the target as punctured. Significantly, for low offset errors resembling those encountered at the Ω60 facility, the SAI approach exhibited superior hot spot performances. However, for target offsets equal to or greater than $1\%R$, HS demonstrated more robustness to variations in target offset. This was evident through higher neutron yields, elevated averaged hot spot temperatures, and a longer-lived hot spot in the HS scheme under such conditions.

It is essential to note that the absence of α-particle energy deposition in these simulations may impact the results. The SAI scheme exhibited a higher hot spot areal density, potentially enabling the hot spot to capture a larger fraction of the α-particles. This suggests that α-particles could deposit their energy more effectively within the hot spot and surrounding layers, increasing the likelihood of heating up and possibly achieving ignition. Therefore, the inclusion of α-particle energy deposition could alter the comparative robustness of the two ignition schemes under specific conditions.

6.4 Perspectives

In the context of using the *ASTER/IFRIIT* coupled code for ICF ignition scale purposes, the incorporation of a polarised model for CBET and accounting for the Langdon effect on CBET gain has already improved the description of laser absorption. However, certain hydrodynamic effects, specifically the influence of high-energy (HE) particles on shock velocity, remain incompletely addressed. Existing simulations suggest a significant effect of the order of $\sim$ 200 ps, as reported in Reference [99]. Nevertheless, these simulations might overestimate HE effects due to the neglect of large-angle collisions. To provide a more accurate representation, a more robust method based on a 3D plasma Monte-Carlo approach, as implemented in References [117], [118], could be considered and integrated into the 3D hydrodynamics codes.

The study on innovative beam chamber geometries for irradiating ICF ignition-scale targets highlights the importance of optimising the irradiation system alongside the beam pattern. However, this investigation was conducted without considering the effects of laser-plasma interaction. A crucial next step in the study involves examining the effects of CBET, a known factor that degrades laser absorption and poses a risk of symmetry breaking. It is worth noting that future direct-drive facilities should consider using large bandwidth lasers to mitigate the deleterious effects of CBET [132], [135]. This additional investigation will contribute to a more comprehensive understanding of the interplay between laser-plasma interactions, hydrodynamics, and beam-target interactions.

Moreover, there are additional unanswered questions in this context. For instance,

determining the optimal number of lasers per beam port for a given design remains an open question. Additionally, selecting designs that facilitate electricity production poses another challenge. It has been observed that mitigating CBET is more effective when employing a higher super-Gaussian order for the beam spatial profile, as highlighted in [132]. Furthermore, investigations indicate that a beamlet-based driver may require approximately 10 beamlets of different wavelengths per port. As a result, a laser system with a total energy of 1.3 MJ, employing beamlets of at least 1.6 kJ each, has the potential to achieve efficient CBET mitigation, particularly with a minimum of 80 ports, as exemplified by the $I80$ geometry.

In light of these considerations, a more comprehensive approach, akin to the methodology employed for PDD at the NIF, as outlined in [136], could be adopted. This involves leveraging Artificial Intelligence (AI) to develop a new, efficient algorithmic approach for creating illumination configurations in laser-driven high-energy density physics experiments. This approach holds promise for streamlining the process and addressing some of the challenges associated with designing and optimizing laser-driven systems.

Additionally, the adaptability of this method is not restricted to spherical Polar Direct-Drive (PDD) configurations; it can be customised for implosion targets as well. Its versatility across different geometries positions it as a valuable tool for optimising illumination uniformity in a variety of scenarios, including hohlraums. The algorithm's significance is further emphasised by its potential application to Direct Drive (DD). Anticipating future DD designs requiring multiple beams per port to balance drive uniformity and chamber efficiency [132], [137], the limitations of traditional techniques become apparent, necessitating iterative optimisation methods for achieving the requisite drive uniformity.

Conclusion

La compréhension des bas modes et du couplage laser-cible joue un rôle crucial dans l'étude de l'énergie de fusion intertielle. La validation des codes à l'état de l'art d'hydrodynamique radiative 3D est ainsi nécessaire. Dans ce contexte, examiner les modèles de CBET devient un aspect essentiel, assurant la précision des simulations, la prédiction et compréhension des expériences et contribuant à la conception des futures installations d'attaque directe. De plus, l'exploration de l'homogénéité de l'éclairement laser sur cible est impérative pour comprendre son impact sur l'ensemble du système. Sur cette base, les objectifs de cette thèse étaient les suivants :

- **Évaluation de la précision du modèle cinétique linéaire de CBET et du couplage laser dans le code couplé d'hydrodynamique radiative 3D *ASTER/IFRIIT* à l'échelle de l'allumage**. Le couplage entre les deux codes a déjà montré des résultats prometteurs et robustes à l'échelle réduite d'OMEGA. *ASTER/IFRIIT* est maintenant testé à l'échelle du NIF dans le cas caractéristique de géométries laser spécifiques et d'intensités laser proches du régime SI où le CBET est prédominant.

- **Optimisation de nouvelles géométries de chambre laser pour les futures installations d'attaque directe à l'échelle de l'allumage**. En utilisant le code de tracé de rayons inverse *IFRIIT* pour illuminer des sphères solides, des géométries innovantes de disposition des faisceaux lasers sont comparées pour étudier leur robustesse face à des erreurs expérimentales persistantes. L'objectif est d'identifier les géométries qui offrent l'éclairement laser le plus optimal pour la FCI en attaque directe.

- **Caractérisation de la robustesse de deux schémas d'allumage aux erreurs expérimentales à l'échelle de l'allumage**. En utilisant le code couplé d'hydrodynamique radiative 3D *ASTER/IFRIIT*, des simulations avec des schémas d'allumage standard par point chaud central et d'allumage par choc à l'échelle de l'allumage sont réalisées. Une géométrie de chambre laser robuste précédemment optimisée est utilisée. L'étude des performances de la cible et du point chaud tout en augmentant les erreurs expérimentales pour les deux schémas est examinée.

Évaluation de la précision du modèle cinétique linéaire de CBET et du couplage laser dans le code 3D *ASTER-/IFRIIT* à l'échelle de l'allumage

En FCI d'attaque directe, des faisceaux lasers de haute puissance sont utilisés pour imploser une coquille sphérique constituée de combustible gazeux DT entouré de DT solide et d'un ablateur en plastique. Dans le schéma du point chaud central, le travail mécanique communiqué au gaz avant la stagnation de la cible enflamme le gaz DT, créant une onde de combustion thermonucléaire dans le combustible DT solide et fournissant une libération d'énergie significative et un gain.

Des schémas alternatifs, tels que l'allumage par choc, séparent les phases de compression et d'allumage afin d'améliorer le gain énergétique et la robustesse du schéma.

Pour de telles intensités laser, le paramètre d'interaction $I\lambda_L^2$ dépasse la valeur seuil de 10^{14} W µm^2/cm^2 (généralement, les lasers de FCI fonctionnent à une longueur d'onde $\lambda_L = 0.351$ µm). L'interaction laser-plasma devient sujette à de nombreux couplages entre les ondes électromagnétiques et les ondes plasma. La plupart de ces processus supplémentaires présentent des comportements non linéaires et sont généralement préjudiciables aux implosions liées à la fusion. Parmi ces couplages, le chevauchement entre plusieurs ondes laser dans le plasma produit des battements ponderomotifs capables de générer des ondes acoustiques ioniques. Un échange d'énergie par diffraction sur une perturbation de densité électronique excitée est susceptible de se produire. Cette interaction à trois ondes est communément appelée CBET.

Le CBET, étant un type de diffusion Brillouin stimulée, peut se produire dans l'ensemble du volume du plasma sous-dense ($n_e \leq n_c$). C'est donc un processus efficace dans les plasmas présentant des longueurs d'échelle importantes, comme c'est le cas pour les expériences de FCI sur le NIF. Le CBET est particulièrement prépondérant dans la géométrie PDD utilisée sur le NIF pour approcher la FCI en attaque directe. En raison de ce phénomène de diffraction, les faisceaux laser ne pénètrent pas suffisamment profondément dans le plasma, entraînant un couplage laser-cible significativement réduit et une amplification des asymétries de bas modes. Le chevauchement des faisceaux est important, et l'échange d'énergie entre eux entraîne des modulations à grande échelle de l'intensité laser.

Récemment, un modèle laser de tracé de rayons inverse sans paramètres *ad hoc*, *IFRIIT*[5], [72], spécifiquement conçu pour la FCI en attaque directe, a été intégré en ligne dans le code d'hydrodynamique radiative 3D *ASTER*[4], [52]. Le CBET a été modélisé de manière efficace dans *IFRIIT* et le couplage entre les deux codes montre des résultats prometteurs et robustes à l'échelle réduite d'OMEGA.

Dans ce contexte, une série d'expériences a été réalisée au NIF pour diagnostiquer le couplage d'énergie en PDD en utilisant des cibles sphériques en plastique. Ces expériences visent à étudier l'efficacité du couplage de l'énergie laser à une cible sphérique avec des intensités de faisceau proches des régimes de l'allumage par choc. Ces sphères solides présentent l'avantage de quantifier le couplage d'énergie sans les défis liés aux instabilités hydrodynamiques des implosions à coquille mince. Des expériences similaires sur OMEGA avec des sphères solides mises à l'échelle ont été réalisées pour tester les arguments d'échelle des implosions PDD d'OMEGA au NIF. Un bon accord a été obtenu entre les données mesurées (trajectoires de choc et arrivée de choc au centre de la cible)

et les trajectoires des simulations d'hydrodynamique radiative 2D *DRACO* utilisant les modèles CBET et de transport de chaleur non local. Cependant, ces modèles à l'échelle du NIF ont été ajustés manuellement pour reproduire les données expérimentales (avec plusieurs paramètres *ad hoc* sur le profil laser et le coefficient de CBET), et ne peuvent donc pas être considérés comme robustes pour cette échelle. De plus, des grandeurs plus détaillées telles que la dépendance angulaire de la lumière diffusée ne sont pas reproduites correctement. En particulier, cela empêche des études plus générales du concept de FCI à ces échelles et en présence de grandes quantités de CBET. À l'inverse, *IFRIIT* n'a aucun paramètre libre dans sa modélisation du CBET, en raison de nouveaux algorithmes mis en œuvre spécifiquement à cette fin. *ASTER/IFRIIT* a été bien validé à l'échelle d'OMEGA et a été appliqué à l'échelle du NIF dans ce travail.

Notre attention initiale s'est portée sur la validation de l'hydrodynamique radiative d'*ASTER* et du modèle laser *IFRIIT* en général. Ce modèle complet intègre le CBET, le transport laser et les calculs d'absorption. Bien que les expériences en PDD impliquent intrinsèquement le CBET, notre effort de validation va au-delà du seul CBET. Cette validation est cruciale pour évaluer l'exactitude de l'hydrodynamique et du couplage en général, fournissant une base solide pour leur application dans des études à l'échelle de l'allumage, mais aussi pour des illuminations de sphères solides ultérieures et des simulations d'implosion 3D à l'échelle de l'allumage.

La caractérisation des tâches des faisceaux NIF défocalisés de 10 mm utilisées dans les expériences SSS a été intégrée dans *IFRIIT* pour fournir une description plus détaillée des faisceaux laser. Le modèle CBET implémenté dans *IFRIIT*, couplé en ligne avec *ASTER*, a été soigneusement étudié à l'échelle de l'allumage/NIF. Cela impliquait une comparaison des positions des chocs et des cartes de lumière diffusée dans des expériences de couplage avec des sphères solides. L'absorption laser dans le code couplé a été validée par rapport aux résultats expérimentaux des diagnostics FABS et SLTD. Bien que l'arrivée temporelle au centre de la cible du choc présentait certaines différences, des améliorations supplémentaires ont été identifiées en incorporant un modèle plus détaillé et complet pour le CBET dans *IFRIIT*, englobant le CBET polarisé et l'effet Langdon sur le CBET. Bien que ce modèle plus avancé demande des ressources informatiques plus importantes (quatre fois plus que le CBET seul), la précision en est améliorée car le modèle décrit le transport et la rotation de la polarisation du laser dans le plasma, son effet sur le couplage CBET et l'effet du CBET lui-même sur la polarisation. De plus, l'utilisation d'un modèle récent pour le logarithme Coulombien, prenant en compte l'effet Langdon, les corrections d'écrantage, et une dépendance sur la fréquence laser plutôt que sur la fréquence du plasma, a montré des résultats prometteurs dans l'absorption laser. Ce modèle a démontré des résultats précis par rapport aux mesures effectuées pour de nombreux tirs OMEGA, notamment à de faibles densités de plasma ($n_e \leq 0,05\ n_c$). Avec ces avancées, le code *ASTER/IFRIIT* se présente comme un outil robuste pour étudier de manière fiable la physique de l'allumage par choc pour la FCI à pleine échelle.

Optimisation de nouvelles géométries de chambres expérimentales pour les futures installations en attaque directe à l'échelle de l'allumage

Les récentes campagnes expérimentales menées au National Ignition Facility ont démontré la crédibilité de la fusion par confinement inertiel comme une approche viable pour la production d'énergie, dépassant le régime d'allumage [2]. Cependant, la méthode d'attaque indirecte, bien qu'elle soit couronnée de succès, peut ne pas être idéale pour des implosions à gain élevé et une production d'énergie fiable. L'approche d'allumage par attaque directe est privilégiée en raison de ses conceptions de cible plus simples et d'un couplage énergétique amélioré, en faisant un candidat prometteur pour la production d'énergie. Malheureusement, il n'existe actuellement aucune installation laser à l'échelle de l'allumage configurée pour l'approche d'attaque directe standard. Les expériences intégrées en attaque directe se sont principalement concentrées sur la compréhension de la physique à des échelles réduites, cherchant à justifier et démontrer la nécessité et la faisabilité de construire une installation laser internationale dédiée à l'attaque directe. Bien que l'attaque directe offre un meilleur couplage énergétique que la méthode d'attaque indirecte, obtenir une homogénéité d'éclairement suffisante reste un défi en raison du nombre limité de faisceaux.

Pour résoudre cette problématique, notre étude s'est concentrée sur trois conceptions de géométrie de chambre différentes : la "charged particle method" $M72$, le "spherical t-design" $T72$ et la méthode des icosahèdres triangulés $I80$.

Le code *IFRIIT* est utilisé hors ligne (sans évolution hydrodynamique du système) pour évaluer l'uniformité sur des cibles à l'échelle de l'allumage. L'outil suppose des faisceaux laser associés à chaque direction d'éclairement, tous dirigés vers le centre de la sphère. Cet outil numérique en 3D évalue l'uniformité de l'éclairement de la capsule, en tenant compte uniquement de l'éclairement direct sans réfraction au cours des premières nanosecondes de l'impulsion laser. Chaque schéma d'éclairement (ici $I80$, $M72$, $T72$) est caractérisé par une non-uniformité intrinsèque, dépendant du profil de puissance du laser. L'étude minimise cette non-uniformité intrinsèque pour chaque design avant d'analyser des facteurs supplémentaires tels que le nombre de faisceaux, les motifs des faisceaux, la mise en forme du laser et les erreurs du système.

Les résultats soulignent l'importance d'une approche de contrôle globale prenant en compte tous ces facteurs pour garantir une uniformité d'éclairement optimale. Il est démontré que l'amélioration d'un seul aspect ne conduit pas nécessairement à des performances accrues ; au contraire, l'optimisation simultanée de tous les facteurs s'avère cruciale. Atteindre une uniformité optimale nécessite donc de contrôler simultanément les profils des faisceaux et de minimiser les imperfections du système. Cette approche permet d'obtenir un niveau élevé d'uniformité d'éclairement avec une faible valeur rms (environ $\sigma_{\text{tot}} \approx 0.5\%$), tout en maintenant $\Sigma_{\text{err}} \leq 1.0\%$.

Après une exploration plus approfondie et la prise en compte des erreurs expérimentales couramment rencontrées dans l'installation laser $\Omega 60$, il est devenu évident que la géométrie $I80$ présentait les résultats les plus robustes. Cela signifie que, parmi les géométries de chambre examinées, $I80$ présente une plus grande résistance aux fluctuations et aux incertitudes introduites par les conditions expérimentales. Cette connaissance présente une valeur substantielle pour la conception et l'optimisation des expériences FCI, en particulier dans les situations où les erreurs expérimentales influencent de manière sig-

nificative les résultats.

L'étude conclut que les configurations $I80$ et $T72_4$ se révèlent plus robustes que les autres face aux erreurs systématiques courantes d'Ω60. Cependant, une optimisation plus poussée, tenant compte des erreurs systématiques, demeure nécessaire. L'analyse supplémentaire suggère également que la configuration $I80$ affiche une plus grande robustesse face aux erreurs systématiques habituelles d'Ω60 et que l'agrandissement de la taille du spot laser a tendance à améliorer l'uniformité de l'illumination au détriment de l'intersection faisceau-cible.

En résumé, optimiser le système d'éclairement conjointement avec la dispostion des faisceaux est crucial. La configuration $I80$, en particulier, montre des perspectives prometteuses pour atteindre une intersection faisceau-cible élevée comparable à Ω60, tout en maintenant une qualité d'éclairement supérieure (RMS d'environ 1% de moins que Ω60).

Caractérisation de la robustesse de deux schémas d'allumage aux erreurs expérimentales à l'échelle de l'allumage

Lors de l'analyse des implosions sphériques en FCI, la qualité d'éclairement émerge comme un élément critique, en particulier au cours des premières étapes du processus d'implosion. Même de légères imperfections dans le schéma d'éclairement peuvent entraîner la génération de bas modes dans la décomposition sphérique des harmoniques de l'intensité laser. La présence de ces modes bas est extrêmement préjudiciable, car elle a le potentiel de dégrader les performances de la cible et, dans des cas sévères, de compromettre la réussite de l'allumage.

S'appuyant sur notre étude, nous avons approfondi la résilience de différents schémas d'allumage, tels que l'allumage standard par point chaud central (HS) et "shock augmented ignition" (SAI), lorsqu'ils sont soumis à l'influence d'erreurs expérimentales. Cette analyse s'est concentrée sur une configuration spécifique de la chambre à faisceaux lasers ($M72$). En exploitant des simulations hydrodynamiques radiatives en 1D et 3D, réalisées respectivement par les codes *CHIC* et *ASTER*, nous avons d'abord caractérisé les performances typiques optimales à l'échelle de l'allumage, en supposant l'absence d'erreurs liées au système.

Pour évaluer l'impact des erreurs expérimentales, nous avons systématiquement augmenté le décalage de la cible (décentralisation de la cible par rapport au centre de la chambre expérimentale), cherchant à déterminer le seuil au-delà duquel les performances de la cible se dégradaient au point de considérer la cible comme percée. De manière significative, pour de faibles erreurs de décalage proches de celles rencontrées à l'installation Ω60, l'approche SAI a montré des performances supérieures du point chaud. Cependant, pour des décalages de cible égaux ou supérieurs à $1\%R$, HS a démontré une plus grande robustesse aux variations du décalage de la cible. Cela s'est manifesté par des rendements en neutrons plus élevés, des températures moyennes du point chaud plus élevées et un point chaud avec une plus longue durée de vie dans le schéma HS dans de telles conditions.

Il est essentiel de noter que l'absence du dépôt d'énergie des particules alphas dans ces simulations peut influencer les résultats. Malgré des performaces moindres au-delà d'un certain degré de décalage de la cible, le schéma SAI a montré une densité surfacique du point chaud plus élevée. Ceci permettant potentiellement au point chaud de capturer une plus grande fraction des particules alphas. Cela suggère que les particules alphas pourraient déposer leur énergie de manière plus efficace au sein du point chaud et des couches environnantes, augmentant ainsi la probabilité de chauffage et éventuellement

d'atteindre l'allumage. Par conséquent, l'inclusion du dépôt d'énergie des particules alphas pourrait modifier la robustesse comparative des deux schémas d'allumage dans des conditions spécifiques.

Perspectives

Dans le contexte de l'utilisation du code couplé *ASTER/IFRIIT* pour des implosions à l'échelle de l'allumage, l'intégration d'un modèle polarisé pour CBET et la prise en compte de l'effet Langdon sur le gain de CBET ont déjà amélioré la description de l'absorption laser. Cependant, certains effets hydrodynamiques, en particulier l'influence des électrons à haute énergie sur la vitesse du choc, restent incomplètement traités. Les simulations existantes suggèrent un effet significatif de l'ordre de ~ 200 ps sur les timings des chocs, comme rapporté dans la référence [99]. Néanmoins, ces simulations pourraient surestimer les effets de HE en raison de la négligence des collisions à grand angle. Pour fournir une représentation plus précise, une méthode plus robuste basée sur une approche de Monte-Carlo plasma en 3D, telle que mise en œuvre dans les références [117], [118], pourrait être envisagée et intégrée à l'avenir dans les codes d'hydrodynamique 3D.

L'étude sur les géométries innovantes de la chambre expérimentales pour l'éclairement des cibles d'allumage en FCI met en évidence l'importance de l'optimisation du système d'éclairement conjointement avec la disposition des faisceaux. Cependant, cette investigation a été réalisée sans prendre en compte les effets de l'interaction laser-plasma. Une étape cruciale à venir dans l'étude consiste à examiner les effets du CBET, un facteur connu pour dégrader l'absorption laser et présenter un risque de rupture de symétrie. Il est à noter que les futures installations d'attaque directe devraient envisager l'utilisation de lasers à large bande pour atténuer les effets néfastes du CBET [132], [135]. Cette investigation supplémentaire contribuera à une compréhension plus complète de l'interaction entre les lasers et le plasma, l'hydrodynamique et les interactions faisceau-cible.

De plus, dans ce contexte, plusieurs questions demeurent sans réponse. Par exemple, la détermination du nombre optimal de lasers par port de faisceau pour une conception donnée reste une question ouverte. De plus, choisir des conceptions qui facilitent la production d'électricité pose un autre défi. On a observé que la réduction du CBET est plus efficace lorsque l'on utilise un ordre super-Gaussien plus élevé pour le profil spatial du faisceau, comme souligné dans [132]. De plus, des études indiquent qu'une infrastructure basée sur des mini-faisceaux peut nécessiter environ 10 petits faisceaux de longueurs d'onde différentes par port. Ainsi, un système laser d'une énergie totale de 1.3 MJ, utilisant des mini-faisceaux d'au moins 1.6 kJ chacun, a le potentiel d'atteindre une atténuation efficace du CBET, en particulier avec un minimum de 80 ports, comme illustrée par la géométrie $I80$.

À la lumière de ces considérations, une approche plus globale, similaire à la méthodologie récemment utilisée pour le PDD au NIF, telle que décrite dans [136], pourrait être adoptée. Cela implique l'utilisation de l'intelligence artificielle pour élaborer une nouvelle approche algorithmique efficace dans la création de configurations d'éclairement pour les expériences de physique à haute densité d'énergie menées par lasers. Cette approche présente des perspectives prometteuses pour rationaliser le processus et relever certains des défis liés à la conception et à l'optimisation des systèmes commandés par laser.

De plus, la flexibilité de cette méthode n'est pas limitée aux configurations sphériques du PDD ; elle peut également être adaptée aux cibles d'implosions. Sa polyvalence sur différentes géométries en fait un outil précieux pour optimiser l'uniformité de l'éclairement dans divers scénarios, y compris les hohlraums. La pertinence de l'algorithme est d'autant plus soulignée par son application potentielle à l'attaque directe. En prévision de futures conceptions d'attaque directe nécessitant plusieurs faisceaux par port pour équilibrer l'uniformité de l'éclairement et l'efficacité de la chambre [132], [137], les limites des techniques traditionnelles deviennent évidentes, nécessitant des méthodes d'optimisation itératives pour atteindre l'uniformité laser requise.

Résumé détaillé

Le concept de la fusion par confinement inertiel (FCI) est de brûler quelques milligrammes de combustible (souvent un mélange de DT) comprimé à plus de 1000 fois la densité solide pendant un intervalle de temps relativement court au sein duquel l'inertie de masse maintient l'ensemble en combustion. Les densités requises peuvent être obtenues en faisant imploser des coquilles par un rayonnement haute-puissance délivré par un laser externe. La méthode d'allumage retenue de nos jours est celle dite par point chaud central. Elle consiste à enflammer la cible grâce à un point chaud qui vérifie les conditions d'allumage et à partir duquel la combustion se propage au DT comprimé et froid environnant. Des méthodes alternatives existent telle que l'allumage par choc qui découple les phases de compression et d'allumage de cible afin de maximiser le gain total. Dans un premier temps, la cible est comprimée avec un laser nanoseconde atteignant des puissances de l'ordre de plusieurs dizaines de TW. La partie externe de la coquille est ablatée, et la cible est comprimée via un effet fusée. Ensuite, une impulsion brève très intense de plusieurs centaines de TW est lancée et créée une onde de choc, dite d'allumage, qui va être amplifiée en convergeant vers le centre et va porter le combustible aux températures et pressions adéquates à l'entretien des réactions de fusion et à l'inflammation du combustible. Dans ce but, la compression doit être particulièrement symétrique et éviter au maximum les instabilités hydrodynamiques. Notamment, les perturbations de bas modes peuvent conduire à la perforation ou à la rupture de la cible en vol, tandis que les perturbations de hauts modes peuvent conduire à un mélange de combustible à petite échelle dans le point chaud ou la perforation de la cible, empêchant ainsi l'allumage.

De plus, lorsque le paramètre d'interaction $I\lambda_L^2$ franchit le seuil de $\sim 10^{14}$ W μm^2/cm^2, l'interaction laser plasma devient sujette à de nombreux couplages entre ondes électromagnétiques et plasma. La plupart de ces processus additionnels ont des comportements non linéaires et sont en général néfastes à l'implosion en FCI. C'est notamment le cas du transfert d'énergie entre faisceaux croisés (CBET). Le CBET est un processus qui se produit lorsque deux ou plusieurs faisceaux laser se croisent dans un plasma et se couplent de manière résonante par le biais d'ondes acoustiques ioniques. Lors des expériences de fusion par confinement inertiel sur les grandes installations laser telles que le LMJ en région bordelaise ou le NIF aux États-Unis, les lasers sont amenés à se propager à travers des plasmas de grandes tailles (plusieurs millimètres). Un grand nombre d'instabilités dites de couplages d'ondes peuvent apparaître, et diffusent la lumière dans une direction différente de l'onde électromagnétique incidente. En particulier, le CBET. L'un des principaux défis à relever dans les conceptions à l'échelle de l'allumage en attaque directe est la perte de pression d'ablation due au CBET. Sa mitigation est une étape cruciale dans la conception de designs de cibles à l'échelle de l'allumage.

Afin de prédire au mieux les expériences en FCI, la simulation numérique joue un rôle

crucial de nos jours. Dans ce but, les codes d'hydrodynamique radiative 3D modélisant les expériences FCI et utilisés pour concevoir des schémas de FCI ont considérablement progressé au cours des dernières années, en particulier lors de la modélisation de cibles à l'échelle réduite du système laser OMEGA. Pour les conceptions à l'échelle de l'allumage, une telle investigation est prospective, car il n'existe à l'heure actuelle aucun système laser à l'échelle de l'allumage en attaque directe, sauf au NIF en géométrie "polar direct drive" (PDD). Dans cette configuration, certains des faisceaux situés aux pôles sont redirigés vers l'équateur et défocalisés afin d'imiter au mieux la FCI en attaque directe.

Le CBET est particulièrement prépondérant dans la géométrie de PDD. Dans cette géométrie, le chevauchement des faisceaux est important et le CBET entraîne des modulations à grande échelle de l'intensité laser. Des expériences de couplage d'énergie, dans le cadre de la campagne SSS, pertinentes pour les conceptions de cibles d'allumage, sont menées au NIF en utilisant une sphère solide en plastique d'un rayon avoisinant les 1100 microns. Ces sphères solides présentent l'avantage de quantifier le couplage d'énergie sans les défis liés aux instabilités hydrodynamiques des implosions à coquille mince. Les implosions PDD du NIF ont mesuré le couplage d'énergie dans une série de tirs jusqu'à une intensité maximale de 3.0×10^{15} Wμm^2/cm^2 avec une impulsion temporelle de 5 à 7 ns. Des expériences similaires sur OMEGA avec des sphères solides mises à l'échelle ont été réalisées pour tester les arguments d'échelle des implosions PDD d'OMEGA au NIF.

Une bonne concordance a été obtenue entre les données mesurées (trajectoires des chocs et arrivée des chocs au centre de la cible) et les trajectoires des simulations 2D du code *DRACO* utilisant les modèles CBET et de transport de chaleur non local. Cependant, ces modèles à l'échelle du NIF ont été ajustés manuellement pour reproduire les données expérimentales (avec plusieurs paramètres ad hoc sur le profil du laser et le coefficient CBET) et ne peuvent donc pas être considérés comme robustes pour cette échelle. De plus, des quantités plus détaillées telles que la dépendance angulaire de la lumière diffusée ne sont pas reproduites correctement. En particulier, cela empêche des études plus générales du concept de la FCI à cette échelle et en présence de grandes quantités de CBET (ce qui est notamment le cas de SI). Récemment, un modèle de suivi inverse des rayons laser sans paramètres *ad hoc*, *IFRIIT*, spécifiquement conçu pour la FCI en attaque directe, a été implémenté en ligne dans le code d'hydrodynamique radiative 3D *ASTER*. Le couplage entre les deux codes montre des résultats prometteurs et robustes à l'échelle réduite d'OMEGA. *ASTER/IFRIIT* a été bien validé à l'échelle d'OMEGA et le principal objectif du projet est de les valider à l'échelle du NIF dans une géométrie PDD en utilisant la campagne expérimentale SSS comme référence.

Après avoir implémenté la défocalisation des faisceaux lasers sur *IFRIIT*, nous avons effectué la simulation de deux tirs ayant eu lieu pendant la campagne de SSS : N190204-003 et N210519. Le modèle CBET mis en œuvre dans *IFRIIT*, couplé en ligne avec *ASTER*, a été étudié à l'échelle de l'allumage/NIF en comparant les positions des chocs et les cartes de lumière diffusée dans des expériences de couplage de sphères solides. L'absorption du laser dans le code couplé concorde avec les résultats expérimentaux de FABS et SLTD (voir Figure 6.2). L'arrivée du choc au centre de la cible reste un peu décalée avec les données expérimentales (voir Figure 6.1), mais peut être améliorée en utilisant un modèle plus détaillé et complet pour le CBET déjà inclus dans *IFRIIT* (CBET polarisé + effet Langdon sur CBET), qui diminue l'absorption du laser. Ces phénomènes supplémentaires n'ont d'abord pas été inclus pour des raisons de temps de calcul (en effet, le CBET polar-

isé nécessite 4 × plus de ressources informatiques que le CBET seul). Enfin, l'utilisation d'un modèle plus récent pour le calcul du logarithme Coulombien pourrait jouer un rôle important dans l'absorption du laser [109]. Ce modèle prend en compte l'effet Langdon, les corrections d'écrantage et une dépendance du logarithme sur la fréquence du laser plutôt que sur la fréquence du plasma, et a déjà montré des résultats précis par rapport aux mesures effectuées pour de nombreux tirs sur OMEGA. Sur la base de ces résultats, le code *ASTER/IFRIIT* peut être utilisé en toute confiance pour étudier la physique de la FCI à pleine échelle.

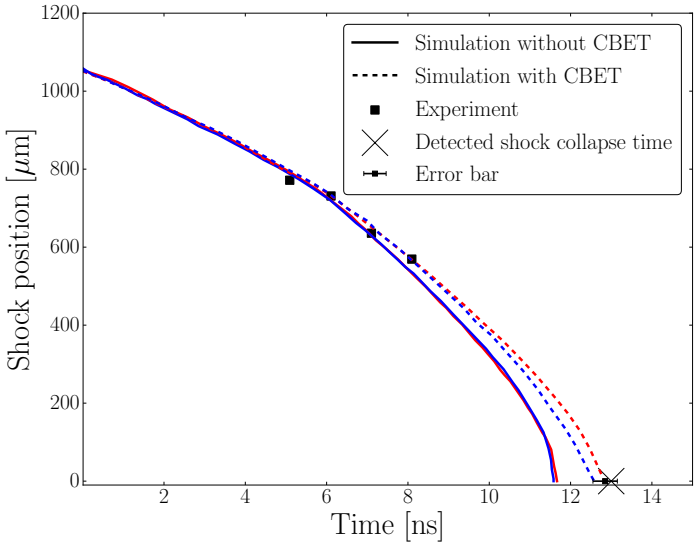

Figure 6.1 – Les positions des chocs équatoriaux et polaires de la simulation 3D *ASTER-/IFRIIT* sont respectivement présentées par des courbes rouges et bleues. Les données expérimentales sont représentées par des carrés sombres, intégrées sur les angles azimutaux et moyennées sur les différents angles polaires du diagnostic (± 22.5°, 67.5°, 122.5° et 157.5°). La trajectoire a été enregistrée à l'aide d'un "pinhole imager" sur une "x-ray framing camera" avec une résolution temporelle de 100 ps et une résolution spatiale de 30 μm. La croix sombre représente le temps d'arrivée du choc au centre de la cible détecté lors de l'expérience.

L'approche d'allumage en attaque directe est privilégiée pour la production d'énergie, car elle présente des conceptions de cibles plus simples et communique plus d'énergie à celles-ci. Actuellement, il n'existe pas d'installation laser à l'échelle d'allumage configurée pour l'approche directe standard.

Bien que l'approche en attaque directe vise à améliorer le couplage énergétique par rapport à l'attaque indirecte, l'attaque directe au laser rend plus difficile l'obtention d'une homogénéité d'éclairement élevée. Jusqu'à présent, les études approfondies sur les schémas d'éclairement en attaque directe ont principalement mis l'accent sur les aspects géométriques [8]–[10]. Cependant, garantir une illumination uniforme d'une bille de combustible reste un défi majeur en FCI, influençant les conceptions de la cible et du réacteur [11]. La qualité d'une illumination peut être décrite par l'écart quadratique moyen :

$$\sigma^2_{\mathrm{rms}} = \frac{1}{4\pi\langle I\rangle^2}\int |I(\theta,\phi) - \langle I\rangle|^2 \mathrm{d}\Omega, \tag{6.4.1}$$

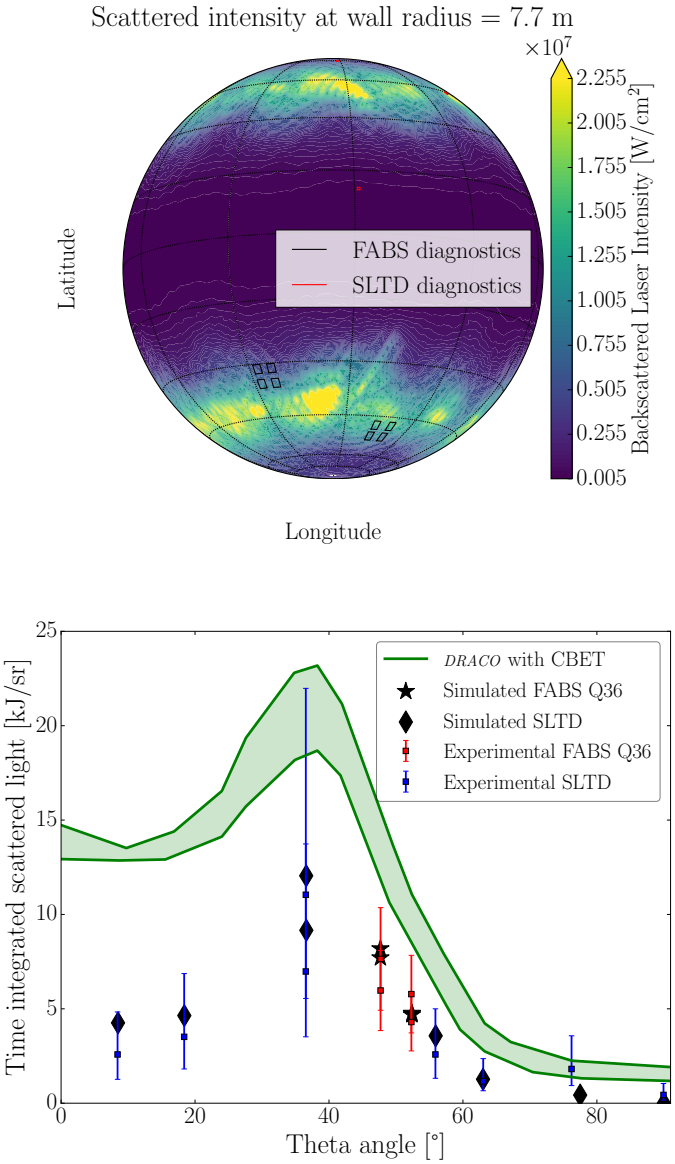

Figure 6.2 – Projection orthogonale de l'intensité laser rétrodiffusée au niveau de la paroi à $t = 100$ ps (en haut). Les carrés noirs et rouges représentent la position et la surface des diagnostics. L'intégrale temporelle de la lumière rétrodiffusée en fonction de l'angle theta/latitude (en bas) est également présentée. Les angles sont affichés de 0 à 90 degrés, car le système est symétrique à l'équateur. Les croix pleines représentent les points de simulation hors ligne et les carrés associés à leurs barres d'erreur respectives sont les points de données expérimentales. Les couleurs, rouge et bleu, correspondent respectivement aux données FABS et SLTD. La courbe verte remplie correspond à la lumière diffusée maximale et minimale depuis le pôle à chaque angle. Elle est obtenue grâce au code *DRACO* [113], qui prend en compte le CBET grâce à un modèle basé sur un multiplicateur d'impulsion laser pour l'absorption.

qui est en fait la non-uniformité angulaire d'une distribution d'intensité laser, $I(\theta, \phi)$, sur une sphère. Nous définissons également $\langle I \rangle = \int I(\theta, \phi) \mathrm{d}\Omega / 4\pi$. Cependant, pour atteindre l'allumage et un gain élevé, une uniformité d'éclairement d'au maximum 1-2% rms est généralement requise [120], [121]. Via des simulations de tracé de rayons avec l'aide d'*IFRIIT*, nous avons étudié 3 différentes géométries : $M72$, $T72$ et $I80$. Ces designs de chambre expérimentale ont un nombre de faisceaux légèrement supérieur à OMEGA (60). Nous avons d'abord procédé à l'optimisation spatiale des faisceaux lasers afin d'obtenir le rms le plus petit possible pour chaque design. Nous avons pu remarquer qu'avec seulement 12 faisceaux de plus qu'à OMEGA, des designs comme $T72$ offraient des configurations avec une qualité d'éclairement jusqu'à environ 20 fois supérieure à OMEGA. Pour tous ces designs, nous n'avons considéré aucune erreur expérimentale. D'un point de vue idéaliste, en ne considérant aucune source d'erreurs expérimentales, les conceptions $T72$ semblent être les mieux adaptées pour les futures installations d'attaque directe. Une question que nous devrions maintenant nous poser est de savoir comment ces erreurs systématiques persistantes peuvent modifier la qualité d'éclairement de la cible ? Quelle est la robustesse des designs aux erreurs expérimentales ?

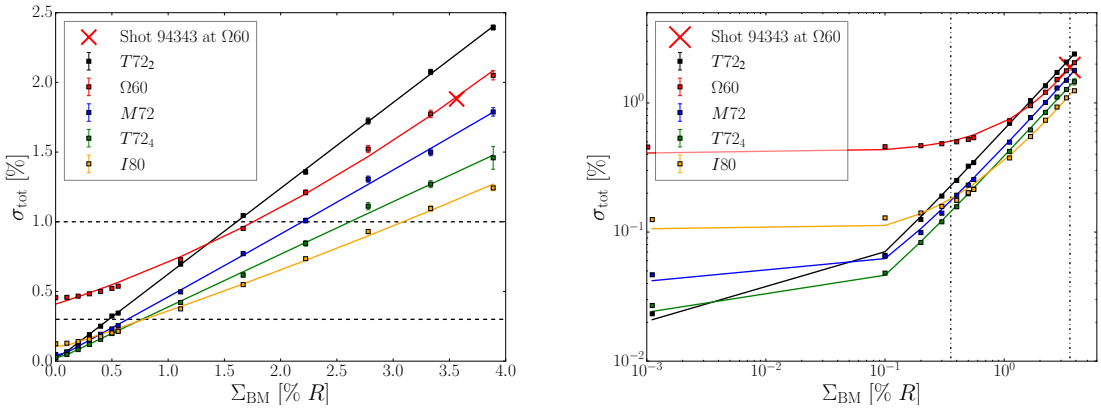

Figure 6.3 – Diagramme de dispersion de σ_{tot} par rapport à l'erreur Σ_{BM} pour toutes les installations. Des courbes ajustées sont tracées pour faciliter la visualisation des données. Chaque point est représenté avec sa barre d'erreur le long de l'axe des y. Les barres d'erreurs sont petites car de nombreux calculs ont été effectués pour chaque erreur Σ. La croix rouge (seulement du côté gauche) représente le tir 94343, l'une des meilleures performances laser à Ω60. Les figures de gauche sont à l'échelle linéaire, les figures de droite sont à l'échelle logarithmique.

Pour répondre à ces questions, nous avons procédé à un échantillonnage gaussien des erreurs que l'on retrouve systématiquement sur toute installation laser : décalage de la cible par rapport au centre de la chambre expérimentale, erreur de pointage des faisceaux et non-équilibre en puissance des faisceaux lasers. Pour chaque erreur, on effectue plusieurs centaines de simulations. L'échantillonnage gaussien et le nombre important de simulations nous permet d'obtenir des résultats robustes statistiques. Pour chaque design, on représente la qualité de l'éclairement σ_{tot} en fonction de l'erreur de décalage de la cible sur la Figure 6.3. Cette étude est montrée plus en détails dans le corps de la thèse.

Les résultats soulignent l'importance d'une approche de contrôle synchronisé prenant en compte tous ces facteurs pour garantir une uniformité d'irradiation optimale. Il est démontré que l'amélioration d'un seul aspect ne conduit pas nécessairement à des performances accrues ; au contraire, l'optimisation simultanée de tous les facteurs s'avère

cruciale. Atteindre une uniformité optimale nécessite donc de contrôler simultanément les profils des faisceaux et de minimiser les imperfections du système. Cette approche permet d'obtenir un niveau élevé d'uniformité d'éclairement avec une faible valeur rms (environ $\sigma_{\text{tot}} \approx 0.5\%$), tout en maintenant $\Sigma_{\text{err}} \leq 1.0\%$.

L'étude conclut que les configurations $I80$ et $T72_4$ se révèlent plus robustes que les autres face aux erreurs systématiques courantes d'$\Omega 60$. Cependant, une optimisation tenant compte des erreurs systématiques dès l'étude des paramètres spatiaux du laser, demeure nécessaire. L'analyse supplémentaire suggère également que la configuration $I80$ affiche une plus grande robustesse face aux erreurs systématiques habituelles d'$\Omega 60$ et que l'agrandissement de la taille du spot laser a tendance à améliorer l'uniformité de l'illumination au détriment de l'intersection faisceau-cible.

En résumé, optimiser le système d'éclairement conjointement avec la dispostion des faisceaux est crucial. La configuration $I80$, en particulier, montre des perspectives prometteuses pour atteindre une intersection faisceau-cible élevée comparable à $\Omega 60$, tout en maintenant une qualité d'éclairement supérieure (RMS d'environ 1% de moins que $\Omega 60$).

Lors de l'analyse des implosions sphériques en FCI, la qualité d'éclairement émerge comme un élément critique, en particulier au cours des premières étapes du processus d'implosion. Même de légères imperfections dans le schéma d'éclairement peuvent entraîner la génération de bas modes dans la décomposition sphérique des harmoniques de l'intensité laser. La présence de ces modes bas est extrêmement préjudiciable, car elle a le potentiel d'influencer négativement les performances de la cible et, dans des cas sévères, de compromettre la réussite de l'allumage.

S'appuyant sur notre précédente étude, nous avons approfondi la résilience de différents schémas d'allumage, tels que l'allumage standard par point chaud central (HS) et "shock augmented ignition" (SAI), lorsqu'ils sont soumis à l'influence d'erreurs expérimentales. Cette analyse approfondie s'est concentrée sur une configuration spécifique de la chambre à faisceaux lasers ($M72$). En exploitant des simulations hydrodynamiques radiatives en 1D et 3D, réalisées respectivement par les codes *CHIC* et *ASTER*, nous avons d'abord caractérisé les performances typiques optimales à l'échelle de l'allumage, en supposant l'absence d'erreurs liées au système.

Pour évaluer l'impact des erreurs expérimentales, nous avons systématiquement augmenté le décalage de la cible (décentralisation de la cible par rapport au centre de la chambre expérimentale), cherchant à déterminer le seuil au-delà duquel les performances de la cible se dégradaient au point de considérer la cible comme percée. De manière significative, pour de faibles erreurs de décalage ressemblant à celles rencontrées à l'installation $\Omega 60$, l'approche SAI a montré des performances supérieures du point chaud. Cependant, pour des décalages de cible égaux ou supérieurs à $1\%R$, HS a démontré une plus grande robustesse aux variations du décalage de la cible. Cela s'est manifesté par des rendements en neutrons plus élevés, des températures moyennes du point chaud plus élevées et un point chaud à plus longue durée de vie dans le schéma HS dans de telles conditions.

Il est essentiel de noter que l'absence du dépôt d'énergie des particules alpha dans ces simulations peut influencer les résultats. Malgré des performaces moindres au-delà d'un certain degré de décalage de la cible, le schéma SAI a montré une densité surfacique du point chaud plus élevée. Ceci permettant potentiellement au point chaud de capturer une plus grande fraction des particules alpha. Cela suggère que les particules alpha pourraient déposer leur énergie de manière plus efficace au sein du point chaud et des couches environnantes, augmentant ainsi la probabilité de chauffage et éventuellement d'atteindre l'allumage. Par conséquent, l'inclusion du dépôt d'énergie des particules alpha pour-

rait modifier la robustesse comparative des deux schémas d'allumage dans des conditions spécifiques.

Bibliography

[1] G. H. Miller, E. I. Moses, and C. R. Wuest, « The national ignition facility », *Optical Engineering*, vol. 43, no. 12, pp. 2841–2853, 2004.

[2] H. Abu-Shawareb, R. Acree, P. Adams, *et al.*, « Lawson criterion for ignition exceeded in an inertial fusion experiment », *Physical review letters*, vol. 129, no. 7, p. 075 001, 2022.

[3] J. Nuckolls, L. Wood, A. Thiessen, and G. Zimmerman, « Laser compression of matter to super-high densities: thermonuclear (ctr) applications », *Nature*, vol. 239, no. 5368, pp. 139–142, 1972.

[4] I. Igumenshchev, V. Goncharov, F. Marshall, *et al.*, « Three-dimensional modeling of direct-drive cryogenic implosions on omega », *Physics of Plasmas*, vol. 23, no. 5, 2016.

[5] A. Colaïtis, R. Follett, J. Palastro, I. Igumenschev, and V. Goncharov, « Adaptive inverse ray-tracing for accurate and efficient modeling of cross beam energy transfer in hydrodynamics simulations », *Physics of Plasmas*, vol. 26, no. 7, 2019.

[6] A. Colaïtis, I. Igumenshchev, D. Turnbull, *et al.*, « 3d simulations of inertial confinement fusion implosions part 2: systematic flow anomalies and impact of low modes on performances in omega experiments », *Plasma Physics and Controlled Fusion*, vol. 65, no. 1, p. 014 005, 2022.

[7] O. Mannion, I. Igumenshchev, K. Anderson, *et al.*, « Mitigation of mode-one asymmetry in laser-direct-drive inertial confinement fusion implosions », *Physics of Plasmas*, vol. 28, no. 4, 2021.

[8] A. J. Schmitt, « Absolutely uniform illumination of laser fusion pellets », *Applied physics letters*, vol. 44, no. 4, pp. 399–401, 1984.

[9] B. Canaud and F. Garaude, « Optimization of laser–target coupling efficiency for direct drive laser fusion », *Nuclear fusion*, vol. 45, no. 12, p. L43, 2005.

[10] M. Temporal and B. Canaud, « Numerical analysis of the irradiation uniformity of a directly driven inertial confinement fusion capsule », *The European Physical Journal D*, vol. 55, pp. 139–145, 2009.

[11] T. Norimatsu, K. Nagai, T. Takeda, K. Mima, and T. Yamanaka, « Update for the drag force on an injected pellet and target fabrication for inertial fusion », *Fusion science and technology*, vol. 43, no. 3, pp. 339–345, 2003.

[12] F. W. Aston, *A new mass-spectrograph and the whole number rule*. 1927.

[13] J. D. Lawson, « Some criteria for a power producing thermonuclear reactor », *Proceedings of the physical society. Section B*, vol. 70, no. 1, p. 6, 1957.

[14] N. Holtkamp, I. P. Team, *et al.*, « An overview of the iter project », *Fusion Engineering and Design*, vol. 82, no. 5-14, pp. 427–434, 2007.

[15] G. Fraley, E. Linnebur, R. Mason, and R. Morse, « Thermonuclear burn characteristics of compressed deuterium-tritium microspheres », *The Physics of Fluids*, vol. 17, no. 2, pp. 474–489, 1974.

[16] S. Atzeni and J. Meyer-ter-Vehn, *The physics of inertial fusion: beam plasma interaction, hydrodynamics, hot dense matter*. OUP Oxford, 2004, vol. 125.

[17] A. Zylstra, A. Kritcher, O. Hurricane, *et al.*, « Experimental achievement and signatures of ignition at the national ignition facility », *Physical Review E*, vol. 106, no. 2, p. 025 202, 2022.

[18] C. Lion, « The lmj program: an overview », in *Journal of Physics: Conference Series*, IOP Publishing, vol. 244, 2010, p. 012 003.

[19] M. Tabak, J. Hammer, M. E. Glinsky, *et al.*, « Ignition and high gain with ultrapowerful lasers », *Physics of Plasmas*, vol. 1, no. 5, pp. 1626–1634, 1994.

[20] M. Tabak, D. Clark, S. Hatchett, *et al.*, « Review of progress in fast ignition », *Physics of Plasmas*, vol. 12, no. 5, 2005.

[21] V. Shcherbakov, « Ignition of a laser-fusion target by a focusing shock wave », *Sov. J. Plasma Phys.(Engl. Transl.);(United States)*, vol. 9, no. 2, 1983.

[22] R. Betti, C. Zhou, K. Anderson, L. Perkins, W. Theobald, and A. Solodov, « Shock ignition of thermonuclear fuel with high areal density », *Physical review letters*, vol. 98, no. 15, p. 155 001, 2007.

[23] A. Vallet, « Hydrodynamic modelling of the shock ignition scheme for inertial confinement fusion », Ph.D. dissertation, Bordeaux, 2014.

[24] S. Obenschain, A. Schmitt, J. Bates, *et al.*, « Direct drive with the argon fluoride laser as a path to high fusion gain with sub-megajoule laser energy », *Philosophical Transactions of the Royal Society A*, vol. 378, no. 2184, p. 20 200 031, 2020.

[25] D. Kehne, M. Karasik, Y. Aglitsky, *et al.*, « Implementation of focal zooming on the nike krf laser », *Review of Scientific Instruments*, vol. 84, no. 1, 2013.

[26] I. B. Zeldovich, Y. P. Raizer, and W. D. Hayes, *Physics of shock waves and high-temperature hydrodynamic phenomena*. Academic Press New York, 1966, vol. 1.

[27] V. Goncharov, J. Knauer, P. McKenty, *et al.*, « Improved performance of direct-drive inertial confinement fusion target designs with adiabat shaping using an intensity picket », *Physics of Plasmas*, vol. 10, no. 5, pp. 1906–1918, 2003.

[28] M. Haines, « A review of the dense z-pinch », *Plasma Physics and Controlled Fusion*, vol. 53, no. 9, p. 093 001, 2011.

[29] M. Roth, T. Cowan, M. Key, *et al.*, « Fast ignition by intense laser-accelerated proton beams », *Physical review letters*, vol. 86, no. 3, p. 436, 2001.

[30] W. M. Manheimer, D. Colombant, and J. Gardner, « Steady-state planar ablative flow », *The Physics of Fluids*, vol. 25, no. 9, pp. 1644–1652, 1982.

[31] L. Spitzer Jr and R. Härm, « Transport phenomena in a completely ionized gas », *Physical Review*, vol. 89, no. 5, p. 977, 1953.

[32] R. Malone, R. McCrory, and R. Morse, « Indications of strongly flux-limited electron thermal conduction in laser-target experiments », *Physical Review Letters*, vol. 34, no. 12, p. 721, 1975.

[33] G. Schurtz, P. D. Nicolaï, and M. Busquet, « A nonlocal electron conduction model for multidimensional radiation hydrodynamics codes », *Physics of plasmas*, vol. 7, no. 10, pp. 4238–4249, 2000.

[34] S. Atzeni, A. Schiavi, J. Honrubia, *et al.*, « Fast ignitor target studies for the hiper project », *Physics of Plasmas*, vol. 15, no. 5, 2008.

[35] J. Breil, S. Galera, and P.-H. Maire, « Multi-material ale computation in inertial confinement fusion code chic », *Computers & fluids*, vol. 46, no. 1, pp. 161–167, 2011.

[36] R. E. Kidder, « Theory of homogeneous isentropic compression and its application to laser fusion », *Nuclear Fusion*, vol. 14, no. 1, p. 53, 1974.

[37] M. D. Rosen, « The physics issues that determine inertial confinement fusion target gain and driver requirements: a tutorial », *Physics of Plasmas*, vol. 6, no. 5, pp. 1690–1699, 1999.

[38] V. Goncharov, O. Gotchev, E. Vianello, *et al.*, « Early stage of implosion in inertial confinement fusion: shock timing and perturbation evolution », *Physics of plasmas*, vol. 13, no. 1, 2006.

[39] R. Nora and R. Betti, « One-dimensional planar hydrodynamic theory of shock ignition », *Physics of Plasmas*, vol. 18, no. 8, 2011.

[40] H. M. Lee, H. Kang, and D. Ryu, « Supersonic collisions between two gas streams », *arXiv preprint astro-ph/9512101*, 1995.

[41] Rayleigh, « Investigation of the character of the equilibrium of an incompressible heavy fluid of variable density », *Proceedings of the London mathematical society*, vol. 1, no. 1, pp. 170–177, 1882.

[42] G. I. Taylor, « The instability of liquid surfaces when accelerated in a direction perpendicular to their planes. i », *Proceedings of the Royal Society of London. Series A. Mathematical and Physical Sciences*, vol. 201, no. 1065, pp. 192–196, 1950.

[43] S. Hu, R. Epstein, W. Theobald, *et al.*, « Direct-drive double-shell implosion: a platform for burning-plasma physics studies », *Physical Review E*, vol. 100, no. 6, p. 063 204, 2019.

[44] T. Luo, J. Wang, C. Xie, M. Wan, and S. Chen, « Effects of compressibility and atwood number on the single-mode rayleigh-taylor instability », *Physics of fluids*, vol. 32, no. 1, 2020.

[45] H. Takabe, K. Mima, L. Montierth, and R. Morse, « Self-consistent growth rate of the rayleigh–taylor instability in an ablatively accelerating plasma », *The Physics of fluids*, vol. 28, no. 12, pp. 3676–3682, 1985.

[46] R. Betti, V. Goncharov, R. á. McCrory, and C. á. Verdon, « Growth rates of the ablative rayleigh–taylor instability in inertial confinement fusion », *Physics of Plasmas*, vol. 5, no. 5, pp. 1446–1454, 1998.

[47] J. H. Gardner, S. E. Bodner, and J. P. Dahlburg, « Numerical simulation of ablative rayleigh–taylor instability », *Physics of Fluids B: Plasma Physics*, vol. 3, no. 4, pp. 1070–1074, 1991.

[48] R. Craxton, K. Anderson, T. Boehly, *et al.*, « Direct-drive inertial confinement fusion: a review », *Physics of Plasmas*, vol. 22, no. 11, 2015.

[49] A. Colaïtis, « Multiscale description of the laser-plasma interaction: application to the physics of shock ignition in inertial confinement fusion », Ph.D. dissertation, Bordeaux, 2015.

[50] R. More, K. Warren, D. Young, and G. Zimmerman, « A new quotidian equation of state (qeos) for hot dense matter », *The Physics of fluids*, vol. 31, no. 10, pp. 3059–3078, 1988.

[51] J. Johnson, « The sesame database », Los Alamos National Lab.(LANL), Los Alamos, NM (United States), Tech. Rep., 1994.

[52] I. Igumenshchev, D. Michel, R. Shah, *et al.*, « Three-dimensional hydrodynamic simulations of omega implosions », *Physics of Plasmas*, vol. 24, no. 5, 2017.

[53] W. Huebner, A. Merts, N. Magee, and M. Argo, « Report la-6760-m », *Los Alamos National Laboratory, Los Alamos, NM*, 1977.

[54] R. Dautray and J. Watteau, *The laser inertial thermo-nuclear fusion. Part 1: the laser-matter interaction. Volume 1*. Editions Eyrolles, 1993.

[55] R. K. Follett, J. G. Shaw, J. F. Myatt, C. Dorrer, D. H. Froula, and J. P. Palastro, « Thresholds of absolute instabilities driven by a broadband laser », *Physics of Plasmas*, vol. 26, no. 6, p. 062 111, Jun. 2019, ISSN: 1070-664X. DOI: 10.1063/1.5098479. eprint: https://pubs.aip.org/aip/pop/article-pdf/doi/10.1063/1.5098479/15971452/062111_1_online.pdf. [Online]. Available: https://doi.org/10.1063/1.5098479.

[56] M. Rosenberg, A. Solodov, J. Myatt, *et al.*, « Origins and scaling of hot-electron preheat in ignition-scale direct-drive inertial confinement fusion experiments », *Physical review letters*, vol. 120, no. 5, p. 055 001, 2018.

[57] M. Hohenberger, P. Radha, J. Myatt, *et al.*, « Polar-direct-drive experiments on the national ignition facility », *Physics of Plasmas*, vol. 22, no. 5, 2015.

[58] C. McKinstrie, J. Li, R. Giacone, and H. Vu, « Two-dimensional analysis of the power transfer between crossed laser beams », *Physics of Plasmas*, vol. 3, no. 7, pp. 2686–2692, 1996.

[59] C. McKinstrie, R. Betti, R. Giacone, T. Kolber, and J. Li, « Two-dimensional stimulated brillouin scattering », *Physical Review E*, vol. 50, no. 3, p. 2182, 1994.

[60] R. Giacone, C. McKinstrie, and R. Betti, « Angular dependence of stimulated brillouin scattering in homogeneous plasma », *Physics of Plasmas*, vol. 2, no. 12, pp. 4596–4605, 1995.

[61] C. McKinstrie, A. Kanaev, V. Tikhonchuk, R. Giacone, and H. Vu, « Three-dimensional analysis of the power transfer between crossed laser beams », *Physics of Plasmas*, vol. 5, no. 4, pp. 1142–1147, 1998.

[62] W. L. Kruer, S. C. Wilks, B. B. Afeyan, and R. K. Kirkwood, « Energy transfer between crossing laser beams », *Physics of Plasmas*, vol. 3, no. 1, pp. 382–385, 1996.

[63] R. Kirkwood, B. Afeyan, W. Kruer, *et al.*, « Observation of energy transfer between frequency-mismatched laser beams in a large-scale plasma », *Physical review letters*, vol. 76, no. 12, p. 2065, 1996.

[64] V. Eliseev, W. Rozmus, V. Tikhonchuk, and C. Capjack, « Interaction of crossed laser beams with plasmas », *Physics of Plasmas*, vol. 3, no. 6, pp. 2215–2217, 1996.

[65] K. Wharton, R. Kirkwood, S. Glenzer, *et al.*, « Observation of energy transfer between identical-frequency laser beams in a flowing plasma », *Physical review letters*, vol. 81, no. 11, p. 2248, 1998.

[66] C. Labaune, H. Baldis, E. Schifano, *et al.*, « Enhanced forward scattering in the case of two crossed laser beams interacting with a plasma », *Physical Review Letters*, vol. 85, no. 8, p. 1658, 2000.

[67] T. Boehly, D. Munro, P. Celliers, *et al.*, « Demonstration of the shock-timing technique for ignition targets on the national ignition facility », *Physics of Plasmas*, vol. 16, no. 5, 2009.

[68] W. Seka, D. Edgell, J. Knauer, *et al.*, « Time-resolved absorption in cryogenic and room-temperature direct-drive implosions », *Physics of Plasmas*, vol. 15, no. 5, 2008.

[69] I. Igumenshchev, D. Edgell, V. Goncharov, *et al.*, « Crossed-beam energy transfer in implosion experiments on omega », *Physics of Plasmas*, vol. 17, no. 12, 2010.

[70] A. Colaïtis, D. Edgell, I. Igumenshchev, *et al.*, « 3d simulations of inertial confinement fusion implosions part 1: inline modeling of polarized cross beam energy transfer and subsequent drive anomalies on omega and nif », *Plasma Physics and Controlled Fusion*, vol. 65, no. 1, p. 014 003, 2022.

[71] A. Colaïtis, I. Igumenshchev, D. Turnbull, *et al.*, « 3d simulations of inertial confinement fusion implosions part 2: systematic flow anomalies and impact of low modes on performances in omega experiments », *Plasma Physics and Controlled Fusion*, vol. 65, no. 1, p. 014 005, 2022.

[72] A. Colaïtis, I. Igumenshchev, J. Mathiaud, and V. Goncharov, « Inverse ray tracing on icosahedral tetrahedron grids for non-linear laser plasma interaction coupled to 3d radiation hydrodynamics », *Journal of Computational Physics*, vol. 443, p. 110 537, 2021.

[73] A. Colaïtis, D. Edgell, I. Igumenshchev, *et al.*, « 3d simulations of inertial confinement fusion implosions part 1: inline modeling of polarized cross beam energy transfer and subsequent drive anomalies on omega and nif », *Plasma Physics and Controlled Fusion*, vol. 65, no. 1, p. 014 003, 2022.

[74] A. C. Hindmarsh, P. N. Brown, K. E. Grant, *et al.*, « Sundials: suite of nonlinear and differential/algebraic equation solvers », *ACM Transactions on Mathematical Software (TOMS)*, vol. 31, no. 3, pp. 363–396, 2005.

[75] X. Ribeyre, G. Schurtz, M. Lafon, S. Galera, and S. Weber, « Shock ignition: an alternative scheme for hiper », *Plasma Physics and Controlled Fusion*, vol. 51, no. 1, p. 015 013, 2008.

[76] L. J. Perkins, R. Betti, K. N. LaFortune, and W. H. Williams, « Shock ignition: a new approach to high gain inertial confinement fusion on the national ignition facility », *Phys. Rev. Lett.*, vol. 103, p. 045 004, 4 Jul. 2009. DOI: 10.1103/PhysRevLett.103.045004. [Online]. Available: https://link.aps.org/doi/10.1103/PhysRevLett.103.045004.

[77] M. Herrmann, M. Tabak, and J. Lindl, « A generalized scaling law for the ignition energy of inertial confinement fusion capsules », *Nuclear Fusion*, vol. 41, no. 1, p. 99, 2001.

[78] W. Kruer, *The physics of laser plasma interactions*. crc Press, 2019.

[79] J. Myatt, A. Maximov, W. Seka, R. Craxton, and R. Short, « Modeling stimulated brillouin scattering in the underdense corona of a direct drive inertial confinement fusion target », *Physics of plasmas*, vol. 11, no. 7, pp. 3394–3403, 2004.

[80] C. Randall, J. R. Albritton, and J. Thomson, « Theory and simulation of stimulated brillouin scatter excited by nonabsorbed light in laser fusion systems », *The Physics of Fluids*, vol. 24, no. 8, pp. 1474–1484, 1981.

[81] I. Igumenshchev, W. Seka, D. Edgell, *et al.*, « Crossed-beam energy transfer in direct-drive implosions », *Physics of Plasmas*, vol. 19, no. 5, p. 056 314, 2012.

[82] P. Michel, L. Divol, E. Williams, *et al.*, « Energy transfer between laser beams crossing in ignition hohlraums », *Physics of Plasmas*, vol. 16, no. 4, p. 042 702, 2009.

[83] S. Skupsky, J. Marozas, R. Craxton, *et al.*, « Polar direct drive on the national ignition facility », *Physics of Plasmas*, vol. 11, no. 5, pp. 2763–2770, 2004.

[84] T. Collins, J. Marozas, K. Anderson, *et al.*, « A polar-drive–ignition design for the national ignition facility », *Physics of Plasmas*, vol. 19, no. 5, p. 056 308, 2012.

[85] P. Radha, M. Hohenberger, D. Edgell, *et al.*, « Direct drive: simulations and results from the national ignition facility », *Physics of Plasmas*, vol. 23, no. 5, p. 056 305, 2016.

[86] T. Boehly, D. Brown, R. Craxton, *et al.*, « Sj bucks, sa letzring, fj marshall, rl mccrory, sfb morse, w. seka, jm soures, and cp verdon », *Opt. Commun*, vol. 133, p. 495, 1997.

[87] V. Goncharov, T. Sangster, T. Boehly, *et al.*, « Demonstration of the highest deuterium-tritium areal density using multiple-picket cryogenic designs on omega », *Physical review letters*, vol. 104, no. 16, p. 165 001, 2010.

[88] T. Sangster, V. Goncharov, R. Betti, *et al.*, « Improving cryogenic deuterium–tritium implosion performance on omega », *Physics of Plasmas*, vol. 20, no. 5, p. 056 317, 2013.

[89] P. Radha, V. Goncharov, T. Collins, *et al.*, « Two-dimensional simulations of plastic-shell, direct-drive implosions on omega », *Physics of Plasmas*, vol. 12, no. 3, p. 032 702, 2005.

[90] A. Bell, R. Evans, and D. Nicholas, « Elecron energy transport in steep temperature gradients in laser-produced plasmas », *Physical Review Letters*, vol. 46, no. 4, p. 243, 1981.

[91] J. Miquel, C. Lion, and P. Vivini, « The laser mega-joule: lmj & petal status and program overview », in *Journal of Physics: Conference Series*, IOP Publishing, vol. 688, 2016, p. 012 067.

[92] J. D. Lindl, P. Amendt, R. L. Berger, *et al.*, « The physics basis for ignition using indirect-drive targets on the national ignition facility », *Physics of plasmas*, vol. 11, no. 2, pp. 339–491, 2004.

[93] C. Li, F. Séguin, J. Frenje, *et al.*, « Effects of nonuniform illumination on implosion asymmetry in direct-drive inertial confinement fusion », *Physical review letters*, vol. 92, no. 20, p. 205 001, 2004.

[94] R. Betti, « A milestone in fusion research is reached », *Nature Reviews Physics*, vol. 5, no. 1, pp. 6–8, 2023.

[95] J. Marozas, F. Marshall, R. Craxton, *et al.*, « Polar-direct-drive simulations and experiments », *Physics of plasmas*, vol. 13, no. 5, 2006.

[96] L. Ceurvorst, W. Theobald, M. Rosenberg, *et al.*, « Development of an x-ray radiography platform to study laser-direct-drive energy coupling at the national ignition facility », *Review of Scientific Instruments*, vol. 93, no. 10, 2022.

[97] S. Regan, V. Goncharov, T. Sangster, *et al.*, « The national direct-drive program: omega to the national ignition facility », *Fusion Science and Technology*, vol. 73, no. 2, pp. 89–97, 2018.

[98] J. Marozas, M. Hohenberger, M. Rosenberg, *et al.*, « First observation of cross-beam energy transfer mitigation for direct-drive inertial confinement fusion implosions using wavelength detuning at the national ignition facility », *Physical review letters*, vol. 120, no. 8, p. 085 001, 2018.

[99] D. Barlow, T. Goffrey, K. Bennett, *et al.*, « Role of hot electrons in shock ignition constrained by experiment at the national ignition facility », *Physics of Plasmas*, vol. 29, no. 8, p. 082 704, 2022.

[100] M. J. Rosenberg, A. A. Solodov, C. Stoeckl, *et al.*, « Hot electron preheat in hydrodynamically scaled direct-drive inertial confinement fusion implosions on the nif and omega », *Physics of Plasmas*, vol. 30, no. 7, 2023.

[101] C. Yeamans, G. Kemp, Z. Walters, *et al.*, « High yield polar direct drive fusion neutron sources at the national ignition facility », *Nuclear Fusion*, vol. 61, no. 4, p. 046 031, 2021.

[102] D. Froula, D. Bower, M. Chrisp, *et al.*, « Full-aperture backscatter measurements on the national ignition facility », *Review of scientific instruments*, vol. 75, no. 10, pp. 4168–4170, 2004.

[103] M. Hohenberger, F. Albert, N. Palmer, *et al.*, « Time-resolved measurements of the hot-electron population in ignition-scale experiments on the national ignition facility », *Review of Scientific Instruments*, vol. 85, no. 11, p. 11D501, 2014.

[104] K. Anderson, R. Betti, P. McKenty, *et al.*, « A polar-drive shock-ignition design for the national ignition facility », *Physics of Plasmas*, vol. 20, no. 5, 2013.

[105] G. Kyrala, S. Dixit, S. Glenzer, *et al.*, « Measuring symmetry of implosions in cryogenic hohlraums at the nif using gated x-ray detectors », *Review of Scientific Instruments*, vol. 81, no. 10, 2010.

[106] L. Ceurvorst, W. Theobald, M. Rosenberg, *et al.*, « Diagnosing polar-direct-drive energy coupling at the national ignition facility », *Bulletin of the American Physical Society*, 2022.

[107] P. Michel, W. Rozmus, E. Williams, *et al.*, « Stochastic ion heating from many overlapping laser beams in fusion plasmas », *Physical Review Letters*, vol. 109, no. 19, p. 195 004, 2012.

[108] Y. T. Lee and R. More, « An electron conductivity model for dense plasmas », *The Physics of fluids*, vol. 27, no. 5, pp. 1273–1286, 1984.

[109] D. Turnbull, J. Katz, M. Sherlock, *et al.*, « Inverse bremsstrahlung absorption », *Physical Review Letters*, vol. 130, no. 14, p. 145 103, 2023.

[110] T. W. Johnston and J. M. Dawson, « Correct values for high-frequency power absorption by inverse bremsstrahlung in plasmas », *The Physics of Fluids*, vol. 16, no. 5, pp. 722–722, 1973.

[111] A. B. Langdon, « Nonlinear inverse bremsstrahlung and heated-electron distributions », *Physical Review Letters*, vol. 44, no. 9, p. 575, 1980.

[112] D. Turnbull, A. Colaïtis, R. Follett, *et al.*, « Crossed-beam energy transfer: polarization effects and evidence of saturation », *Plasma Physics and Controlled Fusion*, vol. 60, no. 5, p. 054 017, 2018.

[113] D. Keller, T. J. B. Collins, J. A. Delettrez, *et al.*, « Draco—a new multidimensional hydrocode », *Bull. Am. Phys. Soc.*, vol. 44, no. 37, 1999.

[114] A. Colaïtis, T. Chapman, D. Strozzi, L. Divol, and P. Michel, « A tesselation-based model for intensity estimation and laser plasma interactions calculations in three dimensions », *Physics of Plasmas*, vol. 25, no. 3, 2018.

[115] R. Betti, W. Theobald, C. Zhou, *et al.*, « Shock ignition of thermonuclear fuel with high areal densities », in *Journal of Physics: Conference Series*, IOP Publishing, vol. 112, 2008, p. 022 024.

[116] A. Colaïtis, G. Duchateau, X. Ribeyre, *et al.*, « Coupled hydrodynamic model for laser-plasma interaction and hot electron generation », *Physical Review E*, vol. 92, no. 4, p. 041 101, 2015.

[117] A. Tentori, A. Colaïtis, and D. Batani, « 3D Monte-Carlo model to study the transport of hot electrons in the context of inertial confinement fusion. Part I », *Matter and Radiation at Extremes*, vol. 7, no. 6, p. 065 902, 2022.

[118] A. Tentori, A. Colaïtis, and D. Batani, « 3D Monte-Carlo model to study the transport of hot electrons in the context of inertial confinement fusion. Part II », *Matter and Radiation at Extremes*, vol. 7, no. 6, p. 065 903, 2022.

[119] M. Murakami, N. Sarukura, H. Azechi, M. Temporal, and A. Schmitt, « Optimization of irradiation configuration in laser fusion utilizing self-organizing electrodynamic system », *Physics of Plasmas*, vol. 17, no. 8, p. 082 702, 2010.

[120] M. Murakami, « Irradiation system based on dodecahedron for inertial confinement fusion », *Applied physics letters*, vol. 66, no. 13, pp. 1587–1589, 1995.

[121] R. McCrory, J. Soures, C. Verdon, *et al.*, « Laser compression and stability in inertial confinement fusion », *Plasma Physics and Controlled Fusion*, vol. 31, no. 10, p. 1517, 1989.

[122] A. Colaïtis, D. Turnbull, I. Igumenschev, *et al.*, « 3d simulations capture the persistent low-mode asymmetries evident in laser-direct-drive implosions on omega », *Physical Review Letters*, vol. 129, no. 9, p. 095 001, 2022.

[123] D. Michel, I. Igumenshchev, A. Davis, *et al.*, « Subpercent-scale control of 3d low modes of targets imploded in direct-drive configuration on omega », *Physical Review Letters*, vol. 120, no. 12, p. 125 001, 2018.

[124] A. Lees, R. Betti, J. Knauer, *et al.*, « Experimentally inferred fusion yield dependencies of omega inertial confinement fusion implosions », *Physical Review Letters*, vol. 127, no. 10, p. 105 001, 2021.

[125] A. Shvydky, W. Trickey, A. Maximov, I. Igumenshchev, P. McKenty, and V. Goncharov, « Optimization of irradiation configuration using spherical t-designs for laser-direct-drive inertial confinement fusion », *Nuclear Fusion*, vol. 63, no. 1, p. 014 004, 2022.

[126] M. Murakami and D. Nishi, « Optimization of laser illumination configuration for directly driven inertial confinement fusion », *Matter and Radiation at Extremes*, vol. 2, no. 2, pp. 55–68, 2017.

[127] P. Delsarte, J.-M. Goethals, and J. J. Seidel, « Spherical codes and designs », in *Geometry and Combinatorics*, Elsevier, 1991, pp. 68–93.

[128] R. Williams, *The geometrical foundation of natural structure: A source book of design*. Dover Publications, 1979.

[129] W. P. Thurston, « Shapes of polyhedra and triangulations of the sphere », *arXiv preprint math/9801088*, 1998.

[130] S. Skupsky and K. Lee, « Uniformity of energy deposition for laser driven fusion », *Journal of Applied Physics*, vol. 54, no. 7, pp. 3662–3671, 1983.

[131] A. Colaiïtis, I. Igumenshchev, D. Turnbull, *et al.*, « 3d simulations of inertial confinement fusion implosions part 2: systematic flow anomalies and impact of low modes on performances in omega experiments », *Plasma Physics and Controlled Fusion*, vol. 65, no. 1, p. 014 005, 2022.

[132] A. Colaiïtis, R. K. Follett, C. Dorrer, *et al.*, « Exploration of cross-beam energy transfer mitigation constraints for designing an ignition-scale direct-drive inertial confinement fusion driver », *Physics of Plasmas*, vol. 30, no. 8, 2023.

[133] R. Scott, D. Barlow, W. Trickey, *et al.*, « Shock-augmented ignition approach to laser inertial fusion », *Physical Review Letters*, vol. 129, no. 19, p. 195 001, 2022.

[134] A. Colaïtis, X. Ribeyre, E. Le Bel, G. Duchateau, P. Nicolaï, and V. Tikhonchuk, « Influence of laser induced hot electrons on the threshold for shock ignition of fusion reactions », *Physics of Plasmas*, vol. 23, no. 7, 2016.

[135] J. Bates, J. Myatt, J. Shaw, *et al.*, « Mitigation of cross-beam energy transfer in inertial-confinement-fusion plasmas with enhanced laser bandwidth », *Physical Review E*, vol. 97, no. 6, p. 061 202, 2018.

[136] D. Barlow, A. Colaïtis, D. Viala, *et al.*, « A new optimization methodology for polar direct drive illuminations at the national ignition facility », *Physical Review Letters*, 2023.

[137] D. Eimerl, E. M. Campbell, W. F. Krupke, *et al.*, « Stardriver: a flexible laser driver for inertial confinement fusion and high energy density physics », *Journal of Fusion Energy*, vol. 33, pp. 476–488, 2014.